



HAL
open science

Collisional excitation of astrophysical molecules induced by H₂O and CO molecules

Michal Zoltowski

► **To cite this version:**

Michal Zoltowski. Collisional excitation of astrophysical molecules induced by H₂O and CO molecules. Astrophysics [astro-ph]. Normandie Université, 2023. English. NNT : 2023NORMLH01 . tel-04171926

HAL Id: tel-04171926

<https://theses.hal.science/tel-04171926>

Submitted on 27 Jul 2023

HAL is a multi-disciplinary open access archive for the deposit and dissemination of scientific research documents, whether they are published or not. The documents may come from teaching and research institutions in France or abroad, or from public or private research centers.

L'archive ouverte pluridisciplinaire **HAL**, est destinée au dépôt et à la diffusion de documents scientifiques de niveau recherche, publiés ou non, émanant des établissements d'enseignement et de recherche français ou étrangers, des laboratoires publics ou privés.



Normandie Université

THÈSE

Pour obtenir le diplôme de doctorat

Spécialité PHYSIQUE

Préparée au sein de l'Université Le Havre Normandie

Collisional Excitation of Astrophysical Molecules Induced by H₂O and CO molecules

Présentée et soutenue par
MICHAL ZOLTOWSKI

Thèse soutenue le 26/01/2023
devant le jury composé de

M. PAUL DAGDIGIAN	EMERITUS ACADEMY PROFESSOR, JOHNS HOPKINS UNIVERSITY	Rapporteur du jury
MME MARIE-LISE DUBERNET	ASTRONOME, OBSERVATOIRE DE PARIS	Rapporteur du jury
M. NICOLAS BIVER	CHARGE DE RECHERCHE, OBSERVATOIRE DE PARIS	Membre du jury
M. ALEXANDRE FAURE	DIRECTEUR DE RECHERCHE, UNIVERSITE GRENOBLE ALPES	Membre du jury
M. PIOTR ZUCHOWSKI	ASSOCIATED PROFESSOR, NICOLAUS COPERNICUS UNIVERSITY TORUN	Membre du jury
M. IAN SIMS	PROFESSEUR DES UNIVERSITES, UNIVERSITE RENNES 1	Président du jury
M. FRANÇOIS LIQUE	PROFESSEUR DES UNIVERSITES, UNIVERSITE RENNES 1	Directeur de thèse
M. JEROME LOREAU	ASSISTANT PROFESSOR, KU LEUVEN	Co-directeur de thèse

Thèse dirigée par **FRANÇOIS LIQUE (Laboratoire Ondes et Milieux Complexes)** et **JEROME LOREAU**



LABORATOIRE ONDES
et MILIEUX COMPLEXES

Tą pracę dedykuje mojemu Dziadkowi Tadeuszowi. Żałuję że nie doczekałeś jej końca.

ACKNOWLEDGEMENT

I would like to express my deepest gratitude and appreciation to my thesis supervisors, Prof. François Lique, Prof. Jérôme Loreau, and Prof. Piotr Żuchowski, for all the support and guidance I received during this journey. I would also like to say a big thank you to my team who has supported me on a daily basis. I have been encouraged, sustained, inspired, and tolerated by the greatest group of friends that one could even imagine. Thank you Amélie for always trying to cheer me up. Thank you Benjamin for all the support and help. Thank you Paul for always helping me with daily problems. Thank you Sandor and Cheikh for all your help in solving problems with my scientific work. Thank you Marie for all the good words and guidance that you gave me. Thank you Rafael for your support during the writing of the thesis. Finally, thank you all for everything - I could not have done it without you! I would like to thank Guillaume Raffy for all the help with setting the calculations on supercomputers. I would also like to thank my external collaborators: Dr. Dariusz Kędziera, Dr. Agata Karska Dr. Jacek Kłos, Dr. Martin Cordiner, and Dr. Alexandre Faure. I would like to thank my colleagues and the administration staff at Le Havre University and Rennes University 1 for all the support in dealing with administrations problems.

The final part of the acknowledgments is dedicated to my parents and friends in Poland, so it will be written in Polish.

Ta praca nie należy tylko do mnie. Nie byłbym w stanie jej ukończyć, gdyby nie najważniejsze osoby w moim życiu. Zaczynając od moich rodziców, Zofii i Stanisława, oraz mojego dziadka Tadeusza, którego już niestety z nami nie ma, a kończąc na moich najbliższych przyjaciółkach, Anrzeju, Dominice i Pawle. Byłem zachęcany, inspirowany i tolerowany nie tylko przez moją rodzinę, ale także przez najwspanialszą grupę przyjaciół, jaką ktokolwiek i kiedykolwiek mógł sobie wyobrazić. Z całego serca dziękuję Wam za wszystko!

ABSTRACT

The accurate determination of physical and chemical conditions in astronomical media can often only be inferred by interpreting molecular spectra. Given the observational progresses afforded with for example the fully operating Atacama Large Millimeter Array telescope and the recently launched James Webb Space Telescope, astronomy enters its golden age, with new molecules detected at an exponential rate. Modelling their spectra requires however to know the population of energy levels of chemical species. Such quantity is easy to derive when the local thermodynamic equilibrium (LTE) is fulfilled. Unfortunately, for most of the astrophysical media, the density is so low that the LTE cannot be maintained. Thus, radiative and collisional properties of the observed molecular species become absolutely needed for interpreting the spectra. This is a real challenge: indeed, whereas radiative properties are characterized by Einstein coefficients, relatively easily obtained through analytical formulas, collisional data are system-specific and much more complicated to obtain, notably because they can only be computed for small molecules (up to a few atoms) colliding with light partners such as hydrogen, helium, or hydrogen molecule. But in media like cometary or planetary atmospheres, the dominant colliders are heavy molecules, such as H_2O , CO , etc. Systems with such colliders are thus creating important methodological and theoretical difficulties for collisional studies. This work focuses on assessing the extent to which already available techniques and methodologies can be optimized to treat these complicated systems. Our methodology was first tested on systems important for modelling the interstellar medium (H_2O - H_2 and its isotopologues), before addressing systems such as CO - CO , H_2O - HNC and H_2O - HCN , which are crucial in better understanding cometary atmospheres. Given that no prospects of *in situ* missions are envisioned in such environments in near future, spectroscopic observations constitute the main access to them: hence the importance to estimate the level of accuracy of the collisional data that can be provided through these optimized methods.

TABLE OF CONTENTS

ACKNOWLEDGEMENT	iv
ABSTRACT	v
LIST OF TABLES	viii
LIST OF ILLUSTRATIONS	ix
CHAPTER 1 : INTRODUCTION	1
1.1 Context	1
1.2 Observational studies	6
1.3 Determining collisional rate coefficients	11
1.4 Outline of the thesis	15
CHAPTER 2 : METHODS	19
2.1 Molecular physics	19
2.2 Ab-initio calculations	23
2.3 Collision Dynamics	29
2.4 Radiative Transfer	40
CHAPTER 3 : COLLISIONS INVOLVING H ₂ O MOLECULES	46
3.1 Scattering Methods	46
3.2 H ₂ O - <i>para</i> -H ₂ system	49
3.3 The HCN/HNC - H ₂ O systems	64
CHAPTER 4 : THE EXCITATION OF CO INDUCED BY CO COLLISIONS : SCATTER- ING CALCULATIONS AND RADIATIVE TRANSFER MODELLING	74
4.1 Methods	74

4.2	CO-CO interaction potential	78
4.3	Rotational structure of CO	79
4.4	Results of scattering calculations	79
4.5	Radiative transfer modeling	91
CHAPTER 5 : SUMMARY AND PERSPECTIVE		101
APPENDICES		106
BIBLIOGRAPHY		151

LIST OF TABLES

TABLE 3.1	Final convergence parameters that were used in the calculations in different ranges of total energies.	52
TABLE 3.2	Rotational constants of water and its isotopologues. The reduced mass in the last column correspond to the reduced mass of the systems for which the species presented were interacting with the hydrogen molecule.	62
TABLE 4.1	Comparison of the interaction energy of the CO-CO system at the positions of global minimum, calculated in three different studies (See text for more details).	79
TABLE 4.2	Cross-sections calculated with CC and CS approach at a total energy of 20 cm^{-1} . Presented cross-sections are in a unit of \AA^2 and were calculated and sum for the first four total angular momenta ($J = 0, 1, 2, 3$). The columns with the "-IDN" shortcut provide results calculated treating CO molecules as indistinguishable. Columns with "-NIDN" provides results where CO were treated as distinguishable molecules.	80
TABLE 4.3	Asymptotic energy levels of the $(\text{CO})_2$ dimer for which the rate coefficients has been computed.	81

LIST OF ILLUSTRATIONS

FIGURE 1.1	Types of the media in the ISM. The dashed line present constant-pressure line. Picture taken from the book <i>Introduction to Astrochemistry</i>	2
FIGURE 1.2	Photograph of C/2012 S1(ISON) taken by Aaron Kingery on November 12, 2013. Credits to NASA/MSFC	4
FIGURE 1.3	Relative abundance with respect to water of selected molecules detected in comets. The blue bars indicate the range of relative abundance that was measured in the different comets. Figure taken from the work of N.Biver and D. Bockel�e-Morvan (2019)	5
FIGURE 1.4	Photography of ALMA, at the Atacama desert. Credit:Clem and Adri Bacri-Normier (wingsforscience.com)/ESO	6
FIGURE 1.5	The photography of the Neptune, taken with the three different telescopes. Credits to Voyager: NASA/JPL-Caltech Hubble: NASA, ESA, A. Simon (Goddard Space Flight Center), and M.H. Wong (University of California, Berkeley) and the OPAL team.	7
FIGURE 1.6	Photos taken by Rosseta probe of the 67P/Churyumov–Gerasimenko comet. Credit: OSIRIS: ESA/ Rosetta/ MPS for OSIRIS Team MPS/ UPD/ LAM/ IAA /SSO /INTA /UPM /DASP /IDA; Nav-Cam: ESA/ Rosetta/ NavCam – CC BY-SA IGO 3.0	8
FIGURE 1.7	Two states model of radiative and collisional processes.	10
FIGURE 2.1	Example of the space-fixed system of coordinates. Blue dot represent particle with the position described by the three coordinates.	31
FIGURE 2.2	The ammonia helium system. The center of the coordinates is in the center of the mass of NH ₃ . The figure was taken from the book <i>Molecular Collisions in the Interstellar Medium</i>	33

FIGURE 2.3	Adiabatic curves represented as a function of distance. The dashed line represents the total scattering energy. The a and b curves are treated as open channels, the c and d as closed ones. Figure taken from Loreau et. al (2018)	38
FIGURE 3.1	The H ₂ O-H ₂ collision system, in Jacobi coordinate system. The θ and ϕ angles describe the position of the H ₂ O-H ₂ , θ' and ϕ' describe orientations of H ₂ molecules, and R is the distance between the both molecules. This plot was taken from the work of Scribano et al.	48
FIGURE 3.2	Comparison of cross-sections obtained with 3 different potentials for the lowest de-excitation transitions. The black line represents cross-sections obtained with 5D rigid rotor potential, the red line represents cross-sections obtained with spherically approximated potential, and green line represents results obtained with the AHR approximation. The figure was taken from the work of Scribano et al.	51
FIGURE 3.3	Cross-sections as a function of convergence parameters at total energy of 1000 cm ⁻¹ (figures in the left column) and 3000 cm ⁻¹ (figures in the right column) for de-excitation transitions 9 ₁₉ → 8 ₀₈	53
FIGURE 3.4	Potential expansion coefficients of H ₂ O (red lines), D ₂ O (blue lines) and H ₂ ¹⁸ O (green lines) molecules. The solid line represent the following set of radial coefficients $\lambda_{l_a, m_a, l_b, l} = 0, 0, 0, 0$, and the dashed line represents $\lambda_{l_a, m_a, l_b, l} = 1, 0, 2, 1$	62
FIGURE 3.5	Cross-sections of the para-water and its isotopologues as a function of collisional energy for fundamental (0 ₀₀ → 1 ₁₁) excitation transitions. The para-H ₂ was used as a collider.	63
FIGURE 3.6	Cross-sections of the para-water and its isotopologues as a function of collisional energy for fundamental (0 ₀₀ → 1 ₁₁) excitation transitions. The ortho-H ₂ was used as a collider.	64
FIGURE 3.7	Representation of the molecular geometry, for the global minimum of the HCN-H ₂ O system.	66

FIGURE 3.8	Representation of the molecular geometry, for the second minimum of the HCN-H ₂ O system.	66
FIGURE 3.9	Representation of the molecular geometry, for the global minimum of the HNC-H ₂ O system.	67
FIGURE 3.10	Representation of the molecular geometry, for the second minimum of the HNC-H ₂ O system.	67
FIGURE 3.11	Comparison of correlation energy as a function of distance for the global minimum of HCN-H ₂ O system. See the text for more detailed information.	69
FIGURE 3.12	Comparison of correlation energy as a function of distance for the second minimum of HCN-H ₂ O system. See the text for more detailed information.	69
FIGURE 3.13	Comparison of correlation energy as a function of distance for the global minimum of HNC-H ₂ O system. See the text for more detailed information.	70
FIGURE 3.14	Comparison of correlation energy as a function of distance for the second minimum of HNC-H ₂ O system. See the text for more detailed information.	70
FIGURE 3.15	Cross-sections for HCN transition from level $j_2 = 0$ to $j_2 = 1$ as a function of the basis size (j_2) of HCN. The values of j_1 refer to the rotational basis size of the <i>para</i> -H ₂ O.	72
FIGURE 3.16	Cross-sections for HNC transition from level $j_2 = 0$ to $j_2 = 1$ as a function of the basis size (j_2) of HNC. The values of j_1 refer to the rotational basis size of the <i>para</i> -H ₂ O.	73
FIGURE 3.17	Examples of adiabats for H ₂ O-HCN. The distance is in units of angstrom, and energy is in units of cm ⁻¹	73
FIGURE 4.1	Representation of the coordinates of the CO-CO system. \mathbf{R} is the distance between center of mass of the monomers, θ_1 and θ_2 are angles of presented vectors of monomers with respect to \mathbf{R} , and ϕ is a torsional angle around \mathbf{R}	75

FIGURE 4.2 CO relative population of level $j = 1$, as a function of CO density.
Calculations were preformed at kinetic temperatures of 10, 50 and
100 K. 100

CHAPTER 1

INTRODUCTION

1.1. Context

1.1.1. Astrochemistry

I would like to start this introduction with a few words about the field I am working on, Astrochemistry. In very general terms, astrochemistry is a science about molecules in space. To provide a more detailed definition, I will cite Dalgarno: *Astrochemistry is the formation, destruction, and excitation of molecules in astronomical environments and their influence on the structure, dynamics, and evolution of astronomical objects. The molecules provide powerful diagnostic probes of the ambient physical conditions in which they are found*¹. These environments have unique conditions and compositions that make them fantastic laboratories, where we can study the molecules and their chemical process of formation and destruction under extreme conditions. Even though we call these media "laboratories" we can only probe them by performing astronomical observations. To interpret the observations, and model the physical conditions in the observed media, astronomers need molecular and spectroscopic data for the observed species. These data, are obtained through experimental and/or theoretical studies. That is why it is a strongly interdisciplinary science connecting chemistry, physics, and astronomy². To progress in astrochemistry, collaboration is needed between astronomers performing observations, the experimentalists and theoreticians, which provide astronomers with the data to analyze the observations.

1.1.2. The Interstellar medium

One of the unique astrochemistry *laboratory* is the interstellar medium (ISM). As the name suggests, the ISM is the space between stars. It is composed of gas (99%) and dust (1%). The dust size is about 1 μm , and it is composed mostly from the silicon and carbon compounds. The gas is mostly composed of molecular and atomic hydrogen, and helium atom, the abundance of other elements or molecules is typically few order magnitude lower. The

matter in the ISM is not uniform. The media gather in form of clumps or filaments that are often called clouds. In Fig. 1.1, the density and temperature dependence is presented for different type of clouds³.

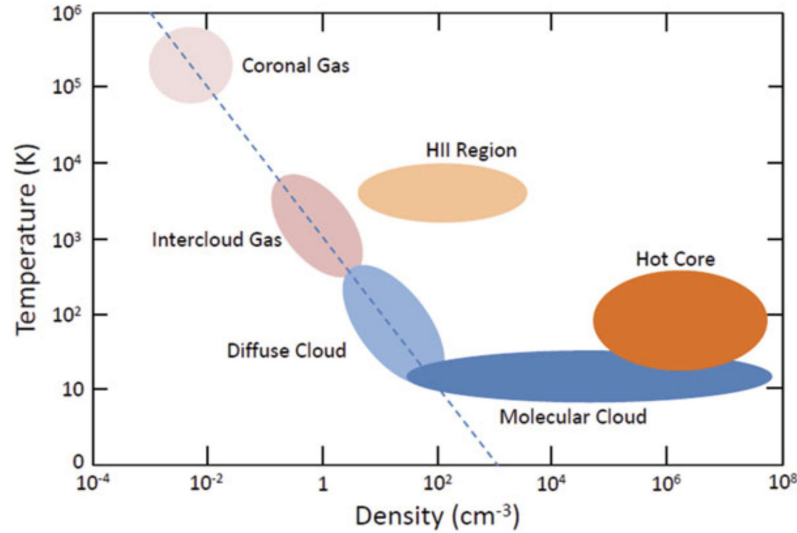


Figure 1.1: Types of the media in the ISM. The dashed line present constant-pressure line. Picture taken from the book *Introduction to Astrochemistry*³

The Coronal Gas, and Intercloud Gas, are often called the hot and warm media respectively. Both these media, together with the HII region, are usually observed close to the stars. In these media, we can find ionized species. Once these species recombine with electrons, temperature starts to decrease and density increases, the diffuse cloud starts to form. This is the place where the hydrogen molecules are formed. While the temperature drops, the density of diffuse cloud starts to increase. The UV radiations can not penetrate the cloud any further, and the abundance of hydrogen molecules starts to dominate over the abundance of hydrogen atoms. At this stage the molecular cloud forms. The molecular cloud is the media were the stars are formed. As soon as the density reaches a certain level, the matter will gravitationally collapse, and a protostar forms. The protostar will go through a few stages of evolution during which the planets and comets are formed. The life of the star end differently depending on its initial mass. The stars with similar mass to our Sun end their life as so called "dwarf" objects after losing a considerable amount of mass, that is

supplied to the nearby interstellar medium. The high mass stars (more than eight solar masses) ends their life in a supernovae explosion. During this process, heavy elements are formed through nucleosynthesis and are ejected into the interstellar medium. This matter allows the creation of new stars, and the cycle repeats. From presented type of clouds the molecules are the most frequently detected in the Diffuse and Molecular clouds³.

1.1.3. Comets

The next astrochemistry *laboratory* that I would like to introduce in this thesis are comets. These are a bit more accessible than ISM, since we can even see them with naked eyes, on night sky. Of course, with such a observation we cannot say anything about them, besides that they exist, so we still need astronomical observations to investigate their physics and chemistry. Nevertheless, since comets are way more accessible than ISM to us, *in situ* measurements are also possible (I will come back to this topic in the next section). Comets are leftovers of planetary formation process during the evolution of our Sun. They can be considered as a time capsule, since spent most of their lives away from the Sun. Thus, they have not been processed thermally on significant levels since their formation. That makes them unique sources of information, that allow us to observe the conditions during planet formation⁴. We can distinguish two main components of the comet. The first one is the icy-rocky nuclei. This is the place where all molecules formed during planet formation process stay frozen for millions of years. Once the comets approach the Sun, they start to sublimate, and those molecules are released to the comet atmosphere called comae. The comae, is the second main component of comets. Its composed of gas and dust particles. By observing and identifying molecules that were released to the comae, we can derive information about chemical and physical compositions during the formation of our planetary system. Comets are mostly built from water, but other volatile molecules such as CO, CO₂, CH₃OH, and even more complex organic molecules such as alcohols, aldehydes are also observed^{5,6}. Examples of such molecules observed in comets together with their relative abundance compared to water are presented in Fig. 1.3. As one can see, there is a lots of organic molecules that can be found in comets. Thus, there is hypothesis, saying that the organic molecules brought

to Earth by comets leads to development of life on our planet. We can divide comets into two main types: long and short periodic. Short periodic comets, are comets that have an orbital time of less than 200 years. They come from the Kuiper belt, region beyond the Neptune orbit. The long periodic comets have orbital time that is bigger than 200 year. These comets are coming to us, from out of our Solar system, mostly from the Oort Cloud. The composition of comets differ greatly from one to another, that is why they make such a great probe to investigate evolution of the star⁴.



Figure 1.2: Photograph of C/2012 S1(ISON) taken by Aaron Kingery on November 12, 2013. Credits to NASA/MSFC

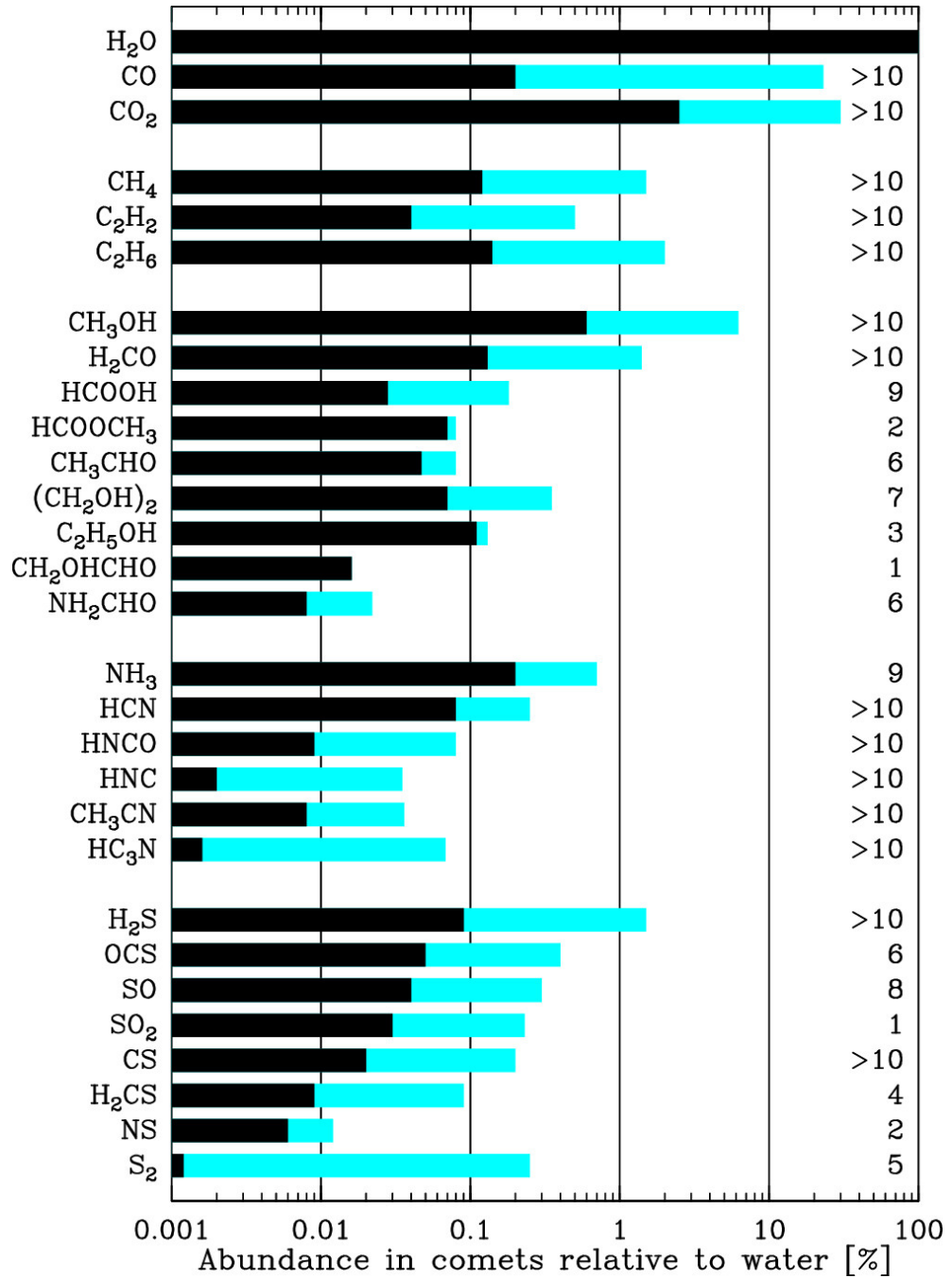


Figure 1.3: Relative abundance with respect to water of selected molecules detected in comets. The blue bars indicate the range of relative abundance that was measured in the different comets. Figure taken from the work of N. Biver and D. Bockelée-Morvan (2019)⁶

1.2. Observational studies

In the previous section I introduced where we can possibly find molecules. Here, I would like to present what kind of tools we can use to perform observations. The different types of transitions are observed in different part of the electromagnetic field. The electronic transitions in the visible and ultraviolet, the ro-vibrational transitions in near and mid infrared, and finally rotational transitions are observed in millimeter, submillimeter and radio part of the spectrum. Here, I will just focus on the last kind of transitions since they are the main aspect of this thesis, and I will present selected telescopes that allow one to observe such transitions of the molecules.

1.2.1. Observational tools

The first one is the Atacama Large Millimeter/Submillimeter Array (ALMA)⁷. It is a composition of 66 antennas (54 of 12 meters and 12 of 7 meters), spread over a distance of 16 kilometers in the Atacama desert in Chile at an altitude of 5000 m above the sea (fig. 1.4). It observes wavelengths from 0.3 mm up to 3.6 mm, giving us insight into the coldest place in our Universe.



Figure 1.4: Photography of ALMA, at the Atacama desert. Credit:Clem and Adri Bacri-Normier (wingsforscience.com)/ESO

The next one is the SOFIA telescope⁸. It is a 2.7-diameter telescope that observes in the infrared range. It is mounted on airplane and observes during flights at the altitude of about 13 km above sea level, where we are also above about 99% of Earth's atmosphere that is blocking the infrared observation. Sofia allowed us to observed objects such as star-forming regions, galaxies, black holes, comets, and asteroids. Unfortunately, the observational mission of this telescope was ended this year (2022) in September.

Next on my list is the successor of the Hubble telescope, the James Webb Space Telescope (JWST)⁹. Recently launched (December 2021), it is observing in the range of 0.6 up to 28.3 μm . It allows us to look into the oldest and faintest galaxies that were formed just after the big bang, as well as to look for Sun-type planetary systems where Earth-like exoplanets can be found. In the picture 1.5, I present a recently taken image of Neptune, compared to the photo taken with the Hubble telescope and Voyager 2 mission.

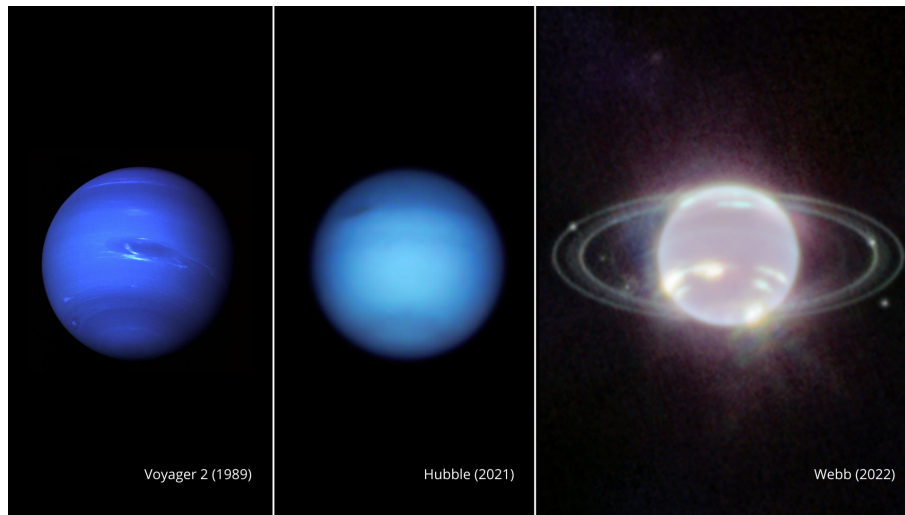


Figure 1.5: The photography of the Neptune, taken with the three different telescopes. Credits to Voyager: NASA/JPL-Caltech Hubble: NASA, ESA, A. Simon (Goddard Space Flight Center), and M.H. Wong (University of California, Berkeley) and the OPAL team.

The last observational tool that I would like to present here, is the Rosetta space probe. The main purpose of this probe was to perform *in situ* observations of 67P/Churyumov–Gerasimenko comet. The probe was equipped with the lander module Philae, that was supposed to land on the comet and perform direct measurements. The main goal of the mission was to charac-

terize the nucleus of the comet, probe its chemical composition, detect what type of volatile molecules are released to the coma. Such data would be a huge step in understanding evolution of the Solar system, origin of comets, and their connection with the ISM. In Fig 1.6 some of the photos of 67P/Churyumov–Gerasimenko comet taken by Rosetta space probe are presented. One of the most interesting finding of the Rosseta mission was to prove the existence of Glycine in the comets. Since the glycine is considered as a one of building blocks of protein, this finding supports the hypothesis that comets could have a huge impact on the development of life on our planet.

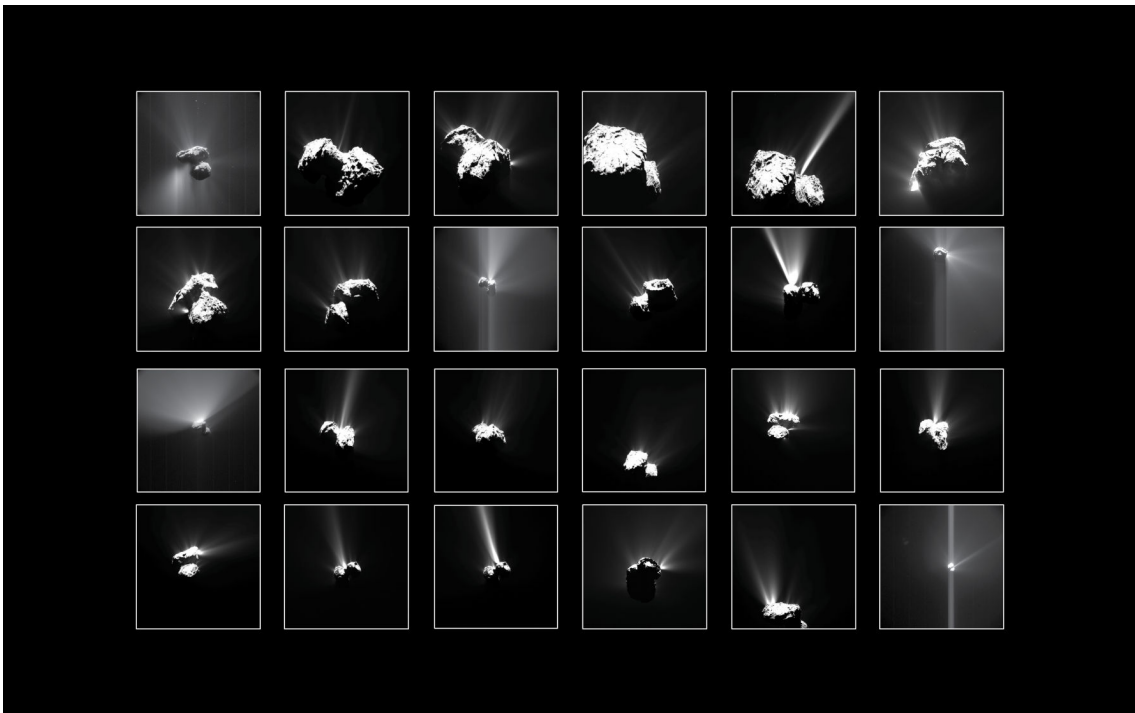


Figure 1.6: Photos taken by Rosseta probe of the 67P/Churyumov–Gerasimenko comet. Credit: OSIRIS: ESA/ Rosetta/ MPS for OSIRIS Team MPS/ UPD/ LAM/ IAA /SSO /INTA /UPM /DASP /IDA; NavCam: ESA/ Rosetta/ NavCam – CC BY-SA IGO 3.0

1.2.2. Detected species

In previous sections I introduced the media where the molecules can be found, and the tools used to search for them. Here I would like discuss what kind of molecules we can find. The very first molecules in the ISM were detected more than eighty years ago^{10–12}. These molecules were CN, CH, and CH⁺. At first, researchers were thinking that these

were fragments of some bigger and more complex molecules, so they did not put much attention to them. The big impact on the detection of new species, had development of radio astronomy in the late 1950s and early 1960s¹³. The first molecule discovered by radio astronomy was OH¹⁴. However, astronomers recognized the importance of the interstellar molecules after the first discovery of NH₃ in 1968¹⁵. The discovery of such a well known molecule in the ISM attracted attention of many researchers since it opened the door to a completely new world of interstellar molecules³. Just one year after this finding, water maser was detected¹⁶, together with the first organic molecule detected in the ISM H₂CO¹⁷. Since that time and to this day, over 270 molecules have been detected in the ISM¹⁸. Most of these molecules were actually detected due to observation at radio frequency. Astronomers detected molecules and ions, as simple as composed of 2 atoms, up to very complex, organic molecules, such as cyclic organic molecules, or fullerenes. Many of the detected molecules cannot be produced on Earth, even in laboratory conditions. This is possible thanks to the unique physical conditions of the ISM, and just this example is showing how fantastic and interesting place the ISM is for researchers.

1.2.3. Modelling of the observations

I have to stress out here, that observing molecules itself is not the only goal of the observations. Thanks to the observation of molecules, we can derive information about the physical and chemical conditions of the media where those molecules are observed. To derive such information, we are trying to reproduce the spectral lines of the molecules that are observed in the media. To correctly model such spectra and derive information about observed media, we must know with the highest possible accuracy the population of energy levels of the observed molecules. Population can be easily derived if a local thermodynamics equilibrium (LTE) is assumed. This assumption can be made if the density of the media is high enough and we can assume that the energy levels of the molecules are populated due to collisions. Unfortunately, LTE usually cannot be maintained in media like ISM due to low density and low temperatures. The analysis of observed molecular spectra then becomes complicated because there is a competition between radiative and collisional processes that drives the

energetic transfer of molecules (see fig.1.7). For the radiative processes, we need to consider absorption (B_{12}), stimulated (B_{21}), and spontaneous emission (A_{21}). In the case of the collisional processes, we will have excitation (C_{12}) and de-excitation (C_{21}). Therefore, in order to properly model the spectra we need to take into account both radiative and collisional processes¹⁹. In the chapter 2, I will describe the radiative transfer modeling in more detail. Here, I would like to stress that radiative properties of molecules are usually well known because they are described by the Einstein coefficient which can be derived from analytical formula or experiments . Unfortunately, the collisional properties are not so easy to derive. For each observed molecule, we need to perform usually long and expensive calculations or do experiments within the conditions similar to the media of interest, with the most abundant molecule in this media as a collider (in the case of the ISM, the dominant colliders can be H_2 , He, H, or electrons, in comets heavier molecules such as CO or H_2O).

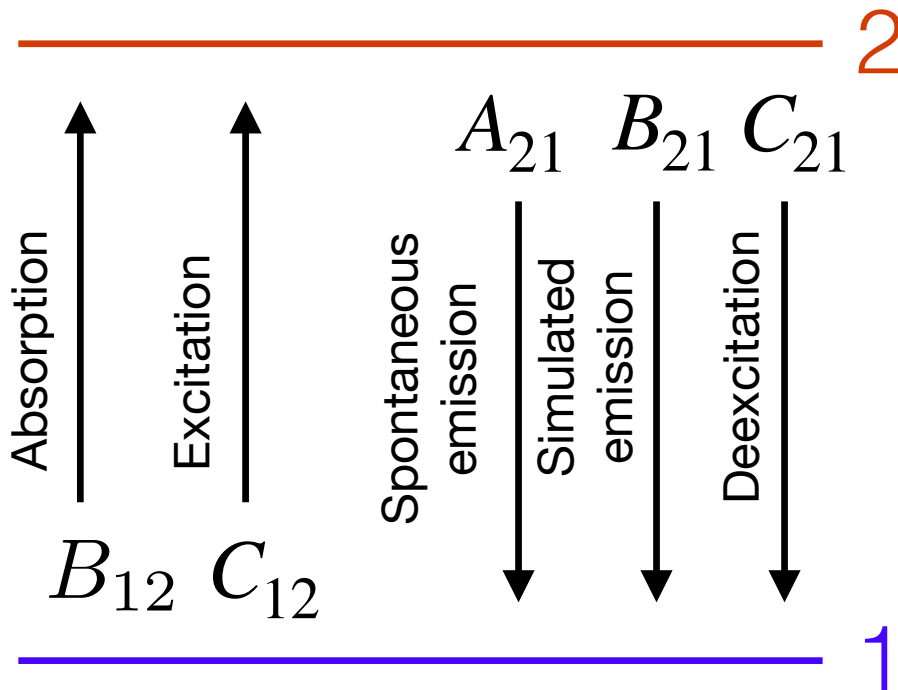


Figure 1.7: Two states model of radiative and collisional processes.

1.3. Determining collisional rate coefficients

In this section, I will present briefly how the collisional rate coefficients are obtained experimentally. Then, I will introduce the state-of-the-art of theoretical studies about collisional rate coefficients. I will discuss about the methodology of such theoretical calculations and summarize the limitations of calculations these days.

1.3.1. Experimental studies

Most of the experimental studies for ro-vibrational energy transfer are done at room temperature, where the collider is usually the noble gas. This temperature is too high for the ISM conditions (temperature of a few kelvins), and except for collisions with helium, collisions with other noble gases are not relevant for the modeling of the ISM. Yet, scientists have tried to overcome those difficulties for the past few decades, with lots of success. I will briefly mention two selected methods to experimentally measure the rate coefficients¹⁹.

The first method is the double resonance method. It combines two sources of radiations. The first is called the "pump", which perturbs our sample molecules. The second one is called "probe" and will be used to track the final population distributions of excited levels once the equilibrium is reached. Using this method, Carty and co-workers²⁰ were able to measure rate coefficients of the CO-He system at a temperature of 15 K. Recently, with this method Labiad and co-workers²¹ measured rate coefficients of the CO-H₂ system in temperature range of 5-20 K.

The second experimental method I will present is the crossed-beam method. As the name suggests, one collides molecules/atoms by crossing two beams. The most crucial parameter in this experiment is collisional energy. It is regulated by the velocity of colliding molecules or by the angles of the beams²². These measurements can be done for very low collisional energy and allow confirming predictions of theoretical studies²³. Unfortunately, there is a disadvantage to this experiment: we cannot obtain the absolute value of the state-to-state cross-section from this method.

1.3.2. State of the art of the theoretical studies

As I briefly presented in previous sections, experimental studies try to reproduce the physical conditions of the ISM to measure collisional rate coefficients. Yet, these studies are still limited, whether it is in terms of temperature or pressure at which experiments operate, or whether in terms of species that can be synthesized in laboratory. This is why theoretical studies are so important. Indeed, theoretical studies do not suffer from such limitations and thus allow to obtain collisional data that can be either complementary to experimental studies or even be the only data available. Unfortunately, theoretical calculations of collisional rate coefficients suffer from other issues: they are often very complicated and expensive in terms of computational resources.

Collisional rate coefficients are calculated under the assumption that the Born-Oppenheimer approximation²⁴ can be applied. This approximation assumes that the motion of the nuclei and of the electrons can be separated due to large difference between their masses. Under this approximation, the Schrödinger equation can be solved in two stages: First, solving the electronic part of the Schrödinger equation, a potential energy surface (PES) of the collisional system representing the electronic interaction for different fixed nuclei positions is needed. Then, using this PES to solve the nuclear Schrödinger equation, one can obtain the cross-sections, and later the collisional rate coefficients.

For this second stage, the theory that has been extensively used up to today and allows one to obtain the most accurate collisional data, is the close coupling (CC) method that was introduced in 1960 by Arthurs and Dalgarno²⁵. Using this method, the problem is reduced to a set of second order coupled derivative equations that need to be solved. Such a calculations were very problematic (and still are, just at a larger scale) in terms of computational operations, since they require to apply time and memory consuming mathematical operations on very large matrices. On top of that, and as mentioned above, solving the CC equations requires an accurate PES for the collisional system considered. That was another problem, since in order to obtain the PES computational demanding calculations were also

needed. The *ab initio* quantum chemistry methods were not as developed as nowadays. This was the two main problems at that time, the lack of computational power to perform CC calculations, and the lack of proper description of the PES of the system.

In the following, I will first focus on the second problem as, today, we can consider that providing a proper description of the PES for a collisional system is a "solved" issue. The first collisional studies were employing very approximate models to try to describe the electronic interaction of the systems²⁶. Even though the description was very inaccurate, the results obtained were still very helpful in the interpretation of the astronomical observations. Since these observations, the astronomical tools were developed allowing observations of higher resolution, and better sensitivities, which leads to discovery of even more molecules. With the exponential increase in the computational resources in the last 50 years, we are now able to obtain PES for very big and complicated systems. Yet, we have to keep in mind that *ab initio* calculations of the PES need to be performed with the highest possible accuracy because the quality of these calculations will directly impact the scattering calculations and, finally, the astrophysical modeling. *Ab-initio* quantum chemistry calculations are the method of choice to obtain such accurate PES. Several methods exist and the choice in one or another depends on the system that one wants to treat, but some general features of the most employed methods can be depicted: The PES with the highest possible accuracy can be obtained using the configuration interaction (CI) method, where all the possible electronic excitations are included (so called full-CI). However, this method can only be used for systems with a small number of electrons due to its huge computational cost. The approach that is the most extensively used these days to compute PESs is the coupled clusters method, or being more specific, a version of this method called CCSD(T)²⁵. Again, the methods mentioned here are not the only possible, but they are the most commonly used these days so, in this manuscript, I will only focus on these two methods. They will be presented and discussed in details in the Chapter 2.

In the last century due to the limitations of the computational resources, the collisional stud-

ies were focused on molecules such as CO, H₂, H₂O, or HCN that were frequently detected in the ISM. Huge contributions to these studies were done by Green and co-workers^{27,28}, Flower and co-workers^{29,30}, and Dalgarno and co-workers^{31,32}. At that time the CC calculations were very computational demanding, thus they were limited for the very low energy regime, and/or for very limited number of transitions.

The approximated methods such as the coupled states (CS)³³ or infinite order (IOS)³⁴, were introduced, in order to perform calculations at higher energy regime, or in some case make them feasible. Unfortunately and even with the enormous growth in the computational power since the first scattering studies, we are still very limited with the systems we can study theoretically. Indeed, the computation time needed to solve the CC equations scales as N^3 , where N is number of channels (quantum states of the colliding partners and their coupling) that need to be included. At the same time the memory scales as N^2 . The conventional limit that we can treat with nowadays resources is about ten thousand channels. Of course, this is not a strict limit, and it can be pushed further depending not only on the computational resources available and the computational time granted on them, but also on other physical parameters such as the range of temperatures for which collisional data is needed.

Such limit is easily exceeded if we consider heavy molecules with a small rotational constant in collision with molecular hydrogen, which is natural choice since it is the most abundant molecule in the ISM. In order to overcome the computational limitations faced when considering the CC method, different approximations can be applied. For instance, we can approximate the hydrogen molecule as a structure-less molecule in the PES (spherical approximation), or consider the Helium as a collider and then apply a scaling law to obtain collisional data with H₂. We can also use approximated methods such as CS and IOS to solve the coupled equations but in both cases, the accuracy of our results will be impacted. In some cases, if collisional data are needed for specific conditions (typically high temperatures) or for very complex molecules, the quantum theory will be dropped and mixed quantum-classical or quasi-classical calculations are performed. Ultimately, the problem comes down

to finding the right method that allows us to find an acceptable balance between feasibility (in terms of computation time) and accuracy of the data. So far, I just referred to the limits encountered when considering collisions with hydrogen molecules, which are the most relevant for the ISM. This is not the case if we want to obtain collisional data for molecules detected in comets. For comets, the dominant colliders are heavy molecules such as water, CO, or CO₂. The PESs constructed for such a systems typically exhibit a very large anisotropy and a deep potential energy well. In such conditions, quantum calculations will be either not feasible (even with approximated methods), or will be extremely demanding in terms of computation resources. In such a case, mixed quantum-classical, quasi-classical or statistical methods such as the statistical adiabatic channel models are needed (SACM)^{35,36} to obtain collision data. The problem in that case is to estimate the accuracy of the data obtained since a comparison with quantum calculations is not feasible, and experimental data for such systems usually do not exist. Even though I still believe that such a calculations should be carried on. Comets are indeed an important source of information as mentioned earlier, and any data that could help with the interpretation of its observations is very valuable.

1.4. Outline of the thesis

The collisional rate coefficients are system specific. As colliders, we should always consider the most abundant molecules in the observed media. For the ISM, the hydrogen atom, the hydrogen molecule, or the helium atom should be considered. However, If we want to model the spectra of the comets, the dominant colliders in this media that will induce collisional excitation are heavy molecules such as H₂O, CO, or CO₂. Also, molecules observed in the comets can be considered as heavy (See Fig. 1.3). In the end, we will have to consider systems that are very heavy and complicated. It is why only for 5 (CO-CO³⁷, CO-H₂O³⁸, H₂O-H₂O³⁹, HCN-H₂O⁴⁰, HF-H₂O⁴¹) systems collisional data for the modeling cometary spectra can be found in the literature. If we look at Fig. 1.3, there are 29 molecules listed that were already observed, and there are more that are not listed in that figure. So we can see that we lack collisional data for such systems.

Therefore, this thesis aims to set up a strategy to obtain collisional data for the molecules in which the water or CO are colliders. For the selected systems that are presented in the next section, I will use available potential interactions or determine new potential interactions between these molecules. I will use available methods to perform quantum and/or statistical calculations and use the molecular data in astrophysical models.

This is purely theoretical. Thus to that, I faced mainly numerical problems. Systems that I have studied were challenging since they require a significant amount of memory and CPU time on supercomputers. I had to go through many tests to optimize calculation parameters and save as much CPU time which is limited on a supercomputer. Finally, I had to choose the most suitable methods to obtain the collisional data with the highest possible accuracy.

1.4.1. Collisional systems studied during thesis

In this section, I will shortly introduce the collisional system that I have studied in my work. For all the presented systems below, I did dynamical calculations based on the potential energy surfaces that were available in the literature or on the new PESs that were provided to me from my collaborators. Once the collisional data were calculated, their impact was tested by performing radiative transfer modeling. Results from this test, with the detailed explained methodology of calculations, were presented in the articles that are enclosed in this manuscript in Chapters 3, 4, and Appendix C.

The H₂O - H₂ and water isotopologues.

Water is one of the most common molecules observed in the interstellar media, close to the star-forming regions. It is also usually the most abundant molecule of cometary media. It is one of the fundamental molecules without which life could never develop⁴². Because of that, the water molecule was very well studied with the collision of H, H₂, He, and electrons (See Żółtowski et al. (2021)⁴³, and reference therein). Thanks to that, collisional data of water molecule cover quite an extensive spectrum of transitions. Yet, I discovered that highly rotational water transitions induced by the collision with the H₂ molecule were not

studied within pure quantum theory. This finding makes this system perfect as the first I have studied. This system was so well studied that I could find lot of helpful information in the literature and getting familiar with scattering theory and yet provided new, very useful data. Such data could be of high interest since the JWST started to operate, and it is observing in the range where the high rotational transitions of water occur. Even though calculations of such high rotational transitions were a challenge. I need to develop a strategy to carry on the calculations. I took the most accurate potential of H₂O - H₂ system available in the literature⁴⁴, which was even further approximated.

In addition to this project, I investigated the isotopic substitution in the water molecule and its impact on the rate coefficients. The isotopologues of water are not observed as frequently as water⁴⁵. However, interpretation of their observation can help better understand the water's chemistry. I performed calculations for the D₂O-H₂ system, using full rigid rotor potential and the most accurate quantum scattering methods, since this time I limit calculations for the transitions between low rotational energy levels of D₂O ($j \leq 8$).

The HCN/HNC - H₂O systems

The HCN and HNC are often observed in the interstellar media. However, in this thesis, these two molecules were studied to help with the modeling of the observation of HCN and HNC in comets. Both of these molecules were observed in comets at small heliocentric distances (< 3 AU), where water production dominates. Thus, it is natural that their excitation is partially due to collisions with water molecules. Although it is generally accepted that the appearance of HCN in the coma is due to sublimation from the nuclei, it is not so evident for HNC⁴⁶. It is assumed that the HNC can also be sublimated from the nuclei as HCN, or it can be created due to the proton reaction exchange of HCN⁴⁷. However, there was also a discussion that HNC can be simply a product of bigger organic molecules dissociation^{48,49}. Therefore, an accurate interpretation of the spectra may help solve this puzzle.

For the HCN/HNC - H₂O systems, new PESs were calculated. I have started work on both

systems and discovered that any quantum calculation would not be feasible. Therefore I started testing the statistical methods. This project is still ongoing, and the preliminary results are presented in chapter 3 of this thesis.

The CO-CO system

The CO-CO system is last on my list. This system was also calculated for the cometary application. Indeed, for the observation of comets at high heliocentric distances (> 3 AU), it was reported that the abundance of the CO molecule could far exceed the abundance of the water. Such observations can be explained by the fact that the sublimation temperature of CO is much lower than that of H₂O molecule⁵⁰. Thus, we should consider the CO a dominant collider in such media.

In the scattering calculations, I used a PES available in the literature⁵¹. The calculations were carried out within complete quantum theory, with some approximation. Finally, the new data were used to perform radiative transfer modeling. This was another challenge because, to the best of my knowledge, there were no reported studies of modeling the excitation of the system with identical molecules. The full discussion about the calculation strategy, methodology, and results are presented in Chapter 4.

1.4.2. Organisation of the manuscript

This thesis is organized as follows: in Chapter 2, I present the theoretical aspect of my study. In Chapter 3, I present my work on scattering involving water molecules. In Chapter 4, I will show the results of my work on the CO-CO system. Finally, Chapter 5 will summarize my thesis and discuss the future perspective of my work.

CHAPTER 2

METHODS

In this chapter, I will present the methodology I used during my thesis. I will start with the description of the molecular system, then introduce the Born-Oppenheimer approximation before briefly presenting the quantum chemistry methods that allow one to calculate interaction energies and construct potential energy surfaces(PES). Next, I will present the quantum scattering theory that allows one to calculate the collisional cross-sections from which rate coefficients can be derived. Finally, I will introduce the radiative transfer theory, where rate coefficients are used.

2.1. Molecular physics

Addressing the scattering problem requires to calculate potential curves or surfaces (depending on the dimensionality of the system). These are usually derived using the Born-Oppenheimer (BO) approximation. The following sections present the molecular system's description and the BO approximation's derivation.

2.1.1. Molecular Hamiltonian

For any molecular system containing M number of nuclei, and N number of electrons, we can write the Hamiltonian, defined as the sum of operators, such as follows:

$$\hat{H} = \hat{T}_e + \hat{T}_n + \hat{V}_{ee} + \hat{V}_{ne} + \hat{V}_{nn} \quad (2.1)$$

The Hamiltonian above contains the following terms (presented in atomic units):

- Kinetic energy of N number of electrons (2.2)
- Kinetic energy of M number of nuclei (2.3)
- Interaction energies

– Electron - electron (2.4)

– Electron -nuclei (2.5)

– Nuclei - nuclei (2.6)

$$\hat{T}_e = -\frac{1}{2} \sum_{i=1}^N \nabla_{\mathbf{r}_i}^2 \quad (2.2)$$

$$\hat{T}_n = -\sum_{i=1}^M \frac{1}{2m_i} \nabla_{\mathbf{R}_i}^2 \quad (2.3)$$

$$\hat{V}_{ee} = \sum_{i=1}^N \sum_{j>i}^N \frac{1}{|\mathbf{r}_i - \mathbf{r}_j|} \quad (2.4)$$

$$\hat{V}_{ne} = \sum_{i=1}^N \sum_{j=1}^M \frac{Z_j}{|\mathbf{r}_i - \mathbf{R}_j|} \quad (2.5)$$

$$\hat{V}_{nn} = \sum_{i=1}^M \sum_{j>i}^M \frac{Z_i Z_j}{|\mathbf{R}_i - \mathbf{R}_j|} \quad (2.6)$$

Where \mathbf{r}_i and \mathbf{R}_i are the position of electrons and nuclei respectively. The m_i is the mass of a given nuclei. The $|\mathbf{r}_i - \mathbf{r}_j|$ are distances between electrons i and j and $|\mathbf{R}_i - \mathbf{R}_j|$ are distances between the i and j nuclei. The nuclear charge is Z . The equation above does not take into account any relativistic effect⁵².

The Schrödinger equation can be solved analytically only for two particles system, the hydrogen atom, which contains only 1 nucleus and 1 electron. For any bigger system than hydrogen, we need to introduce some approximations in order to solve the Schrödinger equation.

2.1.2. Born-Oppenheimer approximation

Born and Oppenheimer, in 1927²⁴, introduced an approximation allowing one to solve the Schrödinger equation for systems with many electrons and nuclei. The idea behind this approximation is that the motion of nuclei is, so to speak, ‘frozen’. Given that the protons are much heavier than the electrons (≈ 1836), one can assume that electrons move much faster than nuclei. In other words, if the nuclei change their positions, we can safely assume that the positions of electrons will adapt instantly. As a result, we can write the molecular Hamiltonian as follows:

$$\hat{H} = \hat{T}_n + \hat{H}_e + \hat{V}_{nn} \quad (2.7)$$

$$\hat{H}_e = \hat{T}_e + \hat{V}_{ee} + \hat{V}_{en} \quad (2.8)$$

The \hat{T}_n operator now represents the molecule’s nuclear kinetic energy for the frozen position of the center of its mass. The \hat{H}_e (2.8) is an electronic Hamiltonian constructed from the kinetic energy of electrons \hat{T}_e , interaction energy between electrons \hat{V}_{ee} , and interaction energy between electrons and frozen nuclei \hat{V}_{en} (we neglect the nuclear kinetic energy term and nuclear repulsion energy). We can thus rewrite the Schrödinger equation as follows:

$$[\hat{T}_n(\mathbf{R}) + \hat{H}_e(\mathbf{r}; \mathbf{R}) + \hat{V}_{nn}(\mathbf{R})]\Psi(\mathbf{r}, \mathbf{R}) = E\Psi(\mathbf{r}, \mathbf{R}) \quad (2.9)$$

The \mathbf{r} and \mathbf{R} are the spatial coordinates of electrons and nuclei respectively. It is necessary to point out here that the semicolon in the argument of \hat{H}_e is a reference to the fact that \mathbf{R} , the frozen position of nuclei, has a parametric dependence. The whole wavefunction can be approximated by:

$$\Psi(\mathbf{r}, \mathbf{R}) \approx \Psi_e(\mathbf{r}; \mathbf{R})f(\mathbf{R}) \quad (2.10)$$

where Ψ_e is the electronic part and $f(\mathbf{R})$ is the nuclear part. Using the wave function defined in the Eq. 2.10, we can separate the Eq. 2.9 into the three following equations:

$$\hat{H}_e(\mathbf{r}; \mathbf{R})\Psi_e(\mathbf{r}; \mathbf{R}) = E_e(\mathbf{R})\Psi_e(\mathbf{r}; \mathbf{R}) \quad (2.11)$$

$$(\hat{H}_e(\mathbf{r}; \mathbf{R}) + V_{nn}(\mathbf{R}))\Psi_e(\mathbf{r}; \mathbf{R}) = U(\mathbf{R})\Psi_e(\mathbf{r}; \mathbf{R}) \quad (2.12)$$

$$(\hat{T}_n(\mathbf{R}) + \hat{U}(\mathbf{R}))f(\mathbf{R}) = Ef(\mathbf{R}) \quad (2.13)$$

Here E_e refers to electron energy. The $U(\mathbf{R})$ is the sum of electron energy and repulsion energy. Another important fact comes from Eq. 2.12. Solving this equation for different positions of nuclei \mathbf{R} allow us to obtain the PES, which can be later used for dynamical calculations⁵².

2.1.3. Interaction energy

Before proceeding with the PES calculations methods, it is important to define the interaction energy (E_{int}). Let's assume a system of two monomers, A and B. For a given \mathbf{R} for the nuclei, we can define the interaction energy as :

$$E_{int}(\mathbf{R}) = E_{AB}(\mathbf{R}) - [E_A(\mathbf{R}) + E_B(\mathbf{R})] \quad (2.14)$$

Where $E_{AB}(\mathbf{R})$ is the total electron energy of the whole system, and the $E_A(\mathbf{R})$ and $E_B(\mathbf{R})$ are the electronic energies of monomer A and B respectively. The electronic energy of both monomers has to be calculated separately as an isolated system. However, when performing electronic calculations on the monomers, the basis set for the entire system should be used (the sum of the basis sets of monomers A and B) in order to avoid the basis set superposition

error⁵³. Performing interaction energy calculations for the different positions of monomers will provide us with the interaction surface (our PES) that is later used in the scattering calculations.

2.2. Ab-initio calculations

In this section I will present very briefly the *ab-initio* quantum chemistry methods that allow to perform calculations of the PES. I focus only on the methods that I have used in my thesis.

2.2.1. The One-Electron Approximation

The idea behind the one-electron approximation is to present a system as a sum of the interactions of a single electron. The electronic Hamiltonian in atomic units can be expressed as :

$$\hat{H} = -\frac{1}{2} \sum_{i=1}^N \Delta_{\mathbf{r}_i} + \sum_{i=1}^N \sum_{j=1}^M \frac{Z_j}{|\mathbf{r}_i - \mathbf{R}_j|} + \sum_{i=1}^N \sum_{j=i+1}^N \frac{1}{|\mathbf{r}_i - \mathbf{r}_j|} \quad (2.15)$$

Focusing only on the first two parts of Eq. 2.15 and performing algebraic operations one can obtain:

$$-\frac{1}{2} \sum_{i=1}^N \Delta_{\mathbf{r}_i} + \sum_{i=1}^N \sum_{j=1}^M \frac{Z_j}{|\mathbf{r}_i - \mathbf{R}_j|} = \sum_{i=1}^N \left(-\frac{1}{2} \Delta_{\mathbf{r}_i} + \sum_{j=1}^M \frac{Z_j}{|\mathbf{r}_i - \mathbf{R}_j|} \right) \quad (2.16)$$

From now on, the terms included within parentheses in 2.16 will be expressed as \hat{h}_i . \hat{h}_i is part of the whole electronic Hamiltonian, but is described by the coordinates of only 1 electron. Expressing the Hamiltonian from Eq. 2.15 with this new operator, we obtain:

$$\hat{H} = \sum_{i=1}^N \hat{h}_i + \sum_{i=1}^N \sum_{j=i+1}^N \frac{1}{|\mathbf{r}_i - \mathbf{r}_j|} \quad (2.17)$$

The one-electron Hamiltonian \hat{h}_i provides information for a single electron of the system,

in a field of effective potential created by rest of the system. For such equation, we can obtain the exact eigenvalue. However, the second term of Eq. 2.17 couples all possible configurations of all the electrons together, and it is impossible to separate their coordinates. Such a problem can be treated with a perturbation method. The \hat{h}_i will be treated as an unperturbed term and the two-electrons interaction as the perturbation term. To solve this problem, a proper wave function must be defined. The wave function must be anti-symmetric with respect to permutations of electronic coordinates, which enforces the Pauli exclusion principle, according to which two electrons with the same spin cannot be on the same orbital. Such a function was proposed by Slater⁵⁴ and is hence called the Slater determinant:

$$\Psi = \frac{1}{\sqrt{N!}} \begin{vmatrix} \phi_1(1) & \phi_1(2) & \dots & \phi_1(N) \\ \phi_2(1) & \phi_2(2) & \dots & \phi_2(N) \\ \dots & \dots & \dots & \dots \\ \phi_N(1) & \phi_N(2) & \dots & \phi_N(N) \end{vmatrix} \quad (2.18)$$

Where the $\phi_i(i)$ is a four dimensional (three coordinates and spin) one-electron function. Therefore, the wavefunction is a product of N one-electron functions $\phi_i(i)$ (spin orbitals). This function is normalized with the factor $\frac{1}{\sqrt{N!}}$ where N is the number of the electrons.

2.2.2. Hartree-Fock Method

The Hartree-Fock (HF) method is used to compute the ground energy state in the N-electrons systems. The name of the method comes from two scientists. Hartree computed the wave function for atoms using the product of spin orbitals. The second one, Fock, proposed asymmetries as the product of the spin-orbitals⁵⁵. The HF method is a variational method for which the trial function is one of the Slater determinants (2.18). The energy in the HF method can be expressed as an eigenvalue of the electronic Hamiltonian:

$$E = \langle \Psi | \hat{H}_e | \Psi \rangle \quad (2.19)$$

In order to determine the best orbitals, we have to minimize the average value of the electronic Hamiltonian (e.g. variational method). This procedure is called the general HF method, and leads to the Fock equations. The Fock equations are solved using an iterative method. We start from initial guess orbitals and use the Slater determinant to solve the Fock equation. The results we obtain are the orbitals of first iteration. We are repeating this process until the new orbitals will not change. Such procedure is commonly known as the self-consistent field. It is our primary source of information about the system, and can be calculated relatively easily and cheaply in terms of computer resources.

2.2.3. Correlation Methods

The HF method is not flawless. This method allows for two electrons with different spin orientations to approach each other or even to 'touch' each other. In reality, this is not possible. Electrons will start to repel each other when getting closer. Taking this into account, we know that we will gain a small part of energy called the 'correlation energy', which refers to the difference between the total energy of the system and the energy obtained from the HF method. In general, the correlation energy is minimal - on average less than 1% of the total energy of the whole system. However, neglecting it might lead to huge errors in describing the energy differences of molecular systems. The HF method does not consider a van der Waals interaction, for example the gaseous methane molecules or noble gas attracting each other, and this is due to the electron correlation of different molecules. The HF method does not predict the condensation of those molecules at low temperatures, which however is proven experimentally. Performing calculations of the F_2 molecule using HF method since it has no potential well, we could come to the conclusion that it should not exist, and yet we know that it does⁵⁶.

The configuration interaction method CI is a method based on variational approaches, where the wavefunction is obtained from the linear combination of the Slater determinant Ψ multiplied by some correlation coefficient c_i :

$$\Phi = \sum_i c_i \Psi_i \quad (2.20)$$

Our Slater determinant Ψ_i is usually built from the spin-orbitals that were calculated in the HF method. In Φ we include, however, not only orbitals which are occupied in ground-state HF determinant but we replace them by virtual ones (orbitals that are not occupied by electrons). Putting upper boundaries for orbital energy, the sum in equation 2.20 is finite and represents the exact result in a given (finite) basis set. This limit is known as full CI (FCI). Unfortunately, the FCI is feasible only for very small systems, due to the enormous cost of the calculation. This is why we are considering only a limited numbers of excitations. The energy that will be thereby obtained will always approximate the exact value from above. For one substitution we will have a single excitation (CIS), double excitations (CISD) if two spin orbitals are substituted and so on.

Another correlation method is called the Coupled Cluster (CC) method. The CC method originated from nuclear physics, and was introduced by Čížek in quantum chemistry calculations²⁵. In the CC method, we define the function of the ground state as it is presented in Eq. 2.21 where Ψ_0 is usually the HF determinant, and \hat{T} is the cluster operator, including the sum of the excitations.

$$\Phi = e^{\hat{T}} \Psi_0 \quad (2.21)$$

where \hat{T} is cluster operator expressed as :

$$\hat{T} = \hat{T}_1 + \hat{T}_2 + \hat{T}_3 + \dots \quad (2.22)$$

where \hat{T}_1 is a single excitation operator, \hat{T}_2 a double excitation operator, and so on and so forth. Using the same number of excitations in \hat{T} as the number of electrons in the system, we

could calculate the 'exact' energy of the system in ground state. However, such calculations are usually not feasible because they are extremely computationally demanding. Hence, we need to limit the number of excitations that we can include in the cluster operator. The most common method used to this day is CCSD(T), where S stands for single, D for double, and T for triple excitation, respectively (the parenthesis around T indicates excitations that were treated perturbatively). Even with such limited excitations, the CCSD(T) method calculations are expensive. The cost of calculations scales as the 7^{th} power of the basis set size, but nonetheless are less expensive than CI methods with triple excitation included (CISDT), that scales with the 8^{th} power of the basis size⁵⁷. Therefore, calculations are usually limited to systems with a limited number of electrons. However, due to efficient implementations, CCSD(T) is workable to systems with up to about 100 electrons.

2.2.4. Basis sets

Once the *ab-initio* method is chosen, the next crucial factor that will influence the accuracy and the calculation cost is the choice of an atomic basis set. For any molecular system, one need to determine the wave function, which is almost always unknown. Therefore, we usually expand this unknown function into a set of well-defined functions. In principle, there is no limitation to the type of function used in the expansion. However, some criteria should guide our choice of the basis function.

First, the desired functions should represent well the physical behavior of our problem. Thanks to that, fewer functions need to be included to obtain an accurate representation of the problem. The second criterion is more practical. We must remember that the functions in our basis need to be integrated. Therefore, choosing the type of functions that will be easy to integrate is convenient. I will refer to the hydrogen atom to illustrate what kind of functions can be used. For the hydrogen atom, the exact solutions of its orbitals are well-known. These results suggest that exponential-type functions centered on the nuclei are a perfect choice. Unfortunately, this type of function is tough to handle iteratively. On the contrary, Gaussian-type functions are much easier to handle in terms of computational

methods. However, they are much poorer in describing the electronic structure. Their distance dependence is r^2 , and they fall off too quickly with increasing distance from the nucleus. Additionally, they have problems describing the behavior near the nucleus, since Gaussian functions have no slope. There is no perfect function that could fulfill both of the aforementioned criteria. The linear combination of the functions helps to overcome some of these problems. Such a method is often called the linear combination of atomic orbitals (LCAO). There is a minimum number of functions that require consideration. The requirement is that we need to include one basis function for each type of orbital that we are considering in our system. We call it the minimal basis set. The latter is usually insufficient to describe the system accurately. Therefore, we include more functions in our basis to improve accuracy. The more functions we include in our basis, the more accuracy we gain, and at the same time, the computational cost will increase. The whole problem is to find a good compromise between accuracy and computational cost⁵⁷.

The atomic basis set that I have used during my PhD were correlation consistent polarized basis proposed by Dunning and co-workers⁵⁸. They proposed that sets of primitive Gaussian functions can effectively and efficiently describe the correlation, if the exponents of the Gaussian functions were optimized in atomic correlation calculation previously. The acronym of such a basis is aug-cc-pVXZ where X = D-double, T-triple, Q-quadruple, stands for the number of atomic orbitals were used to describe one molecular orbital. The first shortcut *aug* stands for augmented. This mean that additional diffuse function with smaller exponent were added for better description. The *cc* in acronym is correlation consistent. The *p* stands from term polarized and its mean that additional functions were added in the basis to help describe polarization of electron density. The *V* stands for valence, which meant that only for the valence orbital multiple atomic function will be used. The *Z* term stands from Greek letter zeta that was often used to denote the exponent in the basis function.

2.2.5. Analytical representation of the PES

With the method presented above, we are able to calculate the interaction energy of the system. Once enough energy points are calculated, we can construct the analytical form of the PES. We will use these energy points to create a 'model' that will describe the interaction of our system. This model is a function with adjustable parameters. Usually, the potential is expanded in set of angular functions (see Eq. 2.23). This expansion is always finite. Once we know the form of the functions and the radial coefficients ν_λ , we can fit or interpolate the interaction energy for any positions of the monomers of our system. This kind of expansion is often used in the numerical codes to perform scattering studies.

$$V(R, \alpha) = \sum_{\lambda} \nu_{\lambda}(R) f_{\lambda}(\alpha) \quad (2.23)$$

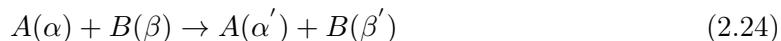
where R is a distance between monomers of our system, α is a set of angular coordinates describing positions of the monomers, ν_λ is a coefficient (coefficients depend only on the distance parameter R), and f_λ is a function (usually orthogonal to all others) that depends only of the set of angular coordinates α .

2.3. Collision Dynamics

The quantum scattering theory was extensively studied and developed in the previous century. Even though the theory was introduced in the early 1960's²⁵, scientists at that time were limited to investigating very few and small (in terms of numbers of atoms) collisional systems because of their small (compared to today's resources) computational power. Since that time, thanks to the enormous growth in computational technology, we have been able to study bigger and more complex systems, necessary for the chemical modelling of astrophysical media. In this section, I will introduce the close-coupling approach to the scattering problem, together with the coupled states approximation and the statistical adiabatic channel method. At the end of this section I will present selected quantum scattering codes, where these methods are implemented.

2.3.1. Scattering process

Let us consider a nonreactive scattering process of species A and B:



α and β correspond to the set of quantum numbers describing the initial state of species A and B, respectively. Therefore the primed α and β will correspond to the set of quantum numbers informing us about the final state of considered species A and B. We can distinguish two kinds of processes. The first one is called elastic scattering. In this type of collision, the internal states of the species before and after the collision are the same. In other words the $\alpha = \alpha'$ and $\beta = \beta'$. The second type is called an inelastic collision. It is the opposite of elastic collisions : the internal state of the species are different before and after collision ($\alpha \neq \alpha'$ and/or $\beta \neq \beta'$). In the inelastic process, we will observe the excitation and/or de-excitation of the species⁵⁹.

2.3.2. Coordinate System

Before proceeding with any calculations it is important to define the coordinate system. It is necessary to define one that properly allows to describe positions for our system, and interaction between molecules. Collision calculations are typically solved in two types of coordinate systems: space-fixed (SF) or body-fixed (BF)⁵⁶. Below we introduce their detailed descriptions.

Space-Fixed coordinates

Let us consider moving molecules in space and bind them rigidly to the Cartesian coordinate system. Usually, the center of the mass of one molecule is chosen as the origin point of the coordinate system. For this kind of systems, the laboratory system of coordinates (space-fixed) is the most appropriate. If molecules do not interact with anything, this will imply that:

- total energy is constant
- total momentum vector is constant
- total angular momentum vector is constant

These physical quantities are preserved due to the homogeneity of time and the uniformity of the heterogeneity and isotropy of space. In order to describe the positions of particles, we use the vectors $\mathbf{r}_i = (x_i, y_i, z_i)$ pointing from the center of our Cartesian coordinate system to the particle (fig.2.1).

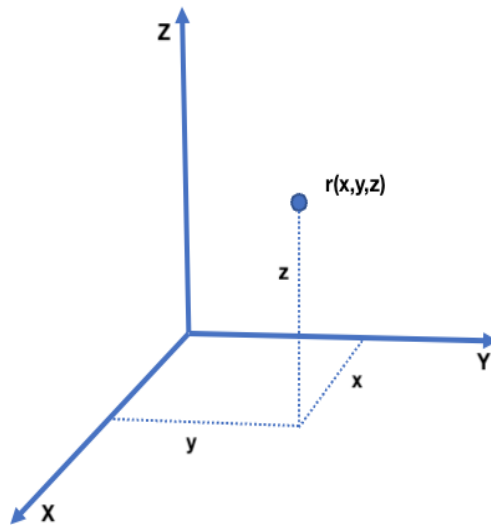


Figure 2.1: Example of the space-fixed system of coordinates. Blue dot represent particle with the position described by the three coordinates.

Body-fixed coordinates

The body-fixed system of coordinates is related to the molecule or molecular system of choice. We can define our coordinate system by attaching the origin to different places, for example:

- As an origin, we choose the position of the center of the mass of our molecule. Positions of all the particles in our system are described by a vector pointing out from the center of the mass. Example of such a system is presented in the fig.2.2.
- We choose the particle of our system and are attaching our coordinate system to it. The positions of the next particles will be described by a vector pointing from the particle that we attach to our coordinate system
- We choose the pair of particles in our system. The vector describing the positions of the next particles will be pointing from the middle of the distance between the paired particle that we choose.

Choosing one system over another can greatly simplify our problem. However, the results we obtain should always be the same no matter which system of coordinates is chosen.

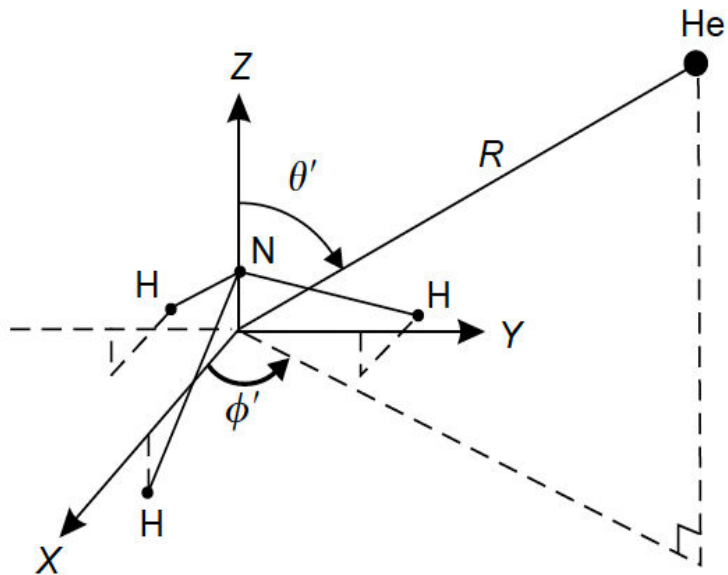


Figure 2.2: The ammonia helium system. The center of the coordinates is in the center of the mass of this system. The figure was taken from the book *Molecular Collisions in the Interstellar Medium*⁶⁰.

2.3.3. Close Coupling approach

The close coupling approach is a rigorous method used to solve the scattering problem of colliding molecules and/or atoms⁶¹. Depending on what kind of systems is considered, we need to specify different expansions of the potential and wave function, although the general methodology stays the same. Here, I present the general procedure of the close-coupling approach without specifying the collisional system. In the next chapters, I will provide the specific character of the wave functions and expansion of the potential depending on the system I have studied.

Using the spherical coordinates, one can consider the scattering Hamiltonian described in the system of coordinates where the center point is in the center of mass of one of the monomers as:

$$\hat{H} = -\frac{\hbar^2}{2\mu} \frac{d^2}{dR^2} + \frac{\hbar^2}{2\mu R^2} \hat{L}^2 + \hat{H}_a + \hat{H}_b + \hat{V}(R, \alpha) \quad (2.25)$$

Where, μ is the reduced mass of the system, R the distance between the centers of mass of our monomers and \hat{L} the operator of the angular momenta. The \hat{H}_a and \hat{H}_b are the Hamiltonians of the monomers of our system, describing their internal structure. Depending on which kind of systems we deal with, these Hamiltonians can contain information about rotations and vibrations of the monomers. $\hat{V}(R, \alpha)$ is the potential energy surface, that describes the interactions between the monomers of our system. The α is a set of angles, which describe the relative orientations of the atoms/molecules in collisions.

Let us define now the wave function. The wave function will be as the Hamiltonians of the monomers e.g. system dependent.

We can present its general form as :

$$\Psi = \frac{1}{R} \sum_{\gamma} |\gamma(\alpha)\rangle \xi_{\gamma}(R) \quad (2.26)$$

Where the $|\gamma(\alpha)\rangle$ are the angular functions that form a basis set that depends of the type of the species in our collisional system. The $\xi_{\gamma}(R)$ are radial functions. They depends on the type of collisions we are dealing with and describe the nuclear motion of the colliding species.

Using the Hamiltonian from Eq. 2.25 and the wave function from Eq. 2.26 to solve the Schrödinger equation by integrating over angular variables, we will obtain a set of coupled equations which can be written in compact form as follows:

$$\left[\frac{\partial^2}{\partial R^2} + \frac{L^2}{R^2} - k^2 + \frac{2\mu}{\hbar^2} \hat{V}(R, \alpha) \right] \Psi = 0 \quad (2.27)$$

$$k^2 = \left(\frac{2\mu}{\hbar^2}\right)(E_{tot} - E_A - E_B) \quad (2.28)$$

Where L is orbital angular momentum, k is a wave vector that contains the total energy E_{tot} and the energy of the internal states of monomers E_1 and E_2 . The difference between total energy and energy of the monomers is the collision energy.

The equation 2.27 can be solved iteratively. In order to solve this second order derivative equation, boundary conditions have to be applied. For $R \rightarrow 0$, the function have to vanish - in other words, $\Psi(R = 0) = 0$. For $R \rightarrow \infty$ where the potential of the system is approaching zero, the system will be described with wavefunction that has following form :

$$\Psi(R \rightarrow \infty) = \sqrt{\frac{\mu}{2\pi\hbar}} \left[\frac{e^{-i(k_{int}R - \frac{l\pi}{2})}}{\sqrt{k_{int}}} \delta_{\gamma,\gamma'} - S \frac{e^{-i(k_{fin}R - \frac{l'\pi}{2})}}{\sqrt{k_{fin}}} \right] \quad (2.29)$$

Where k_{int} and k_{fin} are wave vectors of the initial and final state respectively. The $\delta_{\gamma,\gamma'}$ is a Kronecker delta of the coefficients γ and γ' depends of the system we treat. The S is the so-called scattering matrix. For collisions, the S-matrix contains all the information about initial and final states of the system. Cross-sections can be extracted from the S-matrix using the following formula:

$$\sigma_{i \rightarrow f} = \frac{\pi}{(2j_1 + 1)(2j_2 + 1)k^2} \sum_{J_{tot}} (2J_{tot} + 1) |1 - S_{fi}|^2 \quad (2.30)$$

Where j_1 and j_2 are the angular momenta of monomer 1 and 2 respectively and J_{tot} is the total angular momentum.

2.3.4. Coupled states approximation

Close-coupling calculations are expensive in terms of memory and time. The time needed to solve coupled equation scales approximately as N^3 and the memory need scales as N^2 , where N is the number channels included in the calculations. Therefore, depending on resources that we can use, the limit of what can be solved is usually about 10,000 channels. That is why, even though we have almost exact methods of calculations, it can be used only for small systems and low-energy regimes (the numbers of channels increase with the increase of collision energy, because one has to expand the basis set to converge calculations). Therefore we need an approximation method. One such approximation is the Coupled states approximation. This approximation was introduced by McGuire and Kouri³³. This approximation neglects the off-diagonal elements of l^2 , and approximates the diagonal elements by averaging over orbital momentum. In other words, the eigenvalues of L^2 in CC equations are substituted with constant average angular momentum⁶². This results in decoupling the rotational angular momentum from the orbital angular momentum. The physical interpretation of this substitution is that we are approximating the rotation of the whole system- i.e., omitting Coriolis coupling. The numerical interpretation of this approximation, is that the number of channels will depends only on the size of the basis used in calculations, and stay fixed for total angular momenta. As opposite the numbers of channels in the CC approach increase with the increase of the total angular momenta. To give the example how efficient the CS approximation can be, I will refer to the scattering calculations of the CO-CO system that I performed (this work is presented in further chapter). I did the calculations using the CS approximation. The numbers of channels I needed to consider in the calculations was equal to 2763. Using the supercomputer, calculations of this number of channels for one total angular momenta took approximately 3 days, and 5.2 GB of memory. If I would like to do the same calculations with the same size of basis using the CC method, the number of channels that I would need to be calculated would be approximately 45000. Reminding that the time of calculations increases as N^3 , the time of calculations from 3 days, would increase to approximately 37 years. In case of the memory need instead of 5.2 GB we would

need approximately 1.6 TB. As one can see these numbers are huge, and make the CC calculations not feasible for this particular system. Therefore, the CS approximation, can not only reduce significantly time of calculations and memory need, but also in some cases make calculations feasible. The time saved using the CS method depends on the number of channels that we need to consider in the calculations. The more channels in our calculations, the more time is saved. This approximation can be applied to any desired system, but it is expected to work better with heavier ones, at higher energies⁵⁹.

2.3.5. Statistical adiabatic channel approach

Even though the CS approximation significantly reduces the computational cost of scattering calculations, some of the collisional systems may be too expensive to address or not feasible with the CS method. An alternative to this approximation can be statistical methods. These methods originated from nuclear reactions, and later from chemical reaction studies, where they were extensively used to describe reactions^{63–65}. The statistical methods are based upon the assumption that the collisional partners form a complex during the collisional process. The complex has to live long enough for the initial conditions of the scatters to be forgotten. This implies some limitations and requirements. The statistical methods are expected to work well for strongly bounded systems (system with a deep well). As the formation of the $A + B$ complex system is assumed, a key to statistical methods is the high density of resonances matching the collision energy. This is, indeed, favoured in systems with large reduced mass and deep potentials. The limitation of statistical methods is the temperature. As the temperature is increasing the accuracy of the statistical methods is dropping, as the life time of the complex is no longer long enough. Likewise, the density of states drops for higher temperature. The statistical approach that I will present here is called the statistical adiabatic channel method (SACM)^{35,36}.

The starting point of this method is the coupled radial equation as was presented in the CC formalism. However, here we are excluding the kinetic term and performing diagonalization

of the Hamiltonian before summing over the total angular momenta. We will obtain a set of adiabatic curves. Each of the curves can be associated with the internal states of scatters. The number of adiabatic curves is then equal to the number of possible channels considered in our calculations. In the figure 2.3 an example of the adiabatic curves is presented.

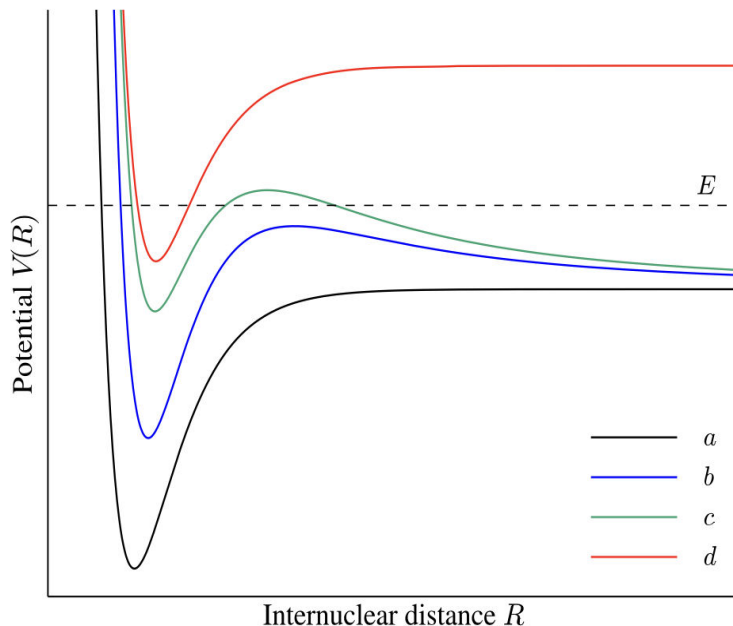


Figure 2.3: Adiabatic curves represented as a function of distance. The dashed line represents the total scattering energy. The a and b curves are treated as open channels, the c and d as closed ones. Figure taken from Loreau et. al (2018)³⁶.

The basic assumption upon which the SACM method relies is that if the kinetic energy is larger than the centrifugal barrier in the entrance channel, the complex can be formed, and the collision can take place. The probability will be solely determined by counting all possible exit channels. This implies that all possible exit channels will have the same weight, and the S matrix is constructed as in Eq. 2.31 for open channels (where $N(E, J)$ is the number of all channels at a given collision energy E and total angular momenta J) and 0 for closed channels. The cross-section is calculated using the Eq. 2.32.

$$|S_{if}(E, J)|^2 = \frac{1}{N(E, J)} \quad (2.31)$$

$$\sigma_{if}(E) = \frac{\pi}{(2j_1 + 1)(2j_2 + 1)k^2} \sum_{J=0}^{\infty} (2J + 1) |S_{if}(E, J)|^2 \quad (2.32)$$

The advantage of the SACM method calculations is that they are relatively 'cheap' compared to the CS calculations. The curves are independent of energy, and we need to calculate them only once for the sum of total angular momentum, whereas with the CS approximation, we need to perform calculations over the whole grid of energy to obtain detailed cross-sections. In addition, the convergence of the rotational basis is much faster because we do not have to include many closed channels to converge the calculation. I will refer again to the CO-CO system as a example. I performed calculations using the CS method. Scattering calculations of this system took almost 2.5 year, using supercomputers. With the SACM method, to obtain results for this same numbers of transitions took approximately 2 months. As one can see, this is significant save of computational time, unfortunately for the CO-CO system, the SACM method did not work as well as I expected (details about this case are presented in chapter 4). However, it was shown with other studies that the accuracy of the SACM results could be as good as CS at low temperatures, which are essential for astrophysical modeling⁶⁶.

2.3.6. Quantum Scattering codes

For all the methods that we have presented (CC, CS, SACM), we need to deal with the equations that need to be solved using numerical methods. The propagation algorithm has to be used. Historically the Numerov or renormalized Numerov algorithm were used⁶⁷. Nowadays, the most common algorithm used for the coupled equation is the hybrid one. In the short range of the PES, where huge anisotropies can be observed, the log-derivative propagator is used⁶⁸, while the Airy propagator is used⁶⁹ in the long range. One of such hybrid propagators was developed by Alexander and Manolopoulos⁷⁰.

These and other propagators are used in the quantum scattering code, to solve the close coupled equation. During my thesis, I have been working with two codes: MOLSCAT⁷¹ and HIBRIDION⁷². Both codes are general purpose quantum scattering codes that were developed in order to treat the coupled-channel method. For both codes, a short introduction together with crucial parameters controlling the calculation process and examples of convergence tests, are presented in Appendix A.

2.4. Radiative Transfer

From the modeling of the molecular spectra of the targeted environments such as ISM or comets, conclusions can be drawn about the physical and chemical conditions of these media. Proper modeling requires the knowledge of the populations of the energy levels of the observed molecules. If we can assume that the LTE conditions are fulfilled, in other words that the observed media is very dense, then populations can be easily derived, due to the fact that the excitation process is dominated by collisional processes. Unfortunately, such a scenario is quite rare in media such as comets or ISM. As a result, both radiative and collisional processes have to be taken into account. Various methods exist that allow to model the spectra, however here I will focus on one of the most frequently used, the radiative transfer model. The basic formalism of the radiative transfer theory, presented further in this section, was adapted from the article of van der Tak and co-workers⁷³.

First, we need to define the quantity called specific intensity I_ν . It describes the amount of energy that is passing through the surface per unit of the surface, solid angle and bandwidth. Then we can define transfer equation as follow:

$$\frac{dI_\nu}{ds} = j_\nu - \alpha_\nu I_\nu \quad (2.33)$$

where ds is the radiation propagating distance, j_ν the local emission coefficient and α_ν the local extinction coefficients. It is common to define the optical depth as $d\tau = \alpha_\nu ds$. Then the transfer equation will take the following form:

$$\frac{dI_\nu}{d\tau} = S_\nu - I_\nu \quad (2.34)$$

where S_ν is a source function defined as:

$$S_\nu = \frac{j_\nu}{\alpha_\nu} \quad (2.35)$$

The local extinction α_ν and local emission j_ν coefficients are defined as follow:

$$\alpha_\nu = \frac{h\nu}{4\pi} \phi(\nu) (n_l B_{lu} + n_u B_{ul}) \quad (2.36)$$

$$j_\nu = \frac{h\nu}{4\pi} n_u A_{ul} \phi(\nu) \quad (2.37)$$

where

$$A_{ul} = \frac{64\pi^4 \nu^3}{3hc^3} \frac{S(\gamma', \gamma)}{g} \quad (2.38)$$

The $\phi(\nu)$ is the function representing line profile of observed molecule, n_u and n_l are populations of the upper and lower levels respectively, A_{ul} is spontaneous emission, B_{ul} stimulated emission and B_{lu} absorption Einstein coefficients. The h is the Planck constant, ν the frequency of transitions, g the degeneracy of the level, and S the line strength factor where the γ' and γ represent the set of the quantum numbers describing upper and lower states of molecule respectively. These sets of quantum numbers will change depending on the type of molecule (linear, asymmetric-top, open-shell, etc.). Therefore, once we know the type of molecules we are observing, we can relatively easily obtain the Einstein coefficients for spontaneous emission. The coefficients for stimulated emission and absorption can be calculated from the following relations:

$$B_{lu} = \frac{c^2}{2h\nu^3} A_{ul} \quad (2.39)$$

$$B_{ul} = \frac{g_u}{g_l} B_{lu} \quad (2.40)$$

where g_u and g_l are the statistical weights of the upper and lower level respectively.

We still need to know, however, how the population is distributed between different levels of the molecule. This can be derived from the statistic equilibrium equation (SE) that takes the following form (in the steady state case):

$$\sum_{l < u} n_u [C_{ul} + B_{ul} J_\nu] - \sum_{l > u} n_l [A_{luj} + B_{luj} J_\nu + C_{lu}] = 0 \quad (2.41)$$

The C_{lu} and C_{ul} in the equation 2.41 are collisional excitations and de-excitations coefficients. They are expressed by the probabilities of the excitation/de-excitation (k - collisional rate coefficients) multiplied to be the density (n) of the collisional partner. Collisional de-excitation process from upper level u to lower level l are expressed with the following formula:

$$C_{ul} = nk_{ul} \quad (2.42)$$

Where n is the density of the collider (cm^{-3}), and k_{ul} the collisional rate coefficients (cm^3s^{-1}) for de-excitation transitions from upper state u to lower state l . The rate coefficients for excitation processes can be obtained from a detailed balance:

$$k_{lu} = k_{ul} \frac{g_u}{g_l} e^{\frac{-h\nu}{k_B T_{kin}}} \quad (2.43)$$

where the g_u and g_l are the statistical weights of the upper and lower levels, respectively, k_B the Boltzmann constant, and T_{kin} the kinetic temperature.

The collision rate coefficients are obtained from the cross-sections (see equation 2.30) calculated in the scattering calculations by averaging them over collisional energy, assuming the Maxwell-Boltzmann distribution:

$$k_{i \rightarrow f}(T) = \left(\frac{8}{\pi \mu k_B^3 T^3} \right)^{\frac{1}{2}} \int_0^{\infty} \sigma_{i \rightarrow f}(E_c) E_c e^{-\frac{E_c}{k_B T}} dE_c \quad (2.44)$$

where μ is the reduced mass of the system, σ a cross-section for a given transition and E_c the collision energy.

In Eq.2.41 the J_ν is a specific intensity that was integrated over solid angle, and averaged over all possible directions:

$$J_\nu = \frac{1}{4\pi} \int I_\nu \phi(\nu) d\nu d\Omega \quad (2.45)$$

We can see that the radiative transfer equations and SE equations as coupled through specific intensity, thus they can not be solved independently since results of one equations depends on the results from the second one. This problem can be greatly simplified, and population of the levels from SE equation can be easily extracted if assumption of the local thermodynamical equilibrium (LTE) will be applied. Population can be then derived from the Boltzmann distribution:

$$\frac{n_u}{n_l} = \frac{g_u}{g_l} \exp\left[\frac{-(E_u - E_l)}{kT}\right] \quad (2.46)$$

where, E_u and E_l are the upper and lower energy levels of the molecule, respectively. Such an approximation can be used only when collisional processes dominate over radiative processes. Or, put differently, if the density of the media is large enough. Unfortunately, for many astronomical media, these conditions are not fulfilled, and we have to take both radiative and collisional processes into account during the radiative transfer modeling. In

this case, we need to obtain collisional data for our molecule of interest. The collisional data are obtained thanks to complex scattering calculations, that are usually long and computationally expensive, and in some cases even impossible if we need to consider complex molecules.

2.4.1. Solving radiative transfer problem

The biggest difficulty with respect to radiative transfer problems is that the populations of the molecule are dependent of the local radiation field. Thus, in order to approach such a problem, iterative methods are needed. This will be especially hard for media where the matter is not distributed homogeneously, and/or the shape of the media is irregular. Fortunately, if we limit our research interests to the global properties of the media, we can significantly reduce our problem. This requires nonetheless to introduce a new term - the geometrical average escape probability β . This term, will express the probability of a photon to escape the medium in which it was created. Advantages of such an approach include the fact that we can neglect the background radiation and any local continuum, and that the β depends only on the optical depth, and is connected to the specific intensities through the following expression:

$$J_\nu = S_\nu(1 - \beta) \tag{2.47}$$

Since the escape probability depends on the optical depth, there were many relations developed by researchers for specific geometries of the media. The most frequently used one, which is also the one that I used during my radiative transfer modeling, is the Large Velocity Gradient approximation (LVG) or ‘Sobolev’ approximation for expanding the spherical shell⁷⁴. This approximation is based on the assumption that photons emitted from any point in the sphere will escape the sphere due to the Doppler shift across the sphere, or will be reabsorbed locally. Such an assumption requires the motion rate (expanding or collapsing) of the sphere to be much greater than the average chaotic motion of the particles in the

media⁷⁵.

To solve such a problem, I have been using the public version of the RADEX code⁷³, for the non-LTE, radiative transfer modeling. In my work, I have not been using this code to model actual observations, but to check the extent to which the new collisional data calculated in this thesis would impact the modeling of astrophysical media. More detailed explanations about modeling with the RADEX code are presented in the articles that are included in chapters 3 and 4 of this thesis.

CHAPTER 3

COLLISIONS INVOLVING H₂O MOLECULES

In this chapter, I will present my work on collisional systems involving the water molecule. For all the systems I studied, the collisional partner for the water molecule was a linear molecule. Thus, in the following sections, I present the close-coupling formalism for asymmetric top-linear molecule collisional systems. Then, I will introduce all the systems, present the potential energy surfaces I used in the calculations, and show the results I have obtained.

3.1. Scattering Methods

The adopted approach for the scattering of an asymmetric top - linear molecule is described in the work of Philips and co-workers.⁷⁶ They presented a close coupling approach for the scattering in the water - hydrogen molecular system.

The asymmetric top wave function can be represented as a combinations of the symmetric top eigenfunctions:

$$W_{\tau,m}^{j_1}(\alpha\beta\gamma) = \sum_k a_{\tau,k}^j \sqrt{\left(\frac{2j+1}{8\pi^2}\right)} D_{k,m}^j(\alpha\beta\gamma) \quad (3.1)$$

where $D_{k,m}^{j_1}(\alpha\beta\gamma)$ are the Wigner rotation matrices, j_1 is the total angular momentum of the rotor (here water molecule), k is projection of angular momenta on the molecule-fixed z axis, and m is projection of angular momenta on the space-fixed z axis. The τ is an index that for $2j_1 + 1$ energy levels for asymmetric top allows one to distinguish them within a given j_1 . It was shown by Arthurs and Dalgarno that it is convenient to couple¹ the relative angular momentum l with the sum of the rotational angular momenta of monomers $\mathbf{j} = \mathbf{j}_1 + \mathbf{j}_2$ into the total angular momentum J using formula $\mathbf{J} = \mathbf{l} + \mathbf{j}$. Such coupling to J makes the Hamiltonian of the system block-diagonal which significantly simplifies the calculations. The wave function of the system can be represented in the following linear combination:

$$\Omega_{j_1 \tau_1 j_2 j_l}^{JM}(\theta, \phi, \theta', \phi', \alpha, \beta, \gamma) = \sum \langle j \mu l m | JM \rangle \langle j_1 m_1 j_2 m_2 | j \mu \rangle W_{\tau_1, m_1}^{j_1}(\alpha \beta \gamma) Y_{j_2 m_2}(\theta, \phi) Y_{lm}(\theta', \phi') \quad (3.2)$$

where $\langle j_1 m_1 j_2 m_2 | j_1 m_1 j_2 m_2 \rangle$ is a Clebsch-Gordan coupling coefficients and $Y_{..}$ are spherical harmonics.

The interaction potential of our system can be expanded in complete orthonormal set of angular functions. In the body fixed system of coordinates we can define the following coordinates, R - distance between monomers, θ, ϕ - coordinates of water and θ', ϕ' - coordinates of hydrogen (see. Fig. 3.1). Using the above coordinates one can express the expansion of the potential in the following form :

$$V(R, \theta, \phi, \theta', \phi') = \sum v_{p_1 q_1 p_2 p}(R) t_{p_1 q_1 p_2 p}(\theta, \phi, \theta', \phi') \quad (3.3)$$

where

$$t_{p_1 q_1 p_2 p}(\theta, \phi, \theta', \phi') = (1 + \delta_{q_1 0})^{-1} \sum \begin{pmatrix} p_1 & p_2 & p \\ r_1 & r_2 & r \end{pmatrix} Y_{p_2 r_2}(\theta', \phi') Y_{pr}(\theta, \phi) [\delta_{q_1 r_1} + -1^{p_1 + q_1 + p_2 + p} \delta_{-q_1 r_1}] \quad (3.4)$$

The $(::)$ is a $3-j$ Wigner symbol, $Y_{..}$ are spherical harmonics, and $\delta_{..}$ is the Kronecker delta.

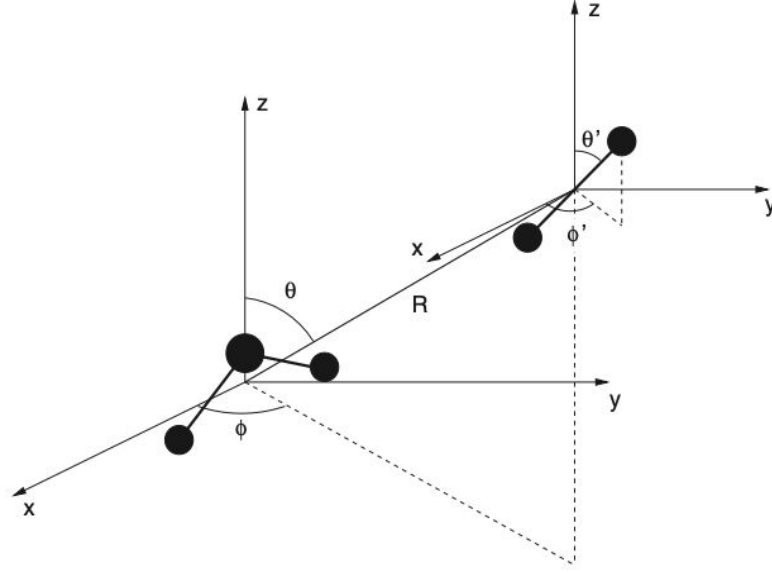


Figure 3.1: The H₂O-H₂ collision system, in Jacobi coordinate system. The θ and ϕ angles describe the position of the H₂O-H₂, θ' and ϕ' describe orientations of H₂ molecules, and R is the distance between the both molecules. This plot was taken from the work of Scribano et al.⁷⁷

Using the expansion of the function from Eq. 3.2 together with the expansion of the potential from Eq. 3.3 and substituting it into Eq. 2.27 we obtain the second order radial differential equation in following form :

$$\left[\frac{d^2}{dR^2} - \frac{l(l+1)}{R^2} + k_{j_1\tau_1j_2}^2 \right] F_{\gamma l \leftarrow \gamma' l}^{JM}(R) = \frac{2m}{\hbar^2} \sum_{\gamma'} \langle \Omega_{\gamma}^{JM} | V | \Omega_{\gamma'}^{JM} \rangle F_{\gamma' l' \leftarrow \gamma' l}^{JM}(R) \quad (3.5)$$

and k is a wave vector that takes following form:

$$k_{j_1\tau_1j_2}^2 = \frac{2\mu}{\hbar^2} (E_{tot} - \epsilon_{j_1\tau_1} - \epsilon_{j_2}) \quad (3.6)$$

here, E is total energy, and ϵ_{j_1} and ϵ_{j_2} are the internal energy of water and hydrogen respectively.

Integrating the interaction potential over all angular coordinates we obtain the coupling matrix elements of the potential:

$$\begin{aligned}
\langle \Omega_{\gamma l}^{JM} | V(R, \theta, \phi, \theta', \phi', \alpha, \beta, \gamma) | \Omega_{\gamma' l'}^{JM} \rangle = & \\
\sum_{p_1 q_1 p_2 p k k'} v_{p_1 q_1 p_2 p} (R) (-1)^{J-j'_1+j'_2-j-k-p} (4\pi)^{-1} & \\
\times \left[(2j_1+1)(2j'_1+1)(2j_2+1)(2j'_2+1)(2j+1)(2j'+1)(2l+1)(2l'+1)(2p_2+1)(2p+1) \right]^{\frac{1}{2}} & \\
\times \begin{pmatrix} l & l' & p \\ 0 & 0 & 0 \end{pmatrix} \begin{pmatrix} j_2 & p_2 & j'_2 \\ 0 & 0 & 0 \end{pmatrix} \begin{pmatrix} l & l' & p \\ j' & j & J \end{pmatrix} \left\{ \begin{matrix} j' & j & p \\ j'_1 & j_1 & p_1 \\ j'_2 & j_2 & p_2 \end{matrix} \right\} a_{\tau_1, k}^{j_1} a_{\tau'_1, k'}^{j'_1} (1 + \delta_{q_1 0})^{-1} & \\
\times \left[\begin{pmatrix} j_1 & p_1 & j'_1 \\ -k & q_1 & k' \end{pmatrix} + (-1)^{p_1+q_1+p_2+p} \begin{pmatrix} j_1 & p_1 & j'_1 \\ -k & -q_1 & k' \end{pmatrix} \right] & \\
\end{aligned} \tag{3.7}$$

The coupling matrix elements are real and are independent of the total projection quantum number M . There is no coupling between different total angular momenta J . In addition the coupled equations can be solved separately for each parity block. The S-matrix is obtained from the asymptotic behaviour of the radial function (see Eq. 2.29). Once the S matrix is derived, we can calculate the state to state cross-section using the following formula:

$$\sigma(j_1 \tau_1 j_2 \rightarrow j'_1 \tau'_1 j'_2) = \frac{\pi}{(2j_1+1)(2j_2+1)k_{j_1 \tau_1 j_2}^2} \sum_{J l l' j j'} (2J+1) |\delta_{l \gamma, l' \gamma'} - S_{l \gamma, l' \gamma'}^J|^2 \tag{3.8}$$

Once the cross-sections are calculated we can obtain the rate coefficients, by assuming a Maxwell-Boltzmann distribution and averaging the cross-sections over the collisional energy (see Eq. 2.44).

3.2. H₂O - *para*-H₂ system

The very first system I studied during my thesis was the H₂O - *para*-H₂ system. Even though the title of my thesis states that I considered excitation by water, in this system, the water molecule is the target. I could try to convince the reader that we could look at this system

from the opposite side and consider the excitation of the hydrogen molecule by water, but unfortunately, this will not work since I consider only the ground state of the *para*-H₂ in the calculations. As one can read in the introduction, water molecule, is a very abundant and important molecule in the ISM. Especially, collisional data of the water-hydrogen system plays an important role in the analysis of the data of star-forming regions. In these regions highly excited rotational transitions of water were observed^{78,79}. This system was already well studied. Earlier collisional data, calculated within a pure quantum theory for the first 45 rotational energy levels of *p*- and *o*-H₂O (rotational levels up to $j = 11$), within a temperature range of 5 - 1500 K can be found in literature⁸⁰. However, there is no data for a higher rotational transition ($j \geq 12$) calculated within a quantum theory. That is why this system was a perfect choice for my first project, where I could learn about quantum scattering theory and yet provide new and useful data for the astronomical needs. Even though this system is not considered as computationally heavy, the calculation of such high rotational transitions was a challenge. I had to set up a strategy that would allow me to complete this task. In the following sections, I will present my approach that I used to perform scattering calculations of this system and the results I obtained.

3.2.1. PES

The PES I have used in the calculation was calculated by Valiron et al.⁴⁴. This is a high-quality PES calculated in the CCSD(T)-R12 level of theory and was already benchmarked with the experimental data, showing excellent accuracy⁸¹⁻⁸³. This is a full 9D potential, that was vibrationally averaged over the ground-state vibrational eigenfunctions of the monomers, to construct a 5D rigid rotor PES. Even, with this approximated 5D PES, the scattering calculations between highly excited rotational levels of water were not feasible, and further approximations were needed. The further approximation requires that the internal structure of the hydrogen is neglected. Thanks to this approximation the dimensions of the potential could be further reduced. I decided to use the adiabatic hinder rotor approximation (AHR) introduced by Scribano et al.⁷⁷ The idea behind AHR approximation is to separate the degrees of freedom of our system into two subgroups. The first one, called "fast", which

involves the coordinates (Θ', ϕ') related to the H_2 molecules. The second group, called "slow" coordinates $(\mathbf{R}, \Theta, \phi)$, provides us information on the position of the center of mass of the hydrogen molecule with respect to the water molecule. Such a separation is possible thanks to the differences in rotational constants of the two molecules (\approx factor 2). Performing this approximation reduces the dimensionality of our potential from 5D to 3D. The hydrogen molecule is treated as a pseudo atom. Therefore its rotational structure is neglected, and in our calculations, we considered hydrogen in the *para*-state of its ground level. This approximation was already tested in the scattering calculations showing great results in comparison with the full 5D potential (see Fig. 3.2).

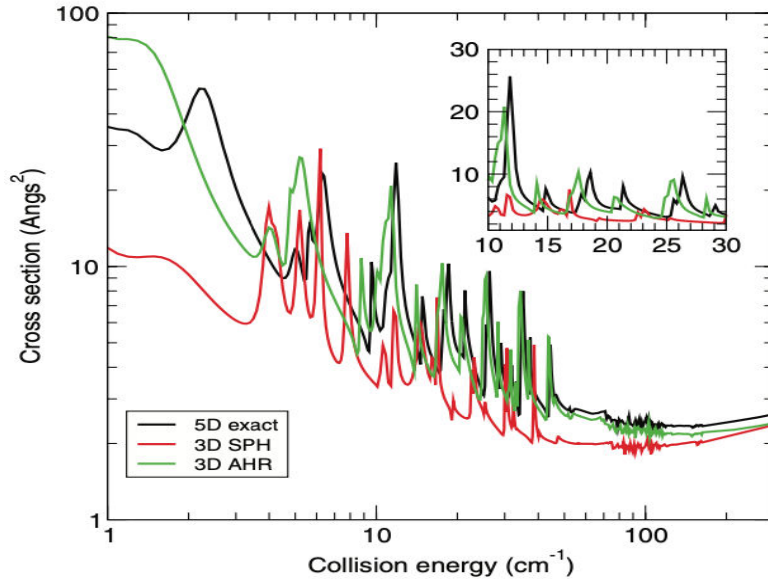


Figure 3.2: Comparison of cross-sections obtained with 3 different potentials for the lowest de-excitation transitions. The black line represents cross-sections obtained with 5D rigid rotor potential⁴⁴, the red line represents cross-sections obtained with spherically approximated potential⁸⁴, and green line represents results obtained with the AHR approximation⁷⁷. The figure was taken from the work of Scribano et al.⁷⁷

3.2.2. Calculations and Results

Scattering calculations were performed using the MOLSCAT scattering code (see Appendix A), with the coupled states approximation. Since, the hydrogen is treated as a pseudo-atom in the calculations, the actual scattering methodology is slightly different compared to the one presented in the methodology section of this chapter. All terms connected to the hydrogen molecule (with index 2) will vanish, and all the equations will be simplified. I started my calculations with a series of convergence tests to optimize the crucial parameters. The results from the tests at total energies of 1000 and 3000 cm^{-1} for JMAX, RMAX, and STEPS are presented in Fig. 3.3. In the case of total angular momenta, the automatic convergence parameter of the Molscat code was used, with the following criteria: DTOL = 0.3 and OTOL = 0.005 for energies up to 8000 cm^{-1} , and DTOL = 0.001 and OTOL = 0.0001 for energies up to 12000 cm^{-1} (explanations of the presented parameters can be found in Appendix A). As we can observe, good convergence is easily achieved for these parameters. The final parameters that were used in the calculations in the different range of collisional energies, are provided in Table 3.1.

Energy Range	0-1000	1001-3000	3001-5000	5001-7000	7001-12000
JMAX	11	19	25	27	29
RMAX	20	20	20	40	50
STEPS	10	10	10	10	10

Table 3.1: Final convergence parameters that were used in the calculations in different ranges of total energies.

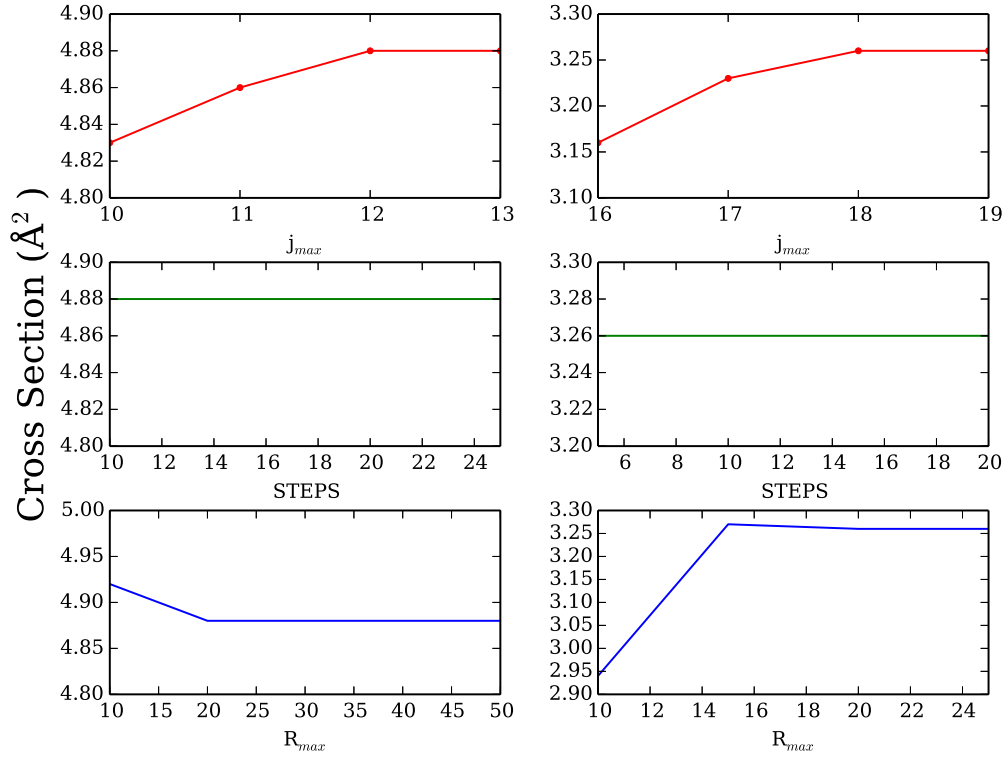


Figure 3.3: Cross-sections as a function of convergence parameters at total energy of 1000 cm^{-1} (figures in the left column) and 3000 cm^{-1} (figures in the right column) for de-excitation transitions $9_{19} \rightarrow 8_{08}$

The final results of my calculations were published in the following article: *Rotational excitation of highly excited H_2O by H_2* . The rate coefficients for temperatures up to 2000K were calculated for both *para*- and *ortho*-water for 97 rotational energy levels. The computed data were compared with the most accurate collisional data, and the results show accuracy within a factor of 2-3. The impact of our collisional data on the radiative transfer modeling was also presented.

Rotational excitation of highly excited H₂O by H₂

Michał Żóltowski,^{1,2,3} François Lique,^{1,2*} Agata Karska³ and Piotr S. Żuchowski³

¹LOMC - UMR 6294, CNRS-Université du Havre, 25 rue Philippe Lebon, BP1123, F-76 063 Le Havre cedex, France

²Univ Rennes, CNRS, IPR (Institut de Physique de Rennes) – UMR 6251, F-35000 Rennes, France

³Faculty of Physics, Astronomy and Informatics, Nicolaus Copernicus University, Grudziadzka 5, PL-87-100 Torun, Poland

Accepted 2021 February 10. Received 2021 February 8; in original form 2021 January 28

ABSTRACT

Water is a key molecule for interstellar chemistry. Observations with *Herschel* telescope show significant population of very high rotational transitions ($j \gtrsim 8$) in young stellar objects, indicating significant amounts of water in hot ($T \gtrsim 1500$ K) and dense ($n \gtrsim 10^6$ cm⁻³) gas. Non-local thermodynamic equilibrium (LTE) modelling of these observations requires the knowledge of the collisional and radiative properties of highly excited water at high temperature. The aim of this work is to calculate a new set of excitation rate coefficients for both *para*- and *ortho*-H₂O induced by collisions with H₂ for energy levels up to $j = 17$. Quantum scattering calculations were performed using a reduced dimensional approach and the coupled states approximation. Rate coefficients were obtained for 97 pure rotational energy levels of both *para*- and *ortho*-H₂O and for temperatures up to 2000 K. With the forthcoming launch of the *James Webb Space Telescope*, these new collisional data will allow us to gain more insight into the physical conditions in star- and planet-forming regions.

Key words: molecular data – molecular processes – ISM: abundances – ISM: molecules.

1 INTRODUCTION

Water (H₂O), as the third most abundant molecule in the Universe (after H₂ and CO), plays an important role as a tracer of physical components of star-forming regions and as a gas coolant in interstellar shocks (Neufeld & Kaufman 1993). Water was first detected through maser emission at 22 GHz (Cheung et al. 1969). Indeed, a maser process can produce a sharp and bright spectral line that can be observed even in distant galaxies (Menten & Melnick 1991). Hence, the water maser at 22 GHz became a powerful tool to trace early phases of star formation both in low- and high-mass stars, and connected with outflows and jets (Furuya 2003).

Observations of pure rotational lines of cosmic water are blocked from the ground by the water that is present in the Earth’s atmosphere, even in the dry and high-altitude observing sites such as the Atacama desert. Then, it is necessary to observe water from space. Several space observatories such as the *Infrared Space Observatory* (ISO; Clegg et al. 1996; de Graauw et al. 1996), the *Submillimeter Wave Astronomy Satellite* (SWAS; Melnick et al. 2000), the *ODIN* satellite (Nordh et al. 2003), or the *Herschel* Space Observatory (*Herschel*; Pilbratt et al. 2010) contributed to the study of interstellar water. Thanks to these space telescopes, we know that water is ubiquitous in protostars and their outflows (Green et al. 2013; Karska et al. 2013, 2018), but relatively scarce in protoplanetary discs (Hogerheijde et al. 2011; Fedele et al. 2013). H₂O is also present in comets and atmospheres of planets in the Solar system (van Dishoeck, Herbst & Neufeld 2013).

High-excitation rotational lines of H₂O are commonly detected in the youngest, most-deeply embedded protostars (Goicoechea et al.

2012; Herczeg et al. 2012). For example, the 8₁₈ – 7₀₇ line at 63.2 μm is detected in ~30 per cent of low-mass protostars (Karska et al. 2018). The most likely mechanism responsible for such excitation conditions are far-UV irradiated shocks associated with outflows (Karska et al. 2014; Melnick & Kaufman 2015).

The *James Webb Space Telescope* (JWST), a new infrared space observatory that will operate soon, is expected to increase the understanding of the physical and chemical conditions of the interstellar medium (ISM). It will observe formation of the very first galaxies, glimpse into dense dusty clouds and galaxies, and observe the birth and evolution of stars and planets (Gardner et al. 2006). Sensitivity and spatial resolution of JWST will allow the detection of rotational emission spectra of water in the range from 2 to 29 μm. This frequency range contains transitions between high rotational levels of H₂O ($j > 12$) that can probably be detected from hot ($T \geq 1500$ K) and dense gas ($n \gtrsim 10^6$ cm⁻³).

In order to interpret these future H₂O observations and infer the physical and the chemical conditions in the ISM, it is necessary to perform excitation and radiative transfer calculations. Such calculations often require to go beyond the local thermodynamical equilibrium (LTE) approximation (Roueff & Lique 2013), in which case collisional and radiative properties of the molecules are needed. In molecular clouds, the dominant collisional partner is H₂ (Roueff & Lique 2013). As mentioned above, water maser emission is frequently detected and modelling of these spectra is not feasible without reliable collisional data.

Numerous works have been devoted to study the collisional rate coefficients for the H₂O–H₂ system so far. First calculations were done by Phillips, Maluendes & Green (1996). The authors calculated rate coefficients for transitions between *para*- and *ortho*-H₂O (hereafter labelled as *p* – H₂O and *o* – H₂O, respectively) rotational levels up to $j = 3$, for temperatures ranging from 20

* E-mail: francois.lique@univ-rennes1.fr

to 140 K. Using an improved potential energy surface (PES) by Faure et al. (2005), Daniel, Dubernet & Grosjean (2011) performed calculations for the first 45 energy levels of *p* – and *o* – H₂O (for rotational levels up to $j = 11$) for temperatures ranging from 5 to 1500 K. Rate coefficients for temperatures up to 2000 K using the quasi-classical trajectories (QCT) approach were also computed by Faure & Josselin (2008). These calculations included ro-vibrational transitions between levels with an internal energy up to 5000 cm⁻¹. The collisions of H₂O with other interstellar colliders (He, H, and e⁻) were also broadly studied. The available data for the H₂O–e⁻ collisions cover the lowest 842 ro-vibrational levels of H₂O, in the 200–5000 K temperature range (Faure, Gorfinkiel & Tennyson 2004; Faure & Josselin 2008). For the H₂O–H collisional system, rate coefficients for transitions between the first 45 energy levels of both *o* – and *p* – H₂O were provided in the 5–1500 K temperature range by Daniel et al. (2015), while for the H₂O–He collisional system, the transition between first 45 energy levels of both symmetries of H₂O were also computed in the 20–2000 K temperature range (Green, Maluendes & McLean 1993; Yang et al. 2013).

Even though the collisional excitations of H₂O by different colliders are well studied, there is still a lack of accurate collisional rate coefficients at high temperatures and for highly excited rotational states. Indeed, the only collisional data available for high temperature media are those of Faure & Josselin (2008) computed using an approximate treatment. It is then necessary to compute pure quantum data for transitions involving rotational energy levels above $j = 11$, and rate coefficients for temperatures above 1500 K. In this paper, we provide new excitation rate coefficients of both *p* – and *o* – H₂O induced by collisions with H₂ including transitions between energy levels up to $j = 17$ (only rotational levels of the ground vibrational states) for temperatures up to 2000 K. This paper is organized as follows. In Section 2, we describe the theoretical approach used for our calculations. In Section 3, we present our results and discuss their astrophysical impact in Section 4. Finally, in Section 5, we provide the conclusions of our work.

2 METHODS

To describe the H₂O rotational states, we use the j_{k_a, k_c} notation, where j is the rotational quantum number and k_a, k_c describes the projection of j along the principal inertia axes. For the H₂ rotational states, we used the j_2 label. Full list of H₂O energy levels considered in this work can be found in the Appendix.

For the scattering calculations, we used the H₂O–H₂ PES calculated by Faure et al. (2005) and benchmarked versus numerous experimental studies (Yang et al. 2011; Ziemkiewicz et al. 2012; Bergeat et al. 2020). As we were only interested in pure rotational excitation, we used the rigid-rotor approximation (Valiron et al. 2008). However, even using a 5D rigid-rotor PES, calculations of cross sections and rate coefficients for transitions between rotational levels with high j , are still extremely CPU and memory consuming.

Hence, we have decided to use the approximation suggested by Scribano, Faure & Lauvergnat (2012) in which the H₂ molecule is treated as a pseudo-atom. This approximation reduces the scattering problem to a 3D problem. This is the so-called adiabatic hinder-rotor (AHR) approximation. AHR is based on the assumption that the hydrogen rotation is much faster than other motions of the system, and as such, can be separated out. More detailed information about this approximation can be found in the work of Zeng et al. (2011). Using such treatment, the rotational structure of H₂ is neglected and the influence of the rotational states of H₂ on the magnitude

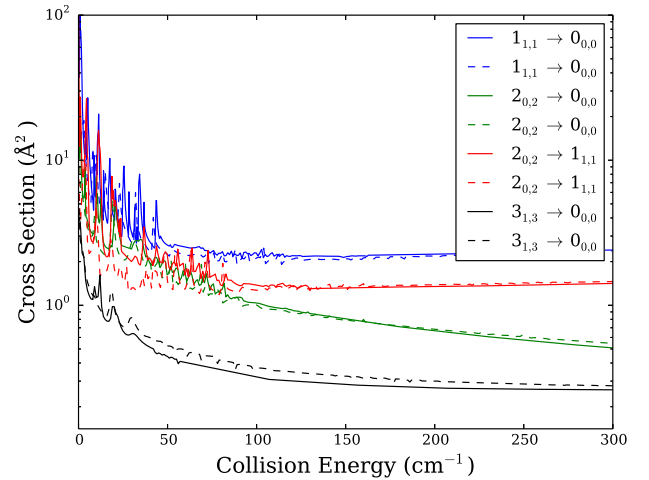


Figure 1. Comparison of the cross-sections as a function of collision energy for the low-lying rotational transitions obtained using the CC (solid line) and CS (dashed line) methods.

of the excitation rate coefficients is omitted since calculation are only performed for H₂ in its ground rotational state. Daniel et al. (2011) showed that rate coefficients calculated with the H₂($j_2 = 2$) collider are very similar to that calculated with the H₂($j_2 = 1$) collider and concluded that, for astrophysical application, it is enough to calculate one of them. In addition, they observed that H₂($j_2 = 2$) (or H₂($j_2 = 1$)) over H₂($j_2 = 0$) rate coefficients ratio goes to unity at high temperatures. It seems then that providing data for only H₂($j_2 = 0$) is accurate enough for high temperature applications, the present goal of this paper. Hereafter, we will not refer again to the j_2 quantum number that describes the hydrogen molecule rotational state.

Our calculations were performed using the MOLSCAT non-reactive quantum scattering code developed by Hutson & Green (1994). As the *ortho*- and *para* levels of H₂O do not interconvert in inelastic collisions, they were treated separately. We calculated state to state cross sections between all rotational energy levels up to $j_{k_a, k_c} = 17_{1,17}$ for *para*-H₂O and $j_{k_a, k_c} = 17_{0,17}$ for *ortho*-H₂O. The diabatic modified log-derivative airy propagator method developed by Alexander & Manolopoulos (1987) was used. For the rotational constants of H₂O, the following values were used: $A = 27.8806$, $B = 14.5216$, and $C = 9.2778$ cm⁻¹, and for H₂, we used $B_0 = 59.322$ cm⁻¹. Reduced mass for the H₂O–H₂ system is $\mu = 1.8128$.

Preliminary calculations shows that in order to reach convergence of the cross-sections for the H₂O energy levels up to $j = 17$, it is necessary to include the energy levels up to $j = 29$ in the rotational basis. With such a large basis, pure close-coupling (CC) calculations (Arthurs, Dalgarno & Bates 1960) are not feasible in terms of computing resources even with a 3D approach. Therefore, we explore the possibility of using the coupled-states (CS) approximation (McGuire & Kouri 1974). Fig. 1 shows a comparison between cross sections obtained at the CC and CS level of theory. As we can see, the CS method cannot describe accurately the resonances in the low collisional energy regime. However, for higher collisional energies, an excellent agreement between CC and CS results is found. Hence, we decided to use the CS approximation for the calculations.

The cross-section calculations were then performed for energy up to 12 000 cm⁻¹ using the CS approximation. We calculated the state-to-state cross sections for transitions between 97 rotational energy levels of *o* – H₂O and 97 rotational energy levels of *p* – H₂O.

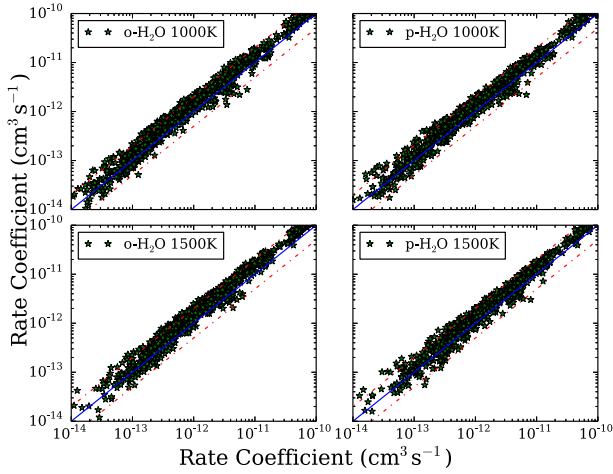


Figure 2. Collisional rate coefficient calculated using the CS method (this work) as a function of collisional rate coefficient calculated using the CC method (Daniel et al. 2011) for *ortho*-H₂O (left-hand column) and *para*-H₂O (right-hand column) and for temperatures of 1000 (upper row) and 1500 K (lower row). The blue line is referred to equal rate coefficients, and the red dashed lines represent a difference of a factor of 2.

Collisional rate coefficients (k) were computed for temperatures up to 2000 K by averaging the cross-section (σ) over the collisional energy (E_c):

$$k(T) = \left(\frac{8}{\pi\mu k_B^3 T^3} \right)^{1/2} \int_0^\infty \sigma(E_c) E_c e^{-E_c/k_B T} dE_c, \quad (1)$$

where μ is the reduced mass of the collisional system, and k_B is the Boltzmann constant.

3 RESULTS

To check the accuracy of our new rate coefficients, we first compare our results with the H₂O–H₂($j_2 = 0$) ones obtained by Daniel et al. (2011). In Fig. 2, we show, at 1000 and 1500 K, the rate coefficients calculated in this work, as a function of corresponding ones of Daniel et al. (2011) for all possible transitions considered by Daniel et al. (2011) (up to $j = 11$). The possibility of H₂ excitation in the data of Daniel et al. (2011) was not considered. In general, our calculations are in good agreement with the results of Daniel et al. (2011), the difference staying within a factor of ~ 1.5 – 2 . Such difference can be partly explained by the fact the H₂ excitation was not included in our calculations. Nevertheless, the differences are reasonable, given the different approaches that were used. As the temperature increases, the differences with respect to reference data decrease.

To better understand the relative magnitudes between inelastic rate coefficients (propensity rules) for various changes of rotational quantum states we compared them for the transitions with fixed initial j , k_a and k_c quantum numbers. In Fig. 3, we present rate coefficients for de-excitation transitions out of the $j_{k_a, k_c} = 14_{1,14}$ level of *o*-H₂O and the $j_{k_a, k_c} = 14_{0,14}$ level of *p*-H₂O. We observe a strong propensity toward the transitions with $\Delta j = 1$ as already noticed by Faure et al. (2007). When the temperature increases, the magnitude of the rate coefficients for $\Delta j = 1$ and $\Delta j > 1$ tends to be closer even if the dominance for the $\Delta j = 1$ remains marked. An interesting feature is seen for the transition to the $j'_{k'_a, k'_c} = 11_{0,11}$ and $11_{1,11}$ levels of *o*-H₂O and *p*-H₂O, respectively. These transitions with $\Delta j = 3$ are similar to transitions with $\Delta j = 2$ at high temperatures showing that

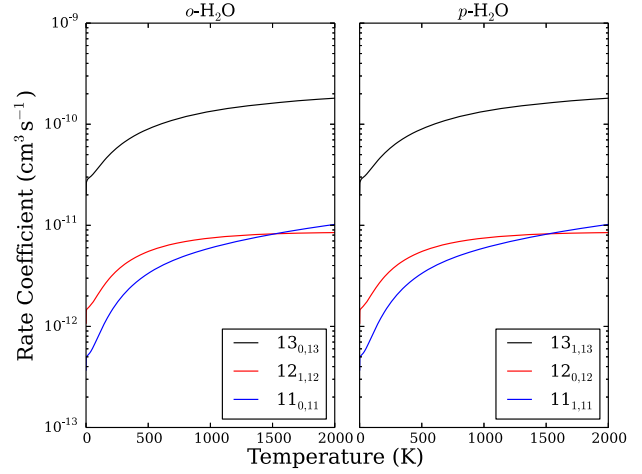


Figure 3. Temperature variation of the collisional rate coefficients for de-excitation transitions out of the level $j_{k_a, k_c} = 14_{1,14}$ (left-hand panel) and $14_{0,14}$ (right-hand panel).

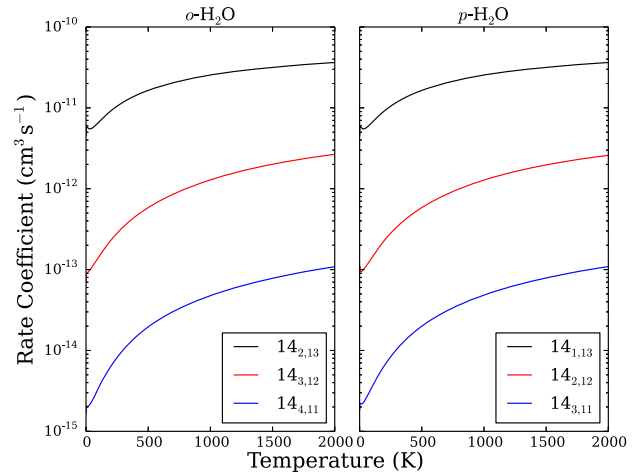


Figure 4. Collisional rate coefficients as a function of temperature, for de-excitation transition where only projection quantum number are changed, within the $j = 14$ level. The left-hand panel presents transitions to the $j'_{k'_a, k'_c} = 14_{1,14}$ level, while the right-hand panel presents transitions to the $j'_{k'_a, k'_c} = 14_{1,14}$.

de-excitation to a much lower levels is also highly probable. In Fig. 4, we present $\Delta j = 0$ de-excitation transitions out of the $j'_{k'_a, k'_c} = 14_{1,14}$ level of *o*-H₂O and of the $j'_{k'_a, k'_c} = 14_{0,14}$ level of *p*-H₂O. For both H₂O symmetries, we observe a clear dominance of de-excitation transitions with $\Delta k_a = 1$ over the whole temperature range.

In general, we retrieve the usual propensity rules for C_{2v} molecules ($\Delta j = 0 \pm 1$; $\Delta k_a = 0 \pm 1$; $\Delta k_c = 0 \pm 1$) (Faure et al. 2007; Bouhafs et al. 2017), showing that the increase of the temperature has almost no influence on the collisional propensity rules. Finally, the rate coefficients with equal j , Δj , Δk_a , Δk_c of both *para* and *ortho* symmetries are almost equal. It seems then possible to limit calculation to only one H₂O symmetry and to extrapolate data for the other as long as high j levels are considered.

4 ASTROPHYSICAL APPLICATIONS

In order to assess the impact of our new data in astrophysical applications, we used the radiative transfer code RADEX (van der

Table 1. Excitation temperature (T_{ex}) (in K) for selected de-excitations transitions at 1000 and 1500 K for $n(\text{H}_2)$ fixed at 10^7 and 10^{12} cm^{-3} .

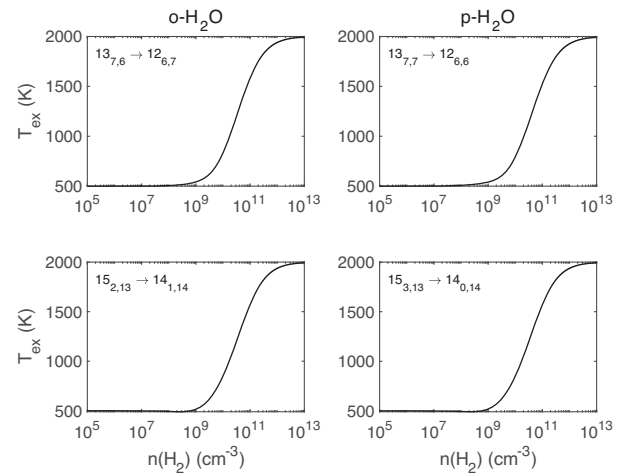
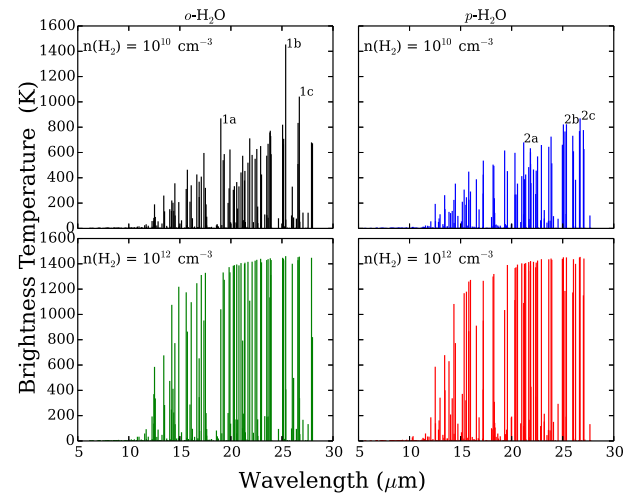
Transition	1000K			1500 K		
	Set 1	Set 2	Set 3	Set 1	Set 2	Set 3
$n(\text{H}_2) = 10^7 \text{ cm}^{-3}$						
$9_{1,9} \rightarrow 8_{0,8}$	507	511	505	502	527	513
$8_{0,8} \rightarrow 7_{1,7}$	503	512	508	508	526	519
$7_{5,3} \rightarrow 6_{6,0}$	1199	781	715	4546	1642	1331
$9_{0,9} \rightarrow 8_{1,8}$	522	503	477	546	509	463
$8_{1,8} \rightarrow 7_{0,7}$	527	511	495	555	525	498
$10_{2,9} \rightarrow 9_{3,6}$	-16790	759	449	-487	2175	481
$n(\text{H}_2) = 10^{12} \text{ cm}^{-3}$						
$9_{1,9} \rightarrow 8_{0,8}$	998	998	1002	1492	1496	1504
$8_{0,8} \rightarrow 7_{1,7}$	1002	999	1001	1508	1500	1504
$7_{5,3} \rightarrow 6_{6,0}$	997	970	983	1355	1430	1490
$9_{0,9} \rightarrow 8_{1,8}$	999	993	979	1498	1481	1446
$8_{1,8} \rightarrow 7_{0,7}$	1000	1001	1001	1500	1501	1503
$10_{2,9} \rightarrow 9_{3,6}$	1042	1119	1291	1613	1799	2448

Note. Three sets of data were used in calculations (see the text for explanation).

Tak et al. 2007) to simulate the non-LTE excitation of H₂O. Our collisional data were combined with spectroscopic data from the LAMDA data base (van der Tak et al. 2020). We also performed calculations using the collisional data of Daniel et al. (2011) obtained for the H₂($j_2 = 0$) collider and available on LAMDA data base (van der Tak et al. 2020). Based on the observations of Herczeg et al. (2012), we set the column density of H₂O to 10^{18} cm^{-2} . The background radiation field was set to 500 K (to avoid convergence issues in radiative transfer calculations at low H₂ density) and we assume line width equal to 10 km s^{-1} (Motttram et al. 2015). The collisional excitation was induced only by H₂. The number density of H₂, $n(\text{H}_2)$, was varied from 10^5 to 10^{13} cm^{-3} .

In Table 1, we show the excitation temperature (T_{ex}) of rotational transitions detected in astrophysical media (Herczeg et al. 2012; Neufeld et al. 2020) using three sets of collisional data. The first set (Set 1) includes the collisional data of Daniel et al. (2011). The second set (Set 2) consists in rate coefficients calculated in this work but only for transitions with $j < 11$ as in Daniel et al. (2011). The third set of data (Set 3) are the present full results including transition between levels up to $j = 17$. The global agreement between the results obtained with the Set 1 and Set 2 data is good (except for maser transition with negative T_{ex}) and not surprising, considering the overall agreement between the present rate coefficients and those of Daniel et al. 2011 (see Fig. 2). However, one can observe that, above 1000 K, the differences in the T_{ex} obtained in the calculations with reduced basis (Set 2) and full basis (Set 3) of rotational energy levels are different, the difference being from a few per cent to 30 per cent (or even higher for the transitions with suprathermal or maser effects). The difference is due to unconverged excitation calculations with respect to rotational basis included in the simulation. Indeed, at temperatures above 1000 K, levels with internal energy above 2000 cm^{-1} can be significantly populated and play an important role in the radiative transfer calculations. Hence, the use of rate coefficients calculated by Daniel et al. (2011) to model rotational spectra above 1000 K might lead to small inaccuracies in radiative transfer calculations. Then, we recommend the use of our new data for the modelling of warm astrophysical media.

In Fig. 5, we present, as a function of $n(\text{H}_2)$, the T_{ex} for transitions between energy levels with internal energy above 1500 cm^{-1} for a temperature of 2000 K. As expected, below a density of 10^7 – 10^8


Figure 5. Excitation temperature (in K) as a function of $n(\text{H}_2)$ for selected transitions. Temperature was set to 2000 K.

Figure 6. Brightness temperatures for pure rotational transitions in the observational wavelength range of the *JWST*. The number in the plots correspond to the following transitions: (1a) $10_{38} \rightarrow 9_{09}$, (1b) $8_{81} \rightarrow 7_{70}$, (1c) $8_{72} \rightarrow 7_{61}$, (2a) $9_{37} \rightarrow 8_{08}$, (2b) $8_{80} \rightarrow 7_{71}$, (2c) $8_{71} \rightarrow 7_{62}$.

cm^{-3} , the excitation temperature is equal to the radiation temperature (500 K in our case). Above this density, the excitation temperatures increase and smoothly reach the kinetic temperature at a density that is the critical density. From these calculations, one can see that LTE conditions are fulfilled when the density of H₂ is above 10^{11} cm^{-3} . Such a high value is not surprising, considering the very fast radiative transitions and demonstrates the importance of non-LTE modelling of H₂O emission from warm ISM.

Finally, we provided the line intensity of all transitions between levels considered in our work that would cover the observation range of *JWST* (5–28 μm). In Fig. 6, we present the simulated H₂O emission spectra at 2000 K for an $n(\text{H}_2)$ value of 10^{10} and 10^{12} cm^{-3} . This corresponds to non-LTE and LTE conditions. We can observe that in the non-LTE case, some of the transitions clearly dominate especially in the wavelength range above 20 μm . It is interesting to note that no maser effects were predicted with such physical conditions. When LTE conditions are reached, it is much more difficult to select lines that could be more intense.

5 CONCLUSIONS

We calculated the excitation cross-sections induced by collision with H_2 for rotational transitions between the first 97 rotational states of *o*- and *p*- H_2O in their ground vibrational level. Calculations up to an energies of $12\,000\text{ cm}^{-1}$ were taken into account allowing us to provide rate coefficients for temperatures up to 2000 K. We found propensity rules in favour of $\Delta j = 0 \pm 1$; $\Delta k_a = 0 \pm 1$; $\Delta k_c = 0 \pm 1$ transitions. We compared our rate coefficients for low lying rotational energy levels with the most accurate rate coefficients of Daniel et al. (2011) and differences of less than a factor of 2 were observed for most of the transitions, hence validating the accuracy of the present data. It is however worth mentioning that collisional excitation by $\text{H}_2(j_2 > 0)$ was not considered here and that assuming similar excitation mechanism for $\text{H}_2(j_2 = 0)$ and $\text{H}_2(j_2 > 0)$ may lead to uncertainties in the observation interpretations (Roueff & Lique 2013) despite previous calculations (Daniel et al. 2011) showed a reasonable agreement between para- and ortho- H_2 data at high temperature.

To evaluate the impact of our new data on the astrophysical modelling, non-LTE excitation and radiative transfer calculations were carried out. The use of our new rate coefficients allowed the production of converged models for high temperatures (up to 2000 K). We also found that non-LTE analysis is mandatory even for modelling emission from warm and dense molecular clouds. Hence, we recommend the use of our new sets of rate coefficients for astrophysical applications and analysis of the forthcoming data from *JWST*.

ACKNOWLEDGEMENTS

FL and MZ acknowledge financial support from the European Research Council (Consolidator Grant COLLEXISM, grant agreement 811363), the Institut Universitaire de France, and the Programme National ‘Physique et Chimie du Milieu Interstellaire’ (PCMI) of (0:funding-source 3:href="http://dx.doi.org/10.13039/501100004794")CNRS/(0:funding-source)/INSU with INC/INP co-funded by CEA and CNES. We wish to acknowledge the support from the CINES/GENCI for awarding us access to the OC-CIGEN supercomputer within the A0090411036 project. PZ is grateful to Polish National Science Center for funding the grant Opus13 2017/25/B/ST4/01486. AK acknowledges support from the Polish National Science Center grant 2016/21/D/ST9/01098 and the First TEAM grant of the Foundation for Polish Science No. POIR.04.04.00-00-5D21/18-00. PZ and MZ acknowledge that calculations have been carried out at the Wrocław Centre for Networking and Supercomputing, Grant 218.

DATA AVAILABILITY

The rate coefficients will be made available to the astrophysical community in the LAMBDA data base (van der Tak et al. 2020).

REFERENCES

Alexander M. H., Manolopoulos D. E., 1987, *J. Chem. Phys.*, 86, 2044
 Arthurs A. M., Dalgarno A., Bates D. R., 1960, *Proc. R. Soc. A*, 256, 540

- Bergeat A., Faure A., Morales S. B., Moudens A., Naulin C., 2020, *J. Phys. Chem. A*, 124, 259
 Bouhafs N., Lique F., Faure A., Bacmann A., Li J., Guo H., 2017, *J. Chem. Phys.*, 146, 064309
 Cheung A. C., Rank D. M., Townes C. H., Thornton D. D., Welch W. J., 1969, *Nature*, 221, 626
 Clegg P. E. et al., 1996, *A&A*, 315, L38
 Daniel F., Dubernet M.-L., Grosjean A., 2011, *A&A*, 536, A76
 Daniel F., Faure A., Dagdigian P. J., Dubernet M. L., Lique F., Forêts G. P. d., 2015, *MNRAS*, 446, 2312
 de Graauw T. et al., 1996, *A&A*, 315, L49
 Faure A., Josselin E., 2008, *A&A*, 492, 257
 Faure A., Gorfinkel J. D., Tennyson J., 2004, *MNRAS*, 347, 323
 Faure A., Valiron P., Wernli M., Wiesenfeld L., Rist C., Noga J., Tennyson J., 2005, *J. Chem. Phys.*, 122, 221102
 Faure A., Crimie N., Ceccarelli C., Valiron P., Wiesenfeld L., Dubernet M. L., 2007, *A&A*, 472, 1029
 Fedele D. et al., 2013, *A&A*, 559, A77
 Furuya R. S., 2003, in De Buizer J. M., van der Blik N. S., eds, ASP Conf. Ser. Vol. 287, Galactic Star Formation Across the Stellar Mass Spectrum. Astron. Soc. Pac., San Francisco, p. 367
 Gardner J. P. et al., 2006, *Space Sci. Rev.*, 123, 485
 Goicoechea J. R. et al., 2012, *A&A*, 548, A77
 Green S., Maluendes S., McLean A. D., 1993, *ApJS*, 85, 181
 Green J. D. et al., 2013, *ApJ*, 770, 123
 Herczeg G. J. et al., 2012, *A&A*, 540, A84
 Hogerheijde M. R. et al., 2011, *Science*, 334, 338
 Hutson J., Green S., 1994, *CCP6*, Daresbury
 Karska A. et al., 2013, *A&A*, 552, A141
 Karska A. et al., 2014, *A&A*, 572, A9
 Karska A. et al., 2018, *ApJS*, 235, 30
 McGuire P., Kouri D. J., 1974, *J. Chem. Phys.*, 60, 2488
 Melnick G. J., Kaufman M. J., 2015, *ApJ*, 806, 227
 Melnick G. J. et al., 2000, *ApJ*, 539, L77
 Menten K. M., Melnick G. J., 1991, *ApJ*, 377, 647
 Mottram J. C., van Dishoeck E. F., Kristensen L. E., San José-García I., 2015, *EAS Publ. Ser.*, 75, 195
 Neufeld D. A., Kaufman M. J., 1993, *ApJ*, 418, 263
 Neufeld D. A. et al., 2021, *ApJ*, 907, 42
 Nordh H. L. et al., 2003, *A&A*, 402, L21
 Phillips T. R., Maluendes S., Green S., 1996, *ApJS*, 107, 467
 Pilbratt G. et al., 2010, *A&A*, 518, L1
 Roueff E., Lique F., 2013, *Chem. Rev.*, 113, 8906
 Scribano Y., Faure A., Lauvergnat D., 2012, *J. Chem. Phys.*, 136, 094109
 Valiron P., Wernli M., Faure A., Wiesenfeld L., Rist C., Kedžuch S., Noga J., 2008, *J. Chem. Phys.*, 129, 134306
 van Dishoeck E. F., Herbst E., Neufeld D. A., 2013, *Chem. Rev.*, 113, 9043
 van der Tak F. F. S., Black J. H., Schöier F. L., Jansen D. J., van Dishoeck E. F., 2007, *A&A*, 468, 627
 van der Tak F. F. S., Lique F., Faure A., Black J. H., van Dishoeck E. F., 2020, *Atoms*, 8, 15
 Yang C. H., Sarma G., Parker D. H., Ter Meulen J. J., Wiesenfeld L., 2011, *J. Chem. Phys.*, 134, 204308
 Yang B., Nagao M., Satomi W., Kimura M., Stancil P. C., 2013, *ApJ*, 765, 77
 Zeng T., Li H., Le Roy R. J., Roy P.-N., 2011, *J. Chem. Phys.*, 135, 094304
 Ziemkiewicz M. P., Pluetzer C., Nesbitt D. J., Scribano Y., Faure A., van der Avoird A., 2012, *J. Chem. Phys.*, 137, 084301

APPENDIX A: H_2O ENERGY LEVELS

Table A1. List of rotational energy levels of p - and o - H_2O considered in this work.

Level	p - H_2O			o - H_2O				
	Energy (cm $^{-1}$)	j	k_a	k_c	Energy (cm $^{-1}$)	j	k_a	k_c
1	0.0000	0	0	0	23.7995	1	0	1
2	37.1583	1	1	1	42.4024	1	1	0
3	70.1328	2	0	2	79.5132	2	1	2
4	95.2454	2	1	1	135.3220	2	2	1
5	136.5875	2	2	0	136.8896	3	0	3
6	142.3308	3	1	3	173.5975	3	1	2
7	206.7204	3	2	2	212.6276	3	2	1
8	222.3100	4	0	4	224.9935	4	1	4
9	276.0991	4	1	3	287.5372	3	3	0
10	287.3395	3	3	1	300.9197	4	2	3
11	316.5789	4	2	2	325.7888	5	0	5
12	326.9712	5	1	5	384.5845	4	3	2
13	385.9196	4	3	1	400.6697	5	1	4
14	417.1190	5	2	4	447.8971	6	1	6
15	447.4126	6	0	6	448.0984	5	2	3
16	494.7131	4	4	0	494.6876	4	4	1
17	506.2744	5	3	3	511.2338	5	3	2
18	544.9161	6	1	5	554.4392	6	2	5
19	587.5593	7	1	7	587.3702	7	0	7
20	605.7415	6	2	4	616.7070	5	4	1
21	616.4831	5	4	2	651.9710	6	3	4
22	665.0452	6	3	3	707.1617	7	1	6
23	712.0419	7	2	6	745.8521	8	1	8
24	745.7807	8	0	8	757.7345	5	5	0
25	757.7315	5	5	1	763.3271	6	4	3
26	764.4009	6	4	2	787.3865	7	2	5
27	820.9444	7	3	5	847.9893	7	3	4
28	886.9597	8	1	7	889.2393	8	2	7
29	903.7995	6	5	1	903.7675	6	5	2
30	922.7281	9	1	9	922.7018	9	0	9
31	935.2775	7	4	4	938.9439	7	4	3
32	990.4116	8	2	6	1012.2686	8	3	6
33	1059.1747	8	3	5	1075.1106	7	5	2
34	1074.9241	7	5	3	1076.5306	6	6	1
35	1076.5309	6	6	0	1084.5508	9	1	8
36	1085.5482	9	2	8	1118.1682	10	1	10
37	1118.1588	10	0	10	1132.1112	8	4	5
38	1141.9110	8	4	4	1212.2662	9	2	7
39	1224.9511	9	3	7	1246.7707	7	6	1
40	1246.7661	7	6	2	1271.4738	8	5	4
41	1272.2458	8	5	3	1296.5841	9	3	6
42	1300.2590	10	1	9	1300.6753	10	2	9
43	1332.1655	11	1	11	1332.1621	11	0	11
44	1353.2791	9	4	6	1374.6989	9	4	5
45	1442.0947	8	6	2	1442.0664	8	6	3
46	1451.0916	7	7	1	1451.0916	7	7	0
47	1451.4286	10	2	8	1458.0679	10	3	8
48	1493.5849	9	5	5	1496.1079	9	5	4
49	1534.4651	11	2	10	1534.2974	11	1	10
50	1557.5445	10	3	7	1564.7175	12	1	12
51	1564.7163	12	0	12	1597.9454	10	4	7

Table A1 – continued

Level	p - H_2O			o - H_2O				
	Energy (cm $^{-1}$)	j	k_a	k_c	Energy (cm $^{-1}$)	j	k_a	k_c
52	1637.4825	10	4	6	1645.5321	8	7	2
53	1645.5326	8	7	1	1662.8555	9	6	3
54	1662.7187	9	6	4	1707.6626	11	2	9
55	1710.8698	11	3	9	1741.2163	10	5	6
56	1748.0507	10	5	5	1786.8443	12	2	11
57	1786.7786	12	1	11	1839.0601	11	3	8
58	1815.8237	13	1	13	1851.8232	13	0	13
59	1864.9743	9	7	3	1864.9783	9	7	2
60	1865.0929	11	4	8	1881.4147	8	8	1
61	1881.4147	8	8	0	1909.0128	10	6	5
62	1909.5344	10	6	4	1928.8364	11	4	7
63	1981.3672	12	2	10	1982.8277	12	3	10
64	2014.0299	11	5	7	2029.7221	11	5	6
65	2057.7826	13	2	12	2057.7574	13	1	12
66	2085.4839	14	0	14	2085.4840	14	1	14
67	2100.0669	9	8	2	2100.0669	9	8	1
68	2109.6921	10	7	3	2109.6705	10	7	4
69	2138.5371	12	3	9	2153.6613	12	4	9
70	2182.1838	11	6	6	2182.8430	11	6	5
71	2246.2282	12	4	8	2272.9791	13	2	11
72	2273.6154	13	3	11	2311.3642	12	5	8
73	2342.2925	12	5	7	2343.6724	10	8	3
74	2343.6729	10	8	2	2347.2692	14	2	13
75	2347.2597	14	1	13	2367.4998	9	9	0
76	2367.4998	9	9	1	2373.6988	15	0	15
77	2373.6988	15	1	15	2379.9933	11	7	4
78	2379.8996	11	7	5	2454.6623	13	3	10
79	2462.6831	13	4	10	2479.3272	12	6	7
80	2483.8652	12	6	6	2583.0564	14	3	12
81	2582.7885	14	2	12	2586.5292	13	4	9
82	2610.3688	10	9	1	2610.3688	10	9	2
83	2612.4461	11	8	4	2612.4492	11	8	3
84	2632.2863	13	5	9	2655.2980	15	1	14
85	2655.3015	15	2	14	2675.9537	12	7	6
86	2680.4681	16	0	16	2680.4681	16	1	16
87	2676.2925	12	7	5	2685.4551	13	5	8
88	2787.4224	14	3	11	2791.3833	14	4	11
89	2803.3018	13	6	8	2814.1268	13	6	7
90	2878.1544	11	9	3	2878.1545	11	9	2
91	2906.6444	12	8	4	2906.6292	12	8	5
92	2909.3466	10	10	0	2909.3466	10	10	1
93	2911.0669	15	3	13	2910.9578	15	2	13
94	2946.4811	14	4	10	2975.7052	14	5	10
95	2981.8787	16	1	15	2981.8800	16	2	15
96	2998.1038	13	7	7	2999.1617	13	7	6
97	3005.7921	17	1	17	3005.7921	17	0	17

Note. The energy (in cm $^{-1}$) is the energy used for scattering calculations that is slightly different from the experimental values.

This paper has been typeset from a $\text{\TeX}/\text{\LaTeX}$ file prepared by the author.

3.2.3. The excitation of water isotopologues

Even though the abundance of deuterium is typically five orders of magnitude lower than hydrogen, we still observe numbers of deuterated molecules. The HDO was observed right after the first detection of H_2O , and recently the D_2O was observed towards a protostar⁸⁵. The accurate determination of the ratio between water isotopologues may help us to understand the water chemistry in interstellar media⁴⁵. This is why it is so important to investigate the impact of the isotopic substitution in the water molecule on the rate coefficients. I investigated two isotopic substitutions of the water molecule. The first one was the substitution of the oxygen atom in the water molecule. I exchanged ^{16}O with ^{18}O . The second substitution was to exchange both hydrogen atoms with deuterium.

3.2.4. The PES of $\text{D}_2\text{O} - \text{H}_2$ and $\text{H}_2^{18}\text{O} - \text{H}_2$ systems

In this project, I used again the water-hydrogen potential calculated by Valiron and co-workers⁴⁴. This time I used the 5D rigid rotor PES without any further approximations. The 9D PES is independent of nuclear masses. Therefore it can be easily transformed for any water isotopologues system. The center of mass and the bond length were shifted as it was presented by Scribano et al⁸⁶. Two PESs for the water isotopologues were constructed - $\text{H}_2^{18}\text{O} - \text{H}_2$ and $\text{D}_2\text{O} - \text{H}_2$ (Faure et al. to be submitted).

3.2.5. Results

The calculations were performed using the MOLSCAT code with close-coupling (CC) method. After the convergence tests, I performed calculations for both systems, in a short range of collisional energy to check how big the effects of the isotopic substitution is on the cross-sections. The results from this test for the ground level transitions are presented in the figure 3.5 for collisions with *para*- H_2 and in the figure 3.6 for collisions with *ortho*- H_2 . The results of D_2O and H_2^{18}O were compared to the results of HDO and H_2O (the cross-sections of H_2O and HDO were provided by A. Faure). As one can observe, in both collisions with *para* and *ortho* H_2 , the cross-sections of H_2^{18}O and H_2O are almost identical in all presented energy ranges. The differences between HDO and D_2O compared with H_2O are

not negligible. For collisions with *para*-H₂, a difference within a factor of 2 is observed for both isotopologues compared to water. In the case of *ortho*-H₂, the cross-sections of HDO have a similar magnitude to the ones of H₂O, but the cross-sections of D₂O are about two times bigger than those of H₂O.

As reported in previous studies these differences may be explained by the shift of the center of mass of the PES, which leads to different expansion coefficients, different rotational constants of the molecules and different reduced masses of the systems. The difference due to the shift of the center of mass, for selected expansion coefficients are presented in Fig. 3.4. As one can see the differences in the coefficients are not negligible, for both isotopologues in comparison to the water molecule. In table 3.2, I present a comparison of the rotational constants and reduced masses (system with hydrogen molecules as colliders) of water and its isotopologues. Upon comparing rotational constants of water with constants of H₂¹⁸O, we can see that the differences are small. Also, with respect to the reduced masses of these two systems, the differences are relatively small. These small differences between rotational constants and reduced masses, together with the first tests, show that oxygen substitutions have a minor effect (within a few %) on the cross-sections and will be even smaller on the rate coefficients. Indeed, as shown in a former study, isotopic substitution of heavy elements like ¹²C with ¹³C and ¹⁴N with ¹⁵N tend to have only a minor impact on the cross-sections and rate coefficients^{87,88}. In the case of D₂O, the differences between cross-sections compared to H₂O are within a factor of 3. Indeed, the reduced mass of the D₂O-H₂ system is the same as that of H₂¹⁸O - H₂. However, the rotational constants of D₂O are almost two times smaller than H₂O's. Such a difference regarding hydrogen substitution was also observed in the case of other systems such as CCH/CCD collisions with H₂⁸⁹ and NH/ND colliding with He⁹⁰.

Results obtained in this work imply that the rate coefficients of H₂¹⁶O can be safely used to model observations of H₂¹⁸O, and that new scattering calculations are not needed for this system. Using rate coefficients of H₂O for modeling spectra of D₂O may lead to wrong results however, so new scattering calculations for the D₂O - H₂ system, are required.

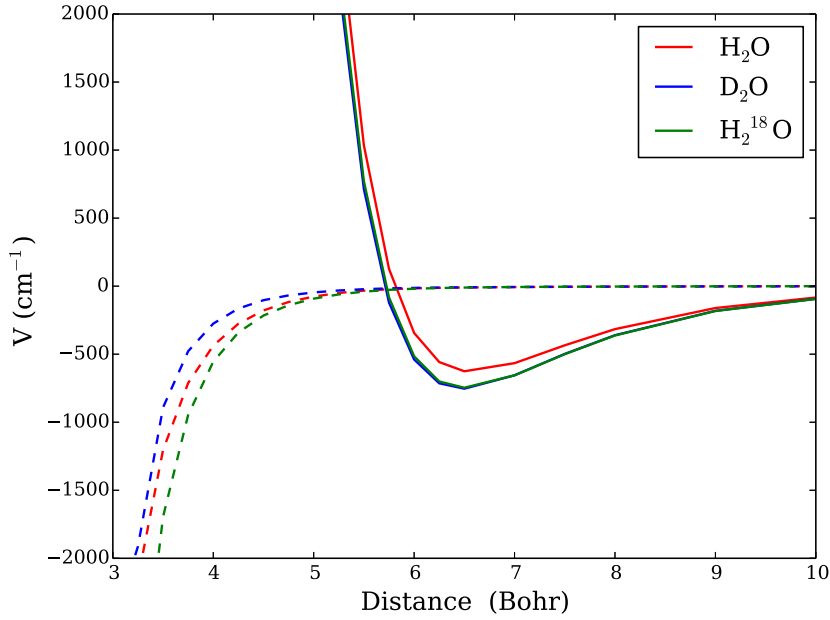


Figure 3.4: Potential expansion coefficients of H₂O (red lines), D₂O (blue lines) and H₂¹⁸O (green lines) molecules. The solid line represent the following set of radial coefficients $\lambda_{l_a, m_a, l_b, l} = 0, 0, 0, 0$, and the dashed line represents $\lambda_{l_a, m_a, l_b, l} = 1, 0, 2, 1$.

Species	A (cm ⁻¹)	B (cm ⁻¹)	C (cm ⁻¹)	Reduced mass
H ₂ O	27.88663	9.27774	14.5217	1.81277373
H ₂ ¹⁸ O	27.53130	9.23809	14.5218	1.83130010
HDO	23.41395	9.10340	6.40628	1.82251621
D ₂ O	15.41998	4.84529	7.27298	1.83130010

Table 3.2: Rotational constants of water and its isotopologues. The reduced mass in the last column correspond to the reduced mass of the systems for which the species presented were interacting with the hydrogen molecule.

Calculations were performed for transitions between rotational energy levels of D₂O up to an internal energy of 300 cm⁻¹. This involves 20 levels of *ortho*-D₂O and 19 levels of *para*-D₂O. In this case, the structure of H₂ was not neglected, therefore for collisions with the *para*-H₂, the ground and first excited level were taken into account. When it comes to *ortho*-H₂, only the ground level was included in the calculations. The following total energy grid was used: up to 500 cm⁻¹, the energy step of 0.25 cm⁻¹ was used, in the 500-700 cm⁻¹ range, the 2 cm⁻¹ energy step was used, in the 700-1000 cm⁻¹ range, the step was increased up 10 cm⁻¹

and finally from 1000-2000 cm^{-1} , the step of 100 cm^{-1} was used. The cross-sections were calculated using the CC method. From the calculated cross-sections, the rate coefficients were derived for temperatures up to 300 K. The full list of energy levels of D_2O and the tables with the calculated rate coefficients are presented in Appendix B. Results for all water isotopologues will be published soon (Faure et al. in prep.).

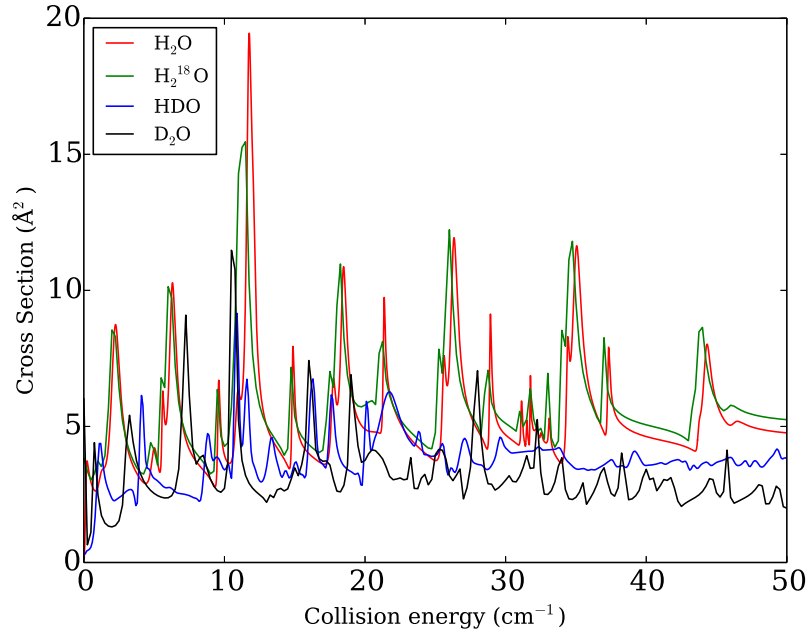


Figure 3.5: Cross-sections of the para-water and its isotopologues as a function of collisional energy for fundamental ($0_{00} \rightarrow 1_{11}$) excitation transitions. The para- H_2 was used as a collider.

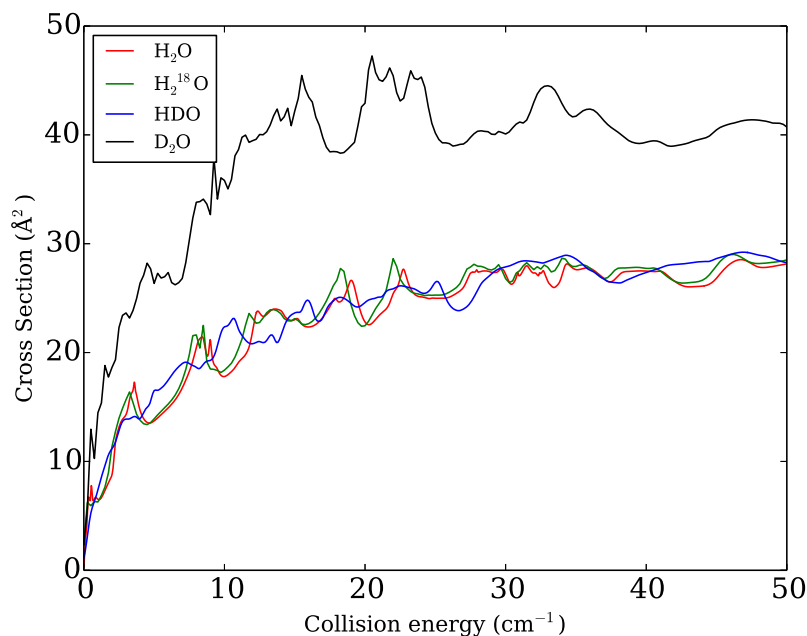


Figure 3.6: Cross-sections of the para-water and its isotopologues as a function of collisional energy for fundamental ($0_{00} \rightarrow 1_{11}$) excitation transitions. The ortho- H_2 was used as a collider.

3.3. The HCN/HNC - H_2O systems

In this section, I present another project of mine involving water molecules as a collider. This project bears on the study of the HCN- H_2O and HNC- H_2O systems. Both HCN and HNC are frequently observed in comets at low heliocentric distances, where the water is considered to be the dominant collider. Therefore, collisional data of both systems are of great importance for modeling the observational spectra of comets. In the literature, we can find the collisional data for HCN- H_2O but only for the *para*-symmetry of water⁴⁰. There is, to the best of my knowledge, no available data for HNC- H_2O . Therefore, my motivation for this project is to provide new collisional data for HCN- H_2O , and the first data for HNC- H_2O .

3.3.1. PES of HCN/HNC - H_2O systems

The PESs of both systems were calculated in collaboration with Dr. Dariusz Kędziera. These potentials were calculated with the symmetry-adapted perturbation theory within

density functional theory (SAPT(DFT))⁹¹ using the autoPES code⁹² and aVQZ basis set. 2833 *ab initio* points were calculated for the HCN - H₂O system, and 2976 points for HNC - H₂O. For both systems, 2 minima were found:

- HCN - H₂O

The first global minimum (Fig. 3.7) was found for a configuration where the hydrogen of HCN approaches the oxygen of the water molecule. The energy for the global minima was found to be about -1852 cm⁻¹ and the distance between this hydrogen and oxygen atoms was found to be 2.044 Å. Comparing this result with the global minima reported by Quintas-Sánchez et al.⁹³, which had an energy of -1814.51 cm⁻¹, we find that the potential well calculated in this work is slightly lower. The second minimum (Fig. 3.8) is located at a geometry where the nitrogen is approaching one of the hydrogens of the water molecule. The distance between these atoms was found to be 2.130 Å, with an energy of -1338.40 cm⁻¹. Comparing this to the second minimum reported by Quintas-Sánchez et al.⁹³, who reported an energy of 1377.30 cm⁻¹, the interaction energy that we determined is in this case slightly higher. Such a difference between the two minima of these two PESs may be accounted for by the different *ab initio* method used in calculations - SAPT(DFT) in this work and CCSD(T) in Quintas-Sánchez et al.⁹³, as well as the basis size used in the calculations.

- HNC - H₂O

Similarly to the HCN system, the first (global) minimum (Fig. 3.9) is also located where the hydrogen from the HNC molecule approaches the oxygen of the water molecule. The distance between these two atoms, i.e. 1.856 Å, suggests that the HNC - H₂O is the van der Waals complex. The well-depth of this system was found to be \approx 2649.10 cm⁻¹. The second minimum (Fig. 3.10) is located at a geometry where the carbon atom is approaching one of the hydrogen atoms of the water molecule. The distance between these two atoms was found to be 2.202 Å, and the interaction energy is 1470.64 cm⁻¹.

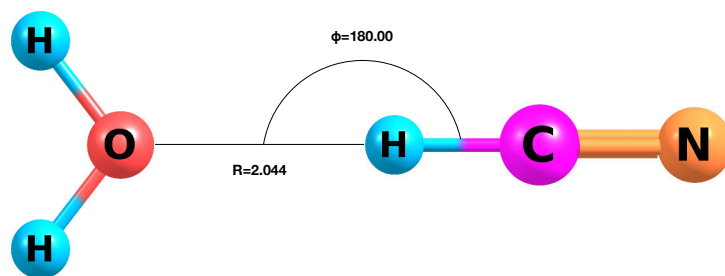


Figure 3.7: Representation of the molecular geometry, for the global minimum of the HCN-H₂O system.

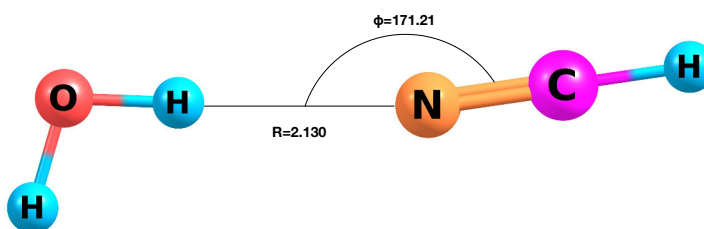


Figure 3.8: Representation of the molecular geometry, for the second minimum of the HCN-H₂O system.

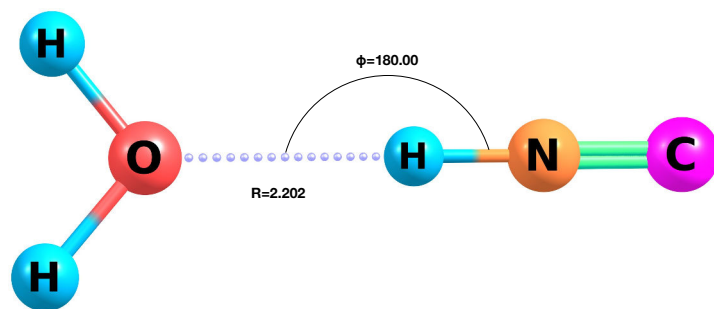


Figure 3.9: Representation of the molecular geometry, for the global minimum of the HNC-H₂O system.

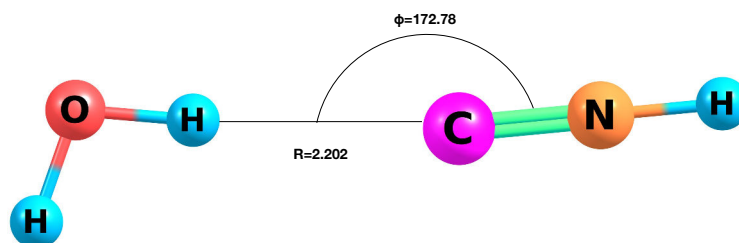


Figure 3.10: Representation of the molecular geometry, for the second minimum of the HNC-H₂O system.

Regarding HNC-H₂O, I have not been able to not find in the literature, any other PES of this system that could be compared to our results. Therefore, in order to validate the accuracy of this PES, and of the PES of HCN-H₂O, I performed *ab initio* calculations for characteristic geometries (the global and local minimums of both PESs) for several distances. Using the MOLPRO *ab initio* code, I performed the calculation using the CCSD(T) method with three basis sets - aVDZ, aVTZ, and aVQZ. The idea behind these calculations with

three different basis was to perform extrapolations to the complete basis set, using a mixed Gaussian/exponential extrapolation scheme (see Eq. 3.9)⁹⁴. Results from this calculations are presented in figures 3.11, 3.12, 3.13, 3.14. For the global minimum of HCN - H₂O, results obtained with the SAPT(DFT) method slightly overestimated the results obtained within the CBS extrapolation. For the second minimum of HCN - H₂O, and for both minima of HNC - H₂O, the energies obtained with SAPT(DFT) method are slightly higher than the one based on CBS. The overall agreement is good. A difference of 3-5 % is observed for the well depth. PESs with such an accuracy are suitable for scattering calculations for astrophysical applications.

$$E_{cbs}(2, 3, 4) = \frac{(1 + e^2)E_2 - (e + e^3 + e^5)E_e + e^6E_4}{(e - 1)(e^5 - e^2 - 1)} \quad (3.9)$$

where e is an exponent, and E_2, E_3, E_4 are energies obtained using the aVDZ, aVTZ, and aVQZ basis sets respectively.

We can clearly see that the potentials are quite different. The global minimum of HNC-H₂O system is around 30% deeper than the one of HCN-H₂O. A similar difference for HCN and HNC, but with different colliders, were also observed. For collisions with the hydrogen molecule and the helium atom, the well depth of HNC-H₂ and HNC-He systems were deeper than the one of HCN-H₂ and HCN-He⁹⁵⁻⁹⁷. These differences in the potential directly lead to differences in the cross-sections. For some of the transitions, differences higher than a factor of 3 were observed between HCN and HNC^{97,98}. Recent experimental collisional studies of HCN-He and HNC-He, were able to confirm the theoretical findings according to which the rate coefficients of HNC-He are much higher than the one of HCN-He.⁹⁹

We can reasonably expect that similar differences in the scattering results will be seen in our case. This is why it is necessary to always treat HCN and HNC as different species in the astrophysical modeling, and the reason why the rate coefficients of one of the systems should not be used as a proxy for the second one.

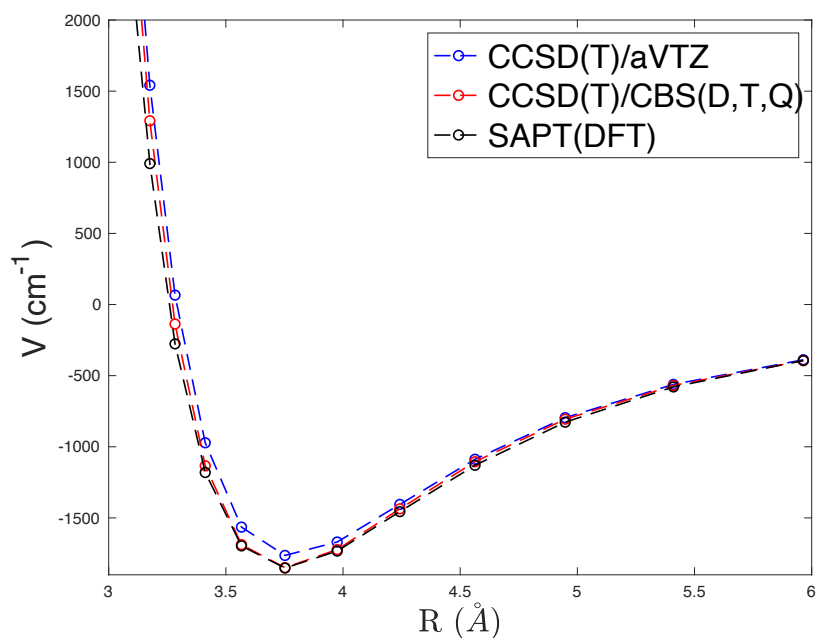


Figure 3.11: Comparison of correlation energy as a function of distance for the global minimum of HCN-H₂O system. See the text for more detailed information.

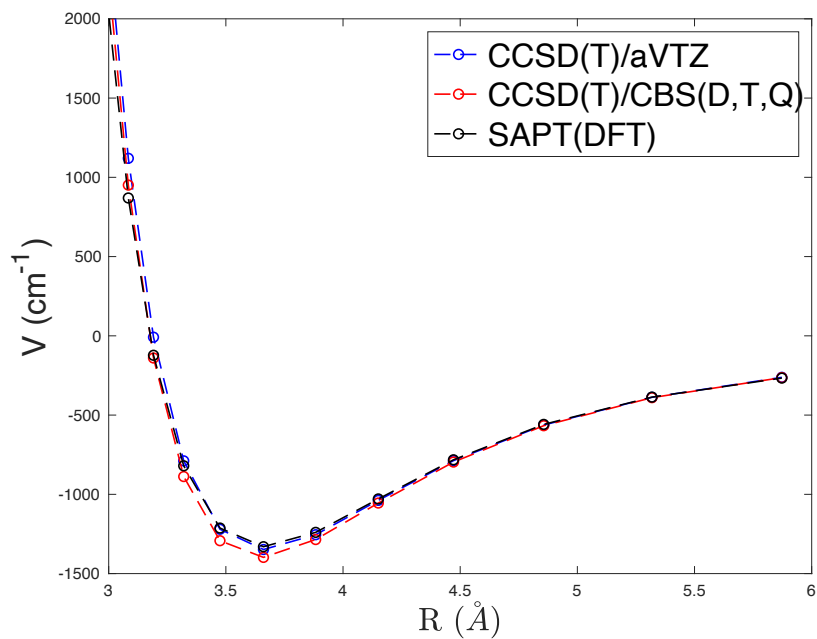


Figure 3.12: Comparison of correlation energy as a function of distance for the second minimum of HCN-H₂O system. See the text for more detailed information.

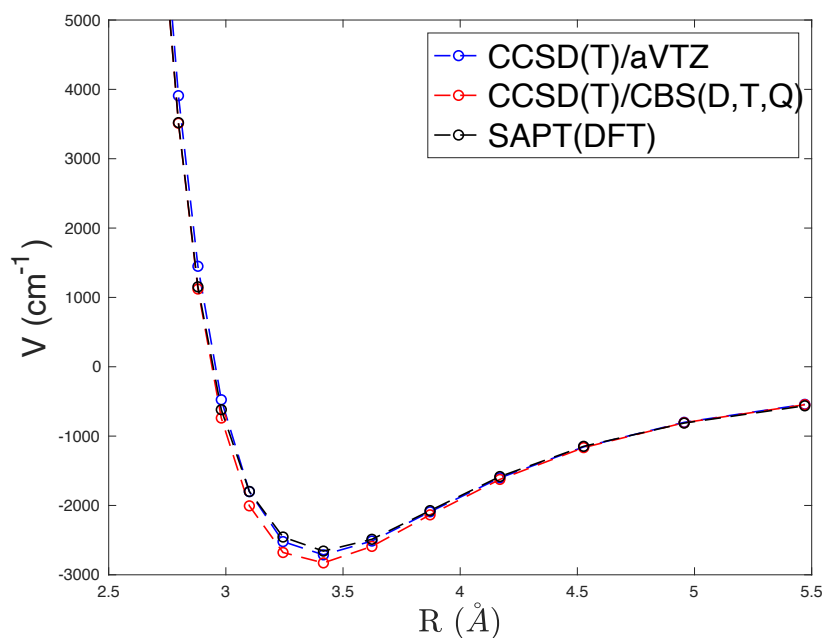


Figure 3.13: Comparison of correlation energy as a function of distance for the global minimum of HNC-H₂O system. See the text for more detailed information.

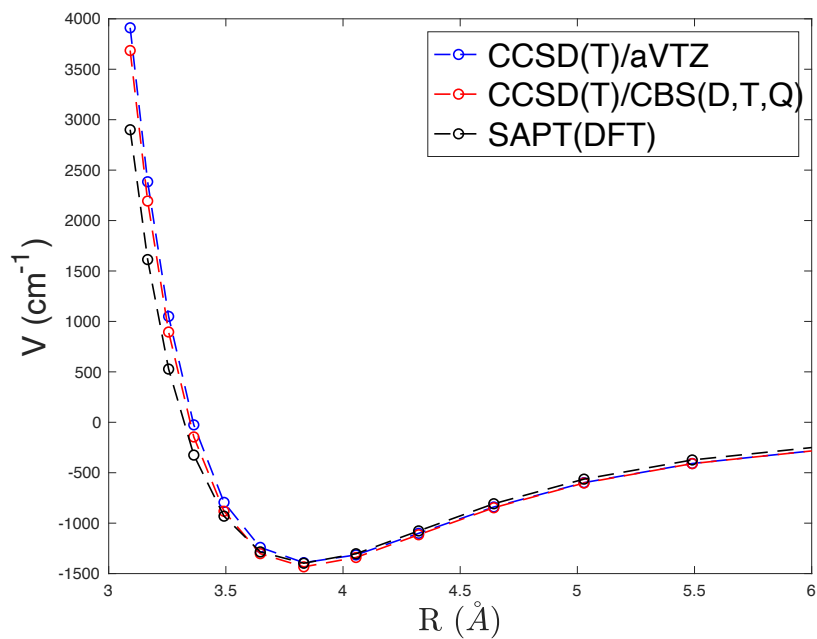


Figure 3.14: Comparison of correlation energy as a function of distance for the second minimum of HNC-H₂O system. See the text for more detailed information.

3.3.2. Scattering Calculations

The PESs of the HCN/HNC-H₂O systems were expanded in a set of radial coefficients—i.e. 595 coefficients for 225 distances— and introduced into the HIBRIDON scattering code. Given that the well of both potentials is very deep, and that, in addition, the rotational constants of HCN and HNC are very small ($\sim 1.5 \text{ cm}^{-1}$), a very big basis should be included in the calculations. Therefore, pure quantum scattering calculations will not be feasible in terms of memory and computational time.

This explains my choice of the SACM method as an alternative. Recent studies for similar systems, HF-H₂O⁴¹ and CO-H₂O³⁸, have showed that this method is suitable for such a complex system. As I mentioned in the previous chapter, the advantage of this method is that we can obtain converged cross-sections with a rotational basis that does not contain many closed channels. Another advantage of this method is that we need to calculate the adiabats only once in the range of the total angular momenta, since they are independent of the energy. However, we should keep in mind that the SACM method is not an *exact* method. Indeed, we need to benchmark it with quantum calculations or experimental data for validation. Therefore, my first test, with both potentials, was to try to reach convergence for the cross-sections just for the total angular momentum $J = 0$, so that we could have a set of benchmark data for the SACM method results. The calculations were performed at a total energy of 30 cm^{-1} with the para-H₂O as a collider. I have fixed the basis size of water at the corresponding rotational level of $j=4, 5, 6, 7, 8$, while increasing the basis size of HNC/HNC. The results of these convergence tests are presented in Figs. 3.15 and 3.16 respectively. As one can see, for all basis of water and the whole rotational basis of HCN/HNC, we do not observe any traces of convergence in the cross-sections.

Thus, the convergence test shows that it is impossible to obtain accurate data for any of the presented systems, even those with the lowest total angular momentum. Thus, the task of evaluating the accuracy of the collisions data obtained in this project is a complex one. The only existing data of HCN-*para*H₂O system were calculated within the CS approximation,

with an estimated convergence of 20%⁴⁰. Thus, comparing future results with the existing ones available in the literature will allow us to roughly confirm the correctness of our calculations depending on their agreement with former results, but will not permit to provide a precise estimate of the accuracy of our data. The only possibility to validate the accuracy of the data that can nowadays be foreseen would be to compare them with experimental results, and thus to hope that such a experiment will be performed in a near future.

I decided to continue directly with the calculations of adiabats for the SACM calculations. I used again the HIBRIDON code to generate the adiabats, with the basis of HCN $j = 10$, and H₂O = 8 , for total angular momenta = 0. These adiabats are presented in Fig. 3.17. These calculations are still an on-going process at the time of this manuscript. I am still testing how far it would be possible to extend the SACM calculations to obtain collisional data for the highest possible transitions of both systems.

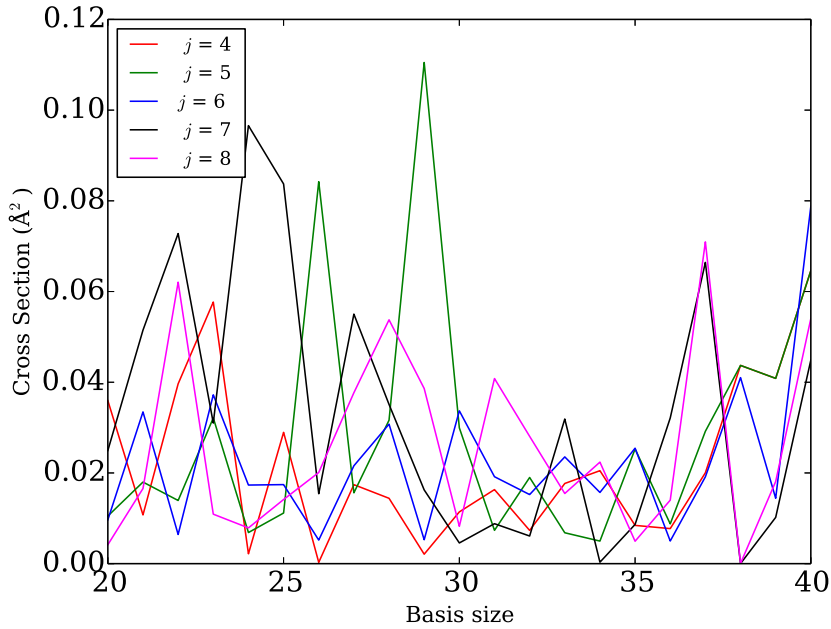


Figure 3.15: Cross-sections for HCN transition from level $j_2 = 0$ to $j_2 = 1$ as a function of the basis size (j_2) of HCN. The values of j_1 refer to the rotational basis size of the *para*-H₂O.

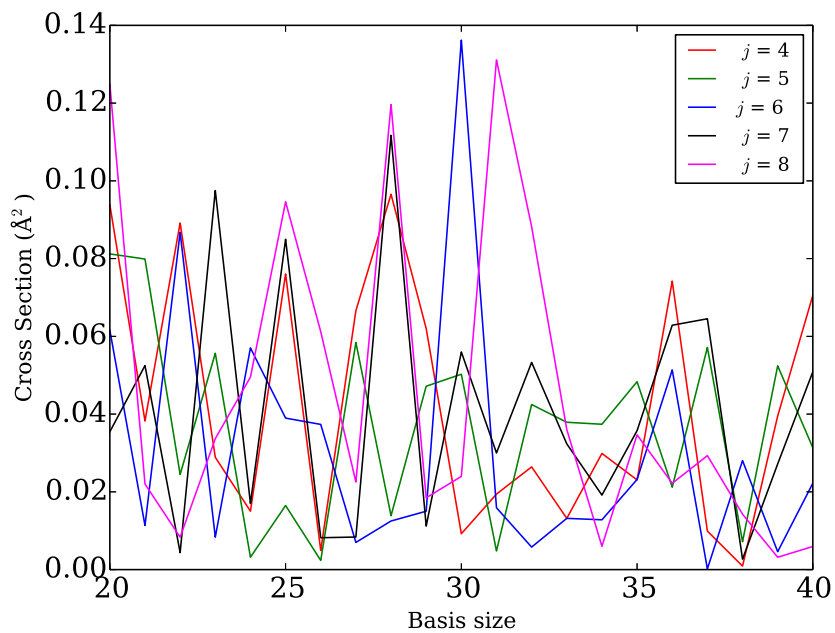


Figure 3.16: Cross-sections for HNC transition from level $j_2 = 0$ to $j_2 = 1$ as a function of the basis size (j_2) of HNC. The values of j_1 refer to the rotational basis size of the *para*-H₂O.

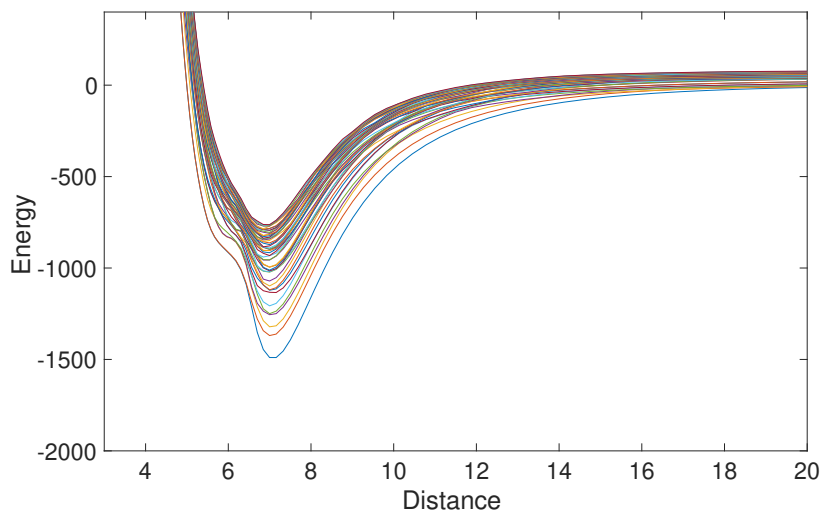


Figure 3.17: Examples of adiabats for H₂O-HCN. The distance is in units of angstrom, and energy is in units of cm^{-1} .

CHAPTER 4

THE EXCITATION OF CO INDUCED BY CO COLLISIONS : SCATTERING CALCULATIONS AND RADIATIVE TRANSFER MODELLING

In this chapter, I will present the study of the collisional excitation of CO induced by CO. This was a computational challenge because this system is considered as very heavy for quantum scattering calculations. This collisional system is, of great importance for the analysis of observational spectra of CO-rich comets. I will present the strategy I set up to obtain collisional data of this system. Then, I will present the impact of the new collisional data on radiative transfer models of CO-dominated comae.

4.1. Methods

The adopted approach for the scattering of two linear molecules is described the work of Green.¹⁰⁰ Green presented a close coupling approach for the scattering of two hydrogen molecules. For simplification the atomic units were adopted. In this formalism, the following Schrodinger equation has to be solved.

$$[H(R, \theta_1, \theta_2, \phi) - E]\Psi(R, \theta_1, \theta_2, \phi) = 0 \quad (4.1)$$

The Hamiltonian in the center of mass coordinate system takes the following form :

$$H = H_1(\theta_1, \phi) + H_2(\theta_2, \phi) + V(\theta_1, \theta_2, \phi, R) + T(R, \theta_1, \theta_2, \phi) \quad (4.2)$$

Where the θ_1 and θ_2 are the angles between the vector \mathbf{R} and the vectors \mathbf{r}_1 and \mathbf{r}_2 of monomers 1 and 2, respectively. ϕ is a rotation of the whole system around the vector \mathbf{R} connecting the center of mass of monomers. R is the distance between two monomers (see Fig. 4.1).

The expansion of the potential will take the following form :

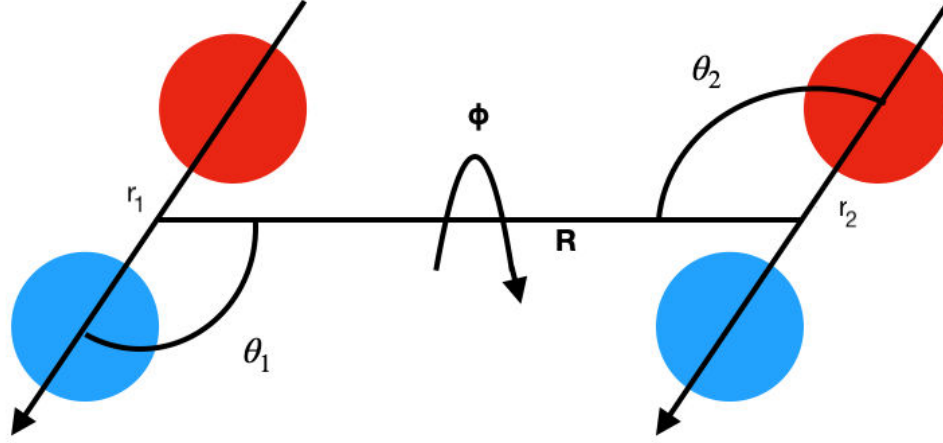


Figure 4.1: Representation of the coordinates of the CO-CO system. \mathbf{R} is the distance between center of mass of the monomers, θ_1 and θ_2 are angles of presented vectors of monomers with respect to \mathbf{R} , and ϕ is a torsional angle around \mathbf{R} .

$$V(R, \theta_1, \theta_2, \phi) = \sum_{l_1 l_2 l} A_{l_1 l_2 l}(R) \sum_{m_1 m_2 m} (l_1 m_1 l_2 m_2 / l_1 l_2 m) Y_{l_1 m_1}(\theta_1, \phi) Y_{l_2 m_2}(\theta_2, \phi) Y_{lm}(\hat{R}) \quad (4.3)$$

where $(l_1 m_1 l_2 m_2 / l_1 l_2 m)$ is a Clebsch-Gordan coefficients and Y_{\dots} are spherical harmonics. The kinetic energy takes the following form :

$$T(R, \theta_1, \theta_2, \phi) = -(1/2\mu) \nabla_R^2 \quad (4.4)$$

where μ is the reduced mass of the CO-CO system. The total wavefunction of our system takes the following form

$$\Psi(R, \theta_1, \theta_2, \phi) = \sum_{J m j_1 j_2 j_{12} L} R^{-1} f_{J m j_1 j_2 j_{12} L}(R) I_{J m j_1 j_2 j_{12} L}(\theta_1, \theta_2, \phi, R) \quad (4.5)$$

where I_{\dots} is:

$$I_{Jm j_1 j_2 j_{12} L}(\theta_1, \theta_2, \phi,) = \sum_{m_1 m_2 m_{12} N} (j_1 m_1 j_2 m_2 / j_1 j_2 j_{12} m_{12})(j_{12} m_{12} L N / j_{12} L J m) \quad (4.6)$$

$$Y_{j_1 m_1}(\theta_1, \phi) Y_{j_2 m_2}(\theta_2, \phi) Y_{LN}(\widehat{R})$$

In the above expression of the wave function we have coupled angular momenta of the monomers ($\mathbf{j}_1 + \mathbf{j}_2 = \mathbf{j}_{12}$), with the orbital angular momenta (L) in order to obtain the total angular momentum J ($\mathbf{J} = \mathbf{j}_{12} + \mathbf{L}$).

Combining the expansion form of Eq. 4.6 with Eq. 4.5 and substituting it into Eq. 4.1 we obtain a set of second order coupled differential equations with the following form:

$$\left[\frac{1}{2\mu} \frac{d^2}{dR^2} - \frac{L(L+1)}{2\mu R^2} + (E - E_\gamma) \right] f_{J\gamma}(R) = \sum_{\gamma'} V_{\gamma, \gamma'}^J(R) f_{J\gamma'}(R) \quad (4.7)$$

where $\gamma = j_1, j_2, j_{12}, L$. Integrating the interaction potential over all angular coordinates we will obtain the coupling matrix elements of the potential:

$$V_{\gamma\gamma'}^J(R) = \int d\theta_1 d\theta_2 d\phi dR I_{J\gamma}(\theta_1 \theta_2, \phi, R) V(\theta_1, \theta_2, \phi, R) I_{J\gamma'}(\theta_1, \theta_2, \phi, R)$$

$$= \sum_{l_1 l_2 l} A_{l_1 l_2 l}(R) (-1)^{J+j_1+j_2+j'_{12}} (4\pi)^{-3/2} ([l]^2 [l_1] [l_2] [j_1] [j_2] [j_{12}] [L] [j'_1] [j'_2] [j'_{12}] [L'])^{1/2}$$

$$\times \begin{pmatrix} l & L' & L \\ 0 & 0 & 0 \end{pmatrix} \begin{pmatrix} l_1 & j'_1 & j_1 \\ 0 & 0 & 0 \end{pmatrix} \begin{pmatrix} l_2 & j'_2 & j_2 \\ 0 & 0 & 0 \end{pmatrix} \left\{ \begin{matrix} L' & L & l \\ j_{12} & j'_{12} & J \end{matrix} \right\} \left\{ \begin{matrix} j'_{12} & j'_2 & j'_1 \\ j_{12} & j_2 & j_1 \\ l & l_2 & l_1 \end{matrix} \right\}$$

$$(4.8)$$

where the $(:::)$, $\{:::\}$ and $\{\vdots\vdots\}$ are 3, 6, 9 -j symbols respectively, and $[n] = (2n+1)$. This mathematical problem is independent of M for each J , and there is no coupling between different J . Solving Eq. 4.7, with the coupling matrix from Eq. 4.8, one obtain the S-matrix

from which cross-section can be extracted using formula Eq. 2.30.

4.1.1. Identical Particle case

In the case of the CO-CO collisional system, we are facing a situation where the target and the projectile are identical molecules. This has some implications in the scattering calculations that we should consider. The function from Eq. 4.6 will take the following form:

$$I_{Jm j_1 j_2 j_{12} L}^{\pm}(\theta_1, \theta_2, \phi, R) = [2(1 + \delta_{j_1 j_2})]^{-\frac{1}{2}} [I_{Jm j_1 j_2 j_{12} L}(\theta_1, \theta_2, \phi, R) \pm (-1)^{\gamma} I_{Jm j_2 j_1 j_{12} L}(\theta_1, \theta_2, \phi, R)] \quad (4.9)$$

here $\gamma = j_1 + j_2 + j_{12} + L$. The linearly independent basis can be obtained by restricting the index pair of $j_1 j_2$ with that of $j_1 \geq j_2$. It should be noted that for $j_1 = j_2$, the I^{\pm} will vanish for the case when $\pm(-)^{\gamma} = -1$ and we do not need to include this term in the expansion.

Using new symmetry angular functions with the corresponding radial function f^{\pm} will lead to a set of coupled equations similar to those presented in Eq. 4.7. We also need to remember that in the matrix elements, we need to consider exchange symmetry. The channels with different parity exchanges will vanish for functions within the parity block (see Eq. 4.10).

$$V_{\gamma\gamma'}^{J\pm}(R) = V_{j_1 j_2 j_{12} L, j_1' j_2' j_{12}' L'}^J \pm (-1)^{j_1 + j_2 - j_{12} + L} \times V_{j_2 j_1 j_{12} L, j_1' j_2' j_{12}' L'}^J \quad (4.10)$$

The asymptotic behavior of the function f^{\pm} will take the following form:

$$f_{J\gamma'}^{\pm} \rightarrow \delta_{\gamma\gamma'} \exp\{-i[k_{\gamma\gamma} R - (l\pi/2)]\} - (k_{\gamma\gamma}/k_{\gamma'\gamma})^{1/2} S_{\gamma\gamma'}^J \{i[k_{\gamma'\gamma} R - (l'\pi/2)]\} \quad (4.11)$$

The formula for the cross-sections will be slightly modified :

$$\sigma_{\gamma\gamma'}^{\pm} = \frac{\pi(1 + \delta_{j_1 j_2})(1 + \delta_{j_1' j_2'})}{(2j_1 + 1)(2j_2 + 1)k_{\gamma\gamma'}^2} \sum_J (2J + 1) |\delta_{\gamma'\gamma} - S_{\gamma'\gamma}^{J\pm}|^2 \quad (4.12)$$

Keeping in mind the restriction that we put on $j_1 \geq j_2$, the above equation will differ only in the degeneracy counting for $j_1 = j_2$ compared to the general formula for cross-section (see Eq. 2.30). Treating the CO-CO system with the identical molecule approach would lead to a significant reduction in the number of channels in the scattering calculations. That would directly lead to a huge reduction in computational time. Unfortunately, I could not apply this approach in my calculations, as we will see below.

4.2. CO-CO interaction potential

To the best of my knowledge, three potential energy surfaces (PESs) of the CO-CO system are available in the literature. Comparison of the interaction energy between PESs, at the positions of global minimum is presented in table 4.1. The level of agreement between all three potential energy surfaces is quite good. A PES of Chen et al.¹⁰¹ that was recently published is a 6D PES that take into account the vibration of the CO monomers. This potential was published in 2020, so almost one year after I started the calculations, and this explains why this PES was not considered. The second 4D PES was calculated by Dawes and co-workers¹⁰². Both CO molecules were treated as a rigid rotor. I performed a series of tests using this potential. Unfortunately, the long-range part ($R > 40$ bohr) is missing. This part is essential for the scattering calculations (especially at low-energy), so I resigned from using this PES. The third PES, and the one I used in my calculations, was the CO-CO potential calculated by Visser et al.⁵¹. This was also a 4D potential where the CO molecules were treated as rigid rotors. It was based on 1512 energy points calculated within CCSD(T) theory level with the aug-cc-pVTZ basis set. The global minimum were found for a distance between two monomers of $R = 8.20 a_0$, with the energy of $V = -135.53 \text{ cm}^{-1}$. This global minimum was found when both CO molecules were set anti-parallel. A second minimum was also reported at an energy of $V = -124.21 \text{ cm}^{-1}$. Both minima are separated by a potential

barrier of the height equal to 72.6 cm^{-1} above the global minima. This PES was validated by comparison with the experimental results showing good agreement between theory and the experiment^{103,104}.

Author	V (cm^{-1})	Distance (a_0)	Θ_1 ($^\circ$)	Θ_2 ($^\circ$)	ϕ ($^\circ$)
Chen et al. ¹⁰¹	-134.52	8.19	134.95	45.05	180
Dawes et al. ¹⁰²	-135.14	8.18	134.58	45.42	180
Visser et al. ⁵¹	-135.53	8.20	134.23	45.77	180

Table 4.1: Comparison of the interaction energy of the CO-CO system at the positions of global minimum, calculated in three different studies (See text for more details).

4.3. Rotational structure of CO

The CO molecule is a closed shell molecule, with a ground electronic state of $^1\Sigma^+$ symmetry. The rotational energy levels of rigid CO molecule, corrected by centrifugal distortion, are obtained from the following formula:

$$E(j) = B_0j(j + 1) - D_0j^2(j + 1)^2 \quad (4.13)$$

Where j is the rotational level, B_0 is a rotational molecule constant, and D_0 is the centrifugal distortion constant.

4.4. Results of scattering calculations

The CO-CO system is challenging for quantum scattering calculations since it involves two heavy molecules with a small rotational constant. In addition, I did not use an indistinguishable molecules approach for this system. Hence, the approach I used leads to almost twice as large a rotational basis as it could be. There were two reasons behind this choice. The first one was for the use of collisional data in astrophysical modeling. Indeed, the radiative transfer modeling always distinguishes between target and collider. The second problem was with the MOLSCAT scattering code. In the case of the close-coupling calculations for identical molecules, for selected transitions, the cross-sections were overestimated by a factor of 2. That would not be a problem because I could divide cross-sections of those transitions and obtain correct results. However, the close-coupling calculations for this system were not

feasible. In my calculations, I used the coupled states (CS) approximation and in the case of the CS approximation, the cross-sections for all the transitions were over or underestimated randomly (see Tab. 4.2). That is why I performed calculations treating both CO molecules as distinguishable linear molecules to ensure that the results I obtained were correct. The calculations were performed for the rotational levels of both CO molecules presented in the Tab. 4.3. The rate coefficients were computed for temperatures up to 150K. The final results were published in two articles. The first article: *Collisional energy transfer in the CO-CO system* contain a detailed explanation of calculation methodology and discussion presenting part of collisional data (for transitions between rotational levels of CO up to internal energy of 160 cm^{-1}). The second article which will be presented in the next section, provides the second part of collisional results, and presents the results of radiative transfer of the CO-CO system.

Transition $j_1, j_2 \rightarrow j_1', j_2'$	CC-IDN	CC-NIDN	CS-IDN	CS-NIDN
1,1 - 0,0	0.12	0.06	0.21	0.10
0,0 - 0,1	0.40	0.40	0.20	0.18
0,2 - 0,0	0.17	0.17	0.07	0.36
0,1 - 0,2	0.60	0.60	0.69	0.39

Table 4.2: Cross-sections calculated with CC and CS approach at a total energy of 20 cm^{-1} . Presented cross-sections are in a unit of \AA^2 and were calculated and sum for the first four total angular momenta ($J = 0, 1, 2, 3$). The columns with the "-IDN" shortcut provide results calculated treating CO molecules as indistinguishable. Columns with "-NIDN" provides results where CO were treated as distinguishable molecules.

Level.	j_1, j_2	Energy (cm ⁻¹)	Level.	j_1, j_2	Energy (cm ⁻¹)
1	0,0	0.000	34	3,6	103.805
2	0,1	3.845	35	3,7	130.712
3	0,2	11.535	36	3,8	161.460
4	0,3	23.069	37	3,9	196.047
5	0,4	38.448	38	3,10	234.474
6	0,5	57.670	39	4,4	76.896
7	0,6	80.735	40	4,5	96.118
8	0,7	107.642	41	4,6	119.184
9	0,8	138.390	42	4,7	146.091
10	0,9	172.978	43	4,8	176.838
11	0,10	211.404	44	4,9	211.426
12	1,1	7.690	45	4,10	249.852
13	1,2	15.379	46	5,5	115.341
14	1,3	26.914	47	5,6	138.406
15	1,4	42.293	48	5,7	165.313
16	1,5	61.515	49	5,8	196.061
17	1,6	84.580	50	5,9	230.648
18	1,7	111.487	51	5,10	269.074
19	1,8	142.235	52	6,6	161.471
20	1,9	176.823	53	6,7	188.378
21	1,10	215.249	54	6,8	219.126
22	2,2	23.070	55	6,9	253.713
23	2,3	34.604	56	6,10	292.139
24	2,4	49.983	57	7,7	215.285
25	2,5	69.205	58	7,8	246.033
26	2,6	92.270	59	7,9	280.620
27	2,7	119.177	60	7,10	319.046
28	2,8	149.925	61	8,8	276.781
29	2,9	184.513	62	8,9	311.368
30	2,10	222.939	63	8,10	349.794
31	3,3	46.139	64	9,9	345.956
32	3,4	61.518	65	9,10	384.382
33	3,5	80.740	66	10,10	422.808

Table 4.3: Asymptotic energy levels of the (CO)₂ dimer for which the rate coefficients has been computed.



Collisional energy transfer in the CO–CO system†

 Michał Żóttowski,^{ab} Jérôme Loreau ^c and François Lique ^{*ab}

 Cite this: *Phys. Chem. Chem. Phys.*,
2022, 24, 11910

An accurate determination of the physical conditions in astrophysical environments relies on the modeling of molecular spectra. In such environments, densities can be so low ($n \ll 10^{10} \text{ cm}^{-3}$) that local thermodynamical equilibrium conditions cannot be maintained. Hence, radiative and collisional properties of molecules are needed to correctly model molecular spectra. For comets at large heliocentric distances, the production of carbon monoxide (CO) gas is found to be larger than the production of water, so that molecular excitation will be induced by collisions with CO molecules. This paper presents new scattering calculations for the collisional energy transfer in CO–CO collisions. Using the quantum coupled states approach, cross sections and rate coefficients are provided between the first 37 rotational states of the CO–CO system. Cross sections were calculated for energies up to 800 cm^{-1} , and excitation rate coefficients were derived for temperatures up to 100 K. In comparison with data available in the literature, significant differences were found, especially for the dominant transitions. Due to the high cost of the calculations, we also investigated the possibility of using an alternative statistical approach to extend our calculations both in terms of rotational states and temperatures considered. The use of these new collisional data should help in accurately deriving the physical conditions in CO-dominated comets.

 Received 4th March 2022,
Accepted 22nd April 2022

DOI: 10.1039/d2cp01065h

rsc.li/pccp

1 Introduction

Comets are valuable sources of information about the evolution of the solar system. Their ice nuclei contain molecules formed at the early stages of planetary formation, and performing spectroscopic observations of the coma, the temporary gaseous atmosphere of a comet, gives insights into the composition of the nucleus. This leads to valuable information about the physical conditions prevailing during planets formation.¹ In addition, astronomical models show that various volatile species in Earth's atmosphere, especially noble gases, might have originated from comets.² Numerous observations of comets have been performed, covering a wide range of wavelengths from ultraviolet, optical, infrared, to radio.¹ One of the most significant studies was carried out by the ROSETTA spacecraft, which performed *in situ* observations of comet 67P/Churyumov–Gerasimenko.³ These observations led to new insights about the composition of cometary ices and atmospheres, which present a huge diversity of molecules including H₂O, CO and CO₂, CH₃OH and CH₄.^{1,4,5}

Extracting information about the physical conditions and chemical composition of comets, and estimating the abundance

of molecules, relies on modeling the observational spectra. The low density conditions in the coma means that the local thermodynamical equilibrium (LTE) is usually not fully achieved, and this modeling requires both radiative and collisional properties of molecules.^{6,7} While radiative data are analytically available for most of the observed molecules, computationally demanding calculations are required to obtain state-to-state collisional rate coefficients. In cometary atmospheres, H₂O, CO, and CO₂ are by far the most abundant species, and it is thus crucial to study the mutual collisional excitation of these molecules. In comets, the excitation of molecules is usually dominated by collisions with H₂O. Several studies involving collisions with water molecules can be found in the literature, from which the collisional systems of H₂O–H₂O,^{8–10} and H₂O–CO,⁷ have the most significant impact for modeling cometary spectra. An important exception is the case of comets at large heliocentric distances, for which the production of gaseous CO is larger than H₂O. Hence, the excitation of molecules in the coma of such comets is mainly due to collisions with CO.^{11–13} Therefore, it is crucial to investigate the excitation of cometary molecules by CO and as a first priority, the mutual interaction of CO molecules to model the physical conditions in these comets.

Rotational energy transfer in CO–CO collisions has been investigated experimentally in a recent study¹⁴ that identified unusual pair-correlated excitation mechanisms. Theoretical data for the CO–CO collisional system also exist.¹⁵ The calculations were performed by combining the time-independent close-coupling method in the low collisional energy regime with the

^a LOMC – UMR 6294, CNRS-Université du Havre, 25 rue Philippe Lebon, BP 1123, F-76063 Le Havre, France. E-mail: francois.lique@univ-rennes1.fr

^b Univ Rennes, CNRS, IPR (Institut de Physique de Rennes) – UMR 6251, F-35000 Rennes, France

^c KU Leuven, Department of Chemistry, B-3001 Leuven, Belgium

† Electronic supplementary information (ESI) available. See DOI: <https://doi.org/10.1039/d2cp01065h>



multi-configuration time-dependent Hartree (MCDTH) approach at higher collisional energies. However, the available rate coefficients only cover transitions from the rotational level $j_1 = j_2 = 0$ to levels with $j'_1, j'_2 < 4$, j_1 and j_2 being the rotational states of the two colliders. Our goal in the present work is to improve existing data by performing time-independent quantum calculations for rotational energy levels of CO up to, possibly, $j_1 = j_2 = 10$ that can be used in modeling of cometary atmospheres.

In this paper, we present cross sections and rate coefficients for transitions between the first 37 rotational states of the CO–CO system (e.g. states with rotational levels up j_1 and $j_2 \leq 6$, for temperatures up to 100 K). In addition, we explore the applicability of a statistical approach to treat such collisional system based on the statistical adiabatic channel method,¹⁶ to obtain data for rotational levels above $j_1 = j_2 = 10$. This method was tested and compared with exact quantum calculations and showed excellent agreement especially in low temperatures regime.^{16–18}

Our paper is organized as follows: In Section 2, we present the methodology of our work. Section 3 discusses our results using quantum-mechanical and statistical approaches to scattering calculations. In Section 4, we discuss the implications of our work and summarize our results.

2 Methodology

2.1 Potential energy surface

In addition of the six-dimensional (6D) potential energy surface (PES) of Chen *et al.*,¹⁹ two accurate 4D CO–CO PESs are available in the literature. The most recent PES²⁰ was calculated a few years ago by means of the coupled-cluster approach, and has been tested *versus* experimental spectroscopic studies,²¹ showing its high accuracy. However, it is not suitable for low-energy collisional excitation calculations since the long-range ($R > 40 a_0$) part of the potential is missing. We therefore decided to use the PES calculated by Vissers *et al.*²² This PES was calculated at the coupled-cluster single double and perturbative triples [CCSD(T)] level of theory, with the augmented correlation-consistent triple zeta basis (aug-cc-pVTZ). The CO molecules were treated as rigid rotors with the CO bond length fixed at $2.132 a_0$. Within the rigid rotor approximation, 4 coordinates ($R, \theta_1, \theta_2, \phi$) are needed to describe this system. R is the length of the vector \mathbf{R} connecting the centers of mass of the two CO monomers, θ_1 and θ_2 are the polar angles relative to \mathbf{R} , and the last angle ϕ is a dihedral angle between the half-planes that contain both CO molecules. Two minima in the PES were found: the first one, which is a local minimum, at $R = 6.95 a_0$, $\theta_1 = 59.63^\circ$, $\theta_2 = 120.37^\circ$ and $\phi = 180.0^\circ$ with a well depth of $V = -124.21 \text{ cm}^{-1}$, and the second one, which is the global minimum of the PES at $R = 8.20 a_0$, $\theta_1 = -134.23^\circ$, $\theta_2 = 45.77^\circ$ and $\phi = 180.0^\circ$ with $V = -135.53 \text{ cm}^{-1}$. The minima are separated by an energetic barrier which is 72.6 cm^{-1} higher than the global minimum. The long range part of the PES has been obtained from an extrapolation of the expansion coefficients assuming a C_n/R^{-n} behavior. The validity of the

extrapolation has been verified by checking that the coefficients have physical meaning. The PES of Vissers *et al.*²² was also benchmarked against experimental studies^{14,21} that demonstrated its high accuracy.

2.2 Scattering calculations

All calculations presented in this work were performed using the MOLSCAT (version 14)²³ scattering code.

2.2.1 Scattering calculations of two identical molecules.

Before proceeding with the details of the scattering calculations, we report an issue with the MOLSCAT code found during this work. Because the scattering system consists in two identical molecules and in order to consider the exchange symmetry of the system, the IDENT option should in principle be applied. Such an option considers the fact that the basis functions corresponding to (j_1, j_2) and (j_2, j_1) are indistinguishable and that only one should be kept, allowing a reduction of the number of channels in the basis by a factor ~ 2 . Such a reduction allows saving a significant amount of computational time and memory. However, using this option leads to wrong results for some transitions. Indeed, when using the close-coupling (CC)²⁴ approach, the cross sections are exactly two times higher for pair–pair transitions ($j_1 = j_2$ and $j'_1 = j'_2$) than what they should be, and when using the coupled states (CS)²⁵ approach, the cross sections for all transitions randomly overestimate or underestimate the actual results. This would not be a real issue if the CC calculations were feasible since the results can easily be corrected from the double counting.²⁶ However, as will be shown in the following sections, the CC calculations were too CPU consuming and we had to use the approximate CS approach for the calculations.

Hence, in our calculations, we considered both CO molecules as distinguishable molecules, one being the target and one being the projectile. Such an approach is also well suited to astrophysical applications since, in radiative transfer calculations, the notion of colliders and targets is necessarily invoked. Approximate conversion from distinguishable to undistinguishable results will be presented in Section 3.2.

2.2.2 Calculations details. An essential parameter for the calculations is the size of the rotational basis set. We first study the convergence of the cross sections with the size of the rotational basis set using the CC approach. Table 1 presents the results performed at an energy of 20 cm^{-1} . The cross sections were summed over total angular momentum values J up to 50. As we can observe, a reasonable convergence (better

Table 1 Cross sections (in \AA^2) at total energy of 20 cm^{-1} for selected $j_1 j_2 \rightarrow j'_1 j'_2$ transitions obtained with a rotational basis that include all levels up to $j_1 = j_2 = j_{\text{max}}$

Transition	$j_{\text{max}} = 7$	$j_{\text{max}} = 8$	$j_{\text{max}} = 9$	$j_{\text{max}} = 10$	$j_{\text{max}} = 11$
00 \rightarrow 11	41.08	35.65	36.21	35.29	35.24
00 \rightarrow 01	40.06	36.30	30.60	29.24	28.93
01 \rightarrow 11	85.24	80.16	80.86	80.49	80.23
02 \rightarrow 01	36.39	34.46	35.32	36.04	35.80



than 2%) is reached with a rotational basis set containing all rotational states up to $j_1 = j_2 = 10$.

Fig. 1 presents additional tests performed at total energies of 100 and 500 cm^{-1} . It displays selected cross sections as a function of increasing rotational basis for $J = 0$. As one can see, at 100 cm^{-1} , the basis set has to include $j_1 = j_2 = 11$ for the cross sections to be converged. At 500 cm^{-1} , rotational levels up to $j_1 = j_2 = 15$ have to be included in order to numerically converge calculations. Such a rotational basis leads to 2736 coupled channels[‡] and would lead to $\sim 45\,000$ coupled channels for $J \geq 15$. With so many coupled channels, calculations using the (almost) exact CC approach are not feasible for large values of J both in terms of memory and CPU time.

Hence, we explore the possibility of using the CS approximation. In order to evaluate the performance of the CS approach compared to CC, we computed excitation cross sections with a limited basis set containing all rotational levels up to $j_{\text{max}} = 7$, expecting that the truncation of the rotational basis would have the same effect on CC and CS results. Fig. 2 presents the CC cross sections as a function of the CS ones for selected values of total energy (20, 50, 100, and 150 cm^{-1}). In the low energy regime, where numerous resonances are found, the differences between CC and CS are below a factor of 1.5–2. When the energy increases, as expected, the differences decrease so that the overall agreement is good for energies above 50 cm^{-1} . Such comparison indicates that the CS approach is a reasonable alternative for the CC one in the case of CO–CO collisions. For temperatures below 50 K, the estimated accuracy of the rate coefficients obtained from the CS approach is expected to be better than a factor of 2 and this accuracy is expected to increase with increasing temperature.

The coupled equations were then solved using the CS approximation with the log-derivative Airy propagator.²⁷ The STEPS parameter of MOLSCAT was set at 20 in order to obtain a step length of the integrator sufficient to achieve the convergence. The integration was performed for distances between $R_{\text{min}} = 5 a_0$ and $R_{\text{max}} = 50 a_0$. The rotational constants of the CO molecules were taken as: $B_e = 1.931 \text{ cm}^{-1}$, $\alpha_e = 1.750 \times 10^{-2} \text{ cm}^{-1}$, $D_e = 6.121 \times 10^{-6} \text{ cm}^{-1}$.²⁸ The reduced mass was set at $\mu = 13.997 \text{ u}$. Excitation cross sections were obtained between rotational states listed in Table 2. The following energy grid was used: in 0–200 cm^{-1} energy range, we used steps of 1 cm^{-1} , in the 200–300 cm^{-1} energy range, the energy step was increased to 5 cm^{-1} , and finally in the 300–800 cm^{-1} energy range, a step of 100 cm^{-1} was used. The number of total angular momentum J needed to converge calculations vary from 35, at low energy, to 130, at the highest energies. From the computed cross sections, we obtain rate coefficients for temperatures up to 100 K using the following formula:

$$k_{j_1 j_2 \rightarrow j_1' j_2'}(T) = \left(\frac{8}{\pi \mu k_B^3 T^3} \right)^{\frac{1}{2}} \int_0^{\infty} \sigma_{j_1 j_2 \rightarrow j_1' j_2'}(E_c) E_c e^{-\frac{E_c}{k_B T}} dE_c \quad (1)$$

[‡] Considering the exchange symmetry, the numbers of channels would still be 1496.

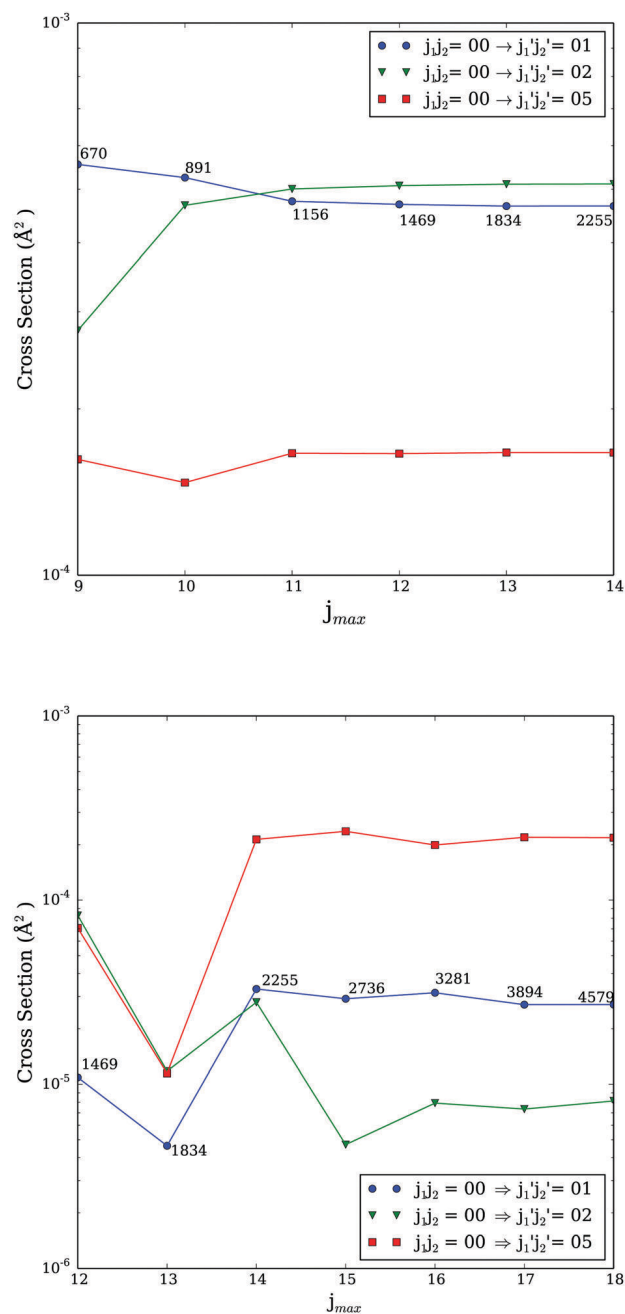


Fig. 1 Excitation cross sections for $J = 0$ computed at 100 cm^{-1} (upper panel) and 500 cm^{-1} (lower panel) as function of the rotational basis. The j_{max} is equal to highest j_1 and j_2 levels included in the calculations. Numbers on the plot indicate the total number of channels including in the calculations.

where, μ is reduced mass of the system, k_B is the Boltzmann constant, $\sigma_{j_1 j_2 \rightarrow j_1' j_2'}$ is the cross section and E_c is collision energy.

3 Results and discussion

Using the methodology described above, we computed state-to-state excitation cross sections for CO–CO collisions. The calculations were performed for energies up to 800 cm^{-1} and cover transitions between levels up to $j_1 = j_2 = 6$. Collisional rate



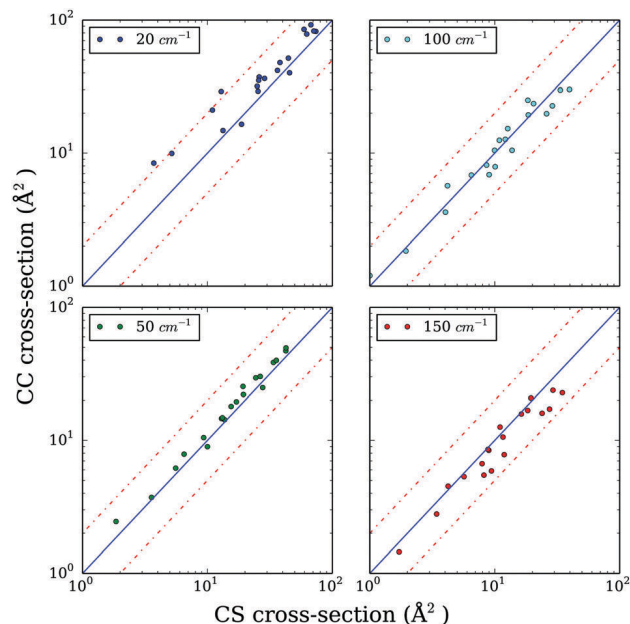


Fig. 2 Systematic comparison of selected CS and CC cross sections at 20, 50, 100 and 150 cm^{-1} . The dashed lines represent a factor of 2 of difference.

Table 2 Dissociating rotational states of the $\text{CO}(j_1)\text{-CO}(j_2)$ system

Level	$j_1 j_2$	Energy (cm^{-1})	Level	$j_1 j_2$	Energy (cm^{-1})
1	00	0.000	20	35	80.739
2	01	3.845	21	16	84.580
3	11	7.690	22	26	92.270
4	02	11.535	23	45	96.118
5	12	15.379	24	36	103.805
6	03	23.069	25	07	107.642
7	22	23.070	26	17	111.487
8	13	26.914	27	55	115.341
9	23	34.604	28	27	119.177
10	04	38.448	29	46	119.186
11	14	42.293	30	37	130.712
12	33	46.139	31	08	138.390
13	24	49.983	32	56	138.406
14	05	57.670	33	18	142.235
15	15	61.515	34	47	146.091
16	34	61.517	35	28	149.925
17	25	69.205	36	38	161.460
18	44	76.896	37	66	161.471
19	06	80.735			

coefficients up to 100 K were derived from these cross sections. Collisional rate coefficients are available as ESI.† All the results presented below have been obtained considering the two CO molecules as distinguishable.

3.1 Propensity rules

In Fig. 3, we present selected CO–CO cross sections corresponding to the excitation from the ground state $j_1 j_2 = 00$ to rotational states in which only one CO molecule is excited. As one can see, the dominant transition is the transition to the $j'_1, j'_2 = 01$ state. The values of the cross sections decrease when $\Delta j'_2$ increases, in agreement with an exponential energy-gap

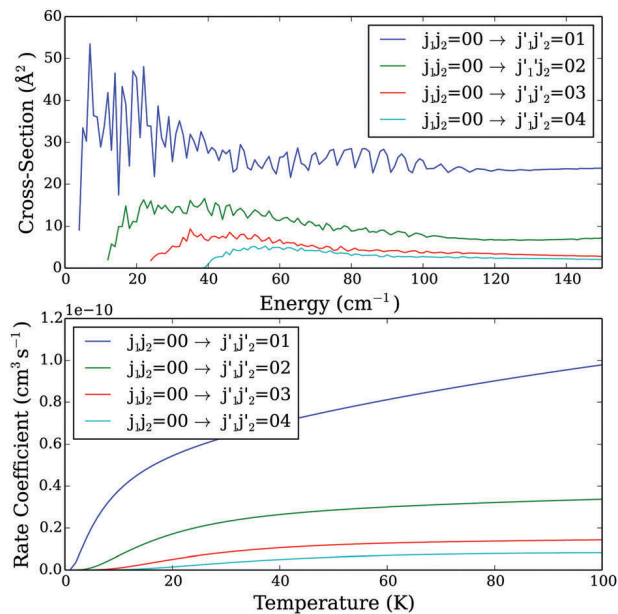


Fig. 3 Excitation cross sections as a function of collision energy (upper panel) and the rate coefficients as a function of temperature (lower panel) from the $j_1 j_2 = 00$ state.

behavior. Obviously, the same propensity rules can be seen when we compare rate coefficients (Fig. 3, lower panel). A similar propensity rule can also be seen when both CO molecules are excited after the collision. Indeed, as one can see on Fig. 4 that presents selected excitation cross sections and rate coefficients from the fundamental $j_1 j_2 = 00$ state, the dominant transition is the one corresponding to the excitation to the $j'_1, j'_2 = 11$ state. More generally, the cross sections decrease with the increase of both j'_1 and j'_2 final levels.

In Fig. 5, we compare the cross sections and rate coefficients for transitions where only one CO molecule is excited to the ones for transitions where both CO molecules are excited. In contrast to previous findings reported by Ndengué *et al.*,¹⁵ we do not observe propensity rules in favor of pair–pair transitions ($j_1 = j_2$ and $j'_1 = j'_2$). We found that the magnitude of the cross sections involving excitation of only one CO molecule is close to the one of the cross sections where both CO molecules are excited.

Propensity rules similar to those reported in our work were observed in previous studies of collisions of two identical molecules. For example, in $\text{H}_2\text{-H}_2$ scattering, the cross sections were found to be larger for transitions where only one molecule is excited compared to the transitions where both colliders are excited.²⁹

3.2 Comparison with previous data

As stated in the introduction, theoretical data for the CO–CO collisional system have been published by Ndengué *et al.*¹⁵ It is then of interest to compare our new data with these existing ones. Ndengué *et al.*¹⁵ performed scattering calculations using the PES of Dawes *et al.*²⁰ The authors combined time-independent quantum CC calculations for energy up to 150 cm^{-1} , with MCTDH calculations for energies above 150 cm^{-1} . In the CC calculations,



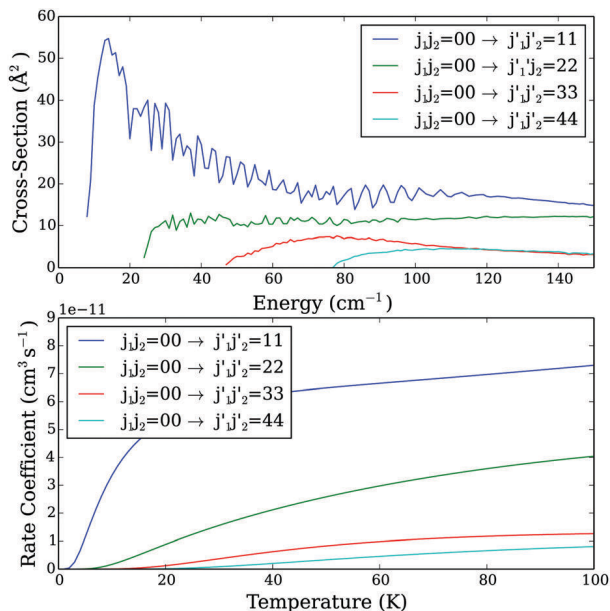


Fig. 4 Excitation cross sections as a function of collision energy (upper panel) and the rate coefficients as a function of temperature (lower panel) from the $j_1j_2 = 00$ state.

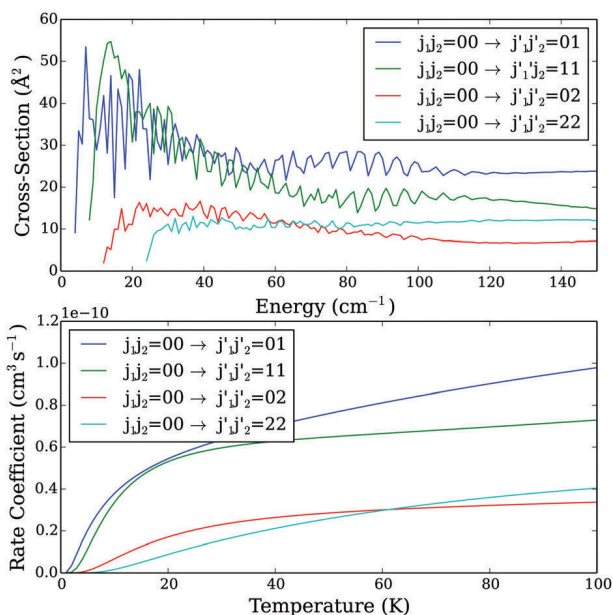


Fig. 5 Excitation cross sections as a function of collision energy (upper panel) and rate coefficients as a function of temperature (lower panel) from level $j_1j_2 = 00$. The presented transitions show comparisons of transitions where one of the CO molecules is excited with transitions where both of them are excited.

they included in the rotational basis set CO levels up to $j_1 = j_2 = 7$. Using the MCTDH method, the basis was substantially increased due to the lower computational cost. The calculations of Ndengué *et al.*¹⁵ were performed treating the CO molecules as indistinguishable particles. We do not focus here on the differences between collisional cross sections above 150 cm^{-1} that are most

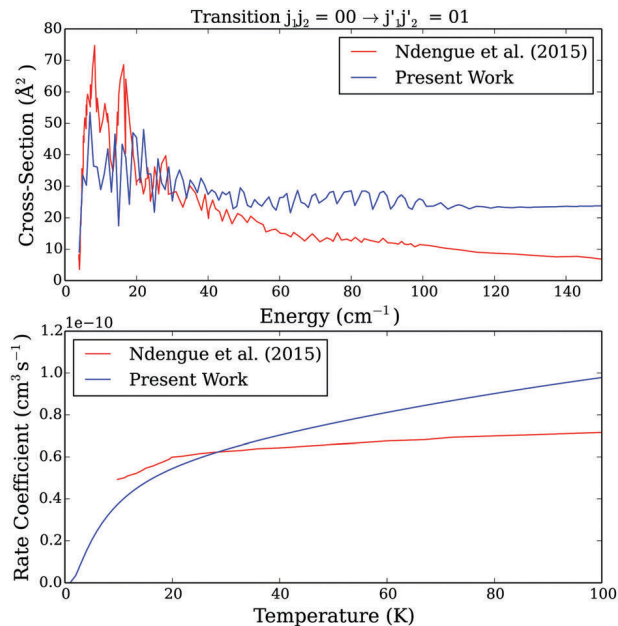


Fig. 6 Comparison between present excitation cross sections as a function of energy and those of Ndengué *et al.*¹⁵ (upper panel) and rate coefficients as a function of temperature (lower panel) for the $j_1j_2 = 00$ to $j'_1j'_2 = 01$ transition.

probably due to different scattering methods (quantum time dependent *vs.* quantum time independent) and that weakly affect the collisional rate coefficients below 100 K.

Fig. 6 and 7 present a comparison of our new collisional data (both the cross sections and rate coefficients) to the ones of Ndengué *et al.*¹⁵ for two selected transitions. Since Ndengué *et al.*¹⁵ considered scattering between indistinguishable particles and performed the calculations with the MOLSCAT code, we also plotted their results for pair-pair transitions divided by two (*e.g.* discussion in Section 2.2.1). For the purpose of the comparison with Ndengué *et al.*¹⁵ results, we also converted our distinguishable results to indistinguishable ones using the following formulae, that are not strictly exact and based on the assumption that quantum interference effects are negligible^{30,31} §

- Pair-pair transitions ($j_1 = j_2$ and $j'_1 = j'_2$)

$$\tau_u(j_1j_2 \rightarrow j'_1j'_2) = \tau_d(j_1j_2 \rightarrow j'_1j'_2) \quad (2)$$

- Pair-no-pair transitions ($j_1 = j_2$ and $j'_1 \neq j'_2$)

$$\tau_u(j_1j_2 \rightarrow j'_1j'_2) = \tau_d(j_1j_2 \rightarrow j'_1j'_2) + \tau_d(j_1j_2 \rightarrow j'_2j'_1) \quad (3)$$

- No-pair-pair transitions ($j_1 \neq j_2$ and $j'_1 = j'_2$)

$$\tau_u(j_1j_2 \rightarrow j'_1j'_2) = \tau_d(j_1j_2 \rightarrow j'_1j'_2) \quad (4)$$

- No-pair-no-pair transitions ($j_1 \neq j_2$ and $j'_1 \neq j'_2$)

§ Note that there is not a clear convergence of the conversion factor to be used (*e.g.* discussion in Perez-Rios *et al.*³¹) and we do not recommend to use our estimated indistinguishable observables for experiments analysis.



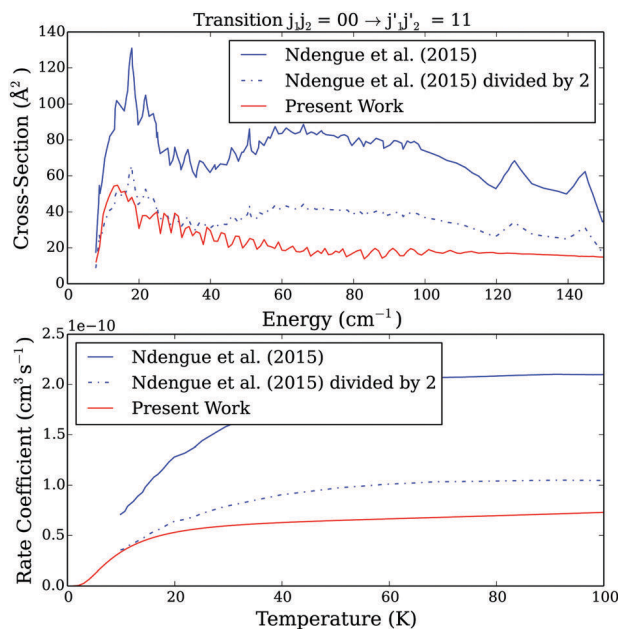


Fig. 7 Comparison between present and Ndengué *et al.*¹⁵ excitation cross sections as a function of energy (upper panel) and rate coefficients as a function of temperature (lower panel) for the $j_1 j_2 = 00 \rightarrow j'_1 j'_2 = 11$ transition. The solid blue line represents results directly taken from Ndengué *et al.*¹⁵ the dashed blue line represents the same results divided by a factor of 2, and the red solid line represents our results.

$$\tau_u(j_1 j_2 \rightarrow j'_1 j'_2) = \tau_d(j_1 j_2 \rightarrow j'_1 j'_2) + \tau_d(j_1 j_2 \rightarrow j'_2 j'_1) \quad (5)$$

where τ_d and τ_u are the distinguishable and undistinguishable observables (cross sections or rate coefficients).

As one can see, differences between the two sets of data are significant (even when corrected for the possible IDENT MOLS-CAT parameter issue). Such differences originate from the different approaches (different CO–CO PESs, different scattering theory and different calculations parameters) used in the scattering studies. It is then of interest to assess the importance of all these different computational aspects in the overall discrepancy between the two sets of data.

The differences induced from the use of different PESs is found to be minor. Indeed, we performed test calculations using the Vissers *et al.*²² PES and calculations parameters reported by Ndengué *et al.*¹⁵ (for energies up to 50 cm^{-1}) and we found that the differences were lower than 10% on the average despite the fact that the resonances seen in the excitation cross sections were slightly shifted. We expect that the difference would be even lower in the case of rate coefficients, where the cross sections are averaged over a thermal distribution of collisional energies.

The impact of the use of the CS vs. CC scattering approach was evaluated in the Section 2. Indeed, Fig. 2 showed that the CC and CS results can differ by up to a factor of 1.5–2 at low collision energies as can be observed when comparing our results to the results from Ndengué *et al.*¹⁵ (Fig. 6 and 7). However, it was also found that the agreement between CC and CS results increases with increasing collision energies. Such an improvement is not seen here.

This can probably be explained this by the size of the rotational basis set used in the two quantum time independent calculations. Ndengué *et al.*¹⁵ used a rotational basis containing all levels with j_1 and j_2 up to 7 that clearly does not allow full convergence of the collisional cross sections (*e.g.* Table 1), the non convergence of the results obviously increasing with increasing energies. Indeed, in order to fully converge our scattering calculations, we used basis $j_1 = j_2 = 15$ and a significant part of the difference between the two sets of data above 100 cm^{-1} can be explained by the lack of convergence of the Ndengué *et al.*¹⁵ calculations with respect to the rotational basis.

3.3 Statistical approach

As we reported, the accuracy of our data for temperatures below 50 K is within a factor of 1.5–2. The pure CC calculations being not feasible, alternative approaches were therefore explored in order to improve accuracy. We decided to investigate the validity of statistical methods to check whether the accuracy of our rate coefficients could be improved in the low temperatures regime and whether the calculations could be extended to transitions involving higher rotational levels. We used the Statistical Adiabatic Chancel Model (SACM) presented in the work of Loreau *et al.*^{16,32} The significant advantage of this method is that the calculations are performed only for one value of the energy since the adiabatic curves are energy-independent. In addition, we could use a much smaller rotational basis set to reach convergence of the cross sections ($j_{\text{max}} = 6$ was enough to obtain converged calculations for transitions between levels up to $j_1 = j_2 = 5$).

We calculated cross sections for transitions between rotational levels up to $j_1 = j_2 = 5$, and rate coefficients for temperatures up to 100 K. In Fig. 8, we show a systematic comparison between rate coefficients obtained using SACM and CS methods. Previous use of the SACM method showed that it works well at low temperatures and starts to deviate from accurate results when the temperature increases.¹⁶ However, in our case, the opposite behavior is observed. As one can see from Fig. 8, at 20 K, the differences between the two sets of data are above a factor of 3 for numerous transitions while the agreement is increasing with increasing temperature.

We have to keep in mind that we compare here two approximate methods. Therefore, we calculated cross sections for a few energies using the almost exact CC method including in the rotational basis levels up to $j_1 = j_2 \leq 10$. Fig. 9 and 10 show an example of comparison of the CS, SACM and the CC cross sections. Generally, we observed that the results obtained with the CS method underestimate the cross sections, while the SACM results slightly overestimate the cross sections compared to the CC ones in the low energy regime. However, both the CS and SACM results stays within a factor of 2 compared to the CC results; therefore, we cannot clearly determine which method is more accurate. In the intermediate region of energy ($30 \leq E_c \leq 70 \text{ cm}^{-1}$), all three methods agrees reasonably well, thereby explaining the fairly good agreement seen in Fig. 8 for temperatures of 50 and 100 K. Important deviations start to occur at higher energies. Indeed, we observe a substantial decrease in



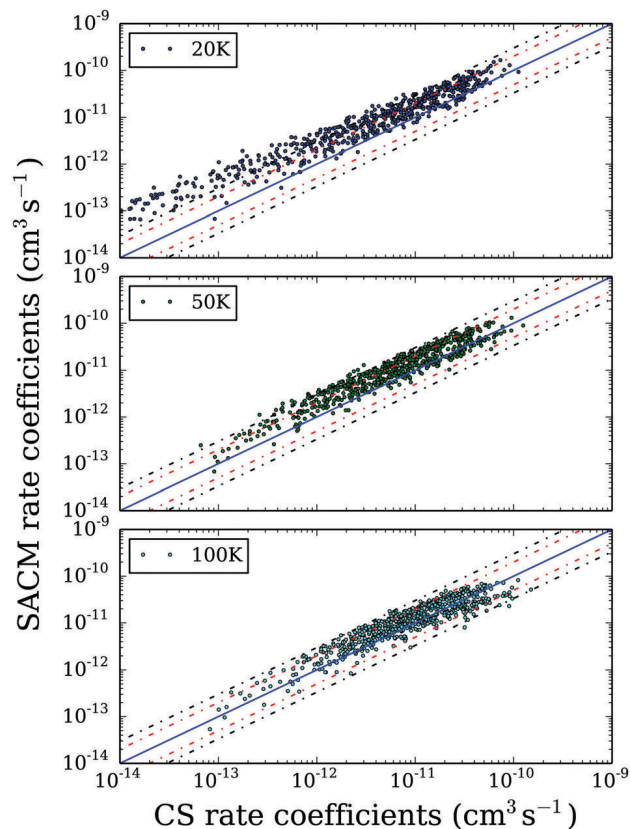


Fig. 8 Systematic comparison of SACM and CS rate coefficients, at temperatures of 20, 50, and 100 K, for all transitions calculated in this work (using the CS method). The blue line represents exact results, red dashed lines represent a factor of 2 difference, and black dashed lines represent a factor of 3 difference.

the cross sections obtained with the SACM method, while the CC and CS results stay in good agreement. We presume that this decrease of cross sections is due to the dense distribution of the accessible (open) channels and also to the fact that the well depth of the CO–CO PES is not large enough for statistical approaches to work above the very low energy regime.¹⁶

We conclude that the rate coefficients obtained with the SACM method may be useful for temperatures up to 100 K. The good agreement between SACM and CS rate coefficients observed at a temperature of 100 K is rather fortuitous and difference above 100 K can become very significant because of the strong deviation between quantum and SACM results at high collisional energies. Therefore, we are not able to extend the rate coefficients to higher temperatures and hence higher rotational levels (populated only at high temperature) using the SACM method.

4 Conclusions

Using the potential of Vissers *et al.*,²² we presented the first complete quantum scattering calculations of CO–CO rotational excitation between first 37 rotational energy states of CO molecules. We obtained state-to-state collisional rate coefficients for temperatures up to 100 K. We estimated that our

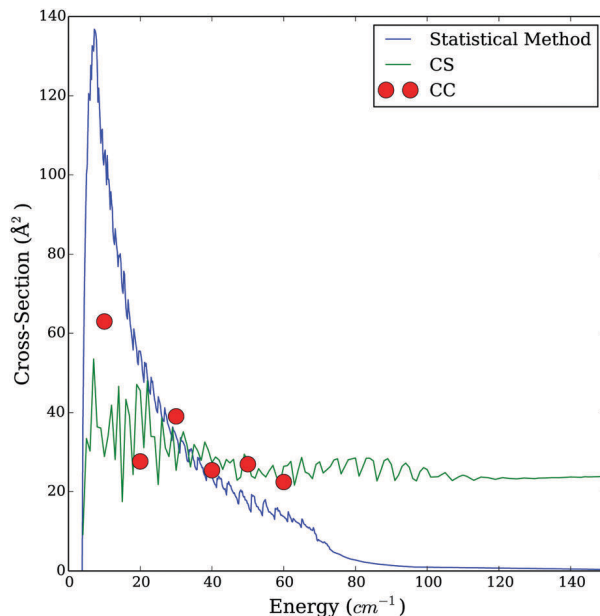


Fig. 9 Comparison of the cross section obtained with the CC, CS and statistical method for the transition $j_1j_2 = 00$ to $j'_1j'_2 = 01$ as a function of energy.

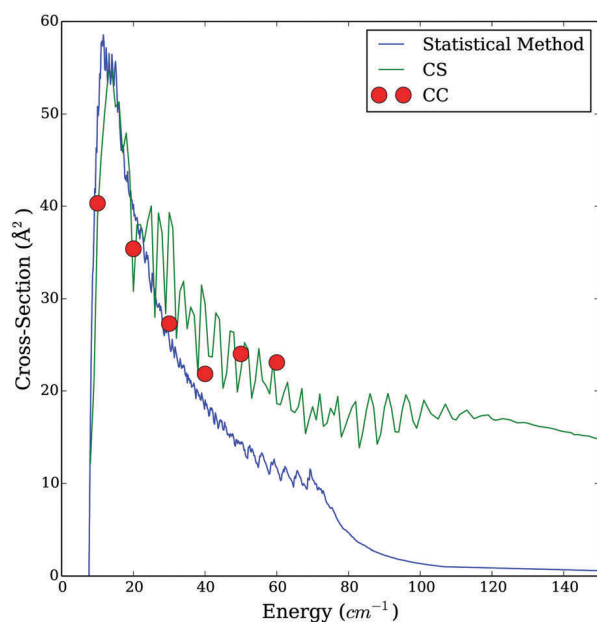


Fig. 10 Comparison of the cross section obtained with the CC, CS and statistical method for the transition $j_1j_2 = 00$ to $j'_1j'_2 = 11$ as a function of energy.

data below 50 K are accurate within a factor of 1.5–2 and that the accuracy increases with increasing temperature.

Significant differences were found between our results and those previously reported by Ndengué *et al.*¹⁵ Transitions towards “pair” rotational levels (with $j_1 = j_2$) seem to be over-estimated by a factor 2. For temperatures above 50 K, we believe that our results are more accurate than the previous ones.



Our convergence tests show that the basis used in the previous study was insufficient. At the same time, we are confident that the basis size used in our work allows us to converge calculations over the whole energy regime considered. The question about the accuracy of the rate coefficients below 50 K remain. Even though the previous calculations were performed using the CC method, their results were only partially converged due to the small basis set. On the contrary, our calculations were converged. However, we used the CS approximation, which was estimated to provide accurate results within a factor of 2 difference.

We tried to improve our data by investigating the possibility of the statistical approach to the CO–CO scattering. The results we obtained do not lead to a clear answer. The agreement was excellent for part of the transitions in the low energy regime. For other transitions, differences of a factor of ~ 2 were observed between SACM and partly converged CC calculations. In addition, for all the considered transitions, we observed a sudden decrease of cross section above 60–70 cm⁻¹. This behavior can be expected when the collision energy becomes comparable to the well depth of the PES, but further investigation on similar systems would be needed.

The CS calculations will be continued using the methodology reported in this work. We will extend data for transitions between levels up to $j_1 = j_2 = 10$. The impact of our data on the astrophysical models, in particular of cometary atmospheres, will be presented in a separate article.

Data availability

The data that support the findings of this study are available within the article and its online ESI.†

Conflicts of interest

There are no conflicts to declare.

Acknowledgements

F. L. and M. Ž. acknowledge financial support from the European Research Council (Consolidator Grant COLLEXISM, grant agreement 811363), the Institut Universitaire de France and the Programme National “Physique et Chimie du Milieu Interstellaire” (PCMI) of CNRS/INSU with INC/INP co-funded by CEA and CNES. We wish to acknowledge the support from the CINES/GENCI for awarding us access to the OCCIGEN supercomputer within the A0090411036 project. M. Ž. acknowledges that calculations have been carried out at the Wrocław Centre for Networking and Supercomputing, Grant 218 (PSZ). M. Ž. thanks B. Desrousseaux, C. Bop, S. Demes, A. Godard Palluet and P. Pirlot for fruitful discussions. J. L. acknowledges support from Internal Funds KU Leuven through Grant 19-00313. M. Ž. acknowledges B. Desrousseaux, A. Godard-Palluet, P. Pirlot, C. Bop, S. Demes and M. Gueguen for their help and support during this work.

Notes and references

- 1 A. Cochran, A.-C. Levasseur-Regourd, M. Cordiner, E. Hadamcik, J. Lasue, A. Gicquel, D. Schleicher, S. Charnley, M. Mumma, L. Paganini, D. Bockelee-Morvan, N. Biver and Y.-J. Kuan, *Space Sci. Rev.*, 2015, **197**, 9–46.
- 2 B. Marty, K. Altwegg, H. Balsiger, A. Bar-Nun, D. V. Bekaert, J.-J. Berthelier, A. Bieler, C. Briois, U. Calmonte, M. Combi, J. D. Keyser, B. Fiethe, S. A. Fuselier, S. Gasc, T. I. Gombosi, K. C. Hansen, M. Hässig, A. Jäckel, E. Kopp, A. Korth, L. L. Roy, U. Mall, O. Mousis, T. Owen, H. Rème, M. Rubin, T. Sémon, C.-Y. Tzou, J. H. Waite and P. Wurz, *Science*, 2017, **356**, 1069–1072.
- 3 K.-H. Glassmeier, H. Boehnhardt, D. Koschny, E. Kührt and I. Richter, *Space Sci. Rev.*, 2007, **128**, 1–21.
- 4 M. J. Mumma and S. B. Charnley, *Annu. Rev. Astron. Astrophys.*, 2011, **49**, 471–524.
- 5 D. Bockelee-Morvan and N. Biver, *Philos. Trans. R. Soc., A*, 2017, **375**, 20160252.
- 6 E. Roueff and F. Lique, *Chem. Rev.*, 2013, **113**, 8906–8938.
- 7 A. Faure, F. Lique and J. Loreau, *Mon. Not. R. Astron. Soc.*, 2020, **493**, 776–782.
- 8 C. Boursier, B. Mandal, D. Babikov and M. L. Dubernet, *Mon. Not. R. Astron. Soc.*, 2020, **498**, 5489–5497.
- 9 G. Buffa, O. Tarrini, F. Scappini and C. Cecchi-Pestellini, *Astrophys. J., Suppl. Ser.*, 2000, **128**, 597–601.
- 10 A. Semenov and D. Babikov, *J. Phys. Chem. A*, 2017, **121**, 4855–4867.
- 11 D. Bockelee-Morvan, J. Crovisier, M. J. Mumma and H. Weaver, in *Comets II*, ed. M. Festou, H. U. Keller and H. A. Weaver, Univ. Arizona Press, Tucson, 2005, pp. 391–423.
- 12 D. Bodewits, J. W. Noonan, P. D. Feldman, M. T. Bannister, D. Farnocchia, W. M. Harris, J.-Y. Li, K. E. Mandt, J. W. Parker and Z.-X. Xing, *Nat. Astron.*, 2020, **4**, 867–871.
- 13 M. A. Cordiner, S. N. Milam, N. Biver, D. Bockelee-Morvan, N. X. Roth, E. A. Bergin, E. Jehin, A. J. Remijan, S. B. Charnley, M. J. Mumma, J. Boissier, J. Crovisier, L. Paganini, Y.-J. Kuan and D. C. Lis, *Nat. Astron.*, 2020, **4**, 861–866.
- 14 Z.-F. Sun, M. C. van Hemert, J. Loreau, A. van der Avoird, A. G. Suits and D. H. Parker, *Science*, 2020, **369**, 307.
- 15 S. A. Ndengué, R. Dawes and F. Gatti, *J. Phys. Chem. A*, 2015, **119**, 7712–7723.
- 16 J. Loreau, F. Lique and A. Faure, *Astrophys. J.*, 2018, **853**, L5.
- 17 M. Konings, B. Desrousseaux, F. Lique and J. Loreau, *J. Chem. Phys.*, 2021, **155**, 104302.
- 18 B. Desrousseaux, M. Konings, J. Loreau and F. Lique, *Phys. Chem. Chem. Phys.*, 2021, **23**, 19202–19208.
- 19 J. Chen, J. Li, J. M. Bowman and H. Guo, *J. Chem. Phys.*, 2020, **153**, 054310.
- 20 R. Dawes, X.-G. Wang and T. Carrington, *J. Phys. Chem. A*, 2013, **117**, 7612–7630.
- 21 L. A. Surin, D. N. Fourzikov, T. F. Giesen, S. Schlemmer, G. Winnewisser, V. A. Panfilov, B. S. Dumesh, G. W. M. Vissers and A. van der Avoird, *J. Phys. Chem. A*, 2007, **111**, 12238–12247.
- 22 G. W. M. Vissers, P. E. S. Wormer and A. van der Avoird, *Phys. Chem. Chem. Phys.*, 2003, **5**, 4767–4771.



- 23 J. Hutson and S. Green, *CCP6*, Daresbury, 1994.
- 24 A. M. Arthurs, A. Dalgarno and D. R. Bates, *Proc. R. Soc. London, Ser. A*, 1960, **256**, 540–551.
- 25 P. McGuire and D. J. Kouri, *J. Chem. Phys.*, 1974, **60**, 2488–2499.
- 26 J. P. Fonfria, A. Ramos, F. Thibault, G. Tejada, J. M. Fernandez and S. Montero, *J. Chem. Phys.*, 2007, **127**, 134305.
- 27 M. H. Alexander and D. E. Manolopoulos, *J. Chem. Phys.*, 1987, **86**, 2044–2050.
- 28 A. L. Floch, *Mol. Phys.*, 1991, **72**, 133–144.
- 29 S. Green, *J. Chem. Phys.*, 1975, **62**, 2271–2277.
- 30 W. M. Huo and S. Green, *J. Chem. Phys.*, 1996, **104**, 7572–7589.
- 31 J. Perez-Rios, G. Tejada, J. M. Fernandez, M. I. Hernandez and S. Montero, *J. Chem. Phys.*, 2011, **134**, 174307.
- 32 J. Loreau, A. Faure and F. Lique, *J. Chem. Phys.*, 2018, **148**, 244308.



4.5. Radiative transfer modeling

As I mentioned in previous sections, the main reason for treating the colliders as distinguishable molecules was the use of the collisional data in the astrophysical modeling. The radiative transfer theory usually distinguishes between the projectile and the target. In addition, radiative transfer models do not consider the possibility of the excitation of the collider (usually the internal structure of the collider is neglected). This approach seems unreasonable when the target and projectile are the same. Therefore, using a simple radiative transfer model, I tried to assess the impact of the different rotational distributions of the CO projectiles on the CO energy levels population. I have studied how the CO/H₂O abundance ratio can influence the modeling population of the CO molecules in a comet at a high heliocentric distance. The following article about *The excitation of CO in CO-dominated cometary comae* presents the results I have obtained for this project.

The excitation of CO in CO-dominated cometary comae

M. Żółtowski,^{1,2} F. Lique,^{2★} J. Loreau,³ A. Faure,⁴ and M. Cordiner^{5,6}

¹LOMC – UMR 6294, CNRS-Université du Havre, 25 rue Philippe Lebon, BP 1123, F-76063 Le Havre, France

²Univ Rennes, CNRS, IPR (Institut de Physique de Rennes) – UMR 6251, F-35000 Rennes, France

³Department of Chemistry, KU Leuven, B-3001 Leuven, Belgium

⁴Univ. Grenoble Alpes, CNRS, IPAG, F-38000 Grenoble, France

⁵Astrochemistry Laboratory, NASA Goddard Space Flight Center, 8800 Greenbelt Road, Greenbelt, MD 20771, USA

⁶Department of Physics, Catholic University of America, Washington, DC 20064, USA

Accepted 2023 January 23. Received 2023 January 6; in original form 2022 November 28

ABSTRACT

An abundance of CO significantly surpassing the abundance of H₂O is observed in the comae of comets at large heliocentric distances. In these environments, CO molecules can be the most abundant species and they may be therefore the dominant projectiles inducing collisional excitation of the cometary molecules. It is thus of high interest to investigate the excitation of CO by CO. This article provides a new set of CO–CO collisional rate coefficients for temperatures up to 150 K and for CO rotational levels j_1 up to 10. These data are obtained from quantum scattering calculations using the coupled states approximation. They are used in a simple radiative transfer model in order to test their impact on the excitation of cometary CO. Because mutual (de-)excitations of the target and projectile are important, the CO projectile was assumed to be thermalized at the kinetic temperature. We found that the non-local thermodynamical equilibrium regime extends for CO densities in the range 10^3 – 10^7 cm⁻³. We also observed that as soon as the CO/H₂O ratio is larger than 70 per cent/30 per cent, the contribution of H₂O collisions can be neglected. Similarly, the excitation of CO by CO may be ignored for relatively low CO/H₂O density ratios (≤ 30 per cent/70 per cent). Finally, when the coma is a ~ 50 per cent/50 per cent mixture of CO and H₂O, the contribution of both colliders is similar and has to be considered.

Key words: molecular data – scattering – comets: general.

1 INTRODUCTION

Comets spend most of their lives far away from the Sun. Therefore, they carry molecular ices that were present during the formation of our Solar system. When they approach the Sun, cometary nuclei release these molecules into an expanding atmosphere (coma). Observing these molecules gives us insight into the chemical and physical conditions at the epoch of comet and giant planet formation. It is then essential to analyse observations of cometary comae as precisely as possible (Cochran et al. 2015).

The most abundant constituent of cometary comae is usually H₂O. Thus, H₂O is often used as a reference to which we compare abundances of the other cometary molecules. The next most abundant molecules observed in typical comets at heliocentric distances of ~ 1 au (Bockelée-Morvan et al. 2004; Bockelée-Morvan & Biver 2017) are respectively CO₂ (up to 30 per cent relative to H₂O), CO (up to 25 per cent relative to H₂O), and CH₃OH (up to 7 per cent relative to H₂O). The abundances of the other molecules usually do not exceed 1 per cent (Bockelée-Morvan & Biver 2017).

However, there are some peculiar comets observed at large heliocentric distances where the production rates of CO and CO₂ are higher than H₂O. For example, in the 29P/Schwassmann–Wachmann 1 comet observed at a heliocentric distance within ~ 2.5 au, the

production of CO molecules was found to be five times larger than that of H₂O (Ootsubo et al. 2012). In the C/2016 R2 (PanSTARRS) comet recently observed at a heliocentric distance of ~ 2.8 – 2.9 au, the CO/H₂O abundance ratio was estimated to be ~ 170 , a ratio 37 times larger than the highest CO/H₂O ratio ever observed (Cordiner et al. 2022). This dominance in the production of CO compared to H₂O is explained by the differences in the CO and H₂O sublimation temperatures (Womack, Sarid & Wierzbos 2017). Indeed, the H₂O ices start to sublimate once the comet approaches our inner Solar system within the distance of ~ 3 au (H₂O molecules having a relatively high sublimation temperature of ~ 150 K) while CO (with a much lower sublimation temperature of ~ 20 – 30 K) starts to sublimate at much larger distance from the Sun, where H₂O is still frozen in the comet nucleus. Therefore, a high CO/H₂O production rate ratio exceeding unity is observed when the comets are observed at large distance (≥ 3 au) from the sun, where the radiation field and nucleus temperature are expected to be weak. Hence, in such comets, the main constituent and then collisional partner for the excitation of cometary molecules is not H₂O but other volatile molecules such as CO or CO₂ (Marboeuf & Schmitt 2014; Womack et al. 2017 and references therein).

The physical conditions in a cometary atmosphere prevent local thermodynamical equilibrium (LTE) to be sustained in the whole coma. Non-LTE excitation/radiative transfer models for comets have been developed for decades and we refer the reader to the chapter by Bodewits et al. (2022) for a recent review. In the following, we

* E-mail: francois.lique@univ-rennes1.fr

will address processes that govern the excitation and emission of CO molecules in the (sub)millimetre range, i.e. CO rotational levels within the ground vibrational state, using a simple excitation model. Going beyond the LTE approximation requires to take into account both radiative and collisional processes. Radiative data for cometary molecules are usually well known from laboratory spectroscopy. At the opposite, collisional data require long and expensive (in terms of memory and CPU time) calculations (Roueff & Lique 2013). In the case of comets, the most important collisional systems involve mutual interactions between CO, CO₂, and H₂O molecules.

Some of these systems have been already the object of molecular scattering studies. Unfortunately, they are computationally too complex to be studied with the almost exact quantum close coupling scattering theory (Arthurs & Dalgarno 1960) and some approximations had to be applied. For the H₂O–H₂O collisional system, Buffa et al. (2000) used a semiclassical treatment based on the dipole–dipole interaction to derive cross-sections. For the same system, Semenov & Babikov (2017) extended the semiclassical approach to include quadrupole interactions and their methodology was tested against the more sophisticated mixed quantum/classical MQCT calculations of Boursier et al. (2020). In the case of CO–H₂O, a first set of data was obtained in the 1990s from line shape measurement by Green (1993). Recently, Faure, Lique & Loreau (2020) provided a more accurate data set of rate coefficients for the CO–H₂O collisions using the statistical adiabatic channel method (Loreau, Lique & Faure 2018). For the CO–CO collisional system, data between the first five rotational levels were provided by Ndengué, Dawes & Gatti (2015) combining both time-independent and approximate time-dependent quantum scattering approaches.

In a previous work by some of us (Cordiner et al. 2022), a preliminary set of CO–CO collisional rate coefficients computed with a full quantum time-independent method but limited to $T = 5$ –30 K and $j = 0$ –6 was published. This data set was extended recently (Żóttowski, Loreau & Lique 2022, hereafter Paper I) to temperatures $T = 5$ –100 K and to the transitions between rotational levels $j = 0$ –7. In the present paper, we provide a new extension of these data sets in order to cover temperatures up to 150 K and transitions between levels up to $j = 10$ for more general use in models. In addition, the new collisional data are used in a simple radiative transfer model of cometary comae (Faure et al. 2020; Loreau, Faure & Lique 2022) in order to test their impact on the excitation of CO. We note that since CO–CO is a system of identical molecules, the distinction between ‘target’ and ‘projectile’ is artificial. To our knowledge, however, public radiative transfer codes do not allow to treat the internal structure of a target and a projectile on equal footing. The common and convenient artefact of target and projectile will be therefore used below, but we will test the sensitivity of the CO (target) population to the actual CO projectile internal states. Finally, we will investigate the impact of different CO/H₂O abundance ratios on the CO (target) level population.

Our article is organized as follows. In Section 2, we present the results of our new scattering calculations. In Section 3, we discuss the impact of our new collisional data on the non-LTE excitation of CO in cometary comae. In Section 4, conclusions are drawn.

2 CO–CO COLLISIONAL RATE COEFFICIENTS

As written in the introduction, we aim here at extending the CO–CO collisional rate coefficients of Paper I to both higher temperatures and higher rotational energy levels. The CO–CO interaction potential and the scattering methodology is essentially the same as in Paper I and we refer the reader to this paper for details. Briefly, the four-dimensional CO–CO rigid rotor potential energy surface calculated

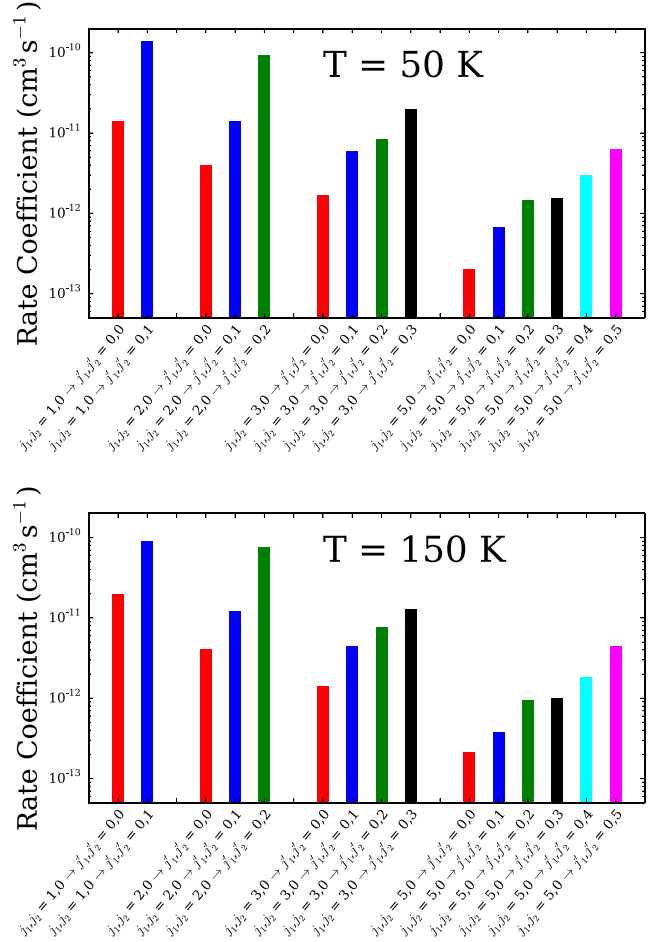


Figure 1. Selective state-to-state rate coefficients at 50 K (upper panel) and 150 K (lower panel).

by Vissers, Wormer & van der Avoird (2003) was used in our calculations and state-to-state cross-sections were calculated with the MOLSCAT scattering code (Hutson & Green 1994). We consider the two colliding species as distinguishable species. We used the coupled states approximation (McGuire & Kouri 1974) that was shown to be accurate for collision energies above 50 cm⁻¹. In the following, j_1 refers to the rotational level of the CO considered as the target and j_2 refers to the rotational level of the CO considered as the projectile. The rotational basis used in the calculations contains all energy levels with $j_1 = j_2 \leq 15$. Such a rotational basis is large enough to converge to better than 10 per cent inelastic cross-sections between levels up to $j_1 = j_2 = 10$. The cross-section calculations were performed for total energies up to 1200 cm⁻¹. This energy range allows to calculate state-to-state rate coefficients for temperatures up to 150 K:

$$k_{j_1 j_2 \rightarrow j'_1 j'_2}(T) = \left(\frac{8}{\pi \mu k_B^3 T^3} \right)^{\frac{1}{2}} \int_0^{\infty} \sigma_{j_1 j_2 \rightarrow j'_1 j'_2}(E_c) E_c e^{-\frac{E_c}{k_B T}} dE_c \quad (1)$$

where μ is reduced mass of the system, k_B is the Boltzmann constant, $\sigma_{j_1 j_2 \rightarrow j'_1 j'_2}$ is the cross-section for the transition $(j_1, j_2) \rightarrow (j'_1, j'_2)$, and E_c is collision energy.

In Fig. 1, state-to-state de-excitation rate coefficients are provided at 50 and 150 K. First, we can observe that the values of the rate coefficients decrease with increasing Δj_1 and/or Δj_2 , in agreement

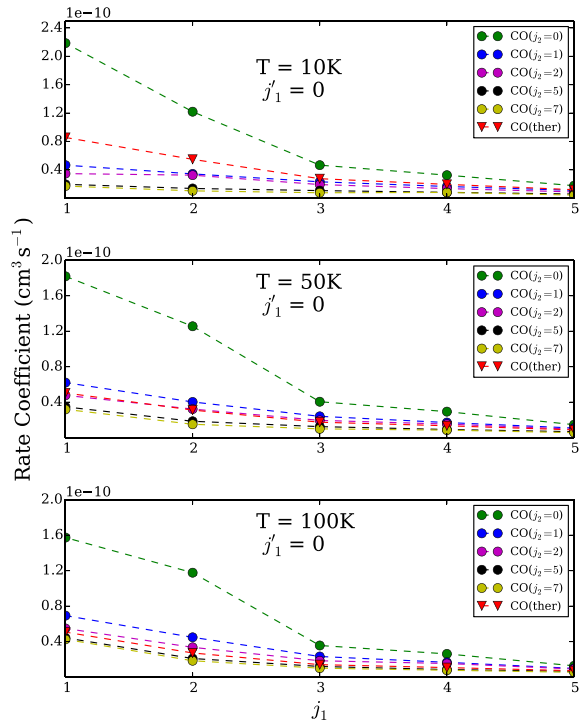


Figure 2. Comparison of effective rate coefficients where the initial projectile’s rotational state was fixed at $j_2 = 0, 1, 2, 5,$ and $7,$ and summed over all possible final states of projectile. De-excitation transitions to the ground state ($j'_1 = 0$) from the first five excited rotational states are presented. The thermalized set of rate coefficients is also plotted for comparison.

with the energy gap law, as already discussed in Paper I. In addition, for a given Δj_1 transition, the rate coefficients increase with increasing Δj_2 . Such behaviour means that the internal energy released by the target is efficiently transferred to the projectile and can be explained by the preference in conserving the collision energy, which implies a conservation of the total internal energy. Finally, we found a significant propensity rule in favour of transitions with $\Delta j_1 = -\Delta j_2$ (transitions with a strict conservation of the internal energy). Such transitions would be purely elastic if the CO molecules were considered indistinguishable in the scattering calculations. This explains the dominance of such transitions in our approach. We did not find any particular temperature dependence of the propensity rules, as expected from the weak temperature dependence of the rate coefficients (see Paper I).

In order to assess the impact of the excitation of the projectile on the magnitude of the rate coefficients, we have computed the ‘effective’ rate coefficients (Phillips, Maluendes & Green 1996) as follows:

$$k_{j_1 \rightarrow j'_1; j_2}(T) = \sum_{j'_2=0}^{10} k_{j_1 j_2 \rightarrow j'_1 j'_2}(T). \quad (2)$$

Fig. 2 presents effective de-excitation rate coefficients $k_{j_1 \rightarrow 0; j_2}$ at $10, 50,$ and 100 K. As one can see, these rate coefficients are decreasing with increasing j_2 . Indeed, the rotational energy spacing increases with increasing j_2 , which leads to smaller rate coefficients (energy gap law). At the exception of the effective rate coefficients for $j_2 = 0$, the variation of the effective rate coefficients with increasing

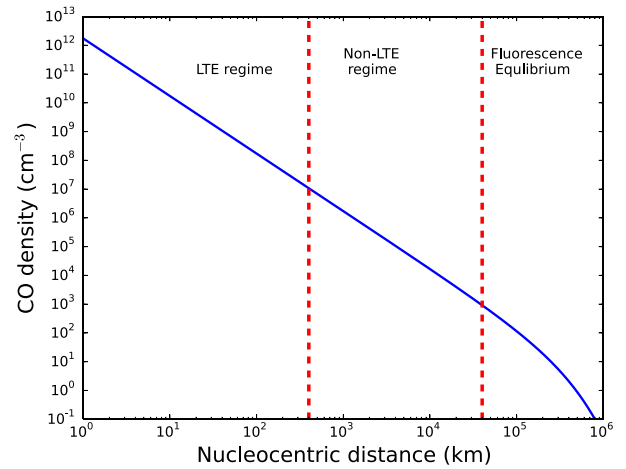


Figure 3. Density profile of the CO molecules in the comet at an heliocentric distance of 3 au, as given by the Haser model. The production rate of CO molecule was set to $Q_{\text{CO}} = 10^{28} \text{ s}^{-1}$, and the photodissociation rate to $\beta_{\text{CO}} = 2.1 \times 10^{-7} \text{ s}^{-1}$ (at $R = 3$ au). The dashed line separate (starting from the left side), the LTE regime, non-LTE regime, and fluorescence regime.

j_2 is moderate and we do not observe any large differences between effective rate coefficients with $j_2 > 2$.

3 ASTROPHYSICAL MODELLING

To assess the impact of the new collisional data on the astrophysical modelling of cometary comae, we performed radiative transfer calculations to simulate the excitation of CO in CO-dominated comae.

Non-LTE radiative transfer calculations were performed with the RADEX code (van der Tak et al. 2007) using the escape probability approximation at a steady state. In the radiative transfer calculations, we consider only radiative and collisional processes in order to model the relative population of the CO rotational levels, i.e. state-selective reactive processes such as photodissociation are neglected. All models presented in this work were performed assuming the typical physical conditions for a CO-dominated coma at an heliocentric distance $R = 3$ au (see below). In order to describe the density profile of CO molecules in the coma, we used a classic Haser model (Haser 1957) that is expressed by the following formula:

$$n_{\text{CO}}(r) = \frac{Q_{\text{CO}}}{4\pi r^2 v} e^{-r \frac{\beta_{\text{CO}}}{v}}, \quad (3)$$

where r is the nucleocentric distance, Q_{CO} is the production rate of the CO molecules fixed at 10^{28} s^{-1} , v is the expansion velocity fixed at 0.46 km s^{-1} , and β_{CO} is the CO photodissociation rate fixed at $2.1 \times 10^{-7} \text{ s}^{-1}$ at $R = 3$ au. The density profile of CO molecules is presented in Fig. 3. Our non-LTE model assumes that the CO rotational population in the coma is at steady state at a given CO density, i.e. at a given r .

The CO target column density $N(\text{CO})$ was not computed self-consistently but was fixed at 10^{14} cm^{-2} . This value corresponds to $r \sim 10^3\text{--}10^4$ km in the above Haser model (equation 3), i.e. to the non-LTE regime (see Fig. 3). As discussed in Faure et al. (2020), the relative populations are not sensitive to the column density provided that $N(\text{CO}) < 10^{16} \text{ cm}^{-2}$, i.e. as long as the lines are optically thin and photon trapping (self-absorption) is not important. The line width was thus set at 0.92 km s^{-1} , which corresponds to twice the expansion velocity for comets at heliocentric distance of

3 au (Dello Russo et al. 2016). We vary the density of the CO projectile from 10^1 to 10^9 cm^{-3} . This density range corresponds to nucleocentric distances of a few tens to a few 10^5 km (see Fig. 3). We considered three different kinetic temperatures: 10, 50, and 100 K. For the radiation field, we used the cosmic microwave background combined with the solar radiation as described in Faure et al. (2020) but adjusted to the distance $R = 3$ au. Our model includes the lowest 80 ro-vibrational levels of CO. Their relative energies and the corresponding transition Einstein coefficients were taken from the HITRAN data base (Gordon et al. 2022). Since our scattering calculations were performed only for transitions between the first 11 lowest rotational levels of CO ($j = 0-10$), the rate coefficients for transitions implying higher energy levels were simply set to zero. The validity of such approximation is justified by the fact that the population of these levels is negligibly small for the physical conditions investigated here (Faure et al. 2020).

3.1 Determining a suitable set of CO–CO collisional rate coefficients

Standard radiative transfer codes such as RADEX distinguish between the target and the projectile and they neglect the internal structure of the latter, i.e. the possibility of the projectile to be (de-)excited. This approach is not suited for collisions between identical molecules since mutual (de-)excitation of the target and the projectile is allowed. Nevertheless, in order to perform RADEX calculations, a set of CO–CO collisional data where the population of the CO projectile is fixed was necessary.

Usually, when considering a projectile with an internal structure, e.g. H_2 , the rate coefficients are taken for a given rotational state j_2 of the projectile that is conserved during the collision such that $j_2 = j'_2$. This approach is valid for inelastic collisions induced by H_2 at low temperature since, due to large energy spacings (≥ 510 K), the probability of H_2 excitation remains small up to ~ 500 K. This is however questionable in the case of collisions induced by heavier projectiles such as CO since they can be easily (de-)excited during the collisional process, even at 10 K, due to small energy spacings (≥ 5.53 K in CO). As an alternative, the rate coefficients can be averaged over a given distribution of the projectile and summed over its final levels. Considering that detailed balance between excitation and de-excitation rate coefficients is imposed in RADEX, the rate coefficients can only be averaged over a thermal distribution of the projectile:

$$k_{j_1 \rightarrow j'_1}(T) = \sum_{j_2=0}^{10} n_{j_2}(T) \sum_{j'_2=0}^{10} k_{j_1 j_2 \rightarrow j'_1 j'_2}(T), \quad (4)$$

$$n_{j_2}(T) = \frac{(2j_2 + 1)e^{-\frac{E_{j_2}}{k_B T}}}{\sum_{j'_2=0}^{10} (2j'_2 + 1)e^{-\frac{E_{j'_2}}{k_B T}}}, \quad (5)$$

where $n_{j_2}(T)$ is the thermal population of the projectile at a temperature T and E_{j_2} is the energy of a rotational level j_2 .

Indeed, the detailed balance relation for scattering between two molecules is the following:

$$k_{j_1 j_2 \rightarrow j'_1 j'_2}(T) = \frac{(2j'_1 + 1)(2j'_2 + 1)}{(2j_1 + 1)(2j_2 + 1)} e^{\frac{(E_{j_1} - E_{j'_1}) + (E_{j_2} - E_{j'_2})}{k_B T}} k_{j'_1 j'_2 \rightarrow j_1 j_2}(T). \quad (6)$$

If these full state-to-state rate coefficients are averaged over a thermal distribution of rotational states of the projectile at the kinetic temperature T and summed over the final rotational states of the

projectile, one does obtain the detailed balance relation for the target:

$$k_{j_1 \rightarrow j'_1}(T) = \frac{(2j'_1 + 1)}{(2j_1 + 1)} e^{\frac{(E_{j_1} - E_{j'_1})}{k_B T}} k_{j'_1 \rightarrow j_1}(T). \quad (7)$$

We insist that $n_{j_2}(T)$ needs to be a thermal distribution, i.e. must obey equation (5). Any other rotational distribution of the projectile (even thermal but at a temperature different from the kinetic temperature) leads to a set of rate coefficients that do not fulfill the detailed balance relation.

In order to test the impact of different rotational distributions of the CO projectile on the level population of the CO target, we performed radiative transfer calculations either considering a projectile in a given and unchanged rotational state ($j_2 = 0$ or 5) or assuming a thermal rotational distribution of the projectile (equation 4). Results are presented in Fig. 4.

As one can see, the differences between the three distributions of j_2 are very significant. These differences simply originate from the magnitude of the set of rate coefficients used in the radiative transfer calculations, the thermally averaged data being much larger than the others. Indeed, as discussed in the previous section, the rate coefficients with excitation or de-excitation of both the target and the projectile exhibit a higher magnitude than those with the excitation of only one CO molecule. Hence, fixing the rotational state of the projectile leads to a significant underestimation of the CO target excitation in a CO-dominated gas. As a consequence, while fixing the projectile in one given rotational state is an attractive approach in terms of implementation (as it obeys detailed balance), it is not recommended in the case of heavy projectile (with energy spacings smaller than the kinetic temperature T) due to the importance of mutual excitations between the target and the projectile.

In order to include the possibility of (de-)excitation of the projectile, one can use the effective rate coefficients and play with the rotational distribution of the projectile, e.g. by defining a rotational temperature (T_{rot}) for the projectile different from the kinetic temperature T . Collisional rate coefficients are thus computed using equation 4, with the n_{j_2} population being calculated for $T_{\text{rot}} \neq T$. We stress again that such set of rate coefficients does not fulfill the detailed balance relation and so the actual excitation and de-excitation rate coefficients must be employed in radiative transfer calculations. We performed some preliminary tests and found that T_{rot} has a significant impact on the CO target population, the best compromise being to use the thermally averaged rate coefficients, i.e. when $T_{\text{rot}} = T$. Thus, while the thermally averaged rate coefficients agree within a factor 2 with the effective rate coefficients (see Fig. 2), the rotational temperature of the projectile plays a non-negligible role in the population of the target. As a result, the full state-to-state rate coefficients (i.e. those defined in equation 6) should be used to solve the (non-linear) statistical equilibrium equations in order to simultaneously solve for the (identical) target and projectile populations. This non-standard problem should be investigated in future works.

In what follows, on we will use the thermally averaged set of rate coefficients, as in Faure et al. (2020) for CO– H_2O .

3.2 Impact of the new data

The results of our non-LTE models are presented in Fig. 5 where the population of levels j_1 is plotted as function of the CO density for kinetic temperatures of 10, 50, and 100 K.

From Fig. 5, we can clearly distinguish three different regimes for all plotted levels (see Fig. 3). The LTE regime will apply for density of CO molecules higher than $\approx 10^7$ cm^{-3} which corresponds to distances $r \leq 400$ km from the nuclei of the comet. The ‘non-LTE’

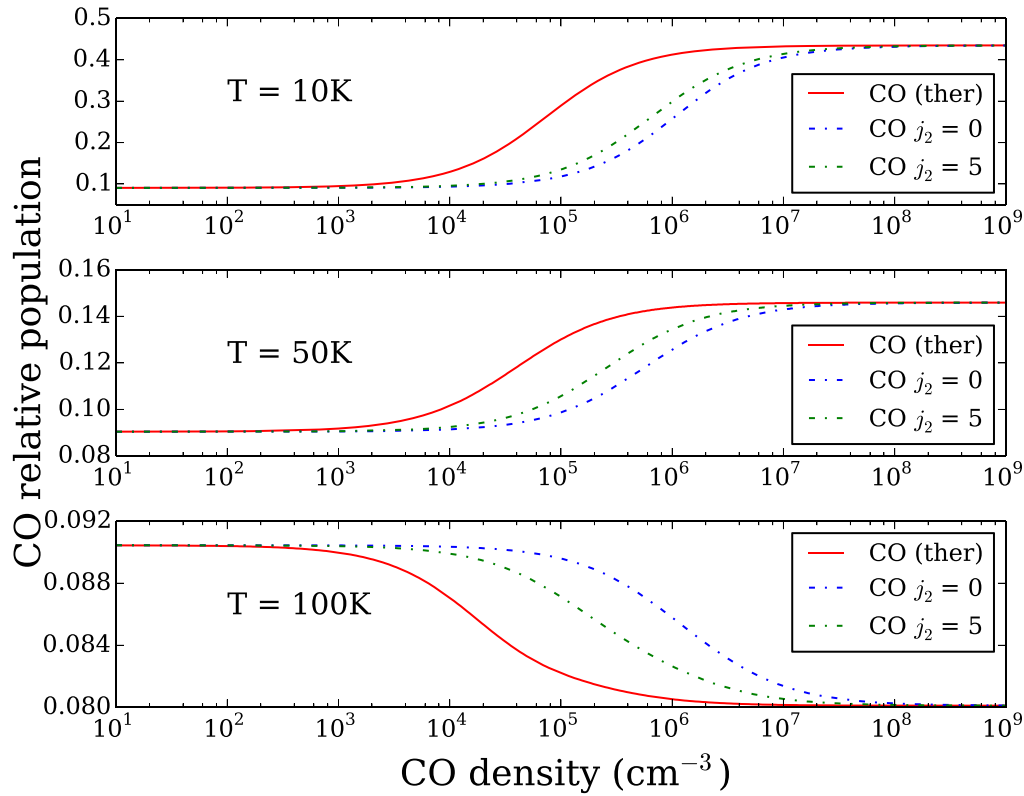


Figure 4. CO relative population of the $j_1 = 1$ state as a function of CO (projectile) density. The excitation of CO is induced by collisions with a thermally averaged projectile (red solid line), a projectile in $j_2 = j'_2 = 0$ state (blue dashed line), and a projectile in $j_2 = j'_2 = 5$ state (green dashed dotted line). Calculations were performed at kinetic temperatures of 10, 50, and 100 K.

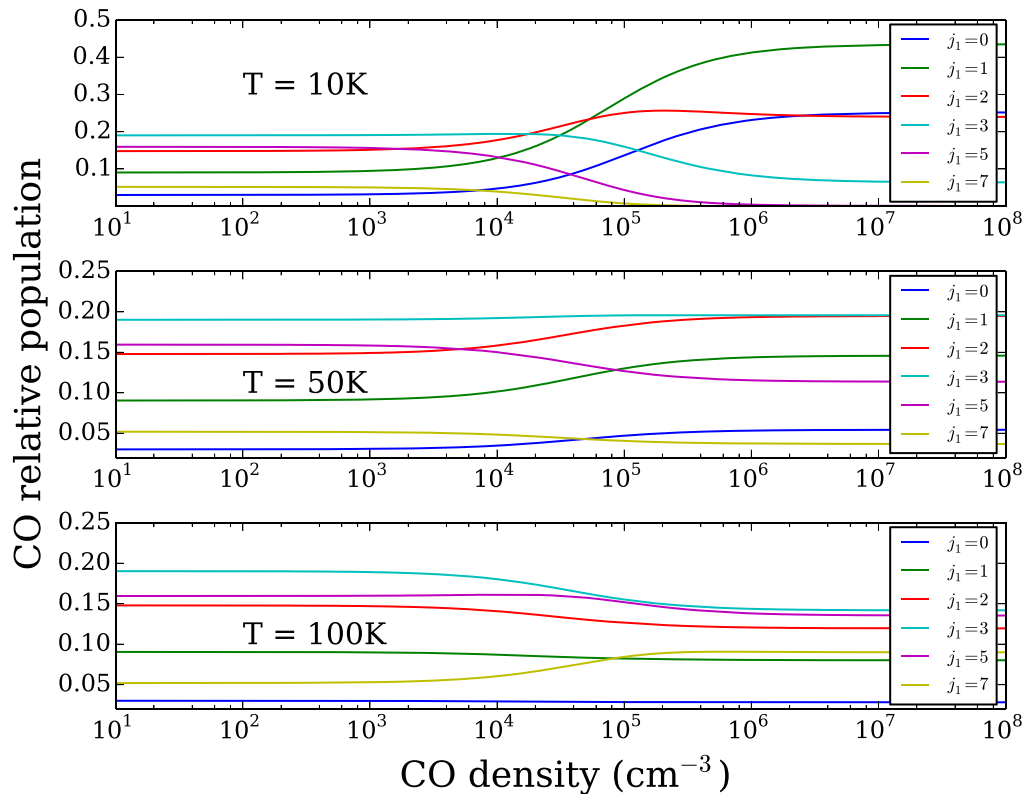


Figure 5. Level populations of CO ($j_1 = 0, 1, 2, 3, 5, 7$) as functions of CO density for temperatures of 10, 50, and 100 K.

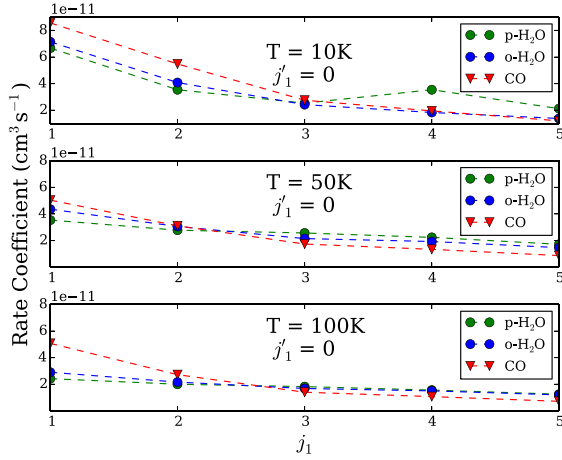


Figure 6. De-excitation transitions to the ground state ($j_1' = 0$) from the first five excited rotational states are presented. The CO data are from this work, and the H₂O data were taken from Faure et al. (2020).

regime (see below) exists for CO densities in the $10^3 - 10^7 \text{ cm}^{-3}$ range which corresponds to nucleocentric distances from ~ 400 to $\sim 40\,000 \text{ km}$. For density lower than 10^3 cm^{-3} and then nucleocentric distances higher than $40\,000 \text{ km}$, the fluorescence equilibrium is established. Thus, although fluorescence equilibrium is also a non-LTE regime, what we call here the non-LTE region of the coma lies between the thermal and fluorescence equilibrium limits. We also notice from Fig. 5 that the density range corresponding to the

non-LTE regime does not significantly vary with temperature at the opposite of the level populations that are strongly dependent on the temperature (in the LTE and non-LTE regime).

As we mentioned in the introduction, H₂O is usually the most abundant molecule in the coma of comets. Therefore, we now compare the excitation of CO induced by collisions with H₂O to the excitation of CO induced by CO. For the CO–H₂O rate coefficients, we used the thermalized set of collisional rate coefficients of Faure et al. (2020). It should be noted that Faure et al. (2020) did not find any significant differences for the excitation of CO induced by ortho- or by para-H₂O.

At first, we compare in Fig. 6 the two sets of rate coefficients at three kinetic temperatures of 10, 50, and 100 K, for de-excitation transitions to the ground rotational level of CO. As one can see, the similarities between the two sets of rate coefficients is high. The highest differences are observed for $\Delta j_1 = 1$ transitions but the deviations remain within a factor 2. One can also notice that the CO–CO rate coefficients are slightly larger than those for CO–H₂O in the case of transitions with small Δj_1 whereas the reverse is seen for large Δj_1 . The CO–H₂O interaction potential well is significantly larger than the CO–CO one and this may explain the larger coupling between rotational states with large Δj_1 .

Finally, we investigated the impact of different CO/H₂O abundance ratios on the population of the CO molecules. We thus performed radiative transfer calculations to determine the CO population in a cometary coma containing both CO and H₂O. We used the following abundance ratios of projectiles: H₂O = 100 per cent, CO/H₂O = 30 per cent/70 per cent, CO/H₂O = 70 per cent/30 per cent, and CO = 100 per cent. In Fig. 7, we present results for the $j_1 = 1$ level

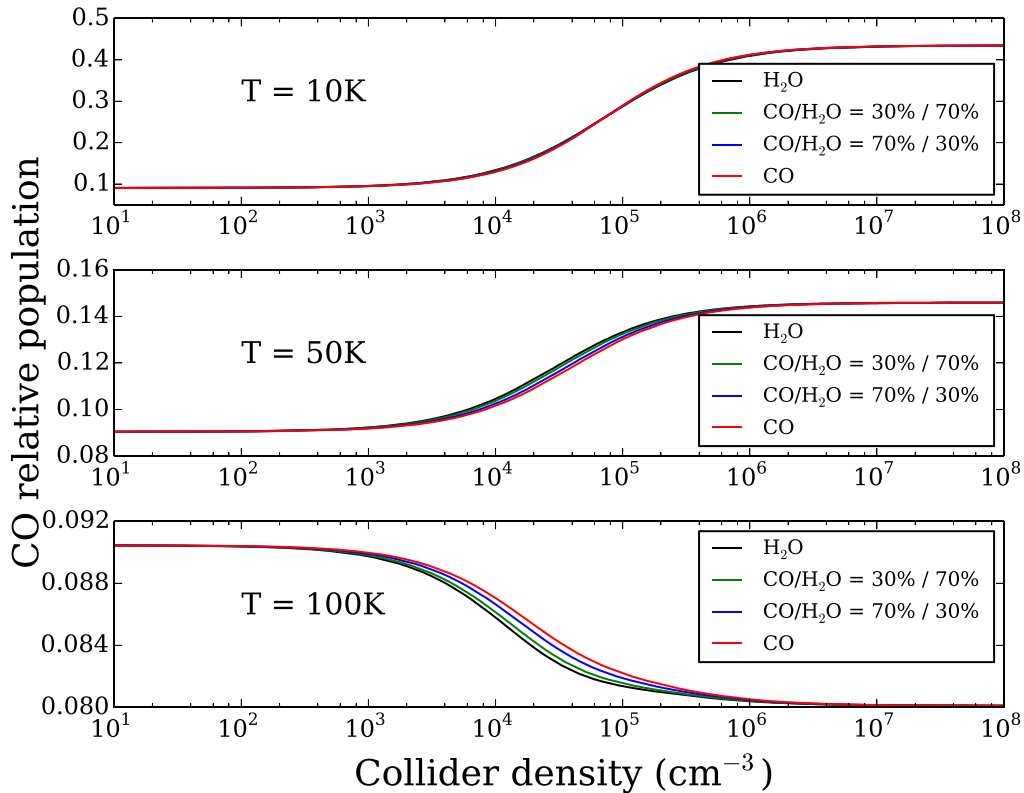


Figure 7. CO relative population for level $j_1 = 1$, as a function of the total density of the projectiles, for different CO and H₂O relative abundances. Calculations were performed at three kinetic temperatures, 10K – upper graph, 50K – middle graph, and 100K bottom graph. The black line presents results obtain with an abundance ratio CO/H₂O = 0 per cent/100 per cent, green line with CO/H₂O = 30 per cent/70 per cent, blue line with CO/H₂O = 70 per cent/30 per cent, and red line with CO/H₂O = 100 per cent/0 per cent.

of CO. We chose only one of the H₂O nuclear-spin symmetry for our modelling, para-H₂O.

For all three kinetic temperatures considered, populations obtained from the four abundance ratios agree relatively well, with however some significant differences. A similar pattern is observed for all j_1 levels of CO despite different temperature effects. Thus, we note that the deviation between models with 0 and 30 per cent of H₂O (red and blue) are minor, suggesting that it is reasonable in CO-dominated comae to neglect the contribution of H₂O collisions. Similarly, for H₂O-dominated comae where the CO/H₂O ratio is lower than 30 per cent/70 per cent, the excitation induced by CO does not play a significant role and can be neglected. We note that when the coma is a ~ 50 per cent/50 per cent mixture of CO and H₂O, the contribution of both colliders is similar and has to be considered. Such a situation might be encountered for CO-rich comets observed at heliocentric $1 \text{ au} < R < 3 \text{ au}$.

4 CONCLUSIONS

We have presented new collisional rate coefficients for the CO–CO collisional system. Data are provided for the transitions between rotational energy levels of the CO molecule up $j_1 = 10$ and for temperatures up to 150 K. The new set of rate coefficients was used in radiative transfer models of CO- and also H₂O-dominated comae. The results indicate that using a set of rate coefficients thermally averaged over the CO projectile is the best approximation so far because mutual excitations between CO target and CO projectile are important. We also found that the non-LTE regime extends for CO densities in the 10^3 – 10^7 cm^{-3} range. Finally, we observed that as soon as the CO/H₂O ratio is larger than 70 per cent/30 per cent, the contribution of H₂O collisions can be neglected. For a recent review of CO/H₂O ratios in comets, the reader is referred to Biver et al. (2022).

These new collisional data should allow a better modelling of the CO column density and physical conditions in CO-dominated comae. We note, however, that we have used thermalized rate coefficients, i.e. assuming that the projectile is thermalized at the kinetic temperature. This is obviously a convenient but crude approximation. In future works, the full state-to-state rate coefficients should be used when solving the statistical equilibrium in order to treat the target and projectile on similar footing. This is required for systems with identical molecules such as CO–CO, H₂O–H₂O, and CO₂–CO₂, of interest in comets. It will be thus necessary to test various numerical methods and approximations.

ACKNOWLEDGEMENTS

FL acknowledges Rennes Metropole for financial support. This research was supported by the CNRS national programme ‘Physique et Chimie du Milieu Interstellaire’. JL acknowledges support from Internal Funds KU Leuven through grant no. 19-00313. MAC was supported by the National Science Foundation under grant no. AST-2009253. We wish to acknowledge the support from the CEA/GENCI for awarding us access to the TGCC/IRENE supercomputer within the A0110413001 project and from Wroclaw Centre for Networking and Supercomputing.

DATA AVAILABILITY

The data underlying this article will be made available through the EMAA,¹ LAMDA (Schöier et al. 2005; van der Tak et al. 2020), and BASECOL (Dubernet et al. 2013) data bases. They are also available on request.

REFERENCES

- Arthurs A. M., Dalgarno A., 1960, *Proc. R. Soc. A*, 256, 540
- Biver N., Dello Russo N., Opitom C., Rubin M., 2022, in , Combi M., eds., *Comets III*. University of Arizona Press, Tucson
- Bockelée-Morvan D., Biver N., 2017, *Philos. Trans. R. Soc. A*, 375, 20160252
- Bockelée-Morvan D., Crovisier J., Mumma M. J., Weaver H. A., 2004, in Festou M. C., Keller H. U., Weaver H. A., eds, *Comets II*. University of Arizona Press, Tucson, p. 391
- Bodewits D., Bonev B. P., Cordiner M. A., Villanueva G. L., 2022, preprint ([arXiv:2209.02616](https://arxiv.org/abs/2209.02616))
- Boursier C., Mandal B., Babikov D., Dubernet M. L., 2020, *MNRAS*, 498, 5489
- Buffa G., Tarrini O., Scappini F., Cecchi-Pestellini C., 2000, *ApJS*, 128, 597
- Cochran A. et al., 2015, *Space Sci. Rev.*, 197
- Cordiner M. A. et al., 2022, *ApJ*, 929, 38
- Daniel F., Dubernet M.-L., Grosjean A., 2011, *A&A*, 536, A76
- Dello Russo N., Kawakita H., Vervack R. J., Weaver H. A., 2016, *Icarus*, 278, 301
- Dubernet M.-L. et al., 2013, *A&A*, 553, A50
- Faure A., Lique F., Loreau J., 2020, *MNRAS*, 493, 776
- Gordon I. et al., 2022, *J. Quant. Spectrosc. Radiat. Transfer*, 277, 107949
- Green S., 1993, *ApJ*, 412, 436
- Haser L., 1957, *Bull. Soc. R. Sci. Liege*, 43, 740
- Hutson J., Green S., 1994, CCP6, Daresbury
- Loreau J., Lique F., Faure A., 2018, *ApJ*, 853, L5
- Loreau J., Faure A., Lique F., 2022, *MNRAS*, 516, 5964
- Marboeuf U., Schmitt B., 2014, *Icarus*, 242, 225
- McGuire P., Kouri D. J., 1974, *J. Chem. Phys.*, 60, 2488
- Ndengué S. A., Dawes R., Gatti F., 2015, *J. Phys. Chem. A*, 119, 7712
- Otsubo T. et al., 2012, *ApJ*, 752, 15
- Phillips T. R., Maluendes S., Green S., 1996, *ApJS*, 107, 467
- Roueff E., Lique F., 2013, *Chem. Rev.*, 113, 8906
- Schöier F. L., Van der Tak F. F. S., van Dishoeck E. F., Black J. H., 2005, *A&A*, 432, 369
- Semenov A., Babikov D., 2017, *J. Phys. Chem. A*, 121, 4855
- van der Tak F. F. S., Black J. H., Schöier F. L., Jansen D. J., van Dishoeck E. F., 2007, *A&A*, 468, 627
- van der Tak F. F. S., Lique F., Faure A., Black J. H., van Dishoeck E. F., 2020, *Atoms*, 8, 15
- Visser G. W. M., Wormer P. E. S., van der Avoird A., 2003, *Phys. Chem. Chem. Phys.*, 5, 4767
- Womack M., Sarid G., Wierzos K., 2017, *PASP*, 129, 031001
- Żółtowski M., Loreau J., Lique F., 2022, *Phys. Chem. Chem. Phys.*, 24, 11910 (Paper I)

¹<https://emaa.osug.fr/>

This paper has been typeset from a \LaTeX file prepared by the author.

There is another possibility to consider excitation of the colider that was not presented in above article. One can use the effective rate coefficients in the models and play with the rotational distribution of the projectile by defining a rotational temperature (T_{rot}) for the projectile. Collisional rate coefficients are then computed using Eq 2 (see article above), the n_{j_2} population being fixed at all temperatures and calculated for $T = T_{rot}$. It was stressed that such set of rate coefficients, despite already used in astrophysical applications⁸⁰, does not fulfilled detailed balance relation that is a prerequisite of any radiative transfer calculations. Nevertheless, I decided to generate two sets of de-excitation effective rate coefficients considering rotational temperatures of 0 and 100 K. At $T_{rot} = 0$ K, only the ground level of the projectile is then considered. The excitation rate coefficients were generated from detailed balance relation. In Fig. 4.2, the results of the radiative transfer models are presented for the $n_{j_1} = 1$ level population of CO using these two sets of data and compared with the results obtained with the thermally averaged set of rate coefficients. Minor differences were observed (below 10%) between populations obtained with the set of thermally average rate coefficients and populations obtained with effective rate coefficients and an average over rotational states based on a rotational temperature. Similar differences in the population levels were observed for the other rotational levels of CO, which suggests that radiative transfer models are weakly dependent on the projectile population as long as effective rate coefficients are considered. Such finding could have been anticipated when looking at the weak variation of the effective rate coefficients with increasing j_2 (see Fig. 2 in above article). In Fig. 2, direct comparison of the thermally averaged rate coefficients with the effective rate coefficients is presented. We can see that the thermally averaged rate coefficients agree within a factor 2 with all effective rate coefficients. To summarize, it was found out, that the modeling of the CO population level is weakly dependent on the population of the projectile so that the thermally averaged set of rate coefficients which fulfilled detailed balance relation is a reasonable approach for astrophysical modeling of the CO observations in CO-dominated comae. Finally, my collisional data were already used to model observation of the CO-rich R2/PanSTARRS comet (See Appendix C).

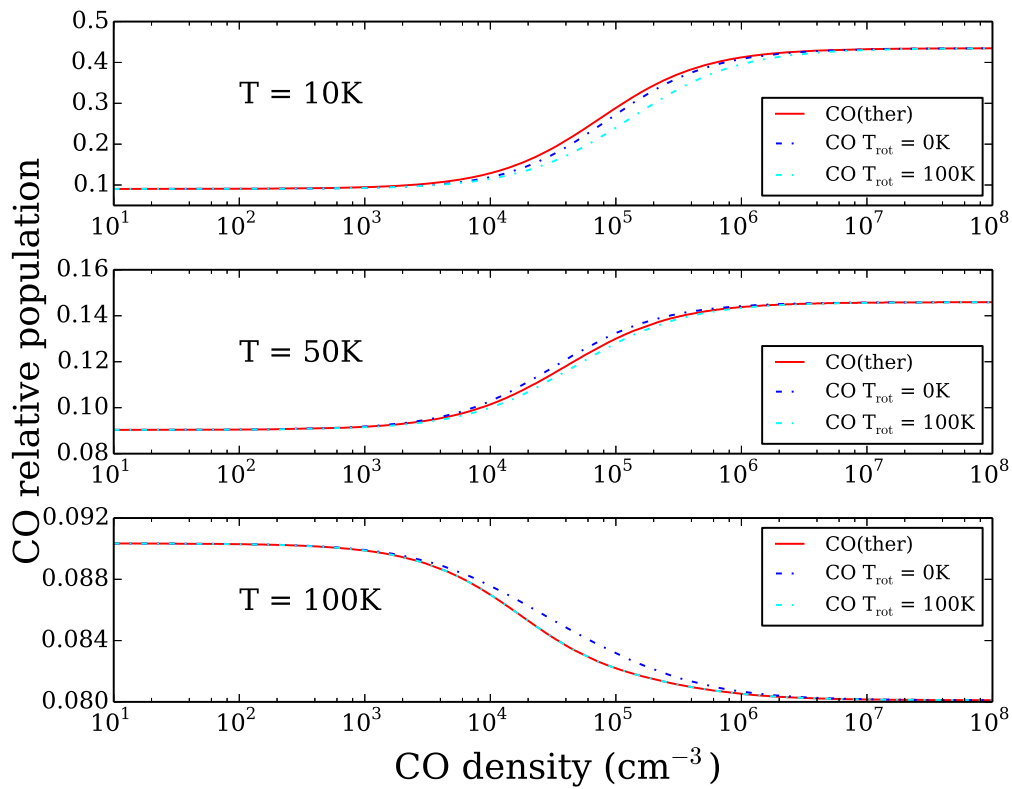


Figure 4.2: CO relative population of level $j = 1$, as a function of CO density. Calculations were performed at kinetic temperatures of 10, 50 and 100 K.

CHAPTER 5

SUMMARY AND PERSPECTIVE

In this thesis, I presented how we can treat the collisional system implying heavy colliders in quantum scattering calculations using available methods. I will now summarize all the projects I have presented in this work.

- The $\text{H}_2\text{O} - \text{H}_2$ system: It is an important system since the water is frequently observed in regions of the ISM, and where the hydrogen molecule is the dominant collider. The newly operating the JWST telescope will observe in the frequency range where high rotational water transitions occur. Collisional data for such transitions will be essential for analyzing observations. Some approximations had to be applied to carry on such calculations. Instead of using the full rigid 5D potential of $\text{H}_2\text{O} - \text{H}_2$ system, we used the adiabatic hinder rotor approximation one⁷⁷. This reduces the dimension of the PES from 5D to 3D. In such approximations, the structure of the hydrogen is neglected, and we are treating it as a pseudo atom. Even with the reduction of the PES, the full close coupling calculations were not feasible. The coupled states approximations was used in the calculations. I tried to push the calculations to the limits, and that resulted in providing the rate coefficients for transitions between 97 levels of *ortho*- and *para*- H_2O , for temperatures up to 2000 K. The accuracy of my data was estimated to be within a factor of 3, making them very useful in astrophysical modeling.
- Water isotopologues: Proper description of the isotopic ratio of the water isotopologues is a key to a better understanding of water chemistry in the ISM. Therefore, I assess how big influence will have the substitute in the H_2O molecule, of oxygen by its heavier isotope ^{18}O , and of both hydrogen atoms by deuterium. In the case of oxygen substitution, the effect was minor, suggesting that the collisional rates of $\text{H}_2^{16}\text{O} - \text{H}_2$, that are widely available in literature can be safely used for modeling of $\text{H}_2^{18}\text{O} - \text{H}_2$ collisions. Unfortunately, we can not do the same in the case of the $\text{D}_2\text{O} - \text{H}_2$. I

observed differences up to a factor of 3 between rate coefficients of the $D_2O - H_2$ and $H_2O - H_2$ for systems. Therefore, I performed the new scattering calculations for the $D_2O - H_2$ system. This time I used full 5D rigid rotor PES and calculations were done with the close-coupling method. I obtained the rate coefficients for temperatures up to 300 K, for the transitions between 20 levels of *ortho*- D_2O , and 19 levels of *para*- D_2O .

- The HCN/HNC - H_2O systems: The HCN and HNC molecules are frequently observed in the cometary atmospheres. Water is usually the most abundant molecule in this media. Therefore it is natural to consider it as a dominant collider. That is why for both HCN - H_2O and HNC - H_2O systems, the collisional data will be of great importance for modeling the spectra of the comets. However, both systems are extremely challenging in terms of scattering calculations. The PES of both systems were calculated using the AUTOPES code with the SAPT(DFT) method. I made a comparison of these potentials. I did ab-initio calculations for characteristic geometries of the two systems, using the CCSD(T) method with aug-cc-pVDZ, aug-cc-pVTZ, aug-cc-pVQZ basis set, and performing extrapolations to the CBS. The highest observed difference between the SAPT(DFT) PES and the CCSD(T) ones was within 10%, validating the SAPT(DFT) potential for the scattering calculations. The pure quantum calculations will not be feasible with the PESs that have such big well-depth. Yet, I tried to converge the lowest possible transitions of HCN/HNC just for the lowest total angular momentum using the close coupling method. These results would have been used as a benchmark for the approximation method. Unfortunately, I was not able to obtain any converged results. The project is still in progress. I am currently working on computing the adiabats that will be used in the SACM method to provide collisional data for this project.
- The CO-CO system: For the comets at high heliocentric distances, we observed CO production rates far exceeding the water production. The CO will start to sublimate much faster than water since it has a lower sublimation temperature. In such comets,

it's natural to consider the CO as a dominant collider. That is why for modeling observation of such a comet, the collisional data of the CO-CO system are of great importance. The CO-CO system was a huge challenge for the scattering calculations. With the small rotational constant of CO the number of channels that I had to consider in the scattering calculations was enormous. Another difficulty that I had to face was that I had to treat the CO-CO system as distinguishable molecules. With such an approach, I could not take advantage of the system's symmetry, and I had to include almost two times more channels in a rotational basis than explicitly considering the symmetry of the system. The main reason for such an approach was the astrophysical application. The radiative transfer theory always distinguishes between the target and the collider molecules. The second reason was that I discovered issues in the scattering code I was using. I performed calculations using the coupled states approximations with the 4D rigid rotor potential. Even though I was using the CS approximation, which significantly reduced the calculations' time and memory needs, each energy point had to be divided into calculations of single total angular momentum. Yet, such calculations usually take 1 to 5 days to finish. Finally, I calculated the rate coefficients for temperatures up to 150 K for the transitions between levels up to $j = 10$. Using this new data set, I presented an approach to the radiative transfer modeling of identical molecules. Additionally, I showed that considering the CO as a dominant and only collider for modeling observation of the CO-dominated comets will lead to slight inaccuracy. Finally, my data was already proven helpful to the community since it was already used in modeling the cometary spectra¹⁰⁵.

The work we have sketched in this dissertation opens many perspectives for the future. In this section, I highlight the future developments that I consider as the most pressing and/or the most important.

My first goal will be to finish the HCN/HNC-water scattering projects. As we mentioned earlier, both molecules were frequently detected in cometary media. Thus, collisional data

for these systems are of high interest for the astronomical community. Moreover, beyond the interpretation of observational spectra, such data can help to find a hint about the creation of the HNC, in the comets, it would help addressing the question of whether HNC was frozen in nuclei and released to the coma through sublimation or whether it was directly created in comae from HCN.

Second, new data for the CO-CO system would be of great help for the modeling of comets at high heliocentric distance. I strongly believe that further works on cometary systems should be focusing on collisions between CO, CO₂ and H₂O. Indeed, these three species are the most abundant molecules in the cometary media, which means that a better understanding of their mutual interactions could be of decisive importance. We can already find collisional data for the H₂O-CO and for H₂O-H₂O system. But the CO-CO₂, CO₂-CO₂ and CO₂-H₂O systems are still missing. The strategy I have developed in the present work may help to address these calculations. In addition, the calculations with the SACM method, showed that such a heavy system can be considered and collisional data can be provided. Therefore, I believe that thanks to further developments of computational science, and with the development of new approximated methods such as SACM, we will be able to calculate more and more complexes of astrophysical interests.

Interesting results were found thanks to the modeling excitation of CO induced by CO and by water. Indeed, this work permitted to find that the CO can be safely considered as the only collider when modeling the spectra of the CO in the CO-dominated comet. This result might have interesting consequences. Scattering calculations considering the linear molecule as a collider are much easier to perform than calculations with the asymmetric top (water) as a collider. Therefore, in the future, it would be worth to investigate the excitation of the other molecules observed in comets at high heliocentric distances, as well as how much an influence would water have on their collisional excitation. If the results are similar to the CO-CO results reported here, we could limit scattering calculations to systems where CO is the only collider and make the task both much easier and faster.

The last point towards which I would like to bring attention is the radiative transfer modeling. To my eyes, the study of the CO-CO system revealed a problem that, sooner or later, the astrophysical community will need to face.

To be sure, it is true that when the dominant colliders are H₂ molecules, the thermal average approach of the rate coefficients worked very well. But this is not always the case. If we need to deal with colliders for which the possibility of excitation is very high in modeled media (or equal to the target if we are dealing with identical molecules), the approach consisting in neglecting the possibility that the collider is excited becomes ill-founded, and the thermal average strategy starts to look as a very crude approximation. In those cases, it seems to me that we should always use the full set of state-to-state rate coefficients, and look for the population of the collider and of the target simultaneously, while solving the SE equation. Of course, this problem is not a trivial one. As such, it requires careful testing of some methods and approximation, but I do believe that its something that should be investigated since it can have a big impact on the analysis spectra of the comets.

APPENDIX A

SCATTERING CODES

A.1. Molscat Scattering Code

Most of the scattering calculations presented in this work were done with MOLSCAT⁷¹ scattering code for nonreactive collisions (version 14). MOLSCAT is a general purpose scattering code, that allows one to perform quantum scattering calculations between two colliders (atoms and/or molecules). Calculations are performed on a grid of energies, only when there is at least one open channel. The iteration of the equations starts at the short range of the potential and it propagates outwards to the long range of the PES where potential starts to be insignificant. The S matrix is derived from the asymptotic behaviour of the wavefunction. The user has to provide the interaction potential of the system of interest, together with the energy level list of the colliding monomers, or the spectroscopic constants that describe the monomers (rotational constants, vibrational constants etc.). In addition the user has to specify a method for solving the coupled equations and choose the type of propagator that will be used. Finally, the user have to optimize a series of parameters in order to obtain the most accurate results. Here, I will present the most important parameters that need to be optimized before the collisional data production. For more detailed explanation about capabilities of the MOLSCAT code, I strongly encourage the reader to look into the official manual of the program¹⁰⁶.

- **JMIN/JMAX** - This parameters regulate the size of the rotational basis used in the scattering calculations. The JMIN - is the lower level, and JMAX is the highest level used in the basis.
- **RMAX** - This parameter is the upper limit of how far the integration will go.
- **STEPS** - It is a number of steps per half-wavelength for the open channel with the highest kinetic energy in the asymptotic region.

- **JTOT** - In the case of reaching a convergence for the total angular momentum (JTOT), the code offers automatic convergence of this parameter. The iterative loop over the total angular momentum in the Molscat is performed until a number of consecutive total angular momenta provides partial cross-sections within the limit defined by the user. The limits are set separately on the diagonal (**DTOL**) and off-diagonal (**OTOL**) results.

There are obviously some limitations, with what can be calculated with MOLSCAT (and any other scattering code). In the close coupling approach computational time is approximately proportional to N^3 where N is number of channels needed to be solved. The memory needs scale as N^2 . The limit on the number of channels that can be treated is not strict number, it can be up to several thousands of channels, depending on the type of the type computer we use for calculations. In the code, numbers of approximations are implemented such as coupled states that, allow extends this limits of calculations, or in some particular cases make the calculations feasible.

A.2. Hibridon Scattering code

HIBRIDON is a package to solve the close coupling equations for scattering of non reactive processes between atoms and/or molecules. In addition, with this code we can treat photodissociation processes, scattering of an atom and/or molecule with surfaces, and bound states of weakly bound complexes. Similarly as in the case of the MOLSCAT code, the iteration starts from the short-range of the potential, and propagates outwards to the asymptotic region. Again, the S matrix is obtained from the asymptotic behaviour of the wavefunction. To perform scattering calculations, the user has to provide the potential energy surface of the system, together with the molecular constants of the monomers, and the reduced mass of the system. Also here, the number of parameters has to be optimized before the data production. Below I will present the crucial parameters that needed to be converged.

- **RSTART /RENDAI /RENLDL** - The RSTART and RENDAI are the starting and ending point of the interaction space, respectively. The variable RENLDL defines a distance (starting from RSTART) until which the log-derivative propagation is performed, and after this point, we switch to the airy propagator, which propagates up to RENDAI.
- **SPAC** - It is a parameter that regulates the interval of the integration when the log-derivative propagator is used.
- **J1MAX /J2MAX** - are parameters that regulates of maximal size of the rotational basis of monomers, that are included in the scattering calculations.
- **JTOT1 /JTOT2 /JTOTD** - These parameters regulate the number of the total angular momenta for which the calculation are performed. JTOT1 is the initial value, JTOT2 is the final value and JTOTD is a step size between two consecutive total angular momenta. Contradictory to the MOLSCAT code, the HIBRIDON code has no functions to reach an automatic convergence of total angular momenta, so the user has to perform convergence of this parameter.

The same limits apply to this code as were applied to the MOLSCAT. The time needed for solving the coupled equations (within the close-coupling method) scales approximately as number of channels N to the power of 3, and the memory needs scale to power of 2. Again, the limits for the maximum number of channels that we can treat will be not strict, and will depend on the resources we can use for calculations. For more detailed information about the HIBRIDON code I encourage the reader to look into the official [website](#) of the code.

APPENDIX B

COLLISIONAL DATA OF D₂O - H₂ SYSTEM

Table of rotational energy levels of *ortho*-D₂O, for which scattering calculations were performed in this work.

Nr.	j	k_a	k_c	Energy (cm ⁻¹)
1	0	0	0	0.0000
2	2	0	2	20.2652
3	1	1	1	35.8884
4	2	0	2	49.3572
5	2	1	1	74.2646
6	3	1	3	74.5193
7	3	2	2	110.1530
8	3	3	1	157.2253
9	4	0	4	115.0581
10	4	1	3	141.2361
11	4	2	2	164.3789
12	4	3	1	206.8764
13	4	4	0	271.3282
14	5	1	5	170.3331
15	5	2	4	217.8184
16	5	3	3	268.1716
17	6	0	6	232.7244
18	6	1	5	280.1043
19	6	2	4	309.9897
20	7	1	7	306.0601

Rotational rate coefficients computed for the 20 first rotational energy levels (see previous table) of *ortho*-D₂O in collision with *para*-H₂. Rate coefficients are provided for temperatures from 10 to 150 K.

Tran.	Initial	Final	10 K	30 K	50 K	70 K	90 K	110 K	130 K	150 K
1	2	1	1.39e-11	1.20e-11	1.13e-11	1.13e-11	1.16e-11	1.21e-11	1.27e-11	1.34e-11
2	3	1	2.65e-11	2.76e-11	2.58e-11	2.42e-11	2.29e-11	2.19e-11	2.10e-11	2.03e-11
3	3	2	2.37e-11	1.66e-11	1.32e-11	1.16e-11	1.08e-11	1.05e-11	1.05e-11	1.07e-11
4	4	1	1.11e-12	7.78e-13	5.41e-13	4.05e-13	3.21e-13	2.66e-13	2.28e-13	2.00e-13
5	4	2	7.82e-11	8.53e-11	8.08e-11	7.60e-11	7.19e-11	6.85e-11	6.56e-11	6.31e-11
6	4	3	1.65e-11	1.52e-11	1.50e-11	1.54e-11	1.62e-11	1.71e-11	1.82e-11	1.94e-11
7	5	1	4.61e-12	5.25e-12	5.35e-12	5.39e-12	5.41e-12	5.40e-12	5.39e-12	5.37e-12
8	5	2	1.17e-11	1.04e-11	1.00e-11	1.01e-11	1.04e-11	1.07e-11	1.12e-11	1.16e-11
9	5	3	1.69e-11	1.36e-11	1.10e-11	9.27e-12	8.10e-12	7.25e-12	6.61e-12	6.11e-12
10	5	4	1.66e-11	1.39e-11	1.24e-11	1.18e-11	1.17e-11	1.19e-11	1.22e-11	1.27e-11
11	6	1	1.94e-12	2.25e-12	2.47e-12	2.65e-12	2.83e-12	3.01e-12	3.20e-12	3.39e-12
12	6	2	1.71e-11	1.64e-11	1.53e-11	1.44e-11	1.37e-11	1.32e-11	1.27e-11	1.24e-11
13	6	3	1.98e-11	1.82e-11	1.67e-11	1.60e-11	1.59e-11	1.60e-11	1.64e-11	1.69e-11
14	6	4	1.00e-11	1.06e-11	9.90e-12	9.14e-12	8.51e-12	8.01e-12	7.61e-12	7.29e-12
15	6	5	6.83e-12	4.84e-12	4.13e-12	3.79e-12	3.66e-12	3.66e-12	3.74e-12	3.88e-12
16	7	1	2.52e-14	6.12e-14	6.21e-14	5.77e-14	5.32e-14	4.92e-14	4.59e-14	4.31e-14
17	7	2	2.18e-12	2.13e-12	2.16e-12	2.22e-12	2.32e-12	2.42e-12	2.54e-12	2.66e-12
18	7	3	8.88e-12	1.07e-11	1.11e-11	1.11e-11	1.11e-11	1.11e-11	1.10e-11	1.09e-11
19	7	4	1.33e-11	1.15e-11	1.11e-11	1.11e-11	1.13e-11	1.17e-11	1.21e-11	1.26e-11
20	7	5	4.43e-11	4.99e-11	4.76e-11	4.50e-11	4.27e-11	4.08e-11	3.92e-11	3.78e-11
21	7	6	1.14e-11	8.82e-12	8.02e-12	7.74e-12	7.74e-12	7.92e-12	8.18e-12	8.51e-12
22	8	1	7.74e-14	7.93e-14	7.92e-14	8.08e-14	8.34e-14	8.65e-14	9.00e-14	9.37e-14
23	8	2	6.44e-13	7.98e-13	8.80e-13	9.61e-13	1.04e-12	1.12e-12	1.19e-12	1.27e-12
24	8	3	3.96e-13	3.74e-13	3.29e-13	3.00e-13	2.83e-13	2.72e-13	2.65e-13	2.61e-13
25	8	4	1.09e-12	1.39e-12	1.48e-12	1.54e-12	1.59e-12	1.64e-12	1.68e-12	1.73e-12
26	8	5	1.70e-11	1.63e-11	1.59e-11	1.59e-11	1.61e-11	1.66e-11	1.71e-11	1.77e-11
27	8	6	1.35e-12	1.41e-12	1.31e-12	1.23e-12	1.18e-12	1.14e-12	1.12e-12	1.10e-12
28	8	7	8.88e-12	1.08e-11	1.04e-11	1.01e-11	1.01e-11	1.02e-11	1.05e-11	1.09e-11
29	9	1	7.67e-14	1.18e-13	1.17e-13	1.15e-13	1.16e-13	1.22e-13	1.30e-13	1.43e-13
30	9	2	2.88e-12	2.67e-12	2.68e-12	2.77e-12	2.90e-12	3.05e-12	3.21e-12	3.38e-12
31	9	3	1.84e-11	1.89e-11	1.82e-11	1.76e-11	1.72e-11	1.68e-11	1.65e-11	1.63e-11
32	9	4	4.52e-12	4.12e-12	4.01e-12	4.07e-12	4.21e-12	4.40e-12	4.63e-12	4.87e-12
33	9	5	1.38e-12	1.33e-12	1.12e-12	9.79e-13	8.91e-13	8.39e-13	8.14e-13	8.07e-13
34	9	6	1.69e-11	1.63e-11	1.54e-11	1.50e-11	1.49e-11	1.51e-11	1.54e-11	1.58e-11
35	9	7	2.53e-12	2.53e-12	2.12e-12	1.80e-12	1.57e-12	1.41e-12	1.29e-12	1.20e-12
36	9	8	1.25e-15	8.11e-14	1.68e-13	2.20e-13	2.54e-13	2.81e-13	3.05e-13	3.29e-13
37	10	1	3.29e-14	2.59e-14	2.24e-14	2.06e-14	1.96e-14	1.91e-14	1.87e-14	1.85e-14
38	10	2	6.54e-13	7.23e-13	7.22e-13	7.12e-13	6.99e-13	6.87e-13	6.75e-13	6.64e-13
39	10	3	1.03e-12	8.12e-13	7.54e-13	7.56e-13	7.86e-13	8.31e-13	8.85e-13	9.44e-13
40	10	4	1.38e-11	1.54e-11	1.59e-11	1.61e-11	1.63e-11	1.64e-11	1.65e-11	1.66e-11
41	10	5	3.30e-12	2.75e-12	2.72e-12	2.81e-12	2.94e-12	3.10e-12	3.26e-12	3.43e-12
42	10	6	2.16e-11	2.37e-11	2.35e-11	2.30e-11	2.26e-11	2.22e-11	2.18e-11	2.14e-11
43	10	7	1.17e-11	8.63e-12	7.47e-12	6.94e-12	6.71e-12	6.64e-12	6.68e-12	6.78e-12
44	10	8	1.29e-13	6.46e-13	7.67e-13	7.61e-13	7.29e-13	6.97e-13	6.71e-13	6.55e-13
45	10	9	9.68e-12	9.60e-12	9.72e-12	1.00e-11	1.05e-11	1.10e-11	1.17e-11	1.23e-11
46	11	1	1.73e-13	2.00e-13	2.16e-13	2.32e-13	2.47e-13	2.62e-13	2.77e-13	2.93e-13
47	11	2	5.55e-13	5.79e-13	5.96e-13	6.25e-13	6.63e-13	7.07e-13	7.55e-13	8.05e-13
48	11	3	1.74e-12	2.11e-12	2.27e-12	2.41e-12	2.54e-12	2.66e-12	2.77e-12	2.87e-12
49	11	4	2.51e-13	4.20e-13	3.98e-13	3.68e-13	3.47e-13	3.36e-13	3.32e-13	3.32e-13
50	11	5	6.71e-12	7.83e-12	8.11e-12	8.23e-12	8.31e-12	8.36e-12	8.39e-12	8.41e-12
51	11	6	4.44e-12	4.73e-12	4.92e-12	5.15e-12	5.41e-12	5.69e-12	5.98e-12	6.28e-12

52	11	7	3.15e-11	3.55e-11	3.49e-11	3.38e-11	3.28e-11	3.19e-11	3.11e-11	3.03e-11
53	11	8	6.20e-12	6.40e-12	5.51e-12	4.96e-12	4.65e-12	4.52e-12	4.48e-12	4.53e-12
54	11	9	2.87e-12	3.80e-12	3.76e-12	3.57e-12	3.38e-12	3.21e-12	3.06e-12	2.93e-12
55	11	10	9.48e-12	1.04e-11	1.11e-11	1.19e-11	1.28e-11	1.38e-11	1.48e-11	1.58e-11
56	12	1	9.64e-16	3.71e-15	3.98e-15	3.66e-15	3.28e-15	2.94e-15	2.66e-15	2.42e-15
57	12	2	1.24e-13	1.46e-13	1.55e-13	1.64e-13	1.75e-13	1.87e-13	2.01e-13	2.15e-13
58	12	3	3.73e-13	3.80e-13	3.79e-13	3.84e-13	3.94e-13	4.08e-13	4.24e-13	4.42e-13
59	12	4	5.49e-13	6.57e-13	7.20e-13	7.93e-13	8.72e-13	9.53e-13	1.04e-12	1.12e-12
60	12	5	2.22e-12	2.33e-12	2.35e-12	2.40e-12	2.47e-12	2.57e-12	2.68e-12	2.81e-12
61	12	6	4.91e-13	6.24e-13	6.75e-13	7.18e-13	7.61e-13	8.04e-13	8.46e-13	8.89e-13
62	12	7	1.04e-11	1.06e-11	1.07e-11	1.09e-11	1.12e-11	1.16e-11	1.21e-11	1.26e-11
63	12	8	3.69e-11	4.18e-11	4.12e-11	3.99e-11	3.86e-11	3.75e-11	3.65e-11	3.55e-11
64	12	9	8.04e-13	8.08e-13	7.16e-13	6.63e-13	6.35e-13	6.23e-13	6.21e-13	6.25e-13
65	12	10	1.73e-12	2.02e-12	1.95e-12	1.86e-12	1.78e-12	1.71e-12	1.65e-12	1.60e-12
66	12	11	8.22e-12	9.17e-12	9.26e-12	9.35e-12	9.56e-12	9.86e-12	1.02e-11	1.06e-11
67	13	1	2.50e-15	2.86e-15	3.22e-15	3.44e-15	3.60e-15	3.75e-15	3.91e-15	4.10e-15
68	13	2	4.66e-14	4.89e-14	5.16e-14	5.46e-14	5.79e-14	6.15e-14	6.52e-14	6.92e-14
69	13	3	6.65e-15	9.59e-15	1.10e-14	1.11e-14	1.07e-14	1.02e-14	9.74e-15	9.41e-15
70	13	4	3.17e-14	4.14e-14	4.41e-14	4.48e-14	4.54e-14	4.64e-14	4.78e-14	4.97e-14
71	13	5	2.18e-13	2.60e-13	2.97e-13	3.39e-13	3.88e-13	4.43e-13	5.01e-13	5.63e-13
72	13	6	5.12e-14	6.16e-14	6.53e-14	6.61e-14	6.65e-14	6.72e-14	6.83e-14	6.98e-14
73	13	7	3.35e-13	4.22e-13	4.65e-13	5.00e-13	5.37e-13	5.77e-13	6.19e-13	6.64e-13
74	13	8	1.86e-11	1.84e-11	1.81e-11	1.82e-11	1.85e-11	1.90e-11	1.96e-11	2.02e-11
75	13	9	5.02e-14	5.70e-14	5.91e-14	6.06e-14	6.26e-14	6.53e-14	6.86e-14	7.26e-14
76	13	10	1.70e-13	1.69e-13	1.67e-13	1.68e-13	1.70e-13	1.75e-13	1.80e-13	1.87e-13
77	13	11	6.18e-13	6.76e-13	6.61e-13	6.49e-13	6.45e-13	6.50e-13	6.60e-13	6.76e-13
78	13	12	8.18e-12	9.59e-12	9.86e-12	9.99e-12	1.02e-11	1.05e-11	1.08e-11	1.12e-11
79	14	1	1.40e-13	1.29e-13	1.27e-13	1.29e-13	1.33e-13	1.39e-13	1.44e-13	1.50e-13
80	14	2	7.42e-14	1.14e-13	1.24e-13	1.34e-13	1.48e-13	1.67e-13	1.91e-13	2.18e-13
81	14	3	5.62e-12	5.16e-12	5.04e-12	5.10e-12	5.25e-12	5.44e-12	5.68e-12	5.93e-12
82	14	4	1.39e-13	2.16e-13	2.10e-13	2.08e-13	2.17e-13	2.37e-13	2.66e-13	3.02e-13
83	14	5	4.34e-13	4.04e-13	3.98e-13	4.05e-13	4.20e-13	4.39e-13	4.61e-13	4.86e-13
84	14	6	1.30e-11	1.40e-11	1.37e-11	1.34e-11	1.31e-11	1.29e-11	1.28e-11	1.27e-11
85	14	7	1.65e-12	2.15e-12	2.25e-12	2.32e-12	2.40e-12	2.50e-12	2.61e-12	2.74e-12
86	14	8	8.62e-13	7.84e-13	6.24e-13	5.17e-13	4.47e-13	4.02e-13	3.73e-13	3.56e-13
87	14	9	1.68e-11	1.73e-11	1.73e-11	1.74e-11	1.77e-11	1.81e-11	1.86e-11	1.92e-11
88	14	10	1.50e-12	1.87e-12	1.81e-12	1.72e-12	1.65e-12	1.59e-12	1.54e-12	1.51e-12
89	14	11	1.47e-12	1.98e-12	1.93e-12	1.88e-12	1.87e-12	1.90e-12	1.96e-12	2.03e-12
90	14	12	4.19e-15	1.44e-13	2.56e-13	3.09e-13	3.34e-13	3.47e-13	3.56e-13	3.64e-13
91	14	13	4.52e-20	7.41e-16	4.87e-15	1.08e-14	1.69e-14	2.28e-14	2.85e-14	3.41e-14
92	15	1	7.14e-16	1.37e-15	1.29e-15	1.16e-15	1.05e-15	9.61e-16	8.95e-16	8.46e-16
93	15	2	2.49e-13	2.44e-13	2.40e-13	2.42e-13	2.45e-13	2.50e-13	2.55e-13	2.60e-13
94	15	3	2.24e-13	2.47e-13	2.62e-13	2.77e-13	2.94e-13	3.11e-13	3.30e-13	3.50e-13
95	15	4	2.69e-12	2.67e-12	2.69e-12	2.77e-12	2.88e-12	3.01e-12	3.15e-12	3.31e-12
96	15	5	1.27e-13	2.19e-13	2.22e-13	2.18e-13	2.18e-13	2.22e-13	2.32e-13	2.45e-13
97	15	6	3.32e-13	3.16e-13	3.00e-13	2.86e-13	2.76e-13	2.69e-13	2.64e-13	2.61e-13
98	15	7	7.17e-12	8.16e-12	8.39e-12	8.53e-12	8.65e-12	8.75e-12	8.84e-12	8.92e-12
99	15	8	1.08e-12	1.56e-12	1.64e-12	1.68e-12	1.72e-12	1.78e-12	1.85e-12	1.93e-12
100	15	9	6.53e-12	7.67e-12	8.07e-12	8.34e-12	8.57e-12	8.75e-12	8.90e-12	9.03e-12
101	15	10	8.84e-12	9.30e-12	9.44e-12	9.65e-12	9.94e-12	1.03e-11	1.07e-11	1.11e-11
102	15	11	1.24e-11	1.36e-11	1.32e-11	1.28e-11	1.23e-11	1.20e-11	1.17e-11	1.14e-11

103	15	12	4.77e-12	5.93e-12	5.46e-12	5.09e-12	4.88e-12	4.81e-12	4.83e-12	4.92e-12
104	15	13	3.32e-16	5.79e-14	1.46e-13	2.05e-13	2.43e-13	2.69e-13	2.91e-13	3.11e-13
105	15	14	7.15e-12	7.60e-12	7.54e-12	7.54e-12	7.64e-12	7.83e-12	8.07e-12	8.35e-12
106	16	1	2.51e-14	2.64e-14	2.73e-14	2.86e-14	3.02e-14	3.20e-14	3.39e-14	3.60e-14
107	16	2	8.51e-14	8.94e-14	9.52e-14	1.03e-13	1.12e-13	1.23e-13	1.35e-13	1.47e-13
108	16	3	1.33e-13	1.34e-13	1.33e-13	1.34e-13	1.37e-13	1.40e-13	1.44e-13	1.48e-13
109	16	4	2.83e-14	3.93e-14	4.48e-14	4.69e-14	4.82e-14	4.93e-14	5.06e-14	5.22e-14
110	16	5	1.52e-12	1.54e-12	1.58e-12	1.64e-12	1.71e-12	1.80e-12	1.89e-12	1.99e-12
111	16	6	2.20e-13	2.73e-13	3.07e-13	3.44e-13	3.85e-13	4.30e-13	4.78e-13	5.28e-13
112	16	7	9.42e-13	9.89e-13	1.01e-12	1.03e-12	1.06e-12	1.10e-12	1.14e-12	1.18e-12
113	16	8	3.47e-12	3.81e-12	3.93e-12	4.02e-12	4.09e-12	4.16e-12	4.23e-12	4.28e-12
114	16	9	6.51e-13	6.50e-13	6.28e-13	6.20e-13	6.24e-13	6.37e-13	6.55e-13	6.78e-13
115	16	10	1.26e-12	1.57e-12	1.71e-12	1.83e-12	1.94e-12	2.05e-12	2.15e-12	2.25e-12
116	16	11	8.59e-12	9.01e-12	9.08e-12	9.30e-12	9.62e-12	1.00e-11	1.04e-11	1.09e-11
117	16	12	2.80e-11	3.06e-11	3.03e-11	2.97e-11	2.91e-11	2.85e-11	2.79e-11	2.74e-11
118	16	13	1.34e-12	2.91e-12	3.23e-12	3.28e-12	3.32e-12	3.38e-12	3.48e-12	3.62e-12
119	16	14	6.51e-13	6.48e-13	5.82e-13	5.41e-13	5.17e-13	5.02e-13	4.92e-13	4.86e-13
120	16	15	1.01e-11	9.55e-12	9.26e-12	9.24e-12	9.40e-12	9.68e-12	1.00e-11	1.04e-11
121	17	1	1.22e-14	1.38e-14	1.52e-14	1.71e-14	1.95e-14	2.23e-14	2.55e-14	2.92e-14
122	17	2	1.60e-13	1.47e-13	1.43e-13	1.43e-13	1.46e-13	1.51e-13	1.56e-13	1.62e-13
123	17	3	1.26e-13	1.50e-13	1.72e-13	1.94e-13	2.21e-13	2.52e-13	2.88e-13	3.29e-13
124	17	4	1.31e-13	1.26e-13	1.29e-13	1.36e-13	1.44e-13	1.53e-13	1.62e-13	1.73e-13
125	17	5	5.61e-14	5.99e-14	5.94e-14	6.14e-14	6.59e-14	7.25e-14	8.09e-14	9.10e-14
126	17	6	7.41e-12	6.81e-12	6.61e-12	6.63e-12	6.76e-12	6.95e-12	7.19e-12	7.45e-12
127	17	7	1.69e-13	2.27e-13	2.15e-13	2.10e-13	2.16e-13	2.30e-13	2.52e-13	2.79e-13
128	17	8	7.96e-14	8.41e-14	7.39e-14	6.68e-14	6.30e-14	6.14e-14	6.16e-14	6.30e-14
129	17	9	9.69e-12	1.05e-11	1.06e-11	1.06e-11	1.06e-11	1.06e-11	1.06e-11	1.07e-11
130	17	10	1.94e-12	2.05e-12	2.10e-12	2.21e-12	2.35e-12	2.51e-12	2.68e-12	2.86e-12
131	17	11	5.96e-13	7.46e-13	6.84e-13	6.24e-13	5.83e-13	5.59e-13	5.48e-13	5.48e-13
132	17	12	3.48e-13	3.78e-13	3.43e-13	3.16e-13	3.02e-13	2.97e-13	2.98e-13	3.04e-13
133	17	13	2.70e-16	1.09e-14	2.06e-14	2.57e-14	2.87e-14	3.08e-14	3.27e-14	3.46e-14
134	17	14	1.99e-11	1.93e-11	1.90e-11	1.90e-11	1.94e-11	1.98e-11	2.04e-11	2.11e-11
135	17	15	8.48e-13	1.24e-12	1.15e-12	1.03e-12	9.38e-13	8.68e-13	8.18e-13	7.82e-13
136	17	16	4.44e-15	1.42e-13	2.60e-13	3.34e-13	3.88e-13	4.36e-13	4.81e-13	5.26e-13
137	18	1	1.01e-15	7.40e-16	6.61e-16	6.33e-16	6.27e-16	6.29e-16	6.36e-16	6.46e-16
138	18	2	4.81e-15	6.64e-15	7.59e-15	8.40e-15	9.20e-15	1.00e-14	1.09e-14	1.19e-14
139	18	3	3.75e-14	3.18e-14	2.90e-14	2.80e-14	2.77e-14	2.79e-14	2.84e-14	2.92e-14
140	18	4	3.10e-14	4.07e-14	4.93e-14	5.82e-14	6.78e-14	7.83e-14	8.96e-14	1.02e-13
141	18	5	1.87e-13	1.81e-13	1.81e-13	1.86e-13	1.93e-13	2.01e-13	2.10e-13	2.18e-13
142	18	6	2.62e-13	2.67e-13	2.70e-13	2.76e-13	2.85e-13	2.94e-13	3.04e-13	3.14e-13
143	18	7	2.39e-12	2.37e-12	2.36e-12	2.39e-12	2.45e-12	2.54e-12	2.63e-12	2.73e-12
144	18	8	1.76e-13	1.14e-13	9.14e-14	8.42e-14	8.46e-14	8.96e-14	9.78e-14	1.09e-13
145	18	9	4.84e-13	3.93e-13	3.61e-13	3.53e-13	3.57e-13	3.68e-13	3.83e-13	4.02e-13
146	18	10	6.56e-12	7.26e-12	7.59e-12	7.91e-12	8.23e-12	8.53e-12	8.82e-12	9.10e-12
147	18	11	4.35e-12	3.81e-12	3.68e-12	3.76e-12	3.93e-12	4.15e-12	4.39e-12	4.66e-12
148	18	12	9.36e-13	7.25e-13	6.19e-13	5.60e-13	5.27e-13	5.11e-13	5.07e-13	5.13e-13
149	18	13	1.57e-13	1.93e-13	1.58e-13	1.33e-13	1.17e-13	1.08e-13	1.03e-13	1.01e-13
150	18	14	6.89e-12	7.64e-12	7.83e-12	8.00e-12	8.16e-12	8.32e-12	8.45e-12	8.56e-12
151	18	15	1.25e-11	1.10e-11	1.03e-11	1.00e-11	1.00e-11	1.02e-11	1.04e-11	1.07e-11
152	18	16	1.98e-12	1.47e-12	1.19e-12	1.02e-12	9.00e-13	8.19e-13	7.63e-13	7.24e-13
153	18	17	7.01e-12	7.29e-12	7.20e-12	7.22e-12	7.35e-12	7.55e-12	7.80e-12	8.10e-12

154	19	1	3.32e-15	3.85e-15	4.24e-15	4.66e-15	5.12e-15	5.61e-15	6.12e-15	6.63e-15
155	19	2	5.25e-15	4.88e-15	4.59e-15	4.57e-15	4.77e-15	5.13e-15	5.62e-15	6.23e-15
156	19	3	8.12e-14	8.47e-14	8.92e-14	9.55e-14	1.03e-13	1.12e-13	1.21e-13	1.31e-13
157	19	4	3.50e-14	2.54e-14	2.10e-14	1.93e-14	1.89e-14	1.93e-14	2.02e-14	2.13e-14
158	19	5	3.02e-14	2.84e-14	2.88e-14	3.07e-14	3.34e-14	3.66e-14	4.02e-14	4.40e-14
159	19	6	1.83e-13	1.92e-13	2.02e-13	2.17e-13	2.34e-13	2.53e-13	2.73e-13	2.93e-13
160	19	7	3.18e-13	2.50e-13	2.17e-13	2.03e-13	1.98e-13	1.97e-13	1.98e-13	2.00e-13
161	19	8	5.53e-13	5.10e-13	4.99e-13	5.04e-13	5.18e-13	5.36e-13	5.57e-13	5.79e-13
162	19	9	3.45e-13	3.51e-13	3.72e-13	4.05e-13	4.46e-13	4.91e-13	5.37e-13	5.85e-13
163	19	10	1.14e-12	1.19e-12	1.20e-12	1.22e-12	1.27e-12	1.32e-12	1.39e-12	1.46e-12
164	19	11	4.91e-12	5.50e-12	5.87e-12	6.22e-12	6.57e-12	6.90e-12	7.20e-12	7.49e-12
165	19	12	3.11e-12	2.47e-12	2.33e-12	2.34e-12	2.43e-12	2.54e-12	2.68e-12	2.83e-12
166	19	13	8.80e-13	5.29e-13	3.82e-13	3.08e-13	2.66e-13	2.41e-13	2.26e-13	2.19e-13
167	19	14	1.57e-12	1.61e-12	1.65e-12	1.72e-12	1.82e-12	1.93e-12	2.04e-12	2.16e-12
168	19	15	1.16e-11	1.26e-11	1.26e-11	1.26e-11	1.26e-11	1.26e-11	1.25e-11	1.25e-11
169	19	16	1.15e-11	8.89e-12	7.53e-12	6.84e-12	6.49e-12	6.34e-12	6.30e-12	6.33e-12
170	19	17	5.62e-13	7.19e-13	7.41e-13	7.41e-13	7.37e-13	7.32e-13	7.29e-13	7.28e-13
171	19	18	1.04e-11	1.07e-11	1.10e-11	1.15e-11	1.21e-11	1.28e-11	1.36e-11	1.45e-11

Rotational rate coefficients computed for the 20 first rotational energy levels (see previous table) of *ortho*-D₂O in collision with *ortho*-H₂. Rate coefficients are provided for temperatures from 10 to 150 K.

Tran.	Initial	Final	10 K	30 K	50 K	70 K	90 K	110 K	130 K	150 K
1	2	1	1.27e-10	1.41e-10	1.46e-10	1.48e-10	1.48e-10	1.48e-10	1.48e-10	1.48e-10
2	3	1	3.34e-11	3.55e-11	3.50e-11	3.47e-11	3.44e-11	3.44e-11	3.44e-11	3.44e-11
3	3	2	1.78e-10	1.66e-10	1.53e-10	1.42e-10	1.34e-10	1.28e-10	1.23e-10	1.19e-10
4	4	1	1.71e-11	2.02e-11	2.02e-11	1.98e-11	1.94e-11	1.90e-11	1.86e-11	1.82e-11
5	4	2	9.48e-11	1.08e-10	1.09e-10	1.08e-10	1.07e-10	1.06e-10	1.05e-10	1.04e-10
6	4	3	2.14e-10	2.40e-10	2.40e-10	2.37e-10	2.34e-10	2.31e-10	2.28e-10	2.26e-10
7	5	1	7.77e-12	9.30e-12	1.06e-11	1.16e-11	1.25e-11	1.31e-11	1.37e-11	1.42e-11
8	5	2	6.65e-11	8.28e-11	9.26e-11	9.93e-11	1.04e-10	1.08e-10	1.11e-10	1.13e-10
9	5	3	3.91e-11	3.89e-11	3.60e-11	3.33e-11	3.10e-11	2.92e-11	2.78e-11	2.66e-11
10	5	4	1.14e-10	1.29e-10	1.34e-10	1.36e-10	1.36e-10	1.36e-10	1.35e-10	1.34e-10
11	6	1	5.53e-12	6.92e-12	7.10e-12	7.07e-12	7.03e-12	7.01e-12	7.03e-12	7.09e-12
12	6	2	2.56e-11	2.83e-11	2.86e-11	2.86e-11	2.86e-11	2.87e-11	2.88e-11	2.89e-11
13	6	3	1.15e-10	1.35e-10	1.42e-10	1.45e-10	1.47e-10	1.49e-10	1.49e-10	1.50e-10
14	6	4	8.85e-11	9.02e-11	8.26e-11	7.54e-11	6.93e-11	6.45e-11	6.05e-11	5.71e-11
15	6	5	5.69e-11	6.05e-11	5.55e-11	5.05e-11	4.65e-11	4.33e-11	4.08e-11	3.88e-11
16	7	1	7.29e-13	6.73e-13	5.94e-13	5.40e-13	5.04e-13	4.80e-13	4.64e-13	4.53e-13
17	7	2	9.58e-12	1.07e-11	1.10e-11	1.13e-11	1.15e-11	1.17e-11	1.20e-11	1.22e-11
18	7	3	3.10e-11	3.27e-11	3.37e-11	3.43e-11	3.47e-11	3.50e-11	3.52e-11	3.54e-11
19	7	4	5.71e-11	6.53e-11	7.14e-11	7.63e-11	8.03e-11	8.36e-11	8.64e-11	8.86e-11
20	7	5	8.31e-11	9.64e-11	9.74e-11	9.64e-11	9.51e-11	9.38e-11	9.26e-11	9.16e-11
21	7	6	1.04e-10	1.14e-10	1.17e-10	1.18e-10	1.18e-10	1.17e-10	1.16e-10	1.15e-10
22	8	1	6.31e-13	6.65e-13	6.98e-13	7.31e-13	7.64e-13	7.97e-13	8.29e-13	8.60e-13
23	8	2	5.72e-12	6.24e-12	6.83e-12	7.45e-12	8.04e-12	8.60e-12	9.11e-12	9.59e-12
24	8	3	3.08e-12	2.92e-12	2.90e-12	2.91e-12	2.93e-12	2.96e-12	3.00e-12	3.03e-12
25	8	4	8.81e-12	9.76e-12	1.03e-11	1.08e-11	1.12e-11	1.15e-11	1.18e-11	1.20e-11
26	8	5	6.98e-11	7.90e-11	8.61e-11	9.26e-11	9.84e-11	1.04e-10	1.08e-10	1.12e-10
27	8	6	8.64e-12	7.86e-12	7.41e-12	7.12e-12	6.94e-12	6.81e-12	6.72e-12	6.66e-12
28	8	7	8.76e-11	9.52e-11	9.69e-11	9.71e-11	9.68e-11	9.64e-11	9.59e-11	9.55e-11
29	9	1	2.17e-12	2.29e-12	2.23e-12	2.17e-12	2.12e-12	2.09e-12	2.08e-12	2.07e-12
30	9	2	7.96e-12	8.36e-12	8.18e-12	8.02e-12	7.93e-12	7.91e-12	7.94e-12	8.00e-12
31	9	3	2.90e-11	3.19e-11	3.37e-11	3.52e-11	3.65e-11	3.78e-11	3.88e-11	3.98e-11
32	9	4	2.62e-11	2.64e-11	2.51e-11	2.38e-11	2.28e-11	2.20e-11	2.14e-11	2.09e-11
33	9	5	1.80e-11	1.59e-11	1.30e-11	1.10e-11	9.62e-12	8.64e-12	7.94e-12	7.43e-12
34	9	6	1.24e-10	1.37e-10	1.43e-10	1.47e-10	1.49e-10	1.51e-10	1.52e-10	1.52e-10
35	9	7	4.92e-11	5.05e-11	4.50e-11	3.98e-11	3.56e-11	3.22e-11	2.94e-11	2.72e-11
36	9	8	1.89e-14	8.53e-13	1.61e-12	2.00e-12	2.19e-12	2.29e-12	2.35e-12	2.40e-12
37	10	1	1.02e-12	1.02e-12	9.98e-13	9.84e-13	9.77e-13	9.74e-13	9.73e-13	9.74e-13
38	10	2	4.96e-12	5.01e-12	4.84e-12	4.69e-12	4.56e-12	4.46e-12	4.37e-12	4.29e-12
39	10	3	1.24e-11	1.33e-11	1.33e-11	1.33e-11	1.33e-11	1.33e-11	1.33e-11	1.33e-11
40	10	4	2.39e-11	2.78e-11	3.09e-11	3.35e-11	3.59e-11	3.80e-11	3.98e-11	4.14e-11
41	10	5	2.28e-11	2.19e-11	2.04e-11	1.92e-11	1.83e-11	1.76e-11	1.70e-11	1.65e-11
42	10	6	5.72e-11	6.33e-11	6.42e-11	6.43e-11	6.41e-11	6.38e-11	6.35e-11	6.31e-11
43	10	7	7.42e-11	7.60e-11	7.41e-11	7.19e-11	6.99e-11	6.81e-11	6.66e-11	6.52e-11
44	10	8	2.27e-12	8.45e-12	9.75e-12	9.72e-12	9.37e-12	8.95e-12	8.56e-12	8.21e-12
45	10	9	1.45e-10	1.57e-10	1.59e-10	1.58e-10	1.57e-10	1.55e-10	1.54e-10	1.52e-10
46	11	1	2.74e-13	3.26e-13	3.66e-13	4.02e-13	4.37e-13	4.72e-13	5.07e-13	5.43e-13
47	11	2	1.27e-12	1.42e-12	1.49e-12	1.56e-12	1.63e-12	1.71e-12	1.78e-12	1.86e-12
48	11	3	4.88e-12	6.48e-12	7.75e-12	8.85e-12	9.82e-12	1.07e-11	1.14e-11	1.21e-11
49	11	4	9.09e-12	1.02e-11	1.05e-11	1.07e-11	1.08e-11	1.09e-11	1.11e-11	1.12e-11
50	11	5	1.49e-11	1.73e-11	1.89e-11	2.02e-11	2.13e-11	2.22e-11	2.30e-11	2.37e-11
51	11	6	2.83e-11	3.29e-11	3.51e-11	3.66e-11	3.78e-11	3.88e-11	3.96e-11	4.04e-11

52	11	7	5.56e-11	6.83e-11	7.32e-11	7.56e-11	7.70e-11	7.78e-11	7.83e-11	7.85e-11
53	11	8	5.39e-11	5.76e-11	5.42e-11	5.04e-11	4.71e-11	4.44e-11	4.22e-11	4.03e-11
54	11	9	3.39e-11	3.63e-11	3.48e-11	3.29e-11	3.11e-11	2.94e-11	2.81e-11	2.68e-11
55	11	10	1.39e-10	1.68e-10	1.82e-10	1.88e-10	1.91e-10	1.92e-10	1.93e-10	1.93e-10
56	12	1	6.03e-14	7.16e-14	7.67e-14	7.98e-14	8.21e-14	8.43e-14	8.64e-14	8.84e-14
57	12	2	6.37e-13	6.67e-13	6.95e-13	7.28e-13	7.65e-13	8.06e-13	8.50e-13	8.96e-13
58	12	3	1.54e-12	1.66e-12	1.77e-12	1.88e-12	2.00e-12	2.12e-12	2.24e-12	2.36e-12
59	12	4	3.62e-12	4.19e-12	4.84e-12	5.49e-12	6.13e-12	6.73e-12	7.29e-12	7.82e-12
60	12	5	5.38e-12	6.13e-12	6.50e-12	6.78e-12	7.04e-12	7.30e-12	7.56e-12	7.82e-12
61	12	6	5.34e-12	6.11e-12	6.63e-12	7.04e-12	7.40e-12	7.71e-12	7.99e-12	8.23e-12
62	12	7	3.94e-11	4.68e-11	5.21e-11	5.67e-11	6.09e-11	6.47e-11	6.80e-11	7.11e-11
63	12	8	7.29e-11	8.96e-11	9.48e-11	9.67e-11	9.73e-11	9.74e-11	9.73e-11	9.71e-11
64	12	9	5.98e-12	5.51e-12	5.20e-12	5.03e-12	4.93e-12	4.86e-12	4.83e-12	4.81e-12
65	12	10	1.65e-11	1.74e-11	1.73e-11	1.70e-11	1.66e-11	1.62e-11	1.59e-11	1.55e-11
66	12	11	8.79e-11	1.09e-10	1.17e-10	1.21e-10	1.23e-10	1.24e-10	1.24e-10	1.24e-10
67	13	1	3.05e-14	2.83e-14	2.87e-14	3.00e-14	3.17e-14	3.38e-14	3.61e-14	3.86e-14
68	13	2	3.15e-13	3.40e-13	3.65e-13	3.95e-13	4.27e-13	4.61e-13	4.96e-13	5.32e-13
69	13	3	1.37e-13	1.36e-13	1.38e-13	1.43e-13	1.49e-13	1.56e-13	1.65e-13	1.74e-13
70	13	4	5.29e-13	5.52e-13	5.80e-13	6.13e-13	6.51e-13	6.92e-13	7.35e-13	7.78e-13
71	13	5	5.25e-12	5.57e-12	5.96e-12	6.42e-12	6.92e-12	7.42e-12	7.93e-12	8.42e-12
72	13	6	5.97e-13	5.75e-13	5.82e-13	6.00e-13	6.25e-13	6.53e-13	6.83e-13	7.14e-13
73	13	7	4.97e-12	5.46e-12	5.80e-12	6.11e-12	6.42e-12	6.71e-12	6.99e-12	7.26e-12
74	13	8	6.23e-11	6.75e-11	7.17e-11	7.62e-11	8.08e-11	8.53e-11	8.96e-11	9.37e-11
75	13	9	5.96e-13	5.31e-13	5.12e-13	5.08e-13	5.13e-13	5.22e-13	5.34e-13	5.49e-13
76	13	10	1.54e-12	1.33e-12	1.26e-12	1.24e-12	1.24e-12	1.25e-12	1.27e-12	1.29e-12
77	13	11	5.85e-12	5.74e-12	5.72e-12	5.73e-12	5.77e-12	5.82e-12	5.88e-12	5.94e-12
78	13	12	5.94e-11	6.88e-11	7.21e-11	7.37e-11	7.46e-11	7.52e-11	7.56e-11	7.60e-11
79	14	1	4.15e-13	4.44e-13	4.51e-13	4.56e-13	4.63e-13	4.72e-13	4.82e-13	4.94e-13
80	14	2	2.04e-12	2.14e-12	2.13e-12	2.13e-12	2.14e-12	2.17e-12	2.21e-12	2.25e-12
81	14	3	6.39e-12	6.68e-12	6.91e-12	7.19e-12	7.53e-12	7.90e-12	8.30e-12	8.71e-12
82	14	4	3.92e-12	3.97e-12	3.88e-12	3.81e-12	3.77e-12	3.77e-12	3.79e-12	3.84e-12
83	14	5	3.29e-12	3.27e-12	3.02e-12	2.81e-12	2.66e-12	2.55e-12	2.48e-12	2.44e-12
84	14	6	1.79e-11	2.16e-11	2.39e-11	2.57e-11	2.74e-11	2.89e-11	3.02e-11	3.13e-11
85	14	7	1.53e-11	1.59e-11	1.50e-11	1.42e-11	1.36e-11	1.32e-11	1.28e-11	1.26e-11
86	14	8	4.66e-12	4.92e-12	4.24e-12	3.64e-12	3.20e-12	2.89e-12	2.67e-12	2.50e-12
87	14	9	9.03e-11	1.14e-10	1.27e-10	1.36e-10	1.42e-10	1.47e-10	1.51e-10	1.54e-10
88	14	10	5.76e-11	5.78e-11	5.40e-11	5.01e-11	4.66e-11	4.35e-11	4.09e-11	3.87e-11
89	14	11	2.72e-11	3.13e-11	2.90e-11	2.65e-11	2.44e-11	2.28e-11	2.15e-11	2.05e-11
90	14	12	7.12e-14	1.87e-12	3.08e-12	3.58e-12	3.76e-12	3.82e-12	3.82e-12	3.80e-12
91	14	13	3.12e-19	4.47e-15	2.92e-14	6.47e-14	1.01e-13	1.37e-13	1.69e-13	2.01e-13
92	15	1	8.73e-14	8.42e-14	8.24e-14	8.18e-14	8.21e-14	8.30e-14	8.43e-14	8.59e-14
93	15	2	8.69e-13	9.26e-13	9.47e-13	9.73e-13	1.00e-12	1.04e-12	1.07e-12	1.11e-12
94	15	3	9.43e-13	8.70e-13	8.39e-13	8.46e-13	8.75e-13	9.16e-13	9.65e-13	1.02e-12
95	15	4	2.30e-12	2.41e-12	2.56e-12	2.77e-12	3.01e-12	3.28e-12	3.56e-12	3.85e-12
96	15	5	3.14e-12	3.35e-12	3.38e-12	3.39e-12	3.42e-12	3.45e-12	3.49e-12	3.54e-12
97	15	6	4.83e-12	4.48e-12	4.33e-12	4.29e-12	4.32e-12	4.37e-12	4.43e-12	4.51e-12
98	15	7	1.29e-11	1.58e-11	1.77e-11	1.93e-11	2.08e-11	2.22e-11	2.34e-11	2.45e-11
99	15	8	1.23e-11	1.34e-11	1.26e-11	1.19e-11	1.12e-11	1.07e-11	1.03e-11	1.00e-11
100	15	9	2.60e-11	3.01e-11	3.22e-11	3.37e-11	3.50e-11	3.62e-11	3.71e-11	3.79e-11
101	15	10	3.41e-11	4.23e-11	4.81e-11	5.30e-11	5.73e-11	6.09e-11	6.40e-11	6.68e-11
102	15	11	4.79e-11	5.62e-11	5.78e-11	5.78e-11	5.72e-11	5.64e-11	5.55e-11	5.46e-11

103	15	12	4.33e-11	5.09e-11	4.99e-11	4.76e-11	4.54e-11	4.35e-11	4.18e-11	4.04e-11
104	15	13	2.89e-15	4.33e-13	1.11e-12	1.61e-12	1.94e-12	2.18e-12	2.36e-12	2.50e-12
105	15	14	9.46e-11	1.06e-10	1.08e-10	1.09e-10	1.10e-10	1.10e-10	1.09e-10	1.09e-10
106	16	1	1.24e-13	1.36e-13	1.49e-13	1.63e-13	1.78e-13	1.93e-13	2.08e-13	2.23e-13
107	16	2	2.70e-13	2.79e-13	2.99e-13	3.22e-13	3.48e-13	3.77e-13	4.07e-13	4.39e-13
108	16	3	3.60e-13	3.75e-13	3.96e-13	4.22e-13	4.52e-13	4.85e-13	5.18e-13	5.53e-13
109	16	4	3.70e-13	3.59e-13	3.58e-13	3.66e-13	3.80e-13	3.98e-13	4.18e-13	4.39e-13
110	16	5	1.77e-12	1.74e-12	1.83e-12	1.95e-12	2.10e-12	2.26e-12	2.43e-12	2.60e-12
111	16	6	2.09e-12	2.43e-12	2.74e-12	3.08e-12	3.42e-12	3.77e-12	4.12e-12	4.46e-12
112	16	7	3.69e-12	3.95e-12	4.12e-12	4.27e-12	4.44e-12	4.60e-12	4.77e-12	4.95e-12
113	16	8	1.37e-11	1.28e-11	1.31e-11	1.37e-11	1.44e-11	1.50e-11	1.56e-11	1.62e-11
114	16	9	3.74e-12	3.92e-12	4.06e-12	4.21e-12	4.36e-12	4.52e-12	4.67e-12	4.81e-12
115	16	10	1.15e-11	1.31e-11	1.40e-11	1.48e-11	1.55e-11	1.61e-11	1.67e-11	1.72e-11
116	16	11	2.91e-11	3.38e-11	3.73e-11	4.08e-11	4.41e-11	4.72e-11	5.01e-11	5.27e-11
117	16	12	6.10e-11	7.32e-11	7.85e-11	8.13e-11	8.29e-11	8.39e-11	8.44e-11	8.48e-11
118	16	13	2.36e-11	3.46e-11	3.56e-11	3.48e-11	3.36e-11	3.23e-11	3.12e-11	3.02e-11
119	16	14	6.56e-12	6.42e-12	6.05e-12	5.82e-12	5.68e-12	5.59e-12	5.53e-12	5.48e-12
120	16	15	8.08e-11	1.02e-10	1.11e-10	1.16e-10	1.19e-10	1.21e-10	1.22e-10	1.23e-10
121	17	1	1.33e-13	1.33e-13	1.37e-13	1.43e-13	1.52e-13	1.64e-13	1.78e-13	1.93e-13
122	17	2	4.96e-13	5.06e-13	5.06e-13	5.12e-13	5.24e-13	5.40e-13	5.59e-13	5.79e-13
123	17	3	2.42e-12	2.50e-12	2.53e-12	2.57e-12	2.63e-12	2.69e-12	2.76e-12	2.83e-12
124	17	4	1.37e-12	1.30e-12	1.21e-12	1.15e-12	1.12e-12	1.10e-12	1.10e-12	1.10e-12
125	17	5	7.92e-13	7.83e-13	7.27e-13	6.96e-13	6.88e-13	6.95e-13	7.13e-13	7.40e-13
126	17	6	8.40e-12	8.21e-12	8.29e-12	8.54e-12	8.90e-12	9.32e-12	9.78e-12	1.03e-11
127	17	7	1.98e-12	2.33e-12	2.30e-12	2.27e-12	2.27e-12	2.29e-12	2.33e-12	2.38e-12
128	17	8	1.59e-12	1.52e-12	1.22e-12	1.01e-12	8.81e-13	7.94e-13	7.37e-13	7.00e-13
129	17	9	1.71e-11	1.95e-11	2.14e-11	2.31e-11	2.48e-11	2.64e-11	2.79e-11	2.92e-11
130	17	10	1.32e-11	1.33e-11	1.28e-11	1.23e-11	1.21e-11	1.19e-11	1.18e-11	1.18e-11
131	17	11	7.70e-12	7.80e-12	7.00e-12	6.30e-12	5.78e-12	5.41e-12	5.14e-12	4.94e-12
132	17	12	5.63e-12	5.76e-12	4.77e-12	4.01e-12	3.48e-12	3.11e-12	2.85e-12	2.66e-12
133	17	13	4.32e-15	1.11e-13	1.79e-13	2.06e-13	2.17e-13	2.22e-13	2.26e-13	2.30e-13
134	17	14	8.38e-11	1.06e-10	1.18e-10	1.27e-10	1.34e-10	1.40e-10	1.45e-10	1.49e-10
135	17	15	5.47e-11	5.32e-11	4.85e-11	4.42e-11	4.06e-11	3.76e-11	3.50e-11	3.28e-11
136	17	16	8.28e-14	2.13e-12	3.39e-12	3.82e-12	3.94e-12	3.93e-12	3.89e-12	3.84e-12
137	18	1	1.62e-14	1.50e-14	1.37e-14	1.31e-14	1.29e-14	1.29e-14	1.31e-14	1.34e-14
138	18	2	1.39e-13	1.34e-13	1.28e-13	1.26e-13	1.27e-13	1.29e-13	1.33e-13	1.38e-13
139	18	3	8.34e-13	7.90e-13	7.79e-13	7.90e-13	8.12e-13	8.39e-13	8.68e-13	8.99e-13
140	18	4	1.22e-12	1.31e-12	1.33e-12	1.36e-12	1.39e-12	1.43e-12	1.46e-12	1.50e-12
141	18	5	8.37e-13	8.61e-13	8.44e-13	8.39e-13	8.44e-13	8.56e-13	8.72e-13	8.92e-13
142	18	6	1.69e-12	1.59e-12	1.53e-12	1.51e-12	1.52e-12	1.54e-12	1.57e-12	1.60e-12
143	18	7	3.22e-12	3.39e-12	3.39e-12	3.45e-12	3.55e-12	3.68e-12	3.83e-12	4.00e-12
144	18	8	1.40e-12	1.35e-12	1.26e-12	1.21e-12	1.20e-12	1.21e-12	1.23e-12	1.27e-12
145	18	9	5.43e-12	5.08e-12	4.79e-12	4.68e-12	4.66e-12	4.69e-12	4.75e-12	4.82e-12
146	18	10	1.74e-11	1.96e-11	2.14e-11	2.34e-11	2.54e-11	2.74e-11	2.93e-11	3.11e-11
147	18	11	1.74e-11	1.76e-11	1.73e-11	1.72e-11	1.73e-11	1.74e-11	1.75e-11	1.77e-11
148	18	12	7.96e-12	7.88e-12	7.00e-12	6.32e-12	5.84e-12	5.50e-12	5.25e-12	5.07e-12
149	18	13	1.34e-12	1.74e-12	1.57e-12	1.37e-12	1.22e-12	1.12e-12	1.04e-12	9.82e-13
150	18	14	2.89e-11	3.27e-11	3.36e-11	3.44e-11	3.52e-11	3.60e-11	3.67e-11	3.74e-11
151	18	15	4.33e-11	4.84e-11	5.22e-11	5.58e-11	5.91e-11	6.19e-11	6.43e-11	6.64e-11
152	18	16	3.35e-11	3.58e-11	3.32e-11	3.03e-11	2.78e-11	2.57e-11	2.39e-11	2.24e-11
153	18	17	1.02e-10	1.11e-10	1.11e-10	1.11e-10	1.10e-10	1.09e-10	1.08e-10	1.08e-10

154	19	1	1.18e-14	1.29e-14	1.40e-14	1.55e-14	1.71e-14	1.89e-14	2.08e-14	2.28e-14
155	19	2	6.22e-14	6.30e-14	6.32e-14	6.52e-14	6.85e-14	7.29e-14	7.79e-14	8.35e-14
156	19	3	2.06e-13	2.28e-13	2.47e-13	2.70e-13	2.98e-13	3.30e-13	3.64e-13	4.01e-13
157	19	4	4.41e-13	4.87e-13	5.14e-13	5.44e-13	5.77e-13	6.11e-13	6.47e-13	6.83e-13
158	19	5	4.62e-13	4.81e-13	4.89e-13	5.02e-13	5.17e-13	5.32e-13	5.47e-13	5.62e-13
159	19	6	3.14e-13	3.64e-13	3.89e-13	4.14e-13	4.42e-13	4.73e-13	5.05e-13	5.39e-13
160	19	7	1.78e-12	1.87e-12	1.89e-12	1.93e-12	1.97e-12	2.02e-12	2.06e-12	2.11e-12
161	19	8	1.99e-12	1.93e-12	1.83e-12	1.78e-12	1.75e-12	1.75e-12	1.76e-12	1.79e-12
162	19	9	1.84e-12	2.32e-12	2.70e-12	3.09e-12	3.47e-12	3.84e-12	4.20e-12	4.55e-12
163	19	10	5.79e-12	6.81e-12	7.37e-12	7.85e-12	8.29e-12	8.71e-12	9.10e-12	9.47e-12
164	19	11	1.17e-11	1.41e-11	1.62e-11	1.84e-11	2.06e-11	2.27e-11	2.47e-11	2.65e-11
165	19	12	1.24e-11	1.29e-11	1.25e-11	1.22e-11	1.21e-11	1.20e-11	1.19e-11	1.19e-11
166	19	13	8.08e-12	6.38e-12	4.88e-12	3.99e-12	3.43e-12	3.06e-12	2.81e-12	2.63e-12
167	19	14	9.14e-12	1.00e-11	1.04e-11	1.07e-11	1.10e-11	1.13e-11	1.16e-11	1.19e-11
168	19	15	3.41e-11	3.84e-11	4.07e-11	4.24e-11	4.39e-11	4.52e-11	4.62e-11	4.71e-11
169	19	16	3.93e-11	4.75e-11	4.85e-11	4.83e-11	4.78e-11	4.73e-11	4.68e-11	4.63e-11
170	19	17	1.31e-11	1.58e-11	1.57e-11	1.52e-11	1.45e-11	1.40e-11	1.35e-11	1.30e-11
171	19	18	1.65e-10	1.99e-10	2.10e-10	2.14e-10	2.15e-10	2.14e-10	2.13e-10	2.11e-10

Table of rotational energy levels of *para*-D₂O, for which scattering calculations were performed in this work.

Nr	j	k _a	k _c	Energy (cm ⁻¹)
1	1	0	1	12.1182
2	1	1	0	22.6929
3	2	1	2	42.0741
4	2	2	1	73.7982
5	3	0	3	70.4812
6	3	1	2	89.0282
7	3	2	1	112.3814
8	3	3	0	157.2826
9	4	1	4	117.3512
10	4	2	3	158.2601
11	4	3	2	206.4843
12	4	4	1	271.3223
13	5	0	5	169.1638
14	5	1	4	205.2484
15	5	2	3	230.3772
16	5	3	2	269.6712
17	6	1	5	233.2780
18	6	2	4	288.4815
19	7	1	7	305.8108

Rotational rate coefficients computed for the 20 first rotational energy levels (see previous table) of *para*-D₂O in collision with *para*-H₂. Rate coefficients are provided for temperatures from 10 to 150 K.

Tran.	Initial	Final	10 K	30 K	50 K	70 K	90 K	110 K	130 K	150 K
1	2	1	2.38e-11	2.14e-11	1.91e-11	1.82e-11	1.82e-11	1.87e-11	1.94e-11	2.03e-11
2	3	1	2.40e-11	2.00e-11	1.80e-11	1.72e-11	1.70e-11	1.73e-11	1.77e-11	1.83e-11
3	3	2	3.52e-11	3.57e-11	3.14e-11	2.80e-11	2.55e-11	2.37e-11	2.23e-11	2.11e-11
4	4	1	1.09e-11	1.22e-11	1.18e-11	1.13e-11	1.09e-11	1.06e-11	1.03e-11	1.01e-11
5	4	2	1.43e-11	1.28e-11	1.24e-11	1.25e-11	1.28e-11	1.32e-11	1.37e-11	1.43e-11
6	4	3	1.03e-11	1.03e-11	9.09e-12	8.57e-12	8.46e-12	8.57e-12	8.83e-12	9.18e-12
7	5	1	2.44e-11	2.47e-11	2.35e-11	2.24e-11	2.16e-11	2.09e-11	2.03e-11	1.99e-11
8	5	2	4.58e-12	5.45e-12	5.49e-12	5.51e-12	5.59e-12	5.74e-12	5.93e-12	6.17e-12
9	5	3	1.37e-11	1.37e-11	1.26e-11	1.19e-11	1.17e-11	1.17e-11	1.19e-11	1.22e-11
10	5	4	4.14e-12	4.21e-12	3.44e-12	2.88e-12	2.49e-12	2.21e-12	2.02e-12	1.87e-12
11	6	1	9.78e-13	7.84e-13	7.21e-13	7.11e-13	7.26e-13	7.55e-13	7.92e-13	8.35e-13
12	6	2	1.64e-11	1.87e-11	1.89e-11	1.88e-11	1.86e-11	1.84e-11	1.82e-11	1.80e-11
13	6	3	3.99e-11	4.35e-11	4.22e-11	4.05e-11	3.89e-11	3.75e-11	3.63e-11	3.52e-11
14	6	4	1.02e-11	7.74e-12	6.72e-12	6.20e-12	5.95e-12	5.87e-12	5.90e-12	6.01e-12
15	6	5	1.16e-11	1.15e-11	1.19e-11	1.24e-11	1.32e-11	1.40e-11	1.49e-11	1.58e-11
16	7	1	3.20e-12	3.86e-12	4.10e-12	4.27e-12	4.40e-12	4.52e-12	4.62e-12	4.70e-12
17	7	2	8.26e-13	9.34e-13	8.46e-13	7.93e-13	7.73e-13	7.74e-13	7.90e-13	8.14e-13
18	7	3	7.41e-12	7.82e-12	8.01e-12	8.26e-12	8.57e-12	8.92e-12	9.30e-12	9.70e-12
19	7	4	5.11e-11	5.65e-11	5.41e-11	5.14e-11	4.90e-11	4.69e-11	4.52e-11	4.37e-11
20	7	5	5.69e-12	7.23e-12	6.71e-12	6.09e-12	5.58e-12	5.16e-12	4.82e-12	4.54e-12
21	7	6	9.17e-12	1.04e-11	1.07e-11	1.11e-11	1.17e-11	1.24e-11	1.31e-11	1.39e-11
22	8	1	1.56e-13	1.75e-13	1.68e-13	1.63e-13	1.62e-13	1.63e-13	1.66e-13	1.69e-13
23	8	2	7.11e-13	8.78e-13	9.84e-13	1.09e-12	1.19e-12	1.28e-12	1.37e-12	1.46e-12
24	8	3	8.59e-13	1.07e-12	1.11e-12	1.14e-12	1.17e-12	1.20e-12	1.23e-12	1.26e-12
25	8	4	1.70e-11	1.62e-11	1.57e-11	1.57e-11	1.60e-11	1.64e-11	1.69e-11	1.75e-11
26	8	5	5.43e-13	5.66e-13	5.36e-13	5.17e-13	5.10e-13	5.12e-13	5.20e-13	5.31e-13
27	8	6	1.72e-12	2.07e-12	1.95e-12	1.82e-12	1.71e-12	1.63e-12	1.57e-12	1.52e-12
28	8	7	8.64e-12	1.11e-11	1.08e-11	1.05e-11	1.04e-11	1.05e-11	1.08e-11	1.11e-11
29	9	1	3.86e-12	3.66e-12	3.70e-12	3.84e-12	4.04e-12	4.27e-12	4.51e-12	4.76e-12
30	9	2	2.18e-13	2.70e-13	2.43e-13	2.31e-13	2.34e-13	2.52e-13	2.80e-13	3.18e-13
31	9	3	1.67e-11	1.70e-11	1.61e-11	1.54e-11	1.49e-11	1.45e-11	1.42e-11	1.39e-11
32	9	4	1.97e-12	2.49e-12	2.37e-12	2.26e-12	2.22e-12	2.22e-12	2.26e-12	2.32e-12
33	9	5	1.50e-11	1.65e-11	1.63e-11	1.62e-11	1.63e-11	1.66e-11	1.70e-11	1.76e-11
34	9	6	3.67e-12	3.97e-12	3.80e-12	3.59e-12	3.40e-12	3.26e-12	3.14e-12	3.04e-12
35	9	7	3.40e-12	3.54e-12	3.18e-12	2.97e-12	2.88e-12	2.88e-12	2.93e-12	3.03e-12
36	9	8	3.58e-15	1.86e-13	3.53e-13	4.31e-13	4.65e-13	4.81e-13	4.91e-13	5.00e-13
37	10	1	1.64e-13	1.96e-13	2.10e-13	2.19e-13	2.29e-13	2.39e-13	2.49e-13	2.61e-13
38	10	2	2.03e-12	2.02e-12	2.04e-12	2.11e-12	2.21e-12	2.33e-12	2.45e-12	2.58e-12
39	10	3	7.00e-13	7.54e-13	7.45e-13	7.38e-13	7.38e-13	7.44e-13	7.54e-13	7.68e-13
40	10	4	7.24e-12	8.13e-12	8.19e-12	8.16e-12	8.12e-12	8.07e-12	8.03e-12	7.99e-12
41	10	5	7.88e-12	9.53e-12	9.99e-12	1.02e-11	1.04e-11	1.05e-11	1.05e-11	1.06e-11
42	10	6	8.53e-12	9.51e-12	9.66e-12	9.86e-12	1.02e-11	1.05e-11	1.10e-11	1.14e-11
43	10	7	2.44e-11	2.69e-11	2.61e-11	2.50e-11	2.40e-11	2.32e-11	2.25e-11	2.19e-11
44	10	8	2.98e-12	4.29e-12	4.15e-12	3.98e-12	3.90e-12	3.92e-12	4.00e-12	4.13e-12
45	10	9	8.20e-12	8.28e-12	7.94e-12	7.82e-12	7.90e-12	8.09e-12	8.35e-12	8.66e-12
46	11	1	1.75e-13	1.70e-13	1.70e-13	1.74e-13	1.79e-13	1.86e-13	1.93e-13	2.00e-13
47	11	2	5.26e-14	7.47e-14	8.36e-14	8.95e-14	9.51e-14	1.01e-13	1.07e-13	1.14e-13
48	11	3	4.56e-13	5.27e-13	5.83e-13	6.46e-13	7.13e-13	7.83e-13	8.55e-13	9.28e-13
49	11	4	2.60e-12	2.67e-12	2.69e-12	2.75e-12	2.84e-12	2.96e-12	3.10e-12	3.25e-12
50	11	5	4.72e-13	4.62e-13	4.38e-13	4.21e-13	4.11e-13	4.08e-13	4.09e-13	4.13e-13
51	11	6	1.17e-12	1.40e-12	1.52e-12	1.62e-12	1.71e-12	1.79e-12	1.86e-12	1.93e-12

52	11	7	1.12e-11	1.11e-11	1.10e-11	1.12e-11	1.15e-11	1.19e-11	1.24e-11	1.28e-11
53	11	8	3.64e-11	4.13e-11	4.07e-11	3.94e-11	3.81e-11	3.70e-11	3.60e-11	3.51e-11
54	11	9	1.00e-12	9.02e-13	8.26e-13	7.77e-13	7.45e-13	7.22e-13	7.06e-13	6.94e-13
55	11	10	8.95e-12	9.11e-12	8.90e-12	8.86e-12	9.00e-12	9.25e-12	9.57e-12	9.95e-12
56	12	1	5.24e-15	6.79e-15	7.96e-15	8.32e-15	8.33e-15	8.26e-15	8.21e-15	8.22e-15
57	12	2	5.41e-14	5.62e-14	5.99e-14	6.36e-14	6.73e-14	7.12e-14	7.51e-14	7.93e-14
58	12	3	2.50e-14	3.36e-14	3.58e-14	3.62e-14	3.66e-14	3.73e-14	3.84e-14	3.99e-14
59	12	4	2.23e-13	2.67e-13	3.03e-13	3.45e-13	3.93e-13	4.46e-13	5.03e-13	5.64e-13
60	12	5	1.87e-14	2.40e-14	2.71e-14	2.85e-14	2.93e-14	3.00e-14	3.09e-14	3.20e-14
61	12	6	7.96e-14	8.67e-14	8.62e-14	8.41e-14	8.24e-14	8.15e-14	8.15e-14	8.21e-14
62	12	7	3.39e-13	4.29e-13	4.73e-13	5.08e-13	5.43e-13	5.82e-13	6.23e-13	6.67e-13
63	12	8	1.89e-11	1.85e-11	1.82e-11	1.83e-11	1.86e-11	1.91e-11	1.96e-11	2.03e-11
64	12	9	1.27e-13	1.22e-13	1.19e-13	1.18e-13	1.19e-13	1.22e-13	1.25e-13	1.29e-13
65	12	10	6.53e-13	6.94e-13	6.76e-13	6.67e-13	6.67e-13	6.76e-13	6.92e-13	7.13e-13
66	12	11	8.14e-12	9.52e-12	9.81e-12	9.95e-12	1.02e-11	1.04e-11	1.08e-11	1.12e-11
67	13	1	7.21e-14	1.17e-13	1.33e-13	1.46e-13	1.63e-13	1.84e-13	2.10e-13	2.39e-13
68	13	2	2.03e-13	1.98e-13	2.03e-13	2.13e-13	2.25e-13	2.38e-13	2.52e-13	2.67e-13
69	13	3	5.42e-12	4.97e-12	4.84e-12	4.88e-12	5.01e-12	5.19e-12	5.41e-12	5.64e-12
70	13	4	2.78e-13	2.27e-13	1.97e-13	1.87e-13	1.89e-13	1.99e-13	2.15e-13	2.37e-13
71	13	5	1.33e-11	1.42e-11	1.39e-11	1.37e-11	1.35e-11	1.33e-11	1.32e-11	1.31e-11
72	13	6	3.28e-12	2.92e-12	2.87e-12	2.95e-12	3.09e-12	3.27e-12	3.46e-12	3.67e-12
73	13	7	1.23e-12	1.16e-12	1.00e-12	8.87e-13	8.15e-13	7.74e-13	7.53e-13	7.48e-13
74	13	8	6.94e-13	6.77e-13	5.29e-13	4.27e-13	3.63e-13	3.23e-13	2.97e-13	2.82e-13
75	13	9	1.82e-11	1.76e-11	1.72e-11	1.72e-11	1.74e-11	1.78e-11	1.82e-11	1.88e-11
76	13	10	1.81e-12	1.68e-12	1.44e-12	1.25e-12	1.12e-12	1.02e-12	9.51e-13	8.99e-13
77	13	11	3.54e-15	1.15e-13	2.20e-13	2.87e-13	3.37e-13	3.80e-13	4.20e-13	4.60e-13
78	13	12	4.82e-20	8.33e-16	5.24e-15	1.12e-14	1.69e-14	2.23e-14	2.74e-14	3.23e-14
79	14	1	3.22e-14	2.78e-14	2.52e-14	2.43e-14	2.42e-14	2.44e-14	2.49e-14	2.55e-14
80	14	2	4.08e-14	6.01e-14	6.97e-14	7.67e-14	8.29e-14	8.88e-14	9.46e-14	1.00e-13
81	14	3	3.92e-13	4.21e-13	4.26e-13	4.30e-13	4.34e-13	4.38e-13	4.42e-13	4.46e-13
82	14	4	1.27e-12	1.22e-12	1.20e-12	1.23e-12	1.27e-12	1.32e-12	1.38e-12	1.44e-12
83	14	5	7.85e-13	6.48e-13	5.99e-13	5.93e-13	6.08e-13	6.36e-13	6.71e-13	7.11e-13
84	14	6	9.64e-12	1.08e-11	1.13e-11	1.16e-11	1.19e-11	1.22e-11	1.25e-11	1.27e-11
85	14	7	3.60e-12	3.25e-12	3.23e-12	3.37e-12	3.57e-12	3.80e-12	4.05e-12	4.31e-12
86	14	8	1.10e-12	7.35e-13	5.64e-13	4.73e-13	4.21e-13	3.91e-13	3.76e-13	3.72e-13
87	14	9	1.21e-11	1.33e-11	1.34e-11	1.35e-11	1.35e-11	1.35e-11	1.35e-11	1.35e-11
88	14	10	1.06e-11	9.15e-12	8.37e-12	8.06e-12	7.99e-12	8.05e-12	8.19e-12	8.38e-12
89	14	11	1.14e-12	1.21e-12	1.07e-12	9.35e-13	8.35e-13	7.62e-13	7.10e-13	6.74e-13
90	14	12	1.32e-17	7.90e-15	2.69e-14	4.47e-14	5.98e-14	7.30e-14	8.51e-14	9.68e-14
91	14	13	8.40e-12	8.58e-12	8.46e-12	8.52e-12	8.73e-12	9.03e-12	9.40e-12	9.81e-12
92	15	1	1.32e-13	1.46e-13	1.57e-13	1.69e-13	1.83e-13	1.97e-13	2.12e-13	2.27e-13
93	15	2	2.18e-14	2.33e-14	2.09e-14	1.95e-14	1.90e-14	1.90e-14	1.94e-14	2.01e-14
94	15	3	3.97e-13	4.09e-13	4.26e-13	4.50e-13	4.80e-13	5.13e-13	5.49e-13	5.85e-13
95	15	4	2.86e-13	3.04e-13	2.86e-13	2.74e-13	2.67e-13	2.63e-13	2.61e-13	2.61e-13
96	15	5	8.31e-13	9.47e-13	1.02e-12	1.10e-12	1.19e-12	1.27e-12	1.35e-12	1.44e-12
97	15	6	7.40e-13	8.26e-13	8.26e-13	8.31e-13	8.50e-13	8.81e-13	9.20e-13	9.65e-13
98	15	7	6.59e-12	7.47e-12	7.85e-12	8.16e-12	8.44e-12	8.68e-12	8.90e-12	9.09e-12
99	15	8	2.02e-12	1.81e-12	1.70e-12	1.68e-12	1.71e-12	1.77e-12	1.84e-12	1.92e-12
100	15	9	2.65e-12	2.73e-12	2.81e-12	2.94e-12	3.11e-12	3.28e-12	3.47e-12	3.66e-12
101	15	10	1.94e-11	2.15e-11	2.13e-11	2.10e-11	2.06e-11	2.03e-11	2.00e-11	1.97e-11
102	15	11	8.97e-12	7.79e-12	6.61e-12	5.96e-12	5.61e-12	5.45e-12	5.40e-12	5.43e-12

103	15	12	1.70e-15	9.52e-14	1.96e-13	2.52e-13	2.80e-13	2.96e-13	3.08e-13	3.19e-13
104	15	13	1.37e-12	1.75e-12	1.77e-12	1.73e-12	1.68e-12	1.63e-12	1.59e-12	1.55e-12
105	15	14	1.03e-11	1.08e-11	1.14e-11	1.21e-11	1.30e-11	1.40e-11	1.49e-11	1.59e-11
106	16	1	2.02e-14	2.19e-14	2.35e-14	2.46e-14	2.57e-14	2.69e-14	2.82e-14	2.97e-14
107	16	2	1.37e-13	1.39e-13	1.47e-13	1.58e-13	1.71e-13	1.86e-13	2.03e-13	2.21e-13
108	16	3	2.29e-14	2.80e-14	3.02e-14	3.12e-14	3.20e-14	3.31e-14	3.44e-14	3.59e-14
109	16	4	1.16e-12	1.19e-12	1.22e-12	1.27e-12	1.33e-12	1.40e-12	1.48e-12	1.56e-12
110	16	5	5.20e-13	5.15e-13	5.18e-13	5.30e-13	5.48e-13	5.69e-13	5.94e-13	6.20e-13
111	16	6	4.49e-13	4.66e-13	5.00e-13	5.50e-13	6.09e-13	6.74e-13	7.41e-13	8.09e-13
112	16	7	4.54e-13	5.42e-13	5.73e-13	5.81e-13	5.89e-13	6.00e-13	6.14e-13	6.32e-13
113	16	8	3.18e-12	3.63e-12	3.80e-12	3.92e-12	4.01e-12	4.10e-12	4.17e-12	4.23e-12
114	16	9	2.81e-13	3.45e-13	3.79e-13	4.14e-13	4.52e-13	4.91e-13	5.32e-13	5.74e-13
115	16	10	8.16e-12	8.13e-12	8.21e-12	8.46e-12	8.79e-12	9.18e-12	9.60e-12	1.00e-11
116	16	11	2.76e-11	3.10e-11	3.09e-11	3.04e-11	2.98e-11	2.93e-11	2.88e-11	2.83e-11
117	16	12	1.62e-12	3.09e-12	3.39e-12	3.41e-12	3.42e-12	3.46e-12	3.54e-12	3.66e-12
118	16	13	6.03e-13	5.99e-13	5.71e-13	5.55e-13	5.49e-13	5.50e-13	5.56e-13	5.66e-13
119	16	14	1.78e-12	1.98e-12	1.97e-12	1.93e-12	1.88e-12	1.83e-12	1.79e-12	1.76e-12
120	16	15	9.27e-12	9.43e-12	9.61e-12	9.92e-12	1.03e-11	1.08e-11	1.14e-11	1.19e-11
121	17	1	1.99e-13	1.84e-13	1.79e-13	1.80e-13	1.84e-13	1.89e-13	1.95e-13	2.02e-13
122	17	2	2.95e-14	3.38e-14	3.66e-14	4.06e-14	4.58e-14	5.22e-14	5.98e-14	6.86e-14
123	17	3	1.42e-13	1.68e-13	1.90e-13	2.12e-13	2.39e-13	2.71e-13	3.09e-13	3.51e-13
124	17	4	7.01e-14	6.95e-14	6.95e-14	7.16e-14	7.53e-14	8.00e-14	8.56e-14	9.17e-14
125	17	5	7.08e-12	6.54e-12	6.38e-12	6.41e-12	6.55e-12	6.74e-12	6.98e-12	7.24e-12
126	17	6	1.01e-13	1.76e-13	1.85e-13	1.90e-13	2.00e-13	2.18e-13	2.43e-13	2.74e-13
127	17	7	5.47e-13	4.94e-13	4.78e-13	4.81e-13	4.92e-13	5.09e-13	5.30e-13	5.53e-13
128	17	8	1.13e-13	1.17e-13	1.04e-13	9.53e-14	9.06e-14	8.93e-14	9.06e-14	9.40e-14
129	17	9	9.57e-12	1.06e-11	1.07e-11	1.07e-11	1.06e-11	1.06e-11	1.06e-11	1.07e-11
130	17	10	1.52e-12	1.81e-12	1.95e-12	2.09e-12	2.22e-12	2.37e-12	2.52e-12	2.67e-12
131	17	11	6.44e-13	6.53e-13	5.42e-13	4.62e-13	4.11e-13	3.78e-13	3.58e-13	3.48e-13
132	17	12	3.73e-16	1.38e-14	2.28e-14	2.60e-14	2.71e-14	2.78e-14	2.84e-14	2.92e-14
133	17	13	1.93e-11	1.89e-11	1.88e-11	1.89e-11	1.93e-11	1.98e-11	2.04e-11	2.11e-11
134	17	14	7.18e-13	1.09e-12	1.11e-12	1.07e-12	1.02e-12	9.84e-13	9.58e-13	9.39e-13
135	17	15	7.61e-13	1.05e-12	1.09e-12	1.11e-12	1.13e-12	1.18e-12	1.23e-12	1.29e-12
136	17	16	3.24e-15	1.00e-13	1.76e-13	2.13e-13	2.30e-13	2.40e-13	2.47e-13	2.53e-13
137	18	1	4.94e-15	5.69e-15	5.87e-15	6.11e-15	6.48e-15	6.97e-15	7.56e-15	8.25e-15
138	18	2	8.39e-14	8.38e-14	8.46e-14	8.66e-14	8.92e-14	9.21e-14	9.52e-14	9.82e-14
139	18	3	1.59e-13	1.56e-13	1.52e-13	1.51e-13	1.51e-13	1.52e-13	1.54e-13	1.56e-13
140	18	4	3.92e-14	4.96e-14	5.50e-14	6.09e-14	6.84e-14	7.74e-14	8.79e-14	9.98e-14
141	18	5	2.15e-13	2.30e-13	2.42e-13	2.56e-13	2.73e-13	2.91e-13	3.10e-13	3.31e-13
142	18	6	3.08e-12	3.07e-12	3.10e-12	3.19e-12	3.31e-12	3.46e-12	3.62e-12	3.79e-12
143	18	7	9.48e-14	1.75e-13	1.82e-13	1.83e-13	1.88e-13	1.99e-13	2.15e-13	2.35e-13
144	18	8	4.53e-13	4.45e-13	4.36e-13	4.39e-13	4.50e-13	4.65e-13	4.84e-13	5.04e-13
145	18	9	2.52e-13	2.17e-13	1.87e-13	1.69e-13	1.57e-13	1.49e-13	1.43e-13	1.39e-13
146	18	10	5.79e-12	6.59e-12	6.89e-12	7.10e-12	7.30e-12	7.48e-12	7.65e-12	7.80e-12
147	18	11	1.66e-12	1.94e-12	2.05e-12	2.17e-12	2.29e-12	2.43e-12	2.57e-12	2.72e-12
148	18	12	4.71e-13	5.56e-13	4.79e-13	4.08e-13	3.58e-13	3.24e-13	3.02e-13	2.89e-13
149	18	13	4.74e-12	5.51e-12	5.81e-12	6.06e-12	6.30e-12	6.51e-12	6.71e-12	6.88e-12
150	18	14	1.01e-11	1.02e-11	1.02e-11	1.03e-11	1.06e-11	1.09e-11	1.13e-11	1.17e-11
151	18	15	6.51e-12	7.17e-12	6.98e-12	6.73e-12	6.51e-12	6.34e-12	6.20e-12	6.08e-12
152	18	16	3.53e-12	4.57e-12	4.50e-12	4.39e-12	4.36e-12	4.40e-12	4.50e-12	4.63e-12
153	18	17	6.70e-12	6.93e-12	6.90e-12	6.93e-12	7.04e-12	7.20e-12	7.42e-12	7.66e-12

Rotational rate coefficients computed for the 20 first rotational energy levels (see previous table) of *para*-D₂O in collision with *ortho*-H₂. Rate coefficients are provided for temperatures from 10 to 150 K.

Tran.	Initial	Final	10 K	30 K	50 K	70 K	90 K	110 K	130 K	150 K
1	2	1	2.68e-10	2.98e-10	2.96e-10	2.90e-10	2.84e-10	2.79e-10	2.74e-10	2.70e-10
2	3	1	1.44e-10	1.54e-10	1.56e-10	1.56e-10	1.55e-10	1.55e-10	1.54e-10	1.53e-10
3	3	2	1.10e-10	1.10e-10	9.97e-11	9.14e-11	8.49e-11	7.99e-11	7.59e-11	7.27e-11
4	4	1	2.60e-11	2.77e-11	2.82e-11	2.85e-11	2.87e-11	2.89e-11	2.90e-11	2.91e-11
5	4	2	7.58e-11	8.93e-11	9.90e-11	1.07e-10	1.12e-10	1.17e-10	1.20e-10	1.23e-10
6	4	3	1.13e-10	1.14e-10	1.13e-10	1.12e-10	1.10e-10	1.09e-10	1.08e-10	1.08e-10
7	5	1	3.63e-11	3.95e-11	4.06e-11	4.15e-11	4.22e-11	4.29e-11	4.34e-11	4.39e-11
8	5	2	3.93e-11	3.81e-11	3.47e-11	3.19e-11	2.97e-11	2.81e-11	2.68e-11	2.59e-11
9	5	3	1.47e-10	1.53e-10	1.52e-10	1.50e-10	1.47e-10	1.45e-10	1.43e-10	1.41e-10
10	5	4	2.91e-11	3.59e-11	3.19e-11	2.80e-11	2.49e-11	2.24e-11	2.05e-11	1.90e-11
11	6	1	1.75e-11	1.95e-11	1.95e-11	1.92e-11	1.89e-11	1.87e-11	1.85e-11	1.84e-11
12	6	2	2.60e-11	3.00e-11	3.21e-11	3.36e-11	3.49e-11	3.59e-11	3.68e-11	3.75e-11
13	6	3	7.52e-11	8.51e-11	8.61e-11	8.56e-11	8.46e-11	8.35e-11	8.25e-11	8.16e-11
14	6	4	7.98e-11	7.97e-11	7.43e-11	6.93e-11	6.51e-11	6.17e-11	5.88e-11	5.65e-11
15	6	5	1.66e-10	1.87e-10	1.91e-10	1.90e-10	1.89e-10	1.88e-10	1.86e-10	1.85e-10
16	7	1	6.72e-12	8.86e-12	1.04e-11	1.17e-11	1.27e-11	1.35e-11	1.42e-11	1.49e-11
17	7	2	9.90e-12	1.08e-11	1.09e-11	1.09e-11	1.09e-11	1.10e-11	1.10e-11	1.11e-11
18	7	3	4.71e-11	5.57e-11	6.02e-11	6.33e-11	6.55e-11	6.73e-11	6.87e-11	6.99e-11
19	7	4	7.85e-11	9.23e-11	9.55e-11	9.63e-11	9.64e-11	9.62e-11	9.58e-11	9.54e-11
20	7	5	4.20e-11	4.16e-11	3.90e-11	3.64e-11	3.41e-11	3.22e-11	3.07e-11	2.93e-11
21	7	6	1.21e-10	1.44e-10	1.55e-10	1.60e-10	1.62e-10	1.64e-10	1.64e-10	1.64e-10
22	8	1	1.59e-12	1.71e-12	1.78e-12	1.85e-12	1.91e-12	1.98e-12	2.04e-12	2.09e-12
23	8	2	6.06e-12	6.76e-12	7.45e-12	8.15e-12	8.82e-12	9.44e-12	1.00e-11	1.05e-11
24	8	3	6.16e-12	7.11e-12	7.60e-12	7.97e-12	8.27e-12	8.53e-12	8.75e-12	8.95e-12
25	8	4	6.84e-11	7.79e-11	8.53e-11	9.18e-11	9.77e-11	1.03e-10	1.07e-10	1.11e-10
26	8	5	5.37e-12	4.70e-12	4.42e-12	4.24e-12	4.13e-12	4.06e-12	4.02e-12	3.99e-12
27	8	6	1.25e-11	1.26e-11	1.23e-11	1.19e-11	1.16e-11	1.13e-11	1.11e-11	1.09e-11
28	8	7	8.95e-11	1.00e-10	1.03e-10	1.03e-10	1.02e-10	1.01e-10	1.01e-10	9.98e-11
29	9	1	6.01e-12	6.86e-12	7.16e-12	7.39e-12	7.63e-12	7.89e-12	8.16e-12	8.45e-12
30	9	2	5.39e-12	5.60e-12	5.36e-12	5.14e-12	4.99e-12	4.89e-12	4.85e-12	4.83e-12
31	9	3	2.16e-11	2.54e-11	2.72e-11	2.86e-11	2.98e-11	3.08e-11	3.16e-11	3.24e-11
32	9	4	2.20e-11	2.16e-11	1.91e-11	1.71e-11	1.57e-11	1.46e-11	1.37e-11	1.31e-11
33	9	5	9.86e-11	1.23e-10	1.35e-10	1.42e-10	1.46e-10	1.49e-10	1.51e-10	1.53e-10
34	9	6	6.96e-11	7.06e-11	6.57e-11	6.06e-11	5.60e-11	5.22e-11	4.89e-11	4.62e-11
35	9	7	4.24e-11	4.79e-11	4.45e-11	4.08e-11	3.77e-11	3.52e-11	3.33e-11	3.17e-11
36	9	8	3.49e-14	1.24e-12	2.24e-12	2.72e-12	2.95e-12	3.06e-12	3.12e-12	3.15e-12
37	10	1	9.60e-13	8.89e-13	8.40e-13	8.23e-13	8.25e-13	8.38e-13	8.59e-13	8.85e-13
38	10	2	2.84e-12	2.98e-12	3.13e-12	3.32e-12	3.54e-12	3.76e-12	4.00e-12	4.24e-12
39	10	3	6.16e-12	6.45e-12	6.49e-12	6.54e-12	6.62e-12	6.72e-12	6.82e-12	6.93e-12
40	10	4	1.75e-11	1.90e-11	1.99e-11	2.07e-11	2.15e-11	2.21e-11	2.27e-11	2.32e-11
41	10	5	2.95e-11	3.34e-11	3.51e-11	3.62e-11	3.71e-11	3.78e-11	3.84e-11	3.88e-11
42	10	6	4.36e-11	5.10e-11	5.67e-11	6.15e-11	6.55e-11	6.88e-11	7.17e-11	7.41e-11
43	10	7	6.52e-11	7.45e-11	7.60e-11	7.56e-11	7.47e-11	7.37e-11	7.27e-11	7.17e-11
44	10	8	4.31e-11	4.90e-11	4.74e-11	4.48e-11	4.23e-11	4.01e-11	3.83e-11	3.67e-11
45	10	9	1.02e-10	1.14e-10	1.17e-10	1.18e-10	1.18e-10	1.17e-10	1.17e-10	1.16e-10
46	11	1	6.24e-13	6.93e-13	7.41e-13	7.90e-13	8.40e-13	8.92e-13	9.43e-13	9.94e-13
47	11	2	5.02e-13	5.50e-13	5.72e-13	5.92e-13	6.13e-13	6.35e-13	6.59e-13	6.83e-13
48	11	3	3.24e-12	3.81e-12	4.31e-12	4.81e-12	5.30e-12	5.77e-12	6.21e-12	6.64e-12
49	11	4	5.82e-12	6.60e-12	6.97e-12	7.26e-12	7.55e-12	7.84e-12	8.13e-12	8.43e-12
50	11	5	3.18e-12	3.40e-12	3.47e-12	3.55e-12	3.63e-12	3.72e-12	3.80e-12	3.88e-12
51	11	6	9.11e-12	1.09e-11	1.19e-11	1.26e-11	1.32e-11	1.37e-11	1.41e-11	1.45e-11

52	11	7	3.96e-11	4.71e-11	5.23e-11	5.69e-11	6.12e-11	6.51e-11	6.87e-11	7.18e-11
53	11	8	7.75e-11	9.31e-11	9.74e-11	9.86e-11	9.87e-11	9.85e-11	9.81e-11	9.76e-11
54	11	9	7.05e-12	6.98e-12	6.66e-12	6.44e-12	6.31e-12	6.21e-12	6.15e-12	6.11e-12
55	11	10	7.16e-11	9.12e-11	9.97e-11	1.04e-10	1.07e-10	1.08e-10	1.09e-10	1.10e-10
56	12	1	7.73e-14	7.70e-14	7.85e-14	8.11e-14	8.49e-14	8.95e-14	9.47e-14	1.00e-13
57	12	2	3.63e-13	3.84e-13	4.12e-13	4.45e-13	4.81e-13	5.19e-13	5.58e-13	5.97e-13
58	12	3	4.10e-13	4.30e-13	4.50e-13	4.75e-13	5.04e-13	5.36e-13	5.70e-13	6.04e-13
59	12	4	5.27e-12	5.57e-12	5.96e-12	6.41e-12	6.90e-12	7.41e-12	7.90e-12	8.39e-12
60	12	5	2.99e-13	2.81e-13	2.83e-13	2.89e-13	2.99e-13	3.11e-13	3.25e-13	3.40e-13
61	12	6	8.55e-13	8.21e-13	8.29e-13	8.51e-13	8.82e-13	9.17e-13	9.55e-13	9.94e-13
62	12	7	5.02e-12	5.52e-12	5.87e-12	6.19e-12	6.50e-12	6.80e-12	7.09e-12	7.36e-12
63	12	8	6.22e-11	6.76e-11	7.18e-11	7.63e-11	8.08e-11	8.53e-11	8.96e-11	9.37e-11
64	12	9	8.36e-13	7.25e-13	7.07e-13	7.10e-13	7.22e-13	7.41e-13	7.65e-13	7.90e-13
65	12	10	5.80e-12	5.58e-12	5.56e-12	5.58e-12	5.63e-12	5.69e-12	5.76e-12	5.83e-12
66	12	11	5.91e-11	6.81e-11	7.13e-11	7.29e-11	7.38e-11	7.45e-11	7.50e-11	7.53e-11
67	13	1	2.61e-12	2.69e-12	2.67e-12	2.66e-12	2.67e-12	2.69e-12	2.73e-12	2.77e-12
68	13	2	1.84e-12	1.74e-12	1.61e-12	1.53e-12	1.47e-12	1.44e-12	1.42e-12	1.42e-12
69	13	3	7.86e-12	7.85e-12	7.90e-12	8.07e-12	8.31e-12	8.61e-12	8.93e-12	9.28e-12
70	13	4	3.07e-12	2.93e-12	2.66e-12	2.48e-12	2.38e-12	2.32e-12	2.30e-12	2.31e-12
71	13	5	2.23e-11	2.50e-11	2.68e-11	2.86e-11	3.02e-11	3.17e-11	3.30e-11	3.42e-11
72	13	6	2.08e-11	2.00e-11	1.87e-11	1.77e-11	1.71e-11	1.66e-11	1.63e-11	1.60e-11
73	13	7	1.38e-11	1.24e-11	1.06e-11	9.20e-12	8.25e-12	7.56e-12	7.07e-12	6.70e-12
74	13	8	5.63e-12	5.37e-12	4.35e-12	3.60e-12	3.08e-12	2.72e-12	2.46e-12	2.27e-12
75	13	9	1.02e-10	1.21e-10	1.32e-10	1.39e-10	1.45e-10	1.49e-10	1.52e-10	1.54e-10
76	13	10	5.37e-11	5.45e-11	4.97e-11	4.48e-11	4.07e-11	3.73e-11	3.44e-11	3.20e-11
77	13	11	4.54e-14	1.45e-12	2.51e-12	2.97e-12	3.17e-12	3.25e-12	3.28e-12	3.30e-12
78	13	12	3.20e-19	4.80e-15	3.11e-14	6.80e-14	1.05e-13	1.38e-13	1.68e-13	1.95e-13
79	14	1	9.95e-13	9.75e-13	9.64e-13	9.68e-13	9.80e-13	9.96e-13	1.01e-12	1.03e-12
80	14	2	1.18e-12	1.26e-12	1.27e-12	1.27e-12	1.28e-12	1.29e-12	1.31e-12	1.32e-12
81	14	3	2.72e-12	2.70e-12	2.64e-12	2.59e-12	2.57e-12	2.56e-12	2.56e-12	2.56e-12
82	14	4	3.33e-12	3.40e-12	3.31e-12	3.26e-12	3.25e-12	3.27e-12	3.31e-12	3.36e-12
83	14	5	8.20e-12	8.39e-12	8.28e-12	8.24e-12	8.26e-12	8.32e-12	8.40e-12	8.49e-12
84	14	6	2.22e-11	2.47e-11	2.71e-11	2.96e-11	3.20e-11	3.42e-11	3.62e-11	3.81e-11
85	14	7	2.04e-11	2.03e-11	1.98e-11	1.95e-11	1.92e-11	1.90e-11	1.88e-11	1.87e-11
86	14	8	8.71e-12	7.21e-12	6.06e-12	5.30e-12	4.79e-12	4.43e-12	4.18e-12	4.00e-12
87	14	9	4.02e-11	4.51e-11	4.61e-11	4.67e-11	4.73e-11	4.77e-11	4.80e-11	4.83e-11
88	14	10	5.77e-11	6.03e-11	6.23e-11	6.38e-11	6.49e-11	6.57e-11	6.63e-11	6.67e-11
89	14	11	2.26e-11	2.61e-11	2.43e-11	2.21e-11	2.02e-11	1.86e-11	1.72e-11	1.61e-11
90	14	12	1.71e-16	7.99e-14	2.59e-13	4.12e-13	5.25e-13	6.08e-13	6.73e-13	7.26e-13
91	14	13	1.24e-10	1.35e-10	1.36e-10	1.34e-10	1.33e-10	1.31e-10	1.30e-10	1.28e-10
92	15	1	2.53e-13	2.84e-13	3.16e-13	3.52e-13	3.92e-13	4.34e-13	4.79e-13	5.25e-13
93	15	2	4.32e-13	4.80e-13	5.01e-13	5.21e-13	5.42e-13	5.65e-13	5.88e-13	6.11e-13
94	15	3	6.09e-13	6.96e-13	7.54e-13	8.10e-13	8.69e-13	9.30e-13	9.93e-13	1.06e-12
95	15	4	2.30e-12	2.52e-12	2.54e-12	2.55e-12	2.56e-12	2.58e-12	2.59e-12	2.61e-12
96	15	5	3.19e-12	4.14e-12	4.93e-12	5.67e-12	6.35e-12	6.99e-12	7.58e-12	8.13e-12
97	15	6	7.38e-12	8.69e-12	9.26e-12	9.68e-12	1.00e-11	1.04e-11	1.07e-11	1.09e-11
98	15	7	1.22e-11	1.55e-11	1.79e-11	2.01e-11	2.22e-11	2.40e-11	2.57e-11	2.72e-11
99	15	8	1.35e-11	1.38e-11	1.27e-11	1.18e-11	1.12e-11	1.07e-11	1.03e-11	1.00e-11
100	15	9	1.63e-11	1.83e-11	1.93e-11	1.99e-11	2.05e-11	2.10e-11	2.15e-11	2.19e-11
101	15	10	4.39e-11	5.14e-11	5.51e-11	5.74e-11	5.91e-11	6.03e-11	6.12e-11	6.18e-11
102	15	11	4.69e-11	5.65e-11	5.62e-11	5.44e-11	5.24e-11	5.06e-11	4.89e-11	4.75e-11

103	15	12	2.13e-14	9.59e-13	1.92e-12	2.48e-12	2.80e-12	2.98e-12	3.10e-12	3.18e-12
104	15	13	2.34e-11	2.61e-11	2.55e-11	2.43e-11	2.31e-11	2.20e-11	2.10e-11	2.02e-11
105	15	14	1.56e-10	1.89e-10	2.02e-10	2.08e-10	2.10e-10	2.11e-10	2.11e-10	2.10e-10
106	16	1	1.24e-13	1.36e-13	1.48e-13	1.60e-13	1.73e-13	1.86e-13	1.99e-13	2.12e-13
107	16	2	2.99e-13	3.19e-13	3.48e-13	3.84e-13	4.25e-13	4.71e-13	5.20e-13	5.72e-13
108	16	3	2.55e-13	2.55e-13	2.59e-13	2.68e-13	2.81e-13	2.97e-13	3.14e-13	3.32e-13
109	16	4	1.27e-12	1.26e-12	1.34e-12	1.45e-12	1.57e-12	1.70e-12	1.83e-12	1.97e-12
110	16	5	1.19e-12	1.31e-12	1.43e-12	1.56e-12	1.69e-12	1.83e-12	1.97e-12	2.11e-12
111	16	6	2.56e-12	3.10e-12	3.65e-12	4.23e-12	4.80e-12	5.36e-12	5.90e-12	6.41e-12
112	16	7	3.85e-12	4.18e-12	4.39e-12	4.56e-12	4.72e-12	4.88e-12	5.03e-12	5.18e-12
113	16	8	1.23e-11	1.19e-11	1.25e-11	1.32e-11	1.39e-11	1.46e-11	1.52e-11	1.58e-11
114	16	9	4.55e-12	5.03e-12	5.39e-12	5.71e-12	6.01e-12	6.28e-12	6.53e-12	6.77e-12
115	16	10	2.76e-11	3.27e-11	3.62e-11	3.94e-11	4.23e-11	4.50e-11	4.74e-11	4.97e-11
116	16	11	5.61e-11	6.78e-11	7.41e-11	7.80e-11	8.04e-11	8.21e-11	8.33e-11	8.41e-11
117	16	12	2.74e-11	3.57e-11	3.63e-11	3.52e-11	3.39e-11	3.26e-11	3.14e-11	3.04e-11
118	16	13	4.82e-12	5.19e-12	5.08e-12	4.99e-12	4.94e-12	4.91e-12	4.90e-12	4.89e-12
119	16	14	2.17e-11	2.40e-11	2.42e-11	2.40e-11	2.35e-11	2.30e-11	2.24e-11	2.19e-11
120	16	15	1.13e-10	1.41e-10	1.51e-10	1.55e-10	1.57e-10	1.58e-10	1.58e-10	1.57e-10
121	17	1	5.19e-13	5.36e-13	5.49e-13	5.64e-13	5.84e-13	6.06e-13	6.29e-13	6.54e-13
122	17	2	4.33e-13	4.24e-13	4.21e-13	4.28e-13	4.46e-13	4.70e-13	5.01e-13	5.37e-13
123	17	3	2.19e-12	2.34e-12	2.40e-12	2.45e-12	2.51e-12	2.58e-12	2.65e-12	2.72e-12
124	17	4	6.60e-13	6.90e-13	6.68e-13	6.49e-13	6.40e-13	6.39e-13	6.45e-13	6.57e-13
125	17	5	7.32e-12	7.34e-12	7.51e-12	7.79e-12	8.17e-12	8.60e-12	9.06e-12	9.55e-12
126	17	6	2.61e-12	2.70e-12	2.71e-12	2.72e-12	2.75e-12	2.80e-12	2.86e-12	2.92e-12
127	17	7	2.40e-12	2.36e-12	2.25e-12	2.17e-12	2.12e-12	2.09e-12	2.08e-12	2.08e-12
128	17	8	8.96e-13	9.02e-13	8.10e-13	7.38e-13	6.93e-13	6.68e-13	6.57e-13	6.55e-13
129	17	9	1.51e-11	1.81e-11	2.02e-11	2.21e-11	2.39e-11	2.55e-11	2.70e-11	2.83e-11
130	17	10	1.08e-11	1.15e-11	1.14e-11	1.12e-11	1.11e-11	1.10e-11	1.10e-11	1.10e-11
131	17	11	4.77e-12	4.45e-12	3.91e-12	3.46e-12	3.14e-12	2.92e-12	2.75e-12	2.64e-12
132	17	12	4.36e-15	1.10e-13	1.80e-13	2.09e-13	2.21e-13	2.27e-13	2.32e-13	2.37e-13
133	17	13	8.50e-11	1.04e-10	1.17e-10	1.26e-10	1.34e-10	1.40e-10	1.45e-10	1.49e-10
134	17	14	4.89e-11	4.87e-11	4.56e-11	4.25e-11	3.98e-11	3.73e-11	3.53e-11	3.34e-11
135	17	15	1.63e-11	1.95e-11	1.82e-11	1.65e-11	1.51e-11	1.40e-11	1.32e-11	1.25e-11
136	17	16	5.70e-14	1.62e-12	2.71e-12	3.17e-12	3.34e-12	3.39e-12	3.40e-12	3.37e-12
137	18	1	1.23e-13	1.16e-13	1.14e-13	1.16e-13	1.20e-13	1.25e-13	1.31e-13	1.37e-13
138	18	2	2.09e-13	2.21e-13	2.30e-13	2.40e-13	2.53e-13	2.67e-13	2.81e-13	2.95e-13
139	18	3	7.57e-13	7.78e-13	7.90e-13	8.12e-13	8.40e-13	8.72e-13	9.07e-13	9.42e-13
140	18	4	8.33e-13	8.80e-13	8.99e-13	9.24e-13	9.55e-13	9.91e-13	1.03e-12	1.07e-12
141	18	5	8.85e-13	8.28e-13	8.01e-13	8.12e-13	8.45e-13	8.91e-13	9.45e-13	1.00e-12
142	18	6	2.42e-12	2.52e-12	2.67e-12	2.88e-12	3.13e-12	3.40e-12	3.70e-12	4.00e-12
143	18	7	2.46e-12	2.70e-12	2.77e-12	2.83e-12	2.89e-12	2.95e-12	3.02e-12	3.09e-12
144	18	8	1.74e-12	1.91e-12	1.88e-12	1.84e-12	1.81e-12	1.80e-12	1.80e-12	1.81e-12
145	18	9	3.62e-12	3.14e-12	2.93e-12	2.86e-12	2.86e-12	2.90e-12	2.95e-12	3.01e-12
146	18	10	1.04e-11	1.30e-11	1.48e-11	1.66e-11	1.82e-11	1.98e-11	2.13e-11	2.27e-11
147	18	11	1.10e-11	1.22e-11	1.21e-11	1.19e-11	1.17e-11	1.16e-11	1.15e-11	1.14e-11
148	18	12	2.29e-12	3.54e-12	3.33e-12	2.98e-12	2.70e-12	2.49e-12	2.33e-12	2.23e-12
149	18	13	2.28e-11	2.56e-11	2.73e-11	2.88e-11	3.02e-11	3.15e-11	3.26e-11	3.36e-11
150	18	14	2.93e-11	3.74e-11	4.32e-11	4.83e-11	5.29e-11	5.69e-11	6.04e-11	6.35e-11
151	18	15	3.97e-11	4.47e-11	4.54e-11	4.51e-11	4.44e-11	4.37e-11	4.29e-11	4.21e-11
152	18	16	2.97e-11	3.81e-11	3.86e-11	3.76e-11	3.64e-11	3.54e-11	3.44e-11	3.36e-11
153	18	17	8.45e-11	9.25e-11	9.47e-11	9.59e-11	9.66e-11	9.69e-11	9.71e-11	9.71e-11

APPENDIX C

The Article "*A SUBLIME 3D Model for Cometary Coma Emission: The Hypervolatile-rich Comet C/2016 R2 (PanSTARRS)*" where the rate coefficients of the CO-CO system calculated in this work, were used for an analysis of the observational spectra of comets.



HAL
open science

A SUBLIME 3D Model for Cometary Coma Emission: The Hypervolatile-rich Comet C/2016 R2 (PanSTARRS)

M. A. Cordiner, I. M. Coulson, E. Garcia-Berrios, C. Qi, François Lique,
Michal Zoltowski, M. de Val-Borro, Y-J Kuan, W-H Ip, S. Mairs, et al.

► **To cite this version:**

M. A. Cordiner, I. M. Coulson, E. Garcia-Berrios, C. Qi, François Lique, et al.. A SUBLIME 3D Model for Cometary Coma Emission: The Hypervolatile-rich Comet C/2016 R2 (PanSTARRS). *The Astrophysical Journal*, American Astronomical Society, 2022, 929 (1), pp.38. 10.3847/1538-4357/ac5893 . hal-03660671v2

HAL Id: hal-03660671

<https://hal.archives-ouvertes.fr/hal-03660671v2>

Submitted on 6 May 2022

HAL is a multi-disciplinary open access archive for the deposit and dissemination of scientific research documents, whether they are published or not. The documents may come from teaching and research institutions in France or abroad, or from public or private research centers.

L'archive ouverte pluridisciplinaire **HAL**, est destinée au dépôt et à la diffusion de documents scientifiques de niveau recherche, publiés ou non, émanant des établissements d'enseignement et de recherche français ou étrangers, des laboratoires publics ou privés.



Distributed under a Creative Commons Attribution | 4.0 International License



A SUBLIME 3D Model for Cometary Coma Emission: The Hypervolatile-rich Comet C/2016 R2 (PanSTARRS)

M. A. Cordiner^{1,2}, I. M. Coulson³, E. Garcia-Berrios^{1,2,4}, C. Qi⁵, F. Lique⁶, M. Zolowski^{6,7}, M. de Val-Borro^{1,2}, Y.-J. Kuan^{8,9}, W.-H. Ip¹⁰, S. Mairs³, N. X. Roth^{1,2}, S. B. Charnley¹, S. N. Milam¹, W.-L. Tseng⁸, and Y.-L. Chuang⁸

¹ Astrochemistry Laboratory, NASA Goddard Space Flight Center, 8800 Greenbelt Road, Greenbelt, MD 20771, USA; martin.cordiner@nasa.gov

² Department of Physics, Catholic University of America, Washington, DC 20064, USA

³ East Asian Observatory, 660 N. A'ohoku Place, Hilo, HI 96720, USA

⁴ Department of Astronomy, University of Illinois, 1002 W. Green St., Urbana, IL 61801, USA

⁵ Harvard-Smithsonian Center for Astrophysics, 60 Garden Street, MS 42, Cambridge, MA 02138, USA

⁶ Université de Rennes 1, Campus de Beaulieu, 263 avenue du Général Leclerc, F-35042 Rennes Cedex, France

⁷ LOMC—UMR 6294, CNRS-Université du Havre, 25 rue Philippe Lebon, BP1123, F-76 063 Le Havre cedex, France

⁸ National Taiwan Normal University, Ting-Chou Road, Taipei 11677, Taiwan, ROC

⁹ Institute of Astronomy and Astrophysics, Academia Sinica, Taipei 106, Taiwan, ROC

¹⁰ Graduate Institute of Space Science, National Central University, Taoyuan City, Taiwan

Received 2021 November 3; revised 2022 February 23; accepted 2022 February 23; published 2022 April 11

Abstract

The coma of comet C/2016 R2 (PanSTARRS) is one of the most chemically peculiar ever observed, in particular due to its extremely high CO/H₂O and N₂⁺/H₂O ratios, and unusual trace volatile abundances. However, the complex shape of its CO emission lines, as well as uncertainties in the coma structure and excitation, has led to ambiguities in the total CO production rate. We performed high-resolution, spatially, spectrally, and temporally resolved CO observations using the James Clerk Maxwell Telescope and Submillimeter Array to elucidate the outgassing behavior of C/2016 R2. Results are analyzed using a new, time-dependent, three-dimensional radiative transfer code (SUBlimating gases in LIME; SUBLIME, based on the open-source version of the LIne Modeling Engine), incorporating for the first time, accurate state-to-state collisional rate coefficients for the CO–CO system. The total CO production rate was found to be in the range of $(3.8 - 7.6) \times 10^{28} \text{ s}^{-1}$ between 2018 January 13 and February 1 (at $r_H = 2.8\text{--}2.9$ au), with a mean value of $(5.3 \pm 0.6) \times 10^{28} \text{ s}^{-1}$. The emission is concentrated in a near-sunward jet, with a half-opening angle of $\sim 62^\circ$ and an outflow velocity of $0.51 \pm 0.01 \text{ km s}^{-1}$, compared to $0.25 \pm 0.01 \text{ km s}^{-1}$ in the ambient (and nightside) coma. Evidence was also found for an extended source of CO emission, possibly due to icy grain sublimation around $1.2 \times 10^5 \text{ km}$ from the nucleus. Based on the coma molecular abundances, we propose that the nucleus ices of C/2016 R2 can be divided into a rapidly sublimating apolar phase, rich in CO, CO₂, N₂, and CH₃OH, and a predominantly frozen (or less abundant), polar phase containing more H₂O, CH₄, H₂CO, and HCN.

Unified Astronomy Thesaurus concepts: Comets (280); Long period comets (933); Submillimeter astronomy (1647); Comet volatiles (2162); High resolution spectroscopy (2096); Radio interferometry (1346); Radiative transfer simulations (1967); De-excitation rates (2066)


1. Introduction

Comets are composed of ice, dust, and debris accreted during the epoch of planet formation. Having spent most of their lives frozen, at large distances from the Sun, cometary nuclei contain some of our solar system's most pristine (thermally unprocessed) material. From studies of their gaseous atmospheres (comae), the properties of the nucleus can be inferred, thereby providing unique insights into the conditions prevalent at the dawn of the solar system.

The long-period comet C/2016 R2 (PanSTARRS) is one of the most chemically peculiar comets ever observed. Early observations at a heliocentric distance of around 3 au revealed a visually blue coma with a highly unusual optical spectrum, dominated by CO⁺ emission, in addition to a rare detection of N₂⁺ (Cochran & McKay 2018), consistent with very strong outgassing of CO and an above average N₂/CO ratio in the

nucleus. Both CO and N₂ sublimate at low temperatures compared to other cometary ices (e.g., Womack et al. 2017), and are therefore considered hypervolatile. Their presence in very high abundances (relative to H₂O) implies that C/2016 R2 formed very cold, and was maintained at temperatures $\lesssim 20 \text{ K}$ for the duration of its lifetime.

Follow-up observations at infrared and millimeter wavelengths confirmed the presence of an exceptionally CO-rich coma, with a low production rate of H₂O (usually the dominant cometary volatile) and extremely unusual abundance ratios for other species compared with the typical cometary population (Biver et al. 2018; Wierzbosch & Womack 2018; McKay et al. 2019). Due to their very different sublimation temperatures, the CO-to-H₂O ratio in cometary comae is known to vary as a function of temperature of the nucleus, so some enhancement in CO/H₂O is expected at the relatively large heliocentric distance (r_H) at which this comet was observed. However, the coma composition of C/2016 R2 clearly differs from other comets observed at similar r_H . Based on Table 7 of Biver et al. (2018), the abundance ratios CO:H₂O:CH₃OH:HCN (normalized to CH₃OH) were 94:0.3:1:0.004 in C/2016 R2 at

 Original content from this work may be used under the terms of the [Creative Commons Attribution 4.0 licence](https://creativecommons.org/licenses/by/4.0/). Any further distribution of this work must maintain attribution to the author(s) and the title of the work, journal citation and DOI.

$r_H = 2.8$ au, 14:43:1:0.08 in C/1995 O1 at 2.8 au, and 24:27:1:0.10 in C/2006 W3 at 3.2–3.3 au (the H_2O abundances in R2 and W3 are from McKay et al. 2019 and Bockelée-Morvan et al. 2010, respectively), highlighting the CO richness of the coma, as well as its strong H_2O and HCN depletions. Cometary and interstellar ice observations have identified the presence of separate polar and apolar ice phases, dominated by H_2O and $[CO + CO_2]$, respectively (Mumma et al. 2011; Boogert et al. 2015; Luspay-Kuti et al. 2015). Studies of coma abundances in C/2016 R2 therefore provide a rare opportunity to investigate volatiles outgassed primarily from the apolar ($CO + CO_2$ dominated) phase, which may provide unique insights into the origin, storage, and outgassing mechanisms of the less abundant ices in cometary nuclei.

Complexity of the C/2016 R2 blueshifted CO rotational line profile, as well as uncertainties in the CO excitation calculation, lead to ambiguity in its interpretation, and estimates for the CO production rate (in 2018 January) range from $Q(CO) = (4.6 \pm 0.4) \times 10^{26} \text{ s}^{-1}$ (Wierzbach & Womack 2018) to $(10.6 \pm 0.5) \times 10^{26} \text{ s}^{-1}$ (Biver et al. 2018). Limited CO mapping by both studies found marginal evidence for extended CO emission beyond that expected based purely on nucleus-driven outgassing, but this possibility has not yet been investigated in detail. Uncertainties therefore remain regarding (1) the intrinsic CO production rate of this comet, (2) the processes by which CO is released into the gas phase, and (3) the detailed coma morphology.

During 2018 January and February, we undertook a program of time-resolved high-resolution spectroscopy, spatial-spectral mapping, and interferometry using the James Clerk Maxwell Telescope (JCMT) and Submillimeter Array (SMA) to elucidate the outgassing behavior of C/2016 R2. The CO $J = 3 - 2$ and $J = 2 - 1$ lines were observed as a probe of the coma kinetic temperature, and based on the strength of the ^{12}CO emission in this comet, we searched for the ^{13}CO isotopologue as a tracer of any unusual isotopic processing in this comet’s natal carbon. We also sought to confirm the comet’s peculiar CO:HCN:CH₃OH:H₂CO ratios through observations of submillimeter rotational lines from these species, and HCO⁺ was observed as a probe of ion chemistry in the outer coma.

The resulting (spectral–spatial–temporal) data set is analyzed using a new, time-dependent, three-dimensional radiative transfer code (SUBlimating gases in LIME; SUBLIME), which is an evolution of the steady-state model used previously by Paganini et al. (2010), Bøgelund & Hogerheijde (2017), de Val-Borro et al. (2018), and Roth et al. (2021a), and includes excitation via collisions with CO and electrons, as well as radiative processes. In Section 5.4, we briefly discuss the conditions for which a time-dependent solution of the molecular excitation produces more accurate results than the steady-state treatment.

The emission line profiles from C/2016 R2 are simulated using a two-component (conical jet + ambient coma) outgassing model, allowing the molecular production rates and outflow velocities to vary as a function of coma position. Due to a lack of known collision cross-sections, previous models for cometary CO emission have relied on approximations for the CO collisional excitation rates. We therefore performed quantum scattering calculations (using the coupled-states approximation; Klos & Lique 2018) to determine, for the first time, accurate state-to-state collisional (de-)excitation rate coefficients for the CO–CO system. The parameters retrieved

from our SUBLIME modeling provide new insights into the coma properties and intrinsic nature of C/2016 R2 (PanSTARRS), one of the most unusual comets of our time.

2. Observations

2.1. James Clerk Maxwell Telescope

Observations of comet C/2016 R2 (PanSTARRS) were conducted during the period 2018 January 13 to 2018 February 1 using the 15 m JCMT atop Maunakea. The comet’s position on the sky was tracked using Jet Propulsion Laboratory (JPL) Horizons ephemeris number 14. During this time, the heliocentric distance decreased from $r_H = 2.9$ to 2.8 au, the geocentric distance increased from $\Delta = 2.1$ to 2.3 au, and the Sun–comet–observer (phase) angle increased from $\phi = 15^\circ$ to 19° .

Spectral line observations were carried out using the RxA3m millimeter-wave receiver (operating at 212 to 274 GHz) and the Heterodyne Array Receiver Program (HARP) 16-element submillimeter focal-plane receiver array (operating at 325 to 375 GHz; Buckle et al. 2009). HARP observations of CO $J = 3 - 2$ were made in two modes: stare and jiggle. During stare observations the pointing receptor, H05, tracked the coordinates of the target while the other receptors (in the square array) each recorded a spectrum at an offset point in the coma. The 30'' spacing between the receptors means that the target field is undersampled during stare observations, as a result of the 14'' telescope beam FWHM at 346 GHz (20'' at 230 GHz). Jiggle observations, on the other hand, are designed to obtain a spatially complete sampling of the target field. We used the HARP4 jiggle pattern to obtain spectra for each point on a $7'' \times 7''$ grid, covering a $2' \times 2'$ map area. Position switching (offset by 300'' in azimuth) was performed for the purpose of subtracting spectral contributions from the terrestrial atmosphere and telescope optics. The performance of the individual HARP receptors was monitored throughout the observations, and any suboptimal receptors were flagged and masked during data reduction.

Most of the spectral data were obtained at a resolution of 31 kHz, across a 250 MHz bandpass, using the Auto Correlation Spectral Imaging System (ACSIS) digital autocorrelation spectrometer. For the ^{13}CO and $C^{18}O$ spectral windows (observed simultaneously), 61 kHz resolution was used, and for CH₃OH, a relatively coarse resolution of 448 kHz (over a 1000 MHz bandpass) was used to cover multiple transitions of CH₃OH in the $J = 7 - 6$ band at 338 GHz.

Standard observatory amplitude and pointing calibrations were performed at regular (at most, hourly) intervals, demonstrating nominal performance. The all-sky pointing performance of JCMT is $\sim 2''$ in each of the (azimuth, elevation) coordinates (Coulson et al. 2020), but telescope tracking accuracy over the course of an hour for a given source is usually better than 1''. Comparison of the actual telescope tracking position (apparent R.A. and decl.) with the ephemeris showed tracking errors to be less than 0''.1 in each coordinate on each night. The observed antenna temperatures (T_A^*) were corrected for sky opacity, forward scattering, and spillover. Beam efficiency (η) was corrected using the standard values of $\eta = 0.60$ for RxA3m and 0.64 for HARP. The resulting main beam brightness temperature scale (T_{MB}) is expected to be accurate to within $\pm 10\%$.

Table 1
Log of JCMT Spectral Line Observations

Date	Species	Transition	Obs. Mode	τ_0	Int. (s)	$\int T_{\text{MB}} dv$ (mK km s ⁻¹)	\bar{v} (km s ⁻¹)	r_{H} (au)	Δ (au)	ϕ (°)
2018-01-13.215	CO	3–2	HARP stare	0.10	600	870(92)	–0.21(0.04)	2.88	2.13	14.8
2018-01-13.253	HCN	4–3	HARP stare	0.10	1200	<78	...	2.88	2.13	14.9
2018-01-13.338	CH ₃ OH	7–6	HARP stare	0.11	900	73(20) ^a	–0.08(0.13) ^a	2.88	2.13	14.9
2018-01-13.401	HCO ⁺	4–3	HARP stare	0.11	900	<93	...	2.88	2.13	14.9
2018-01-13.437	H ₂ CO	5 _{1,5} –4 _{1,4}	HARP stare	0.11	900	<110	...	2.88	2.13	14.9
2018-01-14.206	CO	2–1	RxA3m	0.17	600	542(71)	–0.18(0.08)	2.87	2.14	15.1
2018-01-14.248	CO	3–2	HARP stare	0.17	120	1078(154)	–0.24(0.10)	2.87	2.14	15.1
2018-01-14.260	CO	3–2	HARP stare	0.17	600	926(103)	–0.22(0.05)	2.87	2.14	15.1
2018-01-14.273	CO	3–2	HARP stare	0.17	120	831(131)	–0.21(0.06)	2.87	2.14	15.2
2018-01-14.333	¹³ CO	3–2	HARP stare	0.16	900	<229	...	2.87	2.14	15.2
2018-01-14.333	C ¹⁸ O	3–2	HARP stare	0.16	900	<282	...	2.87	2.14	15.2
2018-01-14.367	CO	3–2	HARP jiggle	0.15	1780	834(114)	–0.25(0.04)	2.87	2.14	15.2
2018-01-14.384	CO	3–2	HARP stare	0.15	120	881(140)	–0.27(0.12)	2.87	2.14	15.2
2018-01-15.197	CO	3–2	HARP stare	0.09	120	1084(130)	–0.21(0.06)	2.87	2.14	15.4
2018-01-15.213	CO	3–2	HARP jiggle	0.08	1780	1145(131)	–0.23(0.02)	2.87	2.14	15.4
2018-01-15.231	CO	3–2	HARP stare	0.08	120	1028(117)	–0.23(0.05)	2.87	2.14	15.4
2018-01-15.253	¹³ CO	3–2	HARP stare	0.08	900	<84	...	2.87	2.14	15.4
2018-01-15.253	C ¹⁸ O	3–2	HARP stare	0.08	900	<112	...	2.87	2.14	15.4
2018-01-15.271	CO	3–2	HARP stare	0.08	120	1015(114)	–0.19(0.05)	2.87	2.14	15.4
2018-01-20.247	CO	3–2	HARP stare	0.06	600	745(76)	–0.23(0.03)	2.85	2.18	16.8
2018-01-25.322	CO	3–2	HARP stare	0.14	600	881(96)	–0.23(0.04)	2.83	2.23	17.9
2018-01-31.338	CO	3–2	HARP stare	0.08	600	910(93)	–0.23(0.03)	2.80	2.29	19.1
2018-02-01.278	CO	3–2	HARP stare	0.14	600	768(84)	–0.18(0.04)	2.80	2.30	19.3

Note.

^a Integrated over the three strongest CH₃OH transitions (see Section 4.6).

Table 1 shows a summary of the JCMT spectral line observations, including the zenith opacity at 225 GHz (τ_0) and on-source integration time per observation (Int.). Integrated line intensities ($\int T_{\text{MB}} dv$) and centroid velocities (\bar{v}) are also given (with 1σ uncertainties in parentheses). The uncertainties on $\int T_{\text{MB}} dv$ include the 10% intensity calibration error, added in quadrature with the statistical error.

2.2. Submillimeter Array

Interferometric observations of C/2016 R2 were made on 2018 February 21 using the Submillimeter Array (SMA), when the comet was at $r_{\text{H}} = 2.7$ au; $\Delta = 2.5$ au; $\phi = 21^\circ$. Five of the SMA (6 m) antennas were online and in the subcompact (SUB) configuration at the time of the observations, resulting in a spatial resolution of $\approx 4''.4 \times 7''.7$ at 230 GHz. The two SMA receivers were both tuned to 1.3 mm to cover the CO $J = 2 - 1$ transition at 230.538 GHz. The SMA Wideband Astronomical ROACH2 Machine (SWARM) correlator provides 8 GHz bandwidth per sideband, divided into four equal-sized chunks with a uniform spectral resolution of 140 kHz (0.18 km s^{-1} at 230 GHz). Position and Doppler-tracking of the comet over a 5 hr observing period was performed using JPL Horizons orbital solution number 14, and compensated for by the correlator in real time.

Calibration of visibility phases and amplitudes was performed using periodic observations of quasars 0336 + 323 and 3c111, at 15 minute intervals. Measurements of Uranus were used to obtain an absolute scale for calibration of the flux densities. All data were phase- and amplitude-calibrated using the Millimeter Interferometer Reduction (MIR) software package.¹¹ The calibrated SMA data were then exported in

uvfits format for subsequent imaging and analysis using the Common Astronomy Software Applications (CASA) software package version 5.1 (Jaeger 2008).

Interferometric imaging and deconvolution was performed using the Hogbom clean algorithm, with a $20''$ mask centered on the peak of CO emission and a threshold of twice the rms noise per channel ($\sigma = 0.19$ Jy). Natural visibility weighting was used and the pixel size was set to $0''.5$.

3. Results

3.1. JCMT CO Spectral Line Time Series

A time series of the observed JCMT CO $J = 3 - 2$ spectra is shown in Figure 1. Individual spectra have been Doppler-corrected for the comet's radial velocity with respect to the observer, and were baseline-subtracted using low-order polynomial fits to the emission-free regions. Spectra in this figure were selected based on on-source integration times of at least 600 s, to exclude the noisier data obtained from shorter-integration spectra on some of the observing dates.

The comet's radial velocity in the cometocentric rest frame increased steadily throughout the period of observations, but the double-peaked line profile, consisting of a strong, narrow blueshifted peak and a weaker redshifted peak remained apparently constant (within the noise). Given the relatively small phase angle (ϕ) of our observations, such blueshifted emission is explained as a result of enhanced outgassing from the side of the nucleus facing the Sun (and Earth), compared with the nightside.

To search for temporal variability in the comet's activity, the spectrally integrated emission line area ($\int T_{\text{MB}} dv$) is plotted as a function of time in Figure 2. No significant time variability was detected, implying that the CO outgassing rate

¹¹ <https://lweb.cfa.harvard.edu/~cqi/mircook.html>

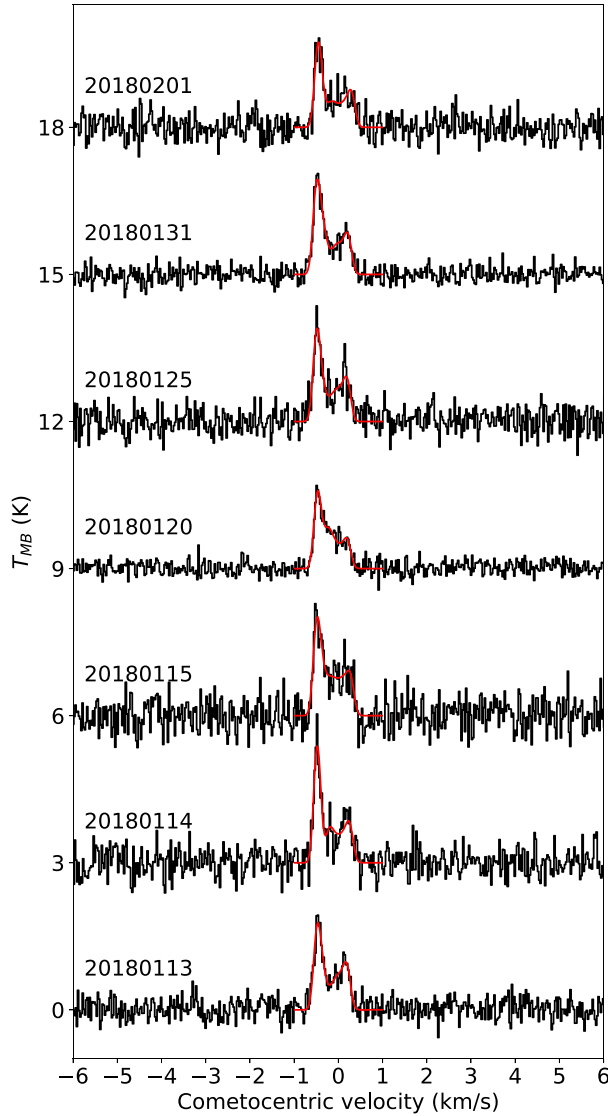


Figure 1. Time sequence of CO $J=3-2$ spectra observed using JCMT (in the cometocentric rest frame), shown with additive baseline offsets. The observing date for each spectrum is given in the format YYYYMMDD. For clarity, only spectra with an on-source observing time of at least 600 s are shown. Best-fitting spectral models are overlaid with red curves (see Section 4.3).

and rotational temperature (T_{rot}) were probably close to steady state during the time period of our observations, although variations in both quantities could have canceled each other out to some degree—the CO $J=3-2$ line intensity varies by a factor of 1.5 between $T_{rot} = 15-25$ K (a plausible range for this comet based on the findings of Biver et al. (2018); see also Section 4.2).

3.2. CO Single-dish Mapping with JCMT HARP

HARP jiggle-map spectral cubes from 2018 January 14 and 2018 January 15 were Doppler-corrected and averaged together (with rejection of masked pixels). The spectrally integrated (moment 0) map of CO $J=3-2$ emission is shown in Figure 3, with contour levels plotted in units of $3\sigma n_c^{-0.5}$, where

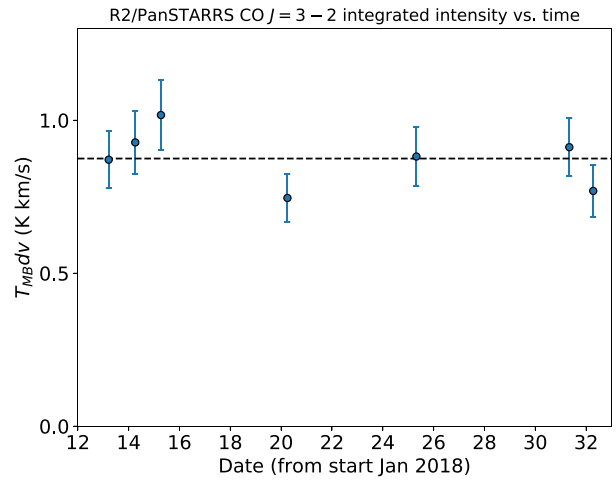


Figure 2. Spectrally integrated CO $J=3-2$ line intensities observed using the JCMT as a function of time, based on the spectra shown in Figure 1. The horizontal line shows the error-weighted mean. Error bars include the statistical uncertainty, with an additional 10% calibration uncertainty added in quadrature.

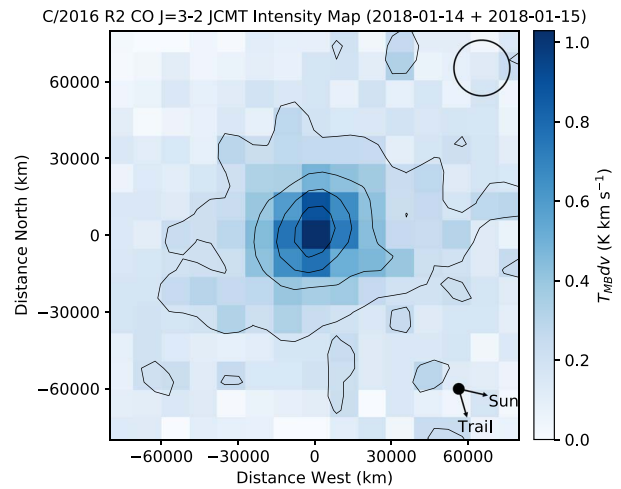


Figure 3. Spectrally integrated CO $J=3-2$ map for comet C/2016 R2 (PanSTARRS), from the average of HARP jiggle observations on 2018 January 14 and 2018 February 15. The FWHM of the circular Gaussian JCMT beam is indicated upper right, and the sky-projected solar and orbital trail (negative of the comet’s velocity) vectors are shown in the lower right. Contours are in units of 3σ and the axes are aligned with the equatorial (R.A./decl.) grid.

σ is the average rms noise of the data cube (equal to $T_{MB} = 72 \text{ mK km s}^{-1}$) and n_c is the number of spectral channels in the moment 0 integral. The CO $J=3-2$ integrated line intensity, averaged over the entire $120'' \times 120''$ HARP data cube, was $164 \pm 19 \text{ mK km s}^{-1}$ on 2018 January 14 and $202 \pm 22 \text{ mK km s}^{-1}$ on 2018 January 15. These values are sufficiently similar (given the uncertainties) to justify combining the two data sets. The CO spatial distributions were also apparently identical on the two dates, with consistent radial intensity profiles (within the uncertainties).

The CO coma is diffuse and spatially extended compared with the 22,000 km JCMT beam, with some weak evidence for deviations from circular symmetry about the nucleus. Emission

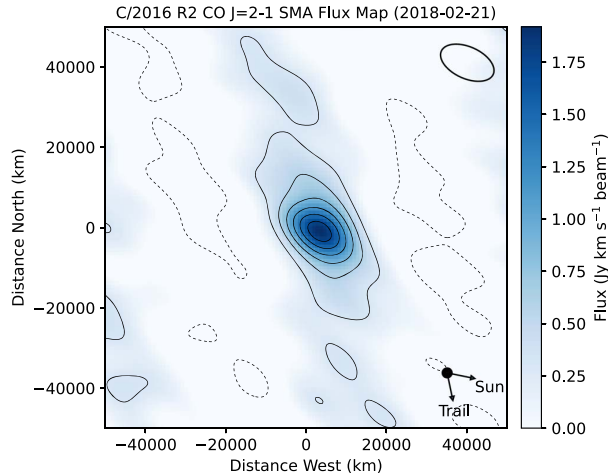


Figure 4. Spectrally integrated CO $J = 2 - 1$ emission map for comet C/2016 R2, obtained using the SMA on 2018 February 21. The FWHM (and orientation) of the elliptical Gaussian restoring beam is indicated (upper right), and the sky-projected solar and orbital trail vectors are shown in the lower right. Contours are in units of 3σ and the axes are aligned with the equatorial (R.A./decl.) grid, with the origin at the SMA phase tracking center. Negative contours are shown with a dashed line style.

is detected (at the 3σ level) up to a radial distance 82,000 km west of the image center, which is in a direction similar to the sky-projected sunward vector (103° clockwise from north), whereas the 3σ contour extends only 58,000 km to the east. The second contour (at 6σ) also shows an excursion in the sunward direction into a pixel with an intensity 2.2σ larger than the mean of the other pixels at the same cometocentric distance. These features provide tentative evidence for preferential outgassing on the illuminated (sunward) side of the nucleus. The (normalized, azimuthally averaged) CO spectral line profile is plotted as a function of distance from the center of the image in Appendix D (Figure 16), and reveals a consistent excess in the blueshifted emission out to cometocentric distances of at least $r_c \sim 80,000$ km.

3.3. CO Interferometric Mapping with the SMA

The CO $J = 2 - 1$ intensity map observed using SMA is shown in Figure 4, integrated over the velocity width of the detected emission. The intensity reaches a peak $2''5$ west of the phase center, which may be partly a result of asymmetrical outgassing in the sunward direction, or errors in the position of the comet nucleus compared with the JPL Horizons ephemeris orbital solution.

The coma shows an extended morphology in an approximately north–south direction, and is less well resolved in the east–west direction, where significant large-scale flux appears to have been resolved out by the interferometer, resulting in negative side lobes (regions with dashed contours) apparent on either side of the comet. Although the orientation of the spatially extended emission (defined by the outermost 3σ contour) matches closely the direction of the comet’s (sky-projected) orbital trail, it also aligns with an axis of strong artifacts in the interferometric point-spread function, so the reality of this asymmetric, extended feature remains questionable.

4. Radiative Transfer Modeling

As a result of near-spherical expansion, cometary comae span an extremely broad range of densities over a short distance. Consequently, their gases are often subject to a range of excitation conditions within a single telescope beam, governed by a balance of microscopic collisional and radiative processes (Bockelée-Morvan et al. 2004a), and are generally not in local thermodynamic equilibrium (LTE). To interpret cometary rotational spectra therefore requires detailed excitation and radiative transfer modeling. Here we introduce a new code called SUBLIME for simulating the rotational emission lines from cometary coma molecules in three dimensions (two spatial and one spectral). The SUBLIME code is based on the open-source version 1.9.3 of the LIME (Line Modeling Engine) code by Brinch & Hogerheijde (2010).¹²

The basic equations of radiative transfer and excitation used in our model are described in Appendix A. Some recently published coma radiative transfer models have invoked the steady-state approximation (e.g., Bøgelund & Hogerheijde 2017; de Val-Borro et al. 2018; Cordiner et al. 2019), setting $dN_i/dt = 0$ in Equation (A4), which allows the energy-level populations to be solved independently (in parallel) at a large number of discrete positions within the region of interest. This approximation facilitates the treatment of complex (3D) coma morphologies, but comes at the expense of discarding the effects of the outflow dynamics, which can be important for molecules such as CO, with small dipole moments and hence slow rotational transitions relative to the dynamical timescale (see Section 5.4).

LIME employs the steady-state approximation. We therefore substantially modified the code to enable the more physically accurate, time-dependent solution of Equation (A4), using the CVODE solver (Hindmarsh 2019) to calculate the molecular excitation along radial trajectories of the outflowing coma gases. The time-dependent solution has previously been implemented in the models of Bockelée-Morvan (1987) and Biver et al. (1999), and allows the temporal evolution of molecular excitation in the rapidly expanding coma to be properly accounted for. The time-dependent version of our code, as used in the present study, ignores the impact of opacity/photon trapping on the molecular excitation, which is negligible for the molecules considered in this study (see Appendix A).

SUBLIME calculates the molecular excitation along radial vectors, which are then interpolated onto an unstructured 3D grid (Delaunay 1934), configured with a density of grid points proportional to the gas density. The broad range of density and size scales in the coma (covering many orders of magnitude, from the \sim kilometer-sized nucleus to the $\sim 10^6$ km-scale outer coma) can thus be sampled much more efficiently than with a uniform grid spacing. To simulate coma asymmetries and jets using this method, the spatial domain is divided into multiple solid-angle regions (Ω_i), each with its own outflow velocity (v_i), kinetic temperature (T_i), and molecular production rate (Q_i). A separate CVODE calculation is performed for each solid-angle region. In the present paper, we use two regions, corresponding to (1) the ambient coma and (2) a conical jet with its apex at the center of the nucleus.

For all models, we used a Delaunay grid with 10,000 points, between $r_c = 500$ m (the assumed radius of the nucleus) and an

¹² Available at <https://github.com/lime-rt/lime/releases>.

outer radius of 10^6 km. Tests showed that this grid density was sufficient to produce reliable spectral line models at the resolution of our observations; adding more grid points did not significantly change the results. The precise grid point locations are selected pseudo-randomly for each model run (Brinch & Hogerheijde 2010), but we fixed the random number generator seed so that an identical grid was produced every time, providing numerical stability in order to facilitate reliable (repeatable) parameter retrievals. During ray tracing, we employed the LIME `traceray_smooth` algorithm, which interpolates the level populations between grid points, thus reducing grid-related artifacts in the output image. A pixel size of $0''.5$ and a channel spacing of 25 m s^{-1} were chosen for the model images to sufficiently sample the spatial and spectral-resolution elements of the JCMT and SMA observations. To accurately capture the rapid (nonlinear) flux increase on subpixel scales toward the center of the image, due to the strongly increasing coma density with decreasing r_c , we employed cartesian supersampling (on a regularly spaced grid of 30×30 rays) for each pixel within the central 4×4 pixel region of each image.

4.1. CO–CO Collision Rate Coefficients

As the dominant coma gas (McKay et al. 2019), CO is the primary collision partner in our model, and is therefore the main species responsible for the redistribution of thermal energy among the rotational states (J) of the observed gases. Knowledge of the CO–CO collision rate coefficients ($k_{J_1 J_2}$) is therefore required to correctly model the CO emission from the comet. Previous studies (Biver et al. 2018; Wierzos & Womack 2018) made gross approximations for these rates, so their results remain uncertain. Here we employ quantum calculations to model the CO–CO collisions, allowing us to accurately determine the CO excitation for the first time in a CO-dominated cometary coma.¹³

To describe the interaction between colliding CO molecules, we used the 4D potential energy surface (PES) with rigid CO molecules calculated by Vissers et al. (2003). The PES was calculated using the coupled-cluster single, double, and perturbative triples (CCSD(T)) method with augmented triple zeta basis (aug-cc-pVTZ). The accuracy of the PES was benchmarked with respect to experimental studies (Surin et al. 2007; Sun et al. 2020). The scattering calculations were performed with the `Moscat` code under the assumption of distinguishable particles (Hutson & Green 1994). A series of tests was performed, revealing that the most accurate close-coupling (CC; Green 1975) approach would not be feasible in terms of computer memory and processing time. We therefore explored the possibility of using the coupled-states (CS) approximation (see Kłos & Lique 2018 for a review of these methods). The differences between CC and CS were found, on average, to be less than a factor of 1.5–2 (and never higher than a factor of 3).

Assuming that we can distinguish the CO molecules, the first one is the target (with the rotational state characterized by quantum number J_1), and the second is the collider (J_2). Collisional rate coefficients $k_{J_1 J_2 \rightarrow J_1' J_2'}$ were then computed by averaging the cross-sections over the Boltzmann distribution of

collisional energies (Equation (1)),

$$k_{J_1 J_2 \rightarrow J_1' J_2'}(T) = \left(\frac{8}{\pi \mu k_B^3 T^3} \right)^{\frac{1}{2}} \int_0^\infty \sigma_{J_1 J_2 \rightarrow J_1' J_2'}(E_c) E_c e^{-\frac{E_c}{k_B T}} dE_c, \quad (1)$$

where μ is the reduced mass of the system, k_B is a Boltzmann constant, σ is the cross-section of a given transition, and E_c is the collisional energy. Rate coefficients used in the radiative transfer model ($k_{J_1 \rightarrow J_1'}(T_{\text{kin}})$; see Appendix B, Table 3) were calculated by averaging over a thermal rotational distribution for the initial excitation state of the collider, and summed over its final state as follows:

$$k_{J_1 \rightarrow J_1'}(T) = N_{J_2=0} \sum_{J_2'} k_{J_1, J_2=0 \rightarrow J_1', J_2'} + N_{J_2=1} \sum_{J_2'} k_{J_1, J_2=1 \rightarrow J_1', J_2'} + \dots \quad (2)$$

where summation is over all possible final states of the collider. N_{J_2} is the (Boltzmann) energy-level population of the collider, given by

$$N_{J_2} = \frac{(2J_2 + 1) e^{-\frac{E_{J_2}}{k_B T}}}{\sum_{J_2} (2J_2 + 1) e^{-\frac{E_{J_2}}{k_B T}}}, \quad (3)$$

where E_{J_2} is its energy level. Calculations were performed up to a collision energy of 300 cm^{-1} and maximum rotational quantum number $J_1 = J_2 = 5$, leading to rate coefficients for kinetic (and rotational) temperatures valid up to 30 K. Such a restricted set of rate coefficients is appropriate for modeling the CO excitation in C/2016 R2 due to the relatively low coma kinetic temperature (~ 20 K; Biver et al. 2018); at this temperature, energy levels above $J = 5$ comprise less than 1% of the total CO population in the collisionally dominated zone. Our model for C/2016 R2 includes levels up to $J = 40$, but for $J > 5$, the CO–CO collision rates are assumed to be the same as for para- H_2 colliding with CO (Yang et al. 2010). A more detailed explanation of the collision rate calculation method, including calculation of rate coefficients for kinetic temperatures up to 100 K, is currently in preparation.

4.2. Modeling the JCMT CO $J = 2 - 1$ and $J = 3 - 2$ Data

On 2018 January 14, the CO $J = 2 - 1$ and $J = 3 - 2$ lines were observed in close succession (within 1.3 hr of each other). Given the lack of significant temporal variability in the $J = 3 - 2$ line strength around this date (Figure 1), differences between the strengths of these two lines can be assumed to originate as a result of (1) their different intrinsic line strengths and (2) differences in the excitation of the upper-state energy level. According to Equation (A4), the level populations depend on the collision rates k_{jn} (where n is the local density), which in turn depend on the CO production rate, coma outflow velocity, and kinetic temperature. Modeling the two CO lines simultaneously therefore provides a diagnostic of the coma temperature, while the line profile provides information on the coma outflow velocity along the line of sight.

There is insufficient information from these relatively low signal-to-noise, 1D spectra to infer the entire coma physical structure, so we adopt a modified Haser (1957) model. The

¹³ Ndengué et al. (2015) previously studied the energy transfer in CO–CO collisions, but their results were only partly converged and contain a systematic error for some (but not all) transition rates.

assumption of isotropically expanding gas, with a constant production rate and outflow velocity (as described by the 1D Haser model), is routinely used for analysis of cometary spectra and images observed across the range of wavelengths (e.g., Bockelée-Morvan et al. 2004a; Cochran et al. 2012; Cordiner et al. 2014). In the case of strongly asymmetric outgassing, however, as observed for C/2016 R2, the assumption of spherical symmetry is no longer applicable, so a more flexible 3D model is required.

In the present study, we adopt the simplest physically reasonable model capable of fitting the observed data. We consider two different outflow components, C_1 and C_2 , corresponding to solid-angle regions Ω_1 , Ω_2 with independent production rates (Q_1 , Q_2) and outflow velocities (v_1 , v_2). This assumes that the nucleus can be divided into two different activity regimes: (1) an ambient outflow from the majority of the (thermally activated) sublimating area of the nucleus, and (2) enhanced gas production from a (set of) spatially confined vent(s) or jet(s), in particular, on the sunward-facing side of the nucleus. Similar two-component models (involving a sunward jet and ambient/isotropic coma, or a hemispherically asymmetric outflow) have been invoked previously to explain asymmetries in high-resolution spectral line profiles from several comets, including 29P/SW1 (Festou et al. 2001), O1/Hale–Bopp (Gunnarsson 2003), 19P/Borelly (Bockelée-Morvan et al. 2004b), 2I/Borisov (Cordiner et al. 2020), 46P/Wirtanen (Roth et al. 2021b), and C/2015 ER61 (Roth et al. 2021a). The increased production rate and outflow velocity measured on the sunward side of these comets is consistent with the results of fluid dynamic and Monte Carlo coma models (Crifo et al. 1999; Fougere et al. 2016), and arises as a result of elevated temperatures in both the coma and the nucleus, due to increased solar insolation. While more complex coma parameterizations can be envisaged, the simplest model capable of fitting the data should be the best constrained, with the additional benefit of being more efficient to configure and run.

We construct a SUBLIME model to simultaneously fit the CO $J=2-1$ and $J=3-2$ line profiles, assuming a constant coma kinetic temperature (after Biver et al. 2018). Component C_1 is defined by a conical region about the subsolar point of the nucleus, with half-opening angle θ , whereas C_2 is the remaining, ambient coma. We used the MPFIT nonlinear least-squares routine (Markwardt 2012) to find the optimal set of parameters (Q_1 , Q_2 , v_1 , v_2 , θ). The model images were convolved with the (Gaussian) JCMT beam pattern and normalized by their respective beam efficiency factors before comparing them with the observations. Statistical (1σ) error estimates are obtained for each parameter from the diagonal elements of the MPFIT covariance matrix.

The best-fitting model spectra are shown in Figure 5, corresponding to $Q_1 = (1.8 \pm 0.4) \times 10^{28} \text{ s}^{-1}$, $Q_2 = (2.2 \pm 0.3) \times 10^{28} \text{ s}^{-1}$, $v_1 = 0.50 \pm 0.01 \text{ km s}^{-1}$, $v_2 = 0.29 \pm 0.02 \text{ km s}^{-1}$, $\theta = 27^\circ \pm 5^\circ$, and $T_{\text{kin}} = 18.7 \pm 2.3 \text{ K}$. The retrieved kinetic temperature is consistent with the range of values 18.6 ± 2.6 to 24.2 ± 7.9 derived by Biver et al. (2018) using multiple lines of CH_3OH on 2018 January 23–24. The total CO gas production rate from our model is $Q_{\text{CO}} = (3.9 \pm 0.7) \times 10^{28} \text{ s}^{-1}$, and the ratio of production rates per unit solid angle between the jet and ambient coma is $R_Q = (Q_1/\Omega_1)/(Q_2/\Omega_2) = 14.5 \pm 3.9$. Given the strong dependence of the production rate for both components on the size of their solid-angle regions, R_Q is a more physically

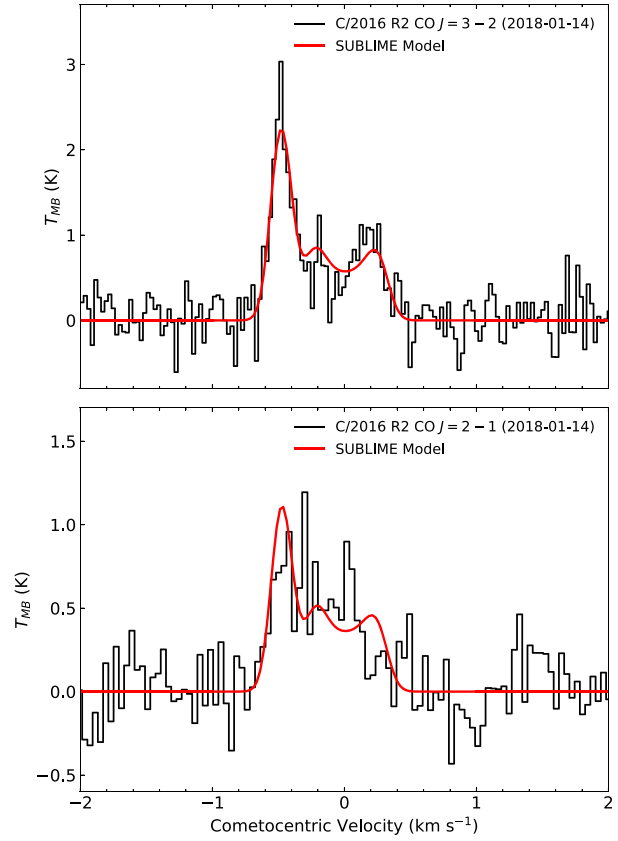


Figure 5. JCMT spectra of CO $J=3-2$ (top) and $J=2-1$ (bottom), in the cometocentric rest frame. The best-fitting SUBLIME model is overlaid with the red curves.

meaningful quantity than the simple ratio of production rates (Q_1/Q_2), and reveals the degree to which the comet’s activity is enhanced due to heating by the Sun in the vicinity of the subsolar point. The overall quality of fit is good considering the noise, and reproduces well the asymmetry of the $J=3-2$ line. We also performed fits allowing the angle of the jet axis to vary with respect to the Sun–comet vector, but the quality of the fit was not significantly improved. Additional models were run allowing different T_{kin} values for the two coma components, with best-fitting results $T_{\text{kin}_1} = 19.3 \pm 3.7 \text{ K}$ and $T_{\text{kin}_2} = 17.9 \pm 4.8 \text{ K}$, but again, the overall quality of the fit was not improved. The consistency of T_{kin_1} and T_{kin_2} (within their respective errors) provides further justification for adopting a uniform T_{kin} value throughout the rest of this study.

4.3. Modeling the Average and Time-series JCMT CO $J=3-2$ Spectra

Given the relative constancy of the comet’s CO emission over time, a useful estimate for the total (time-averaged) CO production rate over the course of our observations was obtained by taking the average of all the JCMT CO ($3-2$) spectral data listed in Table 1. After Doppler-correcting each spectrum to the cometocentric rest frame and weighting them by $1/\sigma^2$, the resulting average spectrum was modeled using the same procedure described above. The best-fitting model is shown in Figure 6, and corresponds to $Q_{\text{CO}} = (5.3 \pm 0.2) \times 10^{28} \text{ s}^{-1}$, $R_Q = 7.4 \pm 0.4$, $v_1 = 0.51 \pm 0.01 \text{ km s}^{-1}$,

Table 2
Best-fit Model Results for Individual JCMT (and SMA) Spectra of C/2016 R2

Date	Q_1 (10^{28} s^{-1})	R_Q	v_1 (km s^{-1})	v_2 (km s^{-1})	θ (deg.)	ϕ_{jet} (deg.)
2018-01-13	4.5 (0.7)	6.8 (4.5)	0.51 (0.01)	0.23 (0.02)	60 (5)	18 (6)
2018-01-14	4.0 (0.9)	10.8 (2.9)	0.50 (0.01)	0.29 (0.02)	32 (7)	7 (10)
2018-01-15	7.4 (1.6)	9.6 (3.1)	0.52 (0.02)	0.31 (0.03)	77 (13)	37 (19)
2018-01-20	3.9 (1.8)	17.2 (10.8)	0.50 (0.01)	0.24 (0.01)	42 (19)	34 (11)
2018-01-25	5.0 (0.9)	10.4 (1.7)	0.53 (0.01)	0.24 (0.02)	58 (6)	20 (7)
2018-01-31	5.7 (0.8)	7.3 (0.7)	0.53 (0.01)	0.26 (0.01)	64 (3)	12 (4)
2018-02-01	4.4 (0.8)	4.9 (0.9)	0.49 (0.01)	0.33 (0.02)	46 (8)	8 (12)
JCMT avg.	5.3 (0.6)	7.4 (0.4)	0.51 (0.01)	0.25 (0.01)	62 (2)	24 (2)
2018-02-21 ^a	6.7 (0.9)	9.2 (1.5)	0.64 (0.02)	0.20 (0.02)	74 (7)	21 ^b

Notes. 1σ statistical uncertainties on each value are given in parentheses. Uncertainties on Q_i include a 10% intensity calibration error, added in quadrature with the statistical error.

^a SMA best-fitting parent visibility model.

^b The jet axis set to direction of the comet–Sun vector due to a lack of constraints caused by the lower spectral resolution of the SMA data.

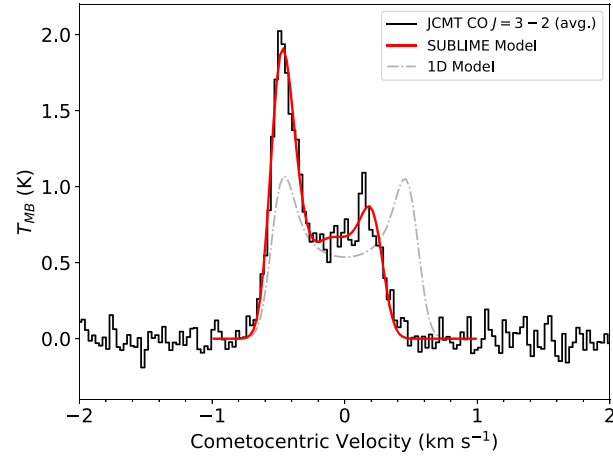


Figure 6. Weighted average CO $J = 3 - 2$ spectrum from the JCMT HARP pointing receptor (in the cometocentric rest frame). The best-fitting SUBLIME 3D model is overlaid using a red curve. The dotted–dashed gray curve shows the best-fitting 1D model, assuming a spherically symmetric coma.

$v_2 = 0.25 \pm 0.01 \text{ km s}^{-1}$, and $\theta = 62^\circ \pm 2^\circ$. In this model the direction of the jet’s axis with respect to the line of sight (ϕ_{jet}) was also allowed to vary, and the best fit was for $\phi_{\text{jet}} = 24^\circ \pm 2^\circ$ ($7^\circ \pm 2^\circ$ away from the mean Sun–comet vector). These values are within 2σ of the parameters derived for the simultaneous fit to the $J = 2 - 1$ and $J = 3 - 2$ data on 2018 January 14. Allowing for an additional 10% calibration error, the total uncertainty on the CO production rate is $0.6 \times 10^{28} \text{ s}^{-1}$.

Individual fits were also performed to the time series of the spectra presented in Figure 1. A good fit was obtained in each case, and the results are given in Table 2. While the majority of these individual fit results are consistent (within $1-2\sigma$) with the average JCMT spectrum, notable deviations include the significantly narrower jet opening angle of $\theta = 32^\circ \pm 7^\circ$ on January 14. On February 1, the ambient coma showed an enhanced outgassing velocity (with $v_2 = 0.33 \pm 0.02 \text{ km s}^{-1}$), which was also accompanied by a reduction in R_Q to 4.9 ± 0.9 . Such variability in the detailed outflow morphology on specific epochs implies some inhomogeneity of the nucleus (and/or its

heating rate), leading to modest changes in the CO outgassing behavior over time.

4.4. Modeling the CO Spatial Distribution

To investigate the spatial morphology of the CO coma, we generated 3D (spectral–spatial) models for comparison with the JCMT HARP image cube. First, a SUBLIME model fit was performed for the CO $3 - 2$ spectrum extracted from the central map pixel (coinciding with the intensity peak in Figure 3), by optimizing the model parameters Q_1 , Q_2 , v_1 , v_2 , θ , and ϕ_{jet} . The model orientation (in the plane of the sky) was fixed so that the jet azimuth angle matched the direction of the sky-projected comet–Sun vector. This best-fitting CO parent model was then convolved by the JCMT beam shape, multiplied by the main beam efficiency and spectrally integrated to obtain the 2D map in the left panel of Figure 7.

Comparison of the contours in this figure with the observed CO map (Figure 3) shows that while the central intensity peak is accurately reproduced, the outermost contour of the observations lies, on average, well outside that of the model. This is more clearly demonstrated by comparing the azimuthally averaged radial profiles ($\langle T_{\text{MB}} \rangle_{\text{az}}$) of the modeled and observed CO emission, which are plotted as a function of distance from the nucleus in Figure 8. The best-fitting parent model (green dotted line) falls off more rapidly with distance than the observed data (filled black circles). This implies the presence of an excess of CO emission at large radii, which cannot be explained solely by CO released from the nucleus at a constant outflow velocity. The JCMT spectral baselines were well behaved over the course of our observations, and care was taken to ensure robust baseline removal through low-order polynomial subtraction, giving confidence regarding the reality of the observed extended CO emission (see also Figure 16).

We quantify the statistical significance of the extended emission using the reduced chi-square statistic $\chi_R^2 = \sum_i (y_i - y_m)^2 / \sigma^2 / d$, where y_i and y_m are the observed and modeled intensities, respectively, and d is the number of degrees of freedom (equal to the number of independent data points minus the number of free model parameters). The model χ_R^2 value is given in the legend of Figure 8, along with the associated probability (P) that the difference between the model and observations is due to statistical chance. With $\chi_R^2 = 2.1$

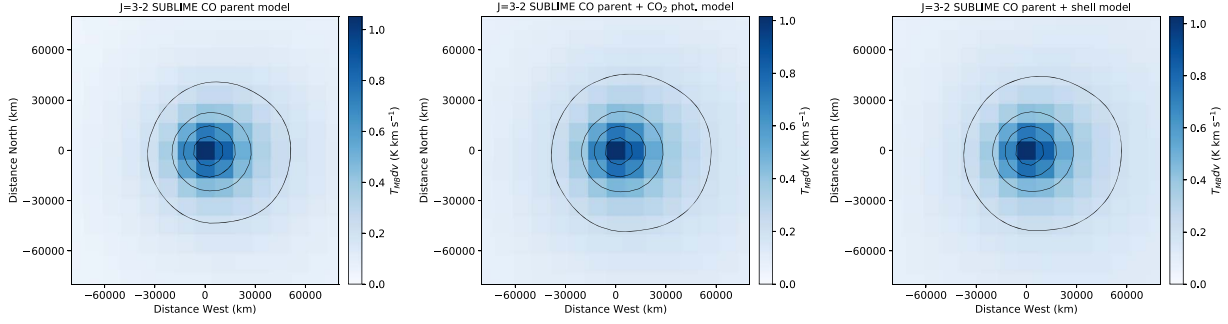


Figure 7. Spectrally integrated model CO $J = 3 - 2$ maps (for comparison with Figure 3), assuming CO solely as a parent molecule (left panel), CO produced from the nucleus plus CO_2 photolysis, with $Q(\text{CO}_2)/Q(\text{CO}) = 6.5$ (center panel), and CO from the nucleus, with an additional CO shell at $r_c \sim 1.4 \times 10^5$ km (right panel). Contour spacings are the same as in Figure 3.

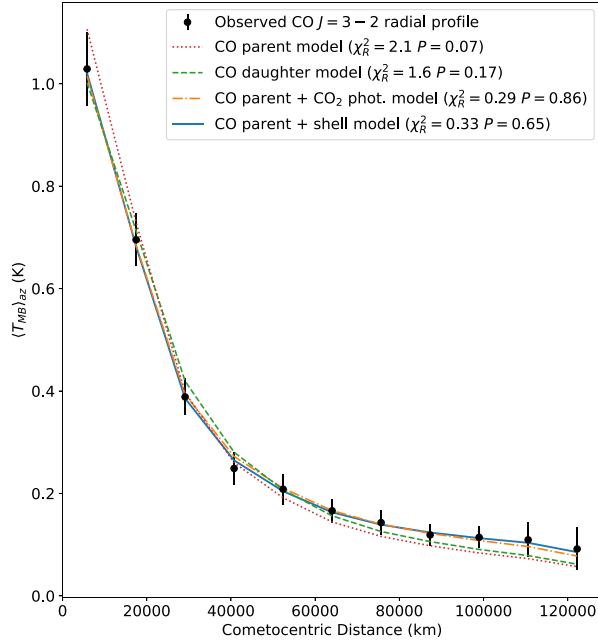


Figure 8. Azimuthal average (in 1-pixel bins) of the JCMT CO $J = 3 - 2$ emission map (Figure 3) as a function of distance from the central pixel (black circles). Best-fitting SUBLIME model results are overlaid, including Haser-type parent and daughter models (see the text). An improved fit is obtained at large radii when including a CO source from CO_2 photolysis (with a large $Q(\text{CO}_2)/Q(\text{CO})$ ratio of 6.5) or with the inclusion of an extended CO shell at $r_s = 1.2 \times 10^5$, with a density enhancement factor of $f = 1.8$.

and $P=0.07$, the CO parent model does not represent a good fit to the observations.

We consider three possibilities to account for the CO excess: (1) a CO $J = 3$ level population that increases more rapidly with distance than predicted, (2) an additional Haser-type extended CO source, and (3) a step-like enhancement in the coma density at a large distance from the nucleus. A reduction in the CO photodissociation rate (Γ_{CO}) would not reproduce the observed emission excess—at $r_H = 2.85$ au, $\Gamma_{\text{CO}} = 9.2 \times 10^{-8} \text{ s}^{-1}$ (Huebner & Mukherjee 2015), so at an outflow velocity of 0.2 km s^{-1} , the CO scale length is 2.2×10^6 km. CO photodissociation is therefore negligible within the 80,000 km JCMT field of view, so reducing Γ_{CO} by a factor of a few (its range of uncertainty) has no noticeable impact on the modeled CO density profile.

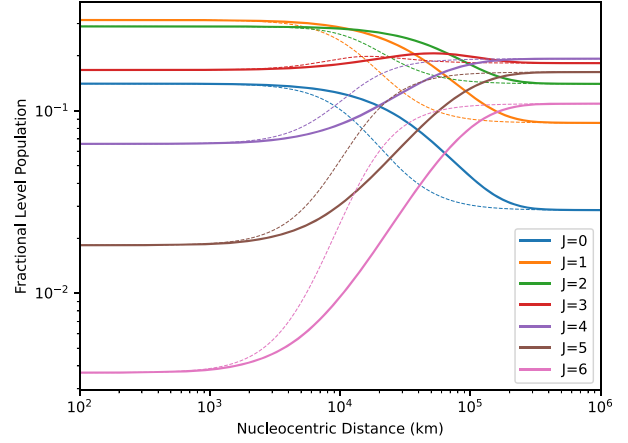


Figure 9. Fractional energy-level populations as a function of radius for the lowest seven CO rotational levels, using our SUBLIME time-dependent excitation model (solid curves) and the LIME steady-state solver (dotted curves). For clarity, only the populations from the higher-density jet component of the model (C_1) is shown. The steady-state model’s failure to account for coma dynamics leads to the onset of non-LTE effects too close to the nucleus.

For option 1, we need to consider the CO rotational level populations. As shown by Figure 9, the population of the $J = 3$ level (red curve) remains relatively constant as a function of distance from the nucleus. This is because the effective pumping rates (G_{ij}) into this level are closely balanced by radiative transitions out of the level, so on the larger distance scales, $\gtrsim 30,000$ km at which the excess CO emission becomes most visible, the $J = 3$ level population is already close to the value attained at fluorescence equilibrium, making excitation effects an unlikely explanation for the observed extended emission.

On smaller distance scales comparable with the size of the (central) JCMT beam, a lower rotational temperature could reduce the CO $3 - 2$ intensity, leading to a shallower radial profile in better agreement with the observations. However, assuming $T_{\text{kin}} = 16.4$ K (the 1σ lower limit derived in Section 4.2), the best-fitting χ_R^2 value is 1.6 with $P = 0.17$, which still does not represent a very good fit. Lower values of T_{kin} also appear less likely given the range of possible T_{kin} values (16–32 K) observed by Biver et al. (2018), so we seek alternative explanations for the shape of the $\langle T_{\text{MB}} \rangle_{\text{az}}$ profile.

The presence of an additional CO source (option 2) is worth considering, in light of previous evidence for extended CO

sources in cometary comae (Cottin & Fray 2008). However, the JCMT map is inconsistent with CO produced solely as a (Haser-type) photochemical daughter species. Our best-fitting SUBLIME model was modified to produce CO from photodissociation of an (unknown) parent molecule, with the production rate (Q_p) and parent photodissociation rate Γ_p free to vary (where $\Gamma_p = v_i/L_p$; v_i is the outflow velocity in conical region i and L_p is the parent scale length). The best-fitting, azimuthally averaged CO daughter model (with $\Gamma_p = 7.3 \times 10^{-5} \text{ s}^{-1}$, $Q_p = 7.0 \times 10^{28} \text{ s}^{-1}$) is shown in Figure 8, and systematically underfits the observed CO emission at large radii (with $\chi_R^2 = 1.6$).

A better fit to the observations can be obtained using a composite CO density profile, where CO is included as both a parent and a daughter species. Figures 7 and 8 show the best-fitting results from such a model, with CO originating from the nucleus at a total production rate of $Q_i = 5.5 \times 10^{28} \text{ s}^{-1}$ and an additional CO source in the coma from CO_2 photolysis ($\text{CO}_2 + h\nu \rightarrow \text{CO} + \text{O}$ at $\Gamma_{\text{CO}_2} = 1.5 \times 10^{-7} \text{ s}^{-1}$; Huebner & Mukherjee 2015). Although this composite model may appear plausible at first glance, and accurately reproduces the CO emission profile, it requires a CO_2 production rate 6.5 times larger than that of CO. Considering that McKay et al. (2019) derived an upper limit of $Q(\text{CO}_2) \lesssim 1.5 \times 10^{28} \text{ s}^{-1}$ based on Spitzer observations from 2018 February 12 and 2018 February 21 (i.e., 3.7 times less than the parent CO source), it seems unlikely that the comet could have been producing so much CO_2 at the time of our JCMT observations only a few weeks prior. Indeed, the large production rate required for any distributed molecular source to adequately fit the excess CO emission at large radii renders this an unlikely scenario in general, regardless of the assumed CO parent.

The possibility of non-Haser-type extended sources should also be considered, which could produce different radial density profiles, potentially resulting in a good fit to the observations. For example, Gunnarsson et al. (2002) developed a model for the sublimation and fragmentation of CO-rich icy grains to explain the extended CO distribution observed in comet 29P. Such detailed physical modeling is beyond the scope of our present study, however, but could be usefully investigated in a future article.

The third explanation we consider for the CO excess is an increase in coma density at large radii, which could result from temporal modulation of the gas production and/or outflow velocity, or a rapid onset of icy grain sublimation far from the nucleus. Slowing of the gas expansion rate in the outer coma (for example, due to sublimation of slow-moving icy grains—see, e.g., Ip 1986; Fougere et al. 2012), would also lead to an increase in gas density. From Appendix D, Figure 16, the CO line profile does not show any obvious evidence for coma deceleration with increasing distance, although we note that the weakness of the extended CO emission shell (representing $\sim 1/6$ of the parent source emission at $r_c = 60,000 \text{ km}$) would make its velocity signature difficult to detect given the noise.

To model such an outer CO shell, we implemented a multiplicative increase in the coma density n at radius r_s , smoothed by an exponential function such that $n(r) = 1 + (f - 1)/(1 + e^{(r_s - r)/w_s})$. The CO initial abundance, density enhancement factor (f), step radius (r_s), and smoothing width (w_s) were optimized to obtain the best fit to $\langle T_{\text{MB}} \rangle_{\text{az}}(r)$, and the resulting azimuthally averaged model emission profile and moment 0 map are shown in Figures 8 and 7, respectively.

The best-fitting model parameters are $f = 1.8$, $r_s = 1.2 \times 10^5 \text{ km}$, and $w_s = 10^3 \text{ km}$, corresponding to $\chi_R^2 = 0.33$ and $P = 0.65$. The small value for w_s implies that the density enhancement occurs abruptly, although larger values of w_s (up to $\sim 10^4 \text{ km}$) also produce radial CO profiles consistent with the observations, within errors. The distance over which the implied density enhancement occurs is therefore not well constrained by our data. This is primarily because the radius of the shell (projected in the plane of the sky) lies just beyond the spatial extent of our JCMT map.

For an outflow velocity of 0.5 km s^{-1} , a factor of approximately two density enhancement at $r_s = 1.2 \times 10^5 \text{ km}$ would be consistent with a corresponding drop in $Q(\text{CO})$ around 67 hr earlier (on January 12), but this seems perhaps unlikely given how uniform the comet’s activity was over the weeks following that date (Figure 1). The individual HARP maps from January 14 and 15 are also consistent with each other (within the 2σ noise level), and do not show any evidence for outward-moving CO density structure(s) over this period, so an onset of icy grain sublimation at large radii is our favored explanation.

Accounting for the extended CO shell leads to a marginally significant reduction in the nucleus production rate retrieved from the JCMT map, from $Q_i(\text{CO}) = (6.1 \pm 0.8) \times 10^{28} \text{ s}^{-1}$ to $(5.4 \pm 1.1) \times 10^{28} \text{ s}^{-1}$. Adding the same extended CO component to our model for the time-averaged JCMT CO spectrum (Figure 6) does not significantly alter the quality of the spectral fit, but the resulting CO production rate from the nucleus ($(4.3 \pm 0.1) \times 10^{28} \text{ s}^{-1}$) is 17% lower.

4.5. SMA CO Visibility Analysis

Radio interferometry is a powerful technique for analyzing the radial distributions of cometary gases to provide insight into their physical and chemical origins in the coma (Boissier et al. 2007; Cordiner et al. 2014; Roth et al. 2021b). This is due to the interferometer’s ability to simultaneously sample emission from a range of spatial scales at high accuracy, from the near-nucleus environment to the outer coma. Interferometric maps (such as the SMA CO map in Figure 4), however, suffer from significant artifacts due primarily to the sparsely filled telescope aperture, as well as Fourier image processing, regridding, and deconvolution artifacts. Cometary coma images suffer in particular from a lack of information on the largest spatial scales missed by the interferometer. Consequently, the preferred method for robustly analyzing interferometric data of such extended sources is by directly modeling the calibrated visibilities recorded by the telescope (i.e., the cross-correlation amplitudes between all antennas, as a function of baseline length).

Visibility models were generated for the SMA CO $J = 2 - 1$ observations of C/2016 R2, using our two-component SUBLIME model to test the same four scenarios as in Section 4.4. First, a fit was performed to the spectral line profile extracted at the emission peak of the SMA CO map (Figure 4). The best-fitting spectral line model is shown in Figure 10, corresponding to $R_Q = 9.2 \pm 1.5$, $v_1 = 0.64 \pm 0.02 \text{ km s}^{-1}$, $v_2 = 0.20 \pm 0.02 \text{ km s}^{-1}$, and $\theta = 74^\circ \pm 7^\circ$; the jet outflow axis was held fixed toward the Sun due to a lack of constraints (resulting from the lower spectral resolution of this data). The different component outflow velocities compared to those derived from the JCMT observations 3–5 weeks earlier (Section 4.3) imply an increase in the jet outflow velocity

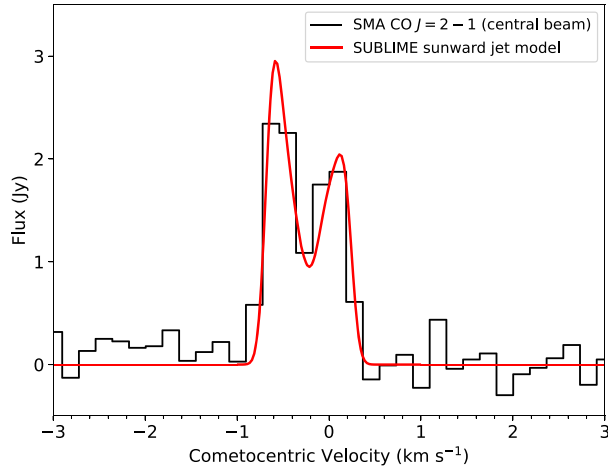


Figure 10. CO $J = 2 - 1$ spectrum observed with the SMA (extracted at the CO emission peak), with the best-fitting two-component SUBLIME model overlaid using a red curve.

accompanied by a slowing of the ambient coma. This could be due to a stronger manifestation of intrinsic coma asymmetry at the higher spatial resolution of the SMA data compared with the JCMT. Changes in CO outflow velocity could also occur as a result of temporal activity variations as the comet moved closer to the Sun.

From this best-fitting base model, additional models were constructed assuming (1) CO solely as a daughter species, with $\Gamma_p = 7.3 \times 10^{-5} \text{ s}^{-1}$ derived from the fit to the JCMT HARP data (Section 4.4); (2) CO as a parent with an additional outer-coma source from CO₂ photolysis; and (3) CO as a parent with an additional extended shell at $r_s = 1.2 \times 10^5 \text{ km}$, with $f = 1.8$. The resulting 3D model images were integrated in the spectral domain and were then multiplied by the (FWHM = 55'') SMA primary beam pattern before sampling in the Fourier domain using the `vis_sample` code (Loomis et al. 2018). Visibility amplitude sampling was performed using the same set of uv distances (baselines) as for the SMA observations (based on the time-averaged antenna positions during the comet observations). A power-law curve (ax^b) was fit through each set of model results (with x as the baseline length, and a and b as free parameters) and plotted along with the observed, time-averaged visibility amplitudes in Figure 11. For clarity, the model visibility curves were scaled vertically in order to pass through the shortest-baseline point. The CO production rate of the best-fitting (scaled) parent model is $Q_t(\text{CO}) = (6.7 \pm 0.6) \times 10^{28} \text{ s}^{-1}$ (the uncertainty increases to $0.9 \times 10^{28} \text{ s}^{-1}$ after the inclusion of a 10% amplitude calibration error). This value is 1.6σ from the mean CO production rate obtained using JCMT, corresponding to a barely significant increase in Q_t with time.

Three of the model curves (parent, parent + CO₂ photolysis, and parent + extended shell) all represent an equally good fit to the observations, falling precisely on top of each other in Figure 11. This implies that SMA would have been blind to the additional CO component observed at large radii in the JCMT maps—i.e., the extended CO component was smooth enough on large angular scales not to be detected on even the shortest SMA baselines. In contrast, the CO daughter model does not fit the observed visibilities well, with insufficient flux on small angular scales (long baselines). Consequently, the SMA observations rule out the possibility of CO being solely a

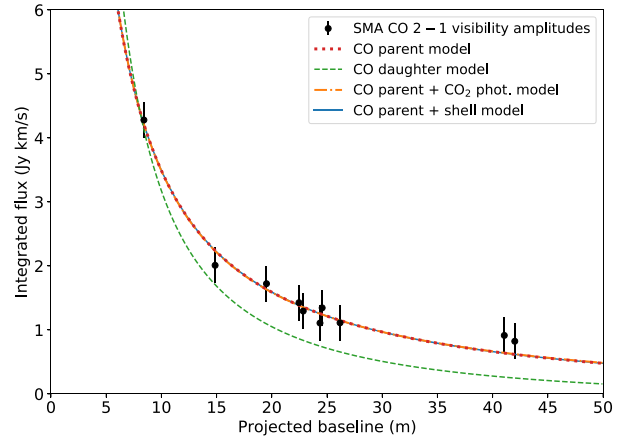


Figure 11. CO $J = 2 - 1$ visibility amplitudes vs. baseline length for C/2016 R2 observed using SMA, including 1σ statistical error bars. Model visibility curves are overlaid for four different CO distributions. The CO parent, parent + CO₂ photolysis, and parent + shell model curves all lie on top of each other, whereas the CO daughter curve differs significantly, underfitting the observations at large baseline (small angular scales).

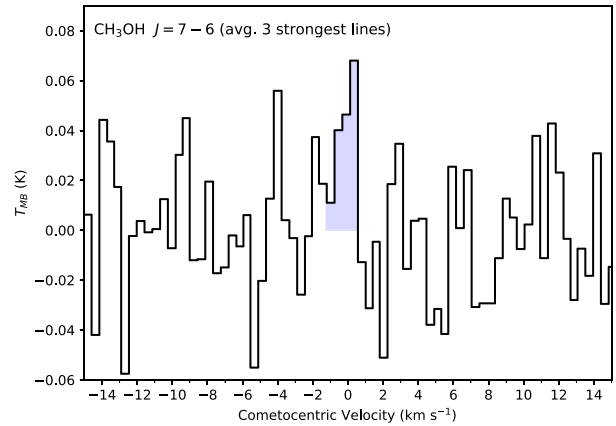


Figure 12. Average (in velocity space) of the three strongest CH₃OH transitions in our JCMT observations ($7_0 - 6_0 E$, $7_{-1} - 6_{-1} E$, and $7_0 - 6_0 A^+$). A tentative feature is present around 0 km s^{-1} (the comet's rest velocity); the blue shaded region shows the velocity range over which significant CO emission was detected.

daughter species in this comet, although significant production at large radii from CO₂ photolysis is still possible.

4.6. Other Molecules from JCMT: CH₃OH, HCN, H₂CO, ¹³CO, and HCO⁺

Our JCMT CH₃OH spectrum covered at least 12 lines of the $K = 7 - 6$ band around 338 GHz (for details of the observed transitions, see Cordiner et al. 2017, their Table 1), but no individual CH₃OH lines were clearly detected in our data. We constructed a preliminary model for the CH₃OH spectrum based on the retrieved coma physical parameters from CO (Section 4.3), and identified three transitions that clearly stood out as stronger than the rest: $J_K = 7_0 - 6_0 E$, $7_{-1} - 6_{-1} E$, and $7_0 - 6_0 A^+$. The observed spectra for these three transitions were then averaged together in velocity space, producing the spectrum in Figure 12. A tentative feature is present around the comet's rest velocity (0 km s^{-1}), with a spectrally integrated

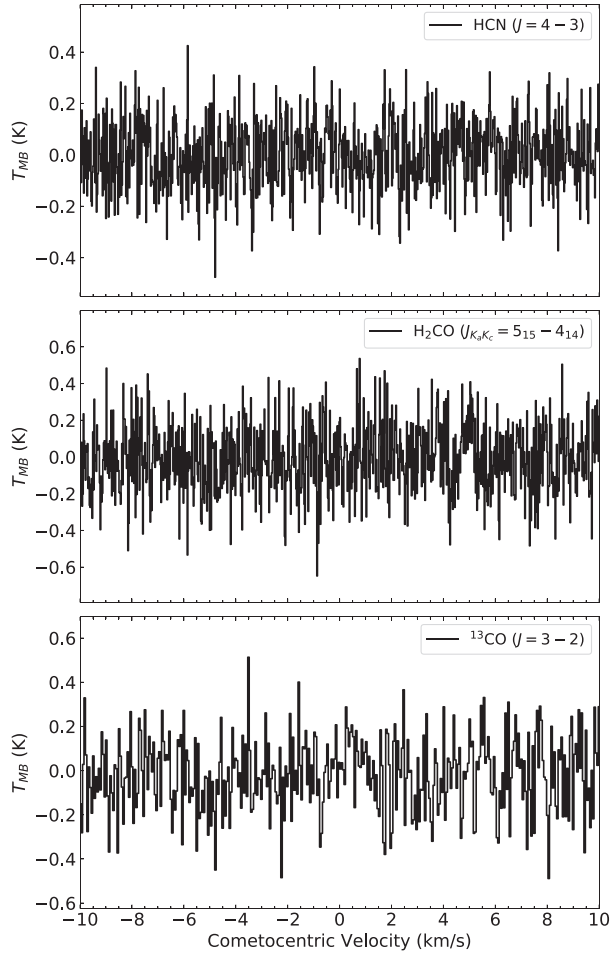


Figure 13. HCN, H₂CO, and ¹³CO spectra observed using JCMT, showing no evidence for detections of these molecules.

intensity (in the range of -1.0 to 0.5 km s⁻¹ shown by the blue shaded region) of $\int T_{\text{MB}} dv = 73 \pm 20$ mK km s⁻¹, corresponding to a 3.6σ detection. Fitting the same three transitions simultaneously using SUBLIME (allowing only the CH₃OH abundance to vary) gave $Q(\text{CH}_3\text{OH}) = (6.7 \pm 2.2) \times 10^{26}$ s⁻¹, which corresponds to a CH₃OH/CO abundance ratio of $1.3 \pm 0.4\%$ at the nucleus. For this model, we adopted CH₃OH–CO collisional transition rates based on the CH₃OH–H₂ rates from Rabli & Flower (2010), with solar pumping rates from Roth et al. (2021a). Uncertainties of a factor of five in the CH₃OH–CO collision rates lead to at most a 7% error on the CH₃OH abundance.

The HCN, H₂CO, and ¹³CO molecules were not detected in our data, as shown by the spectra in Figure 13. Upper limits of 3σ were derived by comparing the spectrally integrated noise level (from -0.8 to 0.5 km s⁻¹) to SUBLIME model line intensities for each molecule (again, using the same coma physical parameters derived in Section 4.3). For HCN we used the same collision and pumping rates as Cordiner et al. (2020), for H₂CO we used the Roth et al. (2021a) rates, and for ¹³CO we used the same rates as for CO. The production rate 3σ upper limits are $Q(\text{HCN}) < 8.3 \times 10^{25}$ s⁻¹, $Q(\text{H}_2\text{CO}) < 2.3 \times 10^{26}$ s⁻¹, and $Q(^{13}\text{CO}) < 2.7 \times 10^{27}$ s⁻¹, corresponding to abundance ratios

HCN/CO $< 0.16\%$, H₂CO/CO $< 0.45\%$, and CO/¹³CO > 19 . The ¹²C/¹³C ratio in CO is therefore consistent with the typical solar system value of 89, as well as the value of 86 ± 9 measured in comet 67P (Altwegg et al. 2019).

We also obtained a nondetection of HCO⁺ $J = 4 - 3$, with $\int T_{\text{MB}} dv < 164$ mK km s⁻¹ (integrated over the velocity range ± 1.5 km s⁻¹). This is about an order of magnitude less than the integrated HCO⁺ $J = 3 - 2$ line brightness observed in comet Hale–Bopp by Milam et al. (2004) using the Sub-Millimeter Telescope (SMT). However, the CO production rate in C/2016 R2 was also less than that in Hale–Bopp by at least an order of magnitude at the time of observation (Biver et al. 1997), so our result does not imply that C/2016 R2 had an unusually low HCO⁺ production rate (considering the importance of CO in coma HCO⁺ synthesis).

5. Discussion

5.1. Comparison with Previous Observations of this Comet

Our primary result is the determination of a revised CO outgassing rate for C/2016 R2: $Q(\text{CO}) = (5.3 \pm 0.6) \times 10^{28}$ s⁻¹ (averaged over the JCMT observing period 2018 January 13 to 2018 February 1). This was subject to a marginally significant rise to $(6.7 \pm 0.9) \times 10^{28}$ s⁻¹ on 2018 February 21, observed using SMA. These results confirm C/2016 R2 as having among the highest CO production rates ever observed in a comet—only a factor of four less than C/1995 O1 (Hale–Bopp) at similar heliocentric distances. Our CO production rates are slightly higher than the average value of $(4.6 \pm 0.4) \times 10^{28}$ s⁻¹ between 2017 December 22 and 2018 January 16 observed by Wierzbach & Womack (2018) using SMT, and similar to the $(5.5 \pm 0.9) \times 10^{28}$ s⁻¹ observed on 2018 February 23 by McKay et al. (2019), consistent with a slow, steady rise in CO activity as the comet moved closer to the Sun (between $r_{\text{H}} = 2.98$ – 2.73 au). The observations by Biver et al. (2018) using the Institute for Radio Astronomy in the Millimeter Range (IRAM) 30 m telescope on 2018 January 24 gave $Q(\text{CO}) = (10.6 \pm 0.5) \times 10^{28}$ s⁻¹, which is approximately double our JCMT value. As shown in Appendix C, the 1D versions of ours and the models of Biver et al. produce near-identical results. The discrepancy in CO production rates is therefore primarily attributable to the unusual complexity of the CO spectral line profile combined with differences between our 3D radiative transfer modeling strategies.

To derive CO production rates, Biver et al. (2018) adopted a spherical coma model divided into three regions of colatitude (γ ; angle measured from the Earth–comet vector), with outflow velocities $v = 0.56$ km s⁻¹ between $\gamma = 0$ – 60° , 0.50 km s⁻¹ between $\gamma = 60^\circ$ – 120° , and no outflow for $\gamma > 120^\circ$. Our model, on the other hand, gives $v_1 = 0.51$ km s⁻¹ in a sunward-facing conical jet and $v_2 = 0.25$ km s⁻¹ in the remaining (ambient) coma. Our chosen model geometry is physically justified based on fluid dynamic and Monte Carlo coma models (e.g., Crifo et al. 1999; Fougere et al. 2016), which show significantly different outflow velocities on the sunward and antisunward sides of the nucleus. The large reduction in the outflow velocity of our model across the entirety of the nightside (most of which overlaps with the $\gamma > 120^\circ$ region of no outflow in the model of Biver et al. 2018) necessitates a lower total production rate in our model compared with that of Biver et al. (2018).

Although our two-component outflow model is sufficient to fit the data in the present study, we concede that it likely represents a simplification of the true physical situation. Continuously variable Q and v as a function of (3D) coma position may be more correct, and could account for smoothly varying temperatures and mixing ratios within the nucleus, while avoiding discontinuities in the model parameters at the (conical) jet boundaries. The reality for C/2016 R2 may therefore involve a continuously variable Q (as in the more complex model presented in Figure 3 of Biver et al. 2018), but with v also allowed to vary more substantially/continuously, as may be expected based on physical models (e.g., Tenishev et al. 2008). Further constraints on the 3D outflow velocity distribution may be obtained from theoretical models, to help break the degeneracy that can occur between Q and v (particularly in the parts of the coma around $\gamma \sim 90^\circ$), in order to obtain the most accurate production rates for an asymmetric coma.

Compared to a completely spherically symmetric outflow model (as used by Wierzbach & Womack 2018 and McKay et al. 2019), our best-fitting two-component model for C/2016 R2 leads to a $\sim 30\%$ lower CO production rate, as a result of reduced outgassing on the antisunward side (see Figure 6). The exact correction factors are, however, dependent on the opening angle of the jet, and are larger if the jet is narrower. Based on the range of opening angles ($\theta = 32\text{--}77^\circ$) obtained on our different JCMT observing dates (Table 2), correction factors in the 29%–48% range are possible, so the CO production rate reported by McKay et al. (2019) should be adjusted to $(2.9\text{--}3.9) \times 10^{28} \text{ s}^{-1}$. Assuming the comet’s H₂O outgassing behavior was similar to that of CO and CH₃OH (see Biver et al. 2018, their Figure 14), the McKay et al. (2019) H₂O production rate may also need to be adjusted. However, the correction factor is much lower for OH (the H₂O daughter fragment observed by McKay et al. 2019), due to the OH kinetic energy gained in the photolysis reaction $\text{H}_2\text{O} + h\nu \rightarrow \text{OH} + \text{H}$, which causes asymmetries in the gas velocity distribution to be smoothed out.

Abundance ratios from a given study tend to be less susceptible to model-dependent and instrumental uncertainties. Our CH₃OH/CO abundance ratio of $1.3\% \pm 0.4\%$ matches the value of Biver et al. (2018) of $1.04\% \pm 0.08\%$, and our HCN/CO and H₂CO/CO upper limits are also consistent with their values of $(3.8 \pm 1.0) \times 10^{-3}\%$ and $0.043\% \pm 0.006\%$, respectively. The CH₃OH/CO ratio is significantly higher than the upper limit of McKay et al. (2019) of 0.38%, which could be indicative of significant temporal variability in the CH₃OH outgassing rate during 2018 January. Alternatively, the higher CH₃OH abundance observed using radio spectroscopy could have been due to additional CH₃OH production in the extended coma (from icy grain sublimation; e.g., Coulson et al. 2017), which was not detected on the smaller angular scales probed by the infrared observations of McKay et al. (2019).

5.2. Molecular Abundances and the True Nature of C/2016 R2 (PanSTARRS)

Using the H₂O production rate from McKay et al. (2019), our JCMT results are consistent with a CO/H₂O ratio ~ 170 , which is ~ 2800 times greater than the average value observed for Oort cloud comets (Dello Russo et al. 2016), and ~ 37 times greater than the highest previously observed in a comet (29P; Ootsubo et al. 2012), thus confirming the extremely CO-rich

nature of C/2016 R2’s coma. The CO/H₂O abundance in cometary comae is observed to vary strongly as a function of heliocentric distance (see Wierzbach & Womack 2018; McKay et al. 2019) due to the very different sublimation temperatures of these gases ($T_{\text{sub}}(\text{CO}) = 24 \text{ K}$ versus $T_{\text{sub}}(\text{H}_2\text{O}) = 152 \text{ K}$), so a reduction in H₂O outgassing is expected for comets at heliocentric distances $\gtrsim 3 \text{ au}$, where the ice temperature falls below $T_{\text{sub}}(\text{H}_2\text{O})$. The CO/H₂O ratio in the coma of C/2016 R2 is several hundred to several thousand times greater than that found in other Oort cloud comets at similar heliocentric distances (Crovisier et al. 1997; Ootsubo et al. 2012; Kawakita et al. 2014), so this comet appears anomalous compared with all those previously observed. It should be kept in mind, however, that the coma abundances are not necessarily representative of those in the nucleus ices.

Cometary nuclei are heterogeneous, containing mixtures of ices in different phases and compositions (A’Hearn et al. 2011; Mumma & Charnley 2011; Altwegg et al. 2019). Chemical differentiation as a function distance below the surface, or the presence of a volatile-depleted outer crust (e.g., Capaccioni et al. 2015), could lead to H₂O being insulated from solar heating while CO continues to sublimate. For example, the 3D numerical nucleus model of Marboeuf & Schmitt (2014) demonstrates that the ratio of CO-to-H₂O production rates could be enhanced by several orders of magnitude by the presence of an insulating dust mantle $\sim 5\text{--}10 \text{ cm}$ thick that hinders H₂O sublimation. Alternatively, a moderate overabundance of CO ice close to the surface could lead to increased cooling by CO sublimation, helping keep the nucleus at a low enough temperature to inhibit H₂O sublimation (Lisse et al. 2021). In that case the comet could maintain a lower H₂O outgassing rate (relative to CO) for a longer duration as it approached the Sun. Either case may not require an extremely anomalous CO/H₂O abundance in the bulk nucleus.

Peculiarities in the coma abundance ratios for several other molecules were reported by Biver et al. (2018) and McKay et al. (2019). Despite similar sublimation temperatures for CH₃OH and HCN (99 K and 95 K, respectively), these two molecules were enriched in the coma (relative to H₂O) by very different amounts: the CH₃OH/H₂O ratio was 163 times the Oort cloud comet average, whereas HCN/H₂O was only 5.9 times the average. Evidently, such enrichment patterns cannot be produced by reduced H₂O outgassing alone, or by a simple temperature dependence of the CH₃OH and HCN sublimation rates. Similarly, the coma CH₄/H₂O ratio is a factor of 206 higher than average, but this is several hundred times less than the CO/H₂O enrichment, despite similar sublimation temperatures for these two molecules (31 K and 24 K, respectively). It is tempting to take such unusual coma abundance patterns to be directly representative of a peculiar nucleus ice composition, but before doing so, it is worth considering the possible role played by ice heterogeneity and molecular trapping at temperatures below $T_{\text{sub}}(\text{H}_2\text{O})$ (i.e., with the comet not yet fully activated).

As shown by laboratory ice sublimation experiments (Collings et al. 2004), volatile gases can be trapped in mixed (H₂O-dominated) ices at temperatures well above their sublimation points, and may be only partially released until the H₂O sublimation temperature is reached ($\sim 150 \text{ K}$). The release of trapped hypervolatiles can also occur as H₂O ice undergoes a phase change from amorphous to crystalline (at $T_{AC} \sim 130 \text{ K}$). Such trapping and release processes are inevitable in mixed

cometary ices, and could explain some of the observed abundance patterns in C/2016 R2. Closely related outgassing behaviors were observed for CO, CO₂, and CH₃OH in comet 67P (Biver et al. 2019; Läuter et al. 2019), consistent with our understanding regarding a common origin for these species in carbon- and oxygen-rich interstellar ices (Fuchs et al. 2009; Garrod & Pauly 2011; Ioppolo et al. 2011). Observations of young stellar objects also indicate mixing of CO, CO₂, and CH₃OH ices in an apolar phase, distinct from the polar, H₂O-dominated ice (Boogert et al. 2015; Penteado et al. 2015). In situ observations of comets 103P (A’Hearn et al. 2011) and 67P (e.g., Migliorini et al. 2016; Gasc et al. 2017) discovered spatial and temporal variations in the coma H₂O/CO₂ ratios, implying nonuniform mixing ratios for these two volatiles within the nucleus. As shown by Davidsson et al. (2021, 2022) for 67P, this could be caused by physical/chemical evolution of the comet’s surface layers due to anisotropic illumination of the comet, but primordial variations in the H₂O/CO₂ ratio intrinsic to the nucleus are also possible. It is therefore plausible that CH₃OH in C/2016 R2 exists as a component within an apolar ice matrix dominated by CO and CO₂, and some of this CH₃OH is released into the coma when CO sublimates (as observed). Meanwhile, a significant CH₃OH component also likely remains frozen as part of the comet’s polar, H₂O-rich ices (Qasim et al. 2018). HCN, on the other hand, could be primarily associated with the (still frozen) H₂O ice rather than the (sublimating) CO component, and would then be only partially outgassed at $T_{\text{sub}}(\text{HCN})$ or T_{AC} . Future studies of cometary CO, CH₃OH, and HCN spatial distributions could help test this hypothesis.

To complete this picture, the C₂H₆ and NH₃ upper limits from McKay et al. (2019) are consistent with moderate-to-no enrichment (with respect to H₂O) and could therefore be associated primarily with the H₂O-dominated ice, while the strongly enriched N₂ and CO₂ are associated more with CO. Observations and laboratory studies show that interstellar CH₄ ice tends to be more associated with H₂O than CO (Öberg et al. 2008; Qasim et al. 2020), while the location of H₂CO ice is less well constrained. The CH₄ and H₂CO enrichment factors in C/2016 R2 (206 and 44, respectively) could thus be explained by the release of trapped volatiles (in H₂O ice) above their respective sublimation temperatures (31 and 64 K; Collings et al. 2004). The increasing similarity to typical abundances (with respect to H₂O) in the sequence CH₄ → H₂CO → HCN is consistent with the decreasing volatility (increasing T_{sub}) of these three species, such that they each behave progressively more like H₂O. We therefore postulate the existence of a rapidly sublimating (apolar) component of ice in C/2016 R2 rich in CO, CO₂, N₂, and CH₃OH, and a second (polar) component containing more CH₄, H₂CO, and HCN mixed with H₂O. If the N₂/CO ratio is higher in the CO-rich ice phase than in the H₂O-rich ice, this could explain why the N₂/CO ratio is lower in fully activated comets than in C/2016 R2.

5.3. Coma Morphology

The highly asymmetric, blueshifted CO line profile of C/2016 R2 is similar to that of the large Centaur 29P/SW 1 (Festou et al. 2001; Gunnarsson et al. 2002), as well as to the CO line profile observed in C/1995 O1 at $r_{\text{H}} \gtrsim 8$ au (Gunnarsson et al. 2003). Our interpretation of the line shape in terms of enhanced CO production and outflow velocity on

the sunward side of the nucleus is consistent with the analysis of the 29P coma by Gunnarsson et al. (2008), and we find a similar ratio of day-to-night hemisphere $Q(\text{CO})$ and v_{out} values in C/2016 R2.

Gunnarsson et al. (2002) also discovered an extended shell of CO emission surrounding 29P, at a cometocentric distance of $r_c \sim 1.4 \times 10^5$ km, based on mapping observations of the $J=2-1$ line in 1998 (although the shell was no longer apparent in 2003 follow-up observations, demonstrating an intermittent nature; Gunnarsson et al. 2008). The spatial properties of this shell are remarkably similar to those of the extended CO emission structure we detected at a similar cometocentric distance in our C/2016 R2 JCMT maps (Section 4.4). Gunnarsson (2003) interpreted the extended CO structure in 29P as arising from sublimation of a population of icy grains long-lived enough to reach 29P’s outer coma. Such an explanation also appears plausible for C/2016 R2, although more detailed modeling would be required to confirm this possibility, and to test the other possible origins for the shell considered in Section 4.4. We do not consider CO₂ to be a likely source for the majority of the extended CO in C/2016 R2 as it would require at least an order of magnitude larger CO₂ production rate than that found by McKay et al. (2019).

A time-variable, diffuse, ring-shaped feature (consistent with excess gas emission) also appeared in the Spitzer IRAC CO + CO₂ images of C/2016 R2 on 2018 February 21—a feature that was not apparent 9 days earlier (see Figure 5 of McKay et al. 2019). The approximate diameter of this ring was also $\sim 1.4 \times 10^5$ km (M. Kelley, 2021, private communication), so it could plausibly be related to the shell-like feature observed using JCMT. Detailed modeling of the Spitzer images will be required to determine the physical properties of this ring, and to confirm whether icy grain sublimation or coma deceleration could be responsible.

On both dates, the Spitzer images also show enhanced gas emission within an angular wedge (of opening angle $\sim 80^\circ$), oriented toward the (sky-projected) comet–Sun vector, with a morphology consistent with a jet or fan emanating from the nucleus. Although this feature may be attributable to a combination of both CO and CO₂ emission, its apparent qualitative similarity to the jet properties derived from modeling our JCMT and SMA data provides further evidence for preferential sunward outgassing from a confined region of the nucleus. This provides additional validation of our two-component coma model.

5.4. Uncertainties in the CO Excitation

Our new CO–CO collisional rate coefficients are considered to be accurate to within about a factor of two (Section 4.1). As shown in Figure 15 (Appendix C), differences in the rates on that order lead only to relatively small discrepancies in the CO rotational level populations, the evolution of which is controlled to a large extent by radiative processes, especially in the outer coma. As a result, varying the collision rates by $\pm 1\%$ in our retrieved CO production rates.

An additional source of error in the CO excitation calculation arises from the fact that the collision rates are tabulated as a function of T_{rot} , which provides only an average measure of the true distribution of energy-level populations. In a non-LTE regime, individual-level populations may deviate from the Boltzmann distribution, in which case the (thermally averaged)

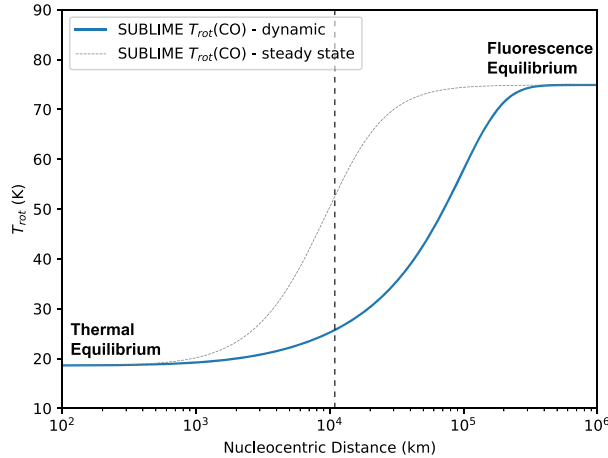


Figure 14. Modeled CO rotational temperature derived using the seven lowest energy levels, from our time-dependent SUBLIME model (solid blue curve) and the steady-state version of the model (dotted gray curve), based on the data shown in Figure 9. The rotational temperature evolves from thermal equilibrium at the gas kinetic temperature (18.7 K) in the collisionally dominated inner coma, to fluorescence equilibrium (at 75 K) in the solar radiation-dominated outer coma. The vertical dashed line shows the radial extent of the 14'' JCMT beam FWHM at the geocentric distance of C/2016 R2 (2.14 au), at 346 GHz.

state-to-state collision rate coefficients are no longer accurate. Perhaps more importantly, the rate coefficients are dependent on T_{rot} as well as T_{kin} , yet for the purpose of choosing rates in our model, we assume $T_{rot} = T_{kin}$, which is only strictly accurate in the collisionally dominated inner coma. Both these issues have negligible impact on the results of our study, however, since the collision rates k_{ij} are found not to vary strongly as a function of T_{rot} , changing by on average only 9% between 10–30 K.

For deriving accurate CO abundances, rather than having the most precise set of collision rate coefficients, it is more important to use the most physically accurate, time-dependent solution to the equation of statistical equilibrium (Bockelee-Morvan 1987; Biver 1997), as opposed to the steady-state approximation (Hogerheijde et al. 2009; de Val-Borro et al. 2018). Figure 9 shows a comparison between the CO level populations as a function of radius using these two different methods, while Figure 14 shows the corresponding rotational temperature behavior. As described by Garcia-Berrios et al. (2020), species with small dipole moments such as CO have long timescales τ_R with respect to spontaneous (and induced) rovibrational radiative transitions. If τ_R is greater than the dynamical timescale in the outflow (i.e., the time for the coma gas to move a given distance r_d), then an accurate calculation of the excitation over distances r_d requires the gas motion to be considered, and the steady-state approximation is no longer valid.

An observational consequence for molecules with large τ_R is that the non-LTE effects occur further out in the coma, because the time-dependent solution (solid curves in Figures 9 and 14) is delayed with respect to the steady-state solution (dashed curves). For the $J=3$ level populations, the discrepancy is minimal (amounting to <1% difference in the $J=3-2$ line integrated intensity). However, for the $J=2-1$ line, the steady-state solution overestimates the line intensity by 19%. For larger beam sizes more sensitive to the non-LTE region of

the coma (between the thermal and fluorescence equilibrium extremes highlighted in Figure 14), the discrepancy can be even larger. Consequently, the use of a time-dependent excitation model is recommended for correct analysis of single-dish cometary CO data. It should be borne in mind that this issue is less severe for molecules with larger dipole moments (and therefore, smaller τ_R values) such as H₂O, HCN, CH₃OH, and H₂CO, although in low-activity comets the premature departure from LTE of the steady-state solution can still lead to some large discrepancies. For example, in a comet at $r_H = \Delta = 1$ au, with $Q(\text{H}_2\text{O}) = 10^{27} \text{ s}^{-1}$, $T_{kin} = 50$ K, and $v_{out} = 0.8 \text{ km s}^{-1}$, the HCN $J=4-3$ line intensity (for a 14'' JCMT beam) is overestimated in the steady-state model by 46%, whereas at $Q(\text{H}_2\text{O}) = 10^{29} \text{ s}^{-1}$ the discrepancy is reduced to only 4%.

6. Conclusions

Based on high-resolution spectral-spatial observations using the JCMT and SMA telescopes during the period 2018 January 13 to 2018 February 21, we confirm the presence of extremely strong, asymmetric CO outgassing from the hypervolatile-rich comet C/2016 R2 (PanSTARRS), with $Q(\text{CO})$ in the range of $(3.8 - 7.6) \times 10^{28} \text{ s}^{-1}$. The observational data were analyzed using a new, time-dependent, 3D radiative transfer code, adopting a two-component model for the expanding coma, for the first time using state-to-state CO-CO collision rates based on quantum scattering calculations using the coupled-states method. We determined the presence of a (near-)sunward CO jet with a (time-variable) half-opening angle of $\theta = 25^\circ - 90^\circ$ (and an average of $\theta = 62^\circ \pm 2^\circ$, offset by $7^\circ \pm 2^\circ$ from the Sun-comet vector). The average jet outflow velocity determined from our JCMT data was $0.51 \pm 0.01 \text{ km s}^{-1}$, while the ambient coma outflow velocity was found to be $0.25 \pm 0.01 \text{ km s}^{-1}$. The total amount of CO produced by the jet was, on average, a factor of two more than that of the ambient coma.

On 2018 January 14–15, we found evidence for extended CO emission that cannot be easily explained by standard nucleus outgassing or excitation effects. The extended emission is therefore interpreted as a possible result of modulation in the CO outgassing rate, deceleration in the outer coma, or sublimation of long-lived icy grains. Subtraction of such an extended CO component from the best-fitting (time-averaged) JCMT 3–2 model results in a 17% reduction in the CO production rate derived for the nucleus. Using the $Q(\text{H}_2\text{O})$ value from McKay et al. (2019), our CO/H₂O ratio is ~ 37 times larger than seen in any comet to date (including the distant Centaur 29P), which, combined with previously noted chemical peculiarities, suggests that C/2016 R2 is among the most unusual comets ever observed.

However, the heterogeneous nature of cometary ices, combined with knowledge that molecular outgassing rates from mixed ices do not necessarily correlate with their sublimation temperatures, means that we cannot yet rule out a bulk composition for C/2016 R2 more similar to the general population of Oort cloud comets than previously inferred. We hypothesize that the ice temperature of C/2016 R2 may have been suppressed by sublimative cooling, or the presence of an unusually thick insulating crust, which prevented the initiation of a more conventional, H₂O-dominated outgassing regime, leading to sublimation rates more heavily influenced by trapping and binding of individual molecules within the bulk

ices. We propose that the observed abundance patterns can be explained by the existence of two ice phases in C/2016 R2, similar to those observed in young stellar objects: (1) an apolar phase, rich in CO, CO₂, N₂, as well as CH₃OH ices; and (2) a polar phase containing larger abundances of CH₄, H₂CO, and HCN mixed in with H₂O ice. More observations of coma chemistry in distant comets (at $r_H \gtrsim 2.5$ au, for which H₂O sublimation is not yet fully activated) will be crucial to better understand this comet's peculiar nature, and to constrain the physical and chemical processes that govern the formation, storage, and release of cometary volatiles below the H₂O sublimation point.

This work was supported by the National Science Foundation under grant No. AST-2009253. The work of S.N.M., N.X.R., M.A.C., E.G.B., and S.B.C. was also supported by NASA's Planetary Science Division Internal Scientist Funding Program through the Fundamental Laboratory Research work package (FLaRe). S.N.M. and S.B.C. were supported by the NASA Astrobiology Institute through the Goddard Center for Astrobiology. The James Clerk Maxwell Telescope is operated by the East Asian Observatory on behalf of The National Astronomical Observatory of Japan, Academia Sinica Institute of Astronomy and Astrophysics, the Korea Astronomy and Space Science Institute, the National Astronomical Observatories of China, and the Chinese Academy of Sciences (grant No. XDB09000000), with additional funding support from the Science and Technology Facilities Council of the United Kingdom and participating universities in the United Kingdom and Canada. The Submillimeter Array is a joint project between the Smithsonian Astrophysical Observatory and the Academia Sinica Institute of Astronomy and Astrophysics and is funded by the Smithsonian Institution and the Academia Sinica. We gratefully acknowledge the assistance of R. Loomis and S. Andrews with the use of the `vis_sample` code. We thank N. Biver for providing comparison radiative transfer model calculations. Thanks also to A. McKay for providing comments on the manuscript regarding the nucleus and coma composition.

Software: CASA (v5.1; Jaeger 2008), SMA-MIR (<https://github.com/qi-molecules/sma-mir>), LIME code (Brinch & Hogerheijde 2010), CVODE solver (Hindmarsh 2019), Moscat (Hutson & Green 1994), `vis_sample` (Loomis et al. 2018), MPFIT (Markwardt 2012).

Appendix A Equations of Radiative Transfer and Molecular Excitation

The intensity of radiation (I_ν) propagating through the coma at a frequency ν is calculated by integrating the equation of radiative transfer as a function of distance along the line of sight (s),

$$\frac{dI_\nu}{ds} = j_\nu - \alpha_\nu I_\nu, \quad (\text{A1})$$

where j_ν and α_ν are the gas emission and absorption coefficients, respectively. These are derived from the Einstein coefficients of the gas (A_{ij} , B_{ij} , and B_{ji} , for a transition between the upper energy level i and lower level j), as

$$j_\nu = \frac{h\nu}{4\pi} N_j A_{ij} \psi_\nu, \quad (\text{A2})$$

$$\alpha_\nu = \frac{h\nu}{4\pi} (N_i B_{ij} - N_j B_{ji}) \psi_\nu, \quad (\text{A3})$$

where N_i , N_j are the number of gas particles per unit volume in levels i and j , respectively, and ψ_ν is a (normalized) line-broadening function for the spectral line of interest (typically a Gaussian for individual, thermally broadened lines).

The number of molecules (per unit volume) in energy level i is obtained as a function of time (t) in the outflowing coma gas by solving the following differential equation (e.g., Crovisier 1987):

$$\frac{dN_i}{dt} = -N_i \left[\sum_{j<i} A_{ij} + \sum_{j \neq i} (B_{ij} J_\nu + k_{ij} n + G_{ij}) \right] + \sum_{j>i} N_j A_{ji} + \sum_{j \neq i} N_j (B_{ji} J_\nu + k_{ji} n + G_{ji}). \quad (\text{A4})$$

In this equation, k_{ij} are the rates at which transitions occur between rotational levels i and j (in the ground vibrational state) due to collisions between the gas particles, n is the number density of colliders (in this case, the CO gas density), and G_{ij} are the effective transition rates due to fluorescence/vibrational pumping by solar radiation, summed over the relevant rovibrational bands (see, e.g., Crovisier & Encrenaz 1983; Bensch & Bergin 2004). The energy-level populations at a given location in the coma depend on the local radiation field, J_ν , which is calculated by summing the incident radiant energy received at that point from all solid angles. In general, this means that Equation (A4) needs to be solved iteratively until convergence of J_ν is achieved. In practice however, for species other than H₂O the optical depth for photons leaving the less dense parts of the coma where non-LTE effects are important tends to be low (i.e., $\tau_\nu \ll 1$). In that case, the stimulated emission and absorption terms ($B_{ji} J_\nu$) are small, and can be neglected. For more optically thick gases, the escape probability method can be used as a quick (and easy to implement) approximation for the effects of photon trapping (e.g., Bockelee-Morvan 1987).

Solar radiation-induced fluorescence (pumping) is responsible for modifying the rotational level populations. Effective pumping rates (G_{ij}) for CO were calculated using the method of Crovisier & Encrenaz (1983), incorporating the latest infrared transition data from the HITRAN catalog (Gordon et al. 2021). The effective pumping rates were summed over all rovibrational transitions involving the ground vibrational state of CO. Excitation of the gases of interest due to collisions with coma electrons has also been implemented in SUBLIME using the method of Biver (1997) and Zakharov et al. (2007), but for the present study focusing on CO emission from a CO-dominated coma, the electron-collision rates are found to be small enough that they can be neglected.

Appendix B State-to-state Collision Rates for the CO–CO System

Table 3 shows collisional (de-excitation) rate coefficients $k_{J_1 \rightarrow J_2} = k_{ji}$ (in cm³ s⁻¹) for gas-phase CO molecules undergoing transitions $J_1 \rightarrow J_2$, as a function of kinetic temperature (T_{kin}). The reverse (excitation) rates are calculated from the principle of detailed balance according to Equation (6) of van der Tak et al. (2007). For further details of the rate coefficient calculations, see Section 4.1.

Table 3
CO–CO State-to-state Collision Rate Coefficients $k_{J_1 \rightarrow J_1'}$ as a Function of T_{kin}

J_1	J_1'	T_{kin}			
		5 K	10 K	20 K	30 K
1	0	2.69e-11	3.61e-11	4.01e-11	4.13e-11
2	0	2.73e-11	3.03e-11	2.97e-11	2.81e-11
2	1	5.56e-11	6.23e-11	6.69e-11	6.70e-11
3	0	1.81e-11	2.02e-11	1.96e-11	1.81e-11
3	1	4.73e-11	5.14e-11	5.40e-11	5.30e-11
3	2	8.19e-11	7.88e-11	7.67e-11	7.50e-11
4	0	1.42e-11	1.49e-11	1.43e-11	1.30e-11
4	1	3.55e-11	3.74e-11	3.73e-11	3.49e-11
4	2	6.01e-11	6.22e-11	6.28e-11	6.10e-11
4	3	5.78e-11	6.66e-11	7.01e-11	6.98e-11
5	0	9.94e-12	9.69e-12	8.43e-12	7.43e-12
5	1	2.82e-11	2.95e-11	2.77e-11	2.54e-11
5	2	4.17e-11	4.30e-11	4.13e-11	3.84e-11
5	3	5.98e-11	6.46e-11	6.36e-11	6.06e-11
5	4	5.59e-11	6.40e-11	6.74e-11	6.64e-11

Appendix C Benchmarking the SUBLIME CO Model

To confirm the accuracy of our coma radiative transfer and excitation model, we compared results with the similar, well-tested model of N. Biver (2021, private communication). Their model has been used to analyze millimeter/submillimeter rotational spectra of numerous comets over the last few decades (e.g., Biver et al. 1999; Bockelée-Morvan et al. 2012; Biver et al. 2016, 2019), and is based on the formalism presented by Crovisier (1987) and Bockelee-Morvan (1987), described in more detail by Biver (1997) and Bockelée-Morvan et al. (2004a). Figure 15 shows a comparison between the computed CO energy-level populations from their model and our SUBLIME model, adopting a spherically symmetric (1D) outflow geometry with $Q(\text{CO}) = 5 \times 10^{28} \text{ s}^{-1}$, a constant kinetic temperature of $T_{\text{kin}} = 20 \text{ K}$, and an outflow velocity of $v_{\text{out}} = 0.5 \text{ km s}^{-1}$, at a heliocentric distance of $r_{\text{H}} = 2.8 \text{ au}$. The results of the Biver et al. (2021, private communication) model are shown with dashed lines, whereas our model is shown with solid lines.

The model populations are in very close agreement considering the complexity of the calculation and the different assumptions regarding the relevant molecular parameters. Outside of the collisionally dominated (LTE) zone, the models diverge slightly, primarily as a result of the different treatments of CO–CO collision rates—we are using quantum-mechanically derived state-specific rate coefficients, whereas their model uses thermalizing rate coefficients based on an (assumed) uniform collisional cross-section. Slight differences are also evident at fluorescence equilibrium (largest nucleocentric distances, where the populations reach a steady state with respect to the solar radiation field), presumably due to small differences in the rovibrational Einstein A coefficients used to derive the pumping rates (our model uses the latest HITRAN data).

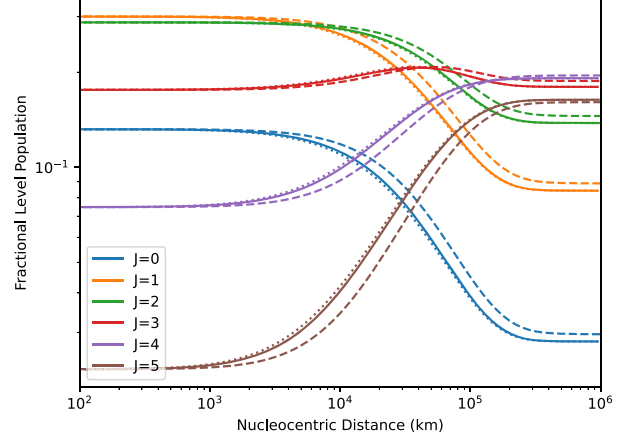


Figure 15. Fractional CO rotational energy-level populations for $J = 0$ – 5 as a function of radius, based on a non-LTE, spherically symmetric coma model with $Q(\text{CO}) = 5 \times 10^{28} \text{ s}^{-1}$, $T_{\text{kin}} = 20 \text{ K}$, $v_{\text{out}} = 0.5 \text{ km s}^{-1}$, and $r_{\text{H}} = 2.8 \text{ au}$. Solid curves are using the time-dependent version of SUBLIME, with CO–CO collision rates from Section 4.1; dotted curves are assuming that the CO–CO collision rates are the same as the CO–H₂ rates from Yang et al. (2010); and dashed curves are using the model of Biver et al. (2018).

As a test of the SUBLIME ray-tracing algorithm, we compared integrated line fluxes from our output model spectral images for two different CO lines, convolved to the JCMT spatial resolution. For the $J = 2 - 1$ line, we obtained $\int T_{\text{R}} dv = 0.37 \text{ K km s}^{-1}$, compared with 0.36 K km s^{-1} from the model of Biver et al. (2019), and for $J = 3 - 2$ we have $\int T_{\text{R}} dv = 0.64 \text{ K km s}^{-1}$, compared with 0.63 K km s^{-1} , again, demonstrating very good agreement between our models, at a level much less than the observational uncertainties.

Figure 15 also shows (with a dotted line) the level populations derived from the same SUBLIME model, but using CO–H₂ rates from Yang et al. (2010) to approximate the CO–CO collision rates, instead of our new state-specific CO–CO rates calculated in Section 4.1 (for $J < 6$). At 20 K, the new rate coefficients differ by up to a factor of 7.1 from those of CO–H₂, with a mean ratio between the new and H₂-derived rates of 2.3. The resulting discrepancy in the final results between coma models using the new rate coefficients as opposed to adopting CO–H₂ rates, however, is relatively small.

Appendix D Azimuthally Averaged JCMT HARP Spectra

Azimuthal averages (about the central pixel) of the JCMT HARP CO 3–2 spectral–spatial data cube are shown in Figure 16. These are based on the average of the HARP jiggle-map observations from 2018 January 14 and 2018 January 15. Each spectrum has been scaled (normalized to the same peak value as the spectrum from the central pixel) to cancel out the rapid decay in the overall line intensity with radius due to the falling coma density. Within the noise, there is no obvious evolution in the spectral line profile with distance from the comet.

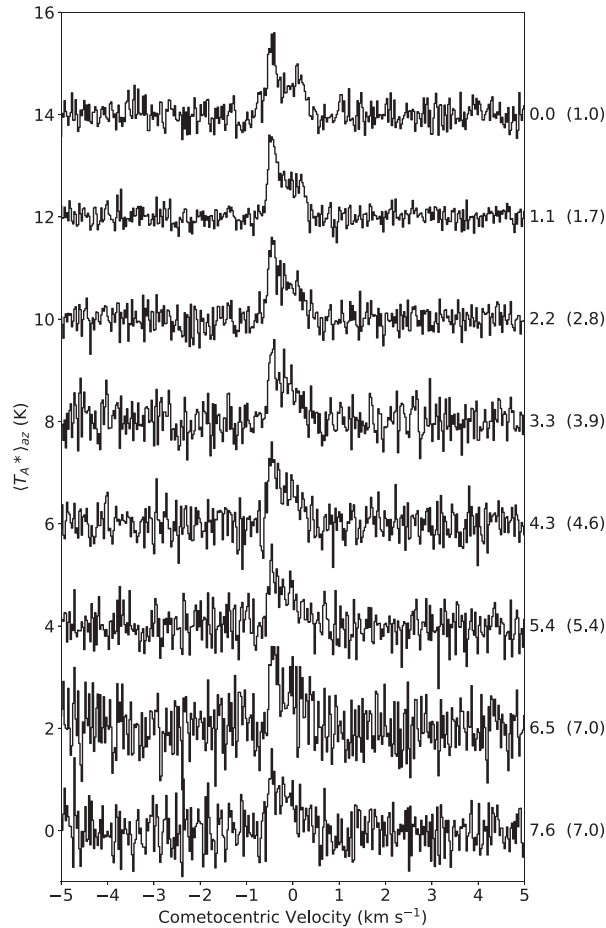


Figure 16. Azimuthally averaged CO 3 – 2 spectra, based on JCMT HARP jiggle maps (combined data from 2018 January 14 and 2018 January 15). These are the mean spectra within successive ring-shaped annuli (1 pixel thick), centered on the nucleus, and show the spectral profile as a function of radial offset from the comet (from top to bottom). The numbers to the right of each spectrum indicate the radius of each annulus in units of 10^4 km. The spectra have each been scaled for display purposes (normalized to the same peak value as the central, 0.0 km spectrum) with scale factors denoted by the numbers in parentheses.

ORCID iDs

M. A. Cordiner <https://orcid.org/0000-0001-8233-2436>
 I. M. Coulson <https://orcid.org/0000-0002-7316-4626>
 E. Garcia-Berrios <https://orcid.org/0000-0002-1069-2931>
 C. Qi <https://orcid.org/0000-0001-8642-1786>
 F. Lique <https://orcid.org/0000-0002-0664-2536>
 M. de Val-Borro <https://orcid.org/0000-0002-0455-9384>
 Y.-J. Kuan <https://orcid.org/0000-0002-4336-0730>
 S. Mairs <https://orcid.org/0000-0002-6956-0730>
 N. X. Roth <https://orcid.org/0000-0002-6006-9574>
 S. B. Charnley <https://orcid.org/0000-0001-6752-5109>
 S. N. Milam <https://orcid.org/0000-0001-7694-4129>
 W.-L. Tseng <https://orcid.org/0000-0001-7322-3801>
 Y.-L. Chuang <https://orcid.org/0000-0001-5653-3584>

References

A’Hearn, M. F., Belton, M. J. S., Delamere, W. A., et al. 2011, *Sci*, **332**, 1396
 Altwegg, K., Balsiger, H., & Fuselier, S. A. 2019, *ARA&A*, **57**, 113

Bensch, F., & Bergin, E. A. 2004, *ApJ*, **615**, 531
 Biver, N. 1997, PhD Thesis, Univ. Paris 7-Didero
 Biver, N., Bockelée-Morvan, D., Colom, P., et al. 1997, *Sci*, **275**, 1915
 Biver, N., Bockelée-Morvan, D., Crovisier, J., et al. 1999, *AJ*, **118**, 1850
 Biver, N., Bockelée-Morvan, D., Hofstadter, M., et al. 2019, *A&A*, **630**, A19
 Biver, N., Bockelée-Morvan, D., Paubert, G., et al. 2018, *A&A*, **619**, A127
 Biver, N., Moreno, R., Bockelée-Morvan, D., et al. 2016, *A&A*, **589**, A78
 Bockelée-Morvan, D. 1987, *A&A*, **181**, 169
 Bockelée-Morvan, D., Biver, N., Colom, P., et al. 2004b, *Icar*, **167**, 113
 Bockelée-Morvan, D., Biver, N., Swinyard, B., et al. 2012, *A&A*, **544**, L15
 Bockelée-Morvan, D., Crovisier, J., Mumma, M. J., & Weaver, H. A. 2004a, in *Comets II*, ed. G. W. Kronk (Tucson, AZ: Univ. Arizona Press), 391
 Bockelée-Morvan, D., Hartogh, P., Crovisier, J., et al. 2010, *A&A*, **518**, L149
 Bøgelund, E. G., & Hogerheijde, M. R. 2017, *A&A*, **604**, A131
 Boissier, J., Bockelée-Morvan, D., Biver, N., et al. 2007, *A&A*, **475**, 1131
 Boogert, A. C. A., Gerakines, P. A., & Whittet, D. C. B. 2015, *ARA&A*, **53**, 541
 Brinch, C., & Hogerheijde, M. R. 2010, *A&A*, **523**, A25
 Buckle, J. V., Hills, R. E., Smith, H., et al. 2009, *MNRAS*, **399**, 1026
 Capaccioni, F., Coradini, A., Filacchione, G., et al. 2015, *Sci*, **347**, aaa0628
 Cochran, A. L., Barker, E. S., & Gray, C. L. 2012, *Icar*, **218**, 144
 Cochran, A. L., & McKay, A. J. 2018, *ApJL*, **854**, L10
 Collings, M. P., Anderson, M. A., Chen, R., et al. 2004, *MNRAS*, **354**, 1133
 Cordiner, M. A., Biver, N., Crovisier, J., et al. 2017, *ApJ*, **837**, 177
 Cordiner, M. A., Milam, S. N., Biver, N., et al. 2020, *NatAs*, **4**, 861
 Cordiner, M. A., Palmer, M. Y., de Val-Borro, M., et al. 2019, *ApJL*, **870**, L26
 Cordiner, M. A., Remijan, A. J., Boissier, J., et al. 2014, *ApJL*, **792**, L2
 Cottin, H., & Fray, N. 2008, *SSRv*, **138**, 179
 Coulson, I. M., Cordiner, M. A., Kuan, Y.-J., et al. 2017, *AJ*, **153**, 169
 Coulson, I. M., Liu, F.-C., Cordiner, M. A., et al. 2020, *AJ*, **160**, 182
 Crifo, J. F., Rodionov, A. V., & Bockelée-Morvan, D. 1999, *Icar*, **138**, 85
 Crovisier, J. 1987, *A&AS*, **68**, 223
 Crovisier, J., & Encrenaz, T. 1983, *A&A*, **126**, 170
 Crovisier, J., Leech, K., Bockelée-Morvan, D., et al. 1997, *Sci*, **275**, 1904
 Davidsson, B. J. R., Birch, S., Blake, G. A., et al. 2021, *Icar*, **354**, 114004
 Davidsson, B. J. R., Samarasinha, N. H., Farnocchia, D., & Gutiérrez, P. J. 2022, *MNRAS*, **509**, 3065
 de Val-Borro, M., Milam, S. N., Cordiner, M. A., et al. 2018, *ATel*, **11254**, 1
 Delaunay, B. 1934, *Bulletin de l’Académie des Sciences de l’URSS*, **6**, 793
 Dello Russo, N., Kawakita, H., Vervack, R. J., & Weaver, H. A. 2016, *Icar*, **278**, 301
 Festou, M. C., Gunnarsson, M., Rickman, H., Winnberg, A., & Tancredi, G. 2001, *Icar*, **150**, 140
 Fougere, N., Altwegg, K., Berthelier, J. J., et al. 2016, *A&A*, **588**, A134
 Fougere, N., Combi, M. R., Tenishev, V., et al. 2012, *Icar*, **221**, 174
 Fuchs, G. W., Cuppen, H. M., Ioppolo, S., et al. 2009, *A&A*, **505**, 629
 Garcia-Berrios, E., Cordiner, M. A., Charnley, S. B., de Val-Borro, M., & Biver, N. 2020, in *14th Europlanet Science Congress 2020*, EPSC2020-426, <https://www.epsc2020.eu/>
 Garrod, R. T., & Pauly, T. 2011, *ApJ*, **735**, 15
 Gasc, S., Altwegg, K., Balsiger, H., et al. 2017, *MNRAS*, **469**, S108
 Gordon, I., Rothman, L., Hargreaves, R., et al. 2021, *JQSRT*, **277**, 107949
 Green, S. 1975, *JChPh*, **62**, 2271
 Gunnarsson, M. 2003, *A&A*, **398**, 353
 Gunnarsson, M., Bockelée-Morvan, D., Biver, N., Crovisier, J., & Rickman, H. 2008, *A&A*, **484**, 537
 Gunnarsson, M., Bockelée-Morvan, D., Winnberg, A., et al. 2003, *A&A*, **402**, 383
 Gunnarsson, M., Rickman, H., Festou, M. C., Winnberg, A., & Tancredi, G. 2002, *Icar*, **157**, 309
 Haser, L. 1957, *BSRSL*, **43**, 740
 Hindmarsh, A. C. 2019, *ODEPACK: Ordinary differential equation solver library*, Astrophysics Source Code Library, ascl:1905.021
 Hogerheijde, M. R., Qi, C., de Pater, I., et al. 2009, *AJ*, **137**, 4837
 Huebner, W. F., & Mukherjee, J. 2015, *P&SS*, **106**, 11
 Hutson, J. M., & Green, S. 1994, *MOLSCAT computer code*, v.14, <https://www.theochem.ru.nl/molscat/Section1.html>
 Ioppolo, S., van Boheemen, Y., Cuppen, H. M., van Dishoeck, E. F., & Linnartz, H. 2011, *MNRAS*, **413**, 2281
 Ip, W. H. 1986, *ApJ*, **300**, 456
 Jaeger, S. 2008, in *ASP Conf. Ser. 394, Astronomical Data Analysis Software and Systems XVII*, ed. R. W. Argyle, P. S. Bunclark, & J. R. Lewis (San Francisco, CA: ASP), 623
 Kawakita, H., Dello Russo, N., Vervack, R. J., et al. 2014, *ApJ*, **788**, 110

- Klos, J., & Lique, F. 2018, in *Cold Chemistry: Molecular Scattering and Reactivity Near Absolute Zero*, ed. O. Dulieu & A. Osterwalder (London: Royal Society of Chemistry), 46
- Läuter, M., Kramer, T., Rubin, M., & Altwegg, K. 2019, *MNRAS*, **483**, 852
- Lisse, C. M., Young, L. A., Cruikshank, D. P., et al. 2021, *Icar*, 356, 114072
- Loomis, R. A., Öberg, K. I., Andrews, S. M., et al. 2018, *AJ*, **155**, 182
- Luspay-Kuti, A., Hässig, M., Fuselier, S. A., et al. 2015, *A&A*, **583**, A4
- Marboeuf, U., & Schmitt, B. 2014, *Icar*, **242**, 225
- Markwardt, C. 2012, MPPFIT: Robust nonlinear least squares curve fitting, Astrophysics Source Code Library, ascl:1208.019
- McKay, A. J., DiSanti, M. A., Kelley, M. S. P., et al. 2019, *AJ*, **158**, 128
- Migliorini, A., Piccioni, G., Capaccioni, F., et al. 2016, *A&A*, **589**, A45
- Milam, S. N., Savage, C., Ziurys, L. M., & Wyckoff, S. 2004, *ApJ*, **615**, 1054
- Mumma, M. J., Bonev, B. P., Villanueva, G. L., et al. 2011, *ApJL*, **734**, L7
- Mumma, M. J., & Charnley, S. B. 2011, *ARA&A*, **49**, 471
- Ndengué, S. A., Dawes, R., & Gatti, F. 2015, *JPCA*, **119**, 7712
- Öberg, K. I., Boogert, A. C. A., Pontoppidan, K. M., et al. 2008, *ApJ*, **678**, 1032
- Ootsubo, T., Kawakita, H., Hamada, S., et al. 2012, *ApJ*, **752**, 15
- Paganini, L., Villanueva, G. L., Lara, L. M., et al. 2010, *ApJ*, **715**, 1258
- Penteado, E. M., Boogert, A. C. A., Pontoppidan, K. M., et al. 2015, *MNRAS*, **454**, 531
- Qasim, D., Chuang, K. J., Fedoseev, G., et al. 2018, *A&A*, **612**, A83
- Qasim, D., Fedoseev, G., Chuang, K. J., et al. 2020, *NatAs*, **4**, 781
- Rabli, D., & Flower, D. R. 2010, *MNRAS*, **406**, 95
- Roth, N. X., Milam, S. N., Cordiner, M. A., et al. 2021a, *ApJ*, **921**, 14
- Roth, N. X., Milam, S. N., Cordiner, M. A., et al. 2021b, *PSJ*, **2**, 55
- Sun, Z.-F., van Hemert, M. C., Loreau, J., et al. 2020, *Sci*, 369, 307
- Surin, L. A., Fourzikov, D. N., Giesen, T. F., et al. 2007, *JPCA*, **111**, 12238
- Tenishev, V., Combi, M., & Davidsson, B. 2008, *ApJ*, **685**, 659
- van der Tak, F. F. S., Black, J. H., Schöier, F. L., Jansen, D. J., & van Dishoeck, E. F. 2007, *A&A*, **468**, 627
- Visser, G. W. M., Wormer, P. E. S., & van der Avoird, A. 2003, *PCCP*, **5**, 4767
- Wierzchos, K., & Womack, M. 2018, *AJ*, **156**, 34
- Womack, M., Sarid, G., & Wierzchos, K. 2017, *PASP*, **129**, 031001
- Yang, B., Stancil, P. C., Balakrishnan, N., & Forrey, R. C. 2010, *ApJ*, **718**, 1062
- Zakharov, V., Bockelée-Morvan, D., Biver, N., Crovisier, J., & Lecacheux, A. 2007, *A&A*, **473**, 303

BIBLIOGRAPHY

- [1] A. Dalgarno, “A serendipitous journey,” *Annual Review of Astronomy and Astrophysics*, vol. 46, no. 1, pp. 1–20, 2008. [Online]. Available: <https://doi.org/10.1146/annurev.astro.46.060407.145216>
- [2] E. F. van Dishoeck, “Astrochemistry: overview and challenges,” *Proceedings of the International Astronomical Union*, vol. 13, no. S332, p. 3–22, 2017.
- [3] S. Yamamoto, *Introduction to Astrochemistry*, 01 2017.
- [4] N. Thomas, “Light curves, orbits, and reservoirs,” in *An Introduction to Comets*. Springer, 2020, pp. 281–397.
- [5] A. Cochran, A.-C. Levasseur-Regourd, M. Cordiner, E. Hadamcik, J. Lasue, A. Gicquel, D. Schleicher, S. Charnley, M. Mumma, L. Paganini, D. Bockelee-Morvan, N. Biver, and Y.-J. Kuan, “The composition of comets,” *Space Science Reviews*, vol. 197, 07 2015.
- [6] N. Biver and D. Bockelée-Morvan, “Complex organic molecules in comets from remote-sensing observations at millimeter wavelengths,” *ACS Earth and Space Chemistry*, vol. 3, no. 8, pp. 1550–1555, 2019. [Online]. Available: <https://doi.org/10.1021/acsearthspacechem.9b00130>
- [7] A. Wootten and A. Thompson, “The atacama large millimeter/submillimeter array,” *Proceedings of the IEEE*, vol. 97, no. 8, pp. 1463–1471, aug 2009. [Online]. Available: <https://doi.org/10.1109%2Fjproc.2009.2020572>
- [8] P. Temi, D. Hoffman, K. Ennico, and J. Le, “Sofia at full operation capability: Technical performance,” *Journal of Astronomical Instrumentation*, vol. 07, no. 04, p. 1840011, 2018. [Online]. Available: <https://doi.org/10.1142/S2251171718400111>
- [9] J. P. Gardner, J. C. Mather, M. Clampin, R. Doyon, M. A. Greenhouse, H. B. Hammel, J. B. Hutchings, P. Jakobsen, S. J. Lilly, K. S. Long, J. I. Lunine, M. J. Mccaughrean, M. Mountain, J. Nella, G. H. Rieke, M. J. Rieke, H.-W. Rix, E. P. Smith, G. Sonneborn, M. Stiavelli, H. S. Stockman, R. A. Windhorst, and G. S. Wright, “The james webb space telescope,” *Space Science Reviews*, vol. 123, no. 4, pp. 485–606, apr 2006. [Online]. Available: <https://doi.org/10.1007%2Fs11214-006-8315-7>
- [10] A. McKellar, “Evidence for the molecular origin of some hitherto unidentified interstellar lines,” *Publications of the Astronomical Society of the Pacific*, vol. 52, no. 307, p. 187, jun 1940. [Online]. Available: <https://dx.doi.org/10.1086/125159>
- [11] W. S. Adams, “What Lies Between the Stars,” *Publication of the Astronomical Society of Pacific*, vol. 53, no. 312, p. 73, Apr. 1941.

- [12] A. E. Douglas and G. Herzberg, “Note on CH⁺ in Interstellar Space and in the Laboratory.” *Astrophysical Journal*, vol. 94, p. 381, Sep. 1941.
- [13] C. H. Townes, “16. microwave and radio-frequency resonance lines of interest to radio astronomy,” *Symposium - International Astronomical Union*, vol. 4, p. 92–103, 1957.
- [14] S. Weinreb, A. H. Barrett, M. L. Meeks, and J. C. Henry, “Radio Observations of OH in the Interstellar Medium,” , vol. 200, no. 4909, pp. 829–831, Nov. 1963.
- [15] A. C. Cheung, D. M. Rank, C. H. Townes, D. D. Thornton, and W. J. Welch, “Detection of NH₃ Molecules in the Interstellar Medium by Their Microwave Emission,” , vol. 21, no. 25, pp. 1701–1705, Dec. 1968.
- [16] Cheung, A. C. and Rank, D. M. and Townes, C. H. and Thornton, D. D. and Welch, W. J., “Detection of Water in Interstellar Regions by its Microwave Radiation,” *Nature*, vol. 221, no. 5181, pp. 626–628, Feb. 1969.
- [17] L. E. Snyder, D. Buhl, B. Zuckerman, and P. Palmer, “Microwave detection of interstellar formaldehyde,” *Phys. Rev. Lett.*, vol. 22, pp. 679–681, Mar 1969. [Online]. Available: <https://link.aps.org/doi/10.1103/PhysRevLett.22.679>
- [18] C. P. Endres, S. Schlemmer, P. Schilke, J. Stutzki, and H. S. Müller, “The cologne database for molecular spectroscopy, cdms, in the virtual atomic and molecular data centre, vamdc,” *Journal of Molecular Spectroscopy*, vol. 327, pp. 95–104, 2016, new Visions of Spectroscopic Databases, Volume II. [Online]. Available: <https://www.sciencedirect.com/science/article/pii/S0022285216300340>
- [19] E. Roueff and F. Lique, “Molecular excitation in the interstellar medium: Recent advances in collisional, radiative, and chemical processes,” *Chem. Rev.*, vol. 113, no. 12, pp. 8906–8938, 2013. [Online]. Available: <https://doi.org/10.1021/cr400145a>
- [20] D. Carty, A. Goddard, I. R. Sims, and I. W. M. Smith, “Rotational energy transfer in collisions between CO(X¹+, v=2, J=0, 1, 4, and 6) and He at temperatures from 294 to 15 K,” *The Journal of Chemical Physics*, vol. 121, no. 10, pp. 4671–4683, 2004. [Online]. Available: <https://doi.org/10.1063/1.1780163>
- [21] H. Labiad, M. Fournier, L. A. Mertens, A. Faure, D. Carty, T. Stoecklin, P. Jankowski, K. Szalewicz, S. D. Le Picard, and I. R. Sims, “Absolute measurements of state-to-state rotational energy transfer between CO and H₂ at interstellar temperatures,” *Phys. Rev. A*, vol. 105, p. L020802, Feb 2022. [Online]. Available: <https://link.aps.org/doi/10.1103/PhysRevA.105.L020802>
- [22] L. Scharfenberg, S. Y. T. van de Meerakker, and G. Meijer, “Crossed beam scattering experiments with optimized energy resolution,” *Phys. Chem. Chem. Phys.*, vol. 13, pp. 8448–8456, 2011. [Online]. Available: <http://dx.doi.org/10.1039/C0CP02405H>

- [23] S. Chefdeville, T. Stoecklin, A. Bergeat, K. M. Hickson, C. Naulin, and M. Costes, "Appearance of Low Energy Resonances in CO-Para- H_2 Inelastic Collisions," *Phys. Rev. Lett.*, vol. 109, p. 023201, Jul 2012. [Online]. Available: <https://link.aps.org/doi/10.1103/PhysRevLett.109.023201>
- [24] M. Born and R. Oppenheimer, "Zur Quantentheorie der Molekeln," *Annalen der Physik*, vol. 389, no. 20, pp. 457–484, Jan. 1927.
- [25] J. Čížek, "On the Correlation Problem in Atomic and Molecular Systems. Calculation of Wavefunction Components in Ursell-Type Expansion Using Quantum-Field Theoretical Methods," , vol. 45, no. 11, pp. 4256–4266, Dec. 1966.
- [26] S. D. Augustin and W. H. Miller, "Semiclassical treatment of atom-asymmetric rotor collisions; rotational excitation of formaldehyde at low energies," *The Journal of Chemical Physics*, vol. 61, no. 8, pp. 3155–3163, 1974. [Online]. Available: <https://doi.org/10.1063/1.1682471>
- [27] S. Green, "Rotational excitation of HD by collisions with He," *Physica*, vol. 76, no. 3, pp. 609–615, 1974. [Online]. Available: <https://www.sciencedirect.com/science/article/pii/003189147490161X>
- [28] S. Green and P. Thaddeus, "Rotational excitation of CO by collisions with He, H, and H_2 under conditions in interstellar cloud," *Astrophys. J.*, vol. 205, pp. 766–785, 1976.
- [29] D. R. Flower, "Rotational excitation of OH by H_2 at interstellar temperatures," *Astronomy and Astrophysics*, vol. 83, no. 1-2, pp. 33–37, Mar. 1980.
- [30] D. Flower, "Collisional pumping of a-doublet transitions in CH and OH by H_2 and He," *Chemical Physics Letters*, vol. 67, no. 2, pp. 475–478, 1979. [Online]. Available: <https://www.sciencedirect.com/science/article/pii/0009261479852082>
- [31] S.-I. Chu and A. Dalgarno, "Rotational excitation of CH^+ by electron impact," *Phys. Rev. A*, vol. 10, pp. 788–792, Sep 1974. [Online]. Available: <https://link.aps.org/doi/10.1103/PhysRevA.10.788>
- [32] T. de Jong, S. Chu, and A. Dalgarno, "Carbon monoxide in collapsing interstellar clouds." *Astrophysical Journal*, vol. 199, pp. 69–78, Jul. 1975.
- [33] P. McGuire and D. J. Kouri, "Quantum mechanical close coupling approach to molecular collisions. jz -conserving coupled states approximation," *The Journal of Chemical Physics*, vol. 60, no. 6, pp. 2488–2499, 1974. [Online]. Available: <https://doi.org/10.1063/1.1681388>
- [34] T. Tsien and R. Pack, "Rotational excitation in molecular collisions. a many-state test of the strong coupling approximation," *Chemical Physics Letters*, vol. 8, no. 6, pp.

- 579–581, 1971. [Online]. Available: <https://www.sciencedirect.com/science/article/pii/0009261471800982>
- [35] B. Desrousseaux, M. Konings, J. Loreau, and F. Lique, “HD-H⁺ collisions: new statistical and quantum state-to-state studies,” *Physical Chemistry Chemical Physics*, vol. 23, pp. 19202–19208, Aug. 2021. [Online]. Available: <https://hal.archives-ouvertes.fr/hal-03323406>
- [36] J. Loreau, F. Lique, and A. Faure, “An Efficient Statistical Method to Compute Molecular Collisional Rate Coefficients,” *The Astrophysical Journal*, vol. 853, no. 1, p. L5, Jan. 2018. [Online]. Available: <https://hal.archives-ouvertes.fr/hal-01917983>
- [37] S. A. Ndengué, R. Dawes, and F. Gatti, “Rotational Excitations in CO-CO Collisions at Low Temperature: Time-Independent and Multiconfigurational Time-Dependent Hartree Calculations,” *Journal of Physical Chemistry A*, vol. 119, no. 28, pp. 7712–7723, Jul. 2015.
- [38] A. Faure, F. Lique, and J. Loreau, “The effect of CO-H₂O collisions in the rotational excitation of cometary CO,” *Monthly Notices of the Royal Astronomical Society*, vol. 493, no. 1, pp. 776–782, 01 2020. [Online]. Available: <https://doi.org/10.1093/mnras/staa242>
- [39] C. Boursier, B. Mandal, D. Babikov, and M. L. Dubernet, “New H₂O–H₂O collisional rate coefficients for cometary applications,” *Monthly Notices of the Royal Astronomical Society*, vol. 498, no. 4, pp. 5489–5497, 09 2020. [Online]. Available: <https://doi.org/10.1093/mnras/staa2713>
- [40] M. Dubernet and E. Quintas-Sánchez, “First quantum study of the rotational excitation of HCN by para-H₂O: Convergence of quantum results, influence of the potential energy surface, and approximate rate coefficients of interest for cometary atmospheres,” *Molecular Astrophysics*, vol. 16, p. 100046, 2019. [Online]. Available: <https://www.sciencedirect.com/science/article/pii/S240567581830040X>
- [41] J. Loreau, A. Faure, and F. Lique, “The effect of water and electron collisions in the rotational excitation of HF in comets,” *Monthly Notices of the Royal Astronomical Society*, 08 2022, stac2378. [Online]. Available: <https://doi.org/10.1093/mnras/stac2378>
- [42] E. F. van Dishoeck, E. Herbst, and D. A. Neufeld, “Interstellar water chemistry: From laboratory to observations,” *Chemical Reviews*, vol. 113, no. 12, pp. 9043–9085, 2013, pMID: 24261880. [Online]. Available: <https://doi.org/10.1021/cr4003177>
- [43] M. Żóltowski, F. Lique, A. Karska, and P. S. Żuchowski, “Rotational excitation of highly excited H₂O by H₂,” *Monthly Notices of the Royal Astronomical Society*, vol. 502, no. 4, pp. 5356–5361, 02 2021. [Online]. Available:

<https://doi.org/10.1093/mnras/stab453>

- [44] P. Valiron, M. Wernli, A. Faure, L. Wiesenfeld, C. Rist, S. Kedžuch, and J. Noga, “R12-calibrated H₂O–H₂ interaction: Full dimensional and vibrationally averaged potential energy surfaces,” , vol. 129, no. 13, p. 134306, 2008. [Online]. Available: <https://doi.org/10.1063/1.2988314>
- [45] A. Faure, L. Wiesenfeld, Y. Scribano, and C. Ceccarelli, “Rotational excitation of mono- and doubly-deuterated water by hydrogen molecules,” *Monthly Notices of the Royal Astronomical Society*, vol. 420, no. 1, pp. 699–704, 01 2012. [Online]. Available: <https://doi.org/10.1111/j.1365-2966.2011.20081.x>
- [46] Agúndez, M., Biver, N., Santos-Sanz, P., Bockelée-Morvan, D., and Moreno, R., “Molecular observations of comets C/2012 S1 (ISON) and C/2013 R1 (Lovejoy): HNC/HCN ratios and upper limits to PH₃,” *A&A*, vol. 564, p. L2, 2014. [Online]. Available: <https://doi.org/10.1051/0004-6361/201423639>
- [47] S. D. Rodgers and S. B. Charnley, “HNC and HCN in Comets,” *The Astrophysical Journal*, vol. 501, no. 2, p. L227, jun 1998. [Online]. Available: <https://dx.doi.org/10.1086/311459>
- [48] D. C. Lis, D. Bockelée-Morvan, J. Boissier, J. Crovisier, N. Biver, and S. B. Charnley, “Hydrogen isocyanide in comet 73p/schwassmann-wachmann (fragment b),” *The Astrophysical Journal*, vol. 675, no. 1, p. 931, mar 2008. [Online]. Available: <https://dx.doi.org/10.1086/527345>
- [49] S. D. Rodgers and S. B. Charnley, “On the origin of HNC in Comet Lee,” *Monthly Notices of the Royal Astronomical Society*, vol. 323, no. 1, pp. 84–92, 05 2001. [Online]. Available: <https://doi.org/10.1046/j.1365-8711.2001.04099.x>
- [50] M. Womack, G. Sarid, and K. Wierchos, “CO in Distantly Active Comets,” *Publications of the Astronomical Society of the Pacific*, vol. 129, no. 973, p. 031001, Mar. 2017.
- [51] G. W. M. Vissers, P. E. S. Wormer, and A. van der Avoird, “An ab initio CO dimer interaction potential and the computation of the rovibrational spectrum of (CO)₂,” *Phys. Chem. Chem. Phys.*, vol. 5, pp. 4767–4771, 2003.
- [52] D. Kedziera and A. Kaczmarek-Kedziera, *Remarks on Wave Function Theory and Methods*. Cham: Springer International Publishing, 2017, pp. 123–171. [Online]. Available: https://doi.org/10.1007/978-3-319-27282-5_3
- [53] S. Boys and F. Bernardi, “The calculation of small molecular interactions by the differences of separate total energies. some procedures with reduced errors,” *Molecular Physics*, vol. 19, no. 4, pp. 553–566, 1970. [Online]. Available:

<https://doi.org/10.1080/00268977000101561>

- [54] J. C. Slater, “The Theory of Complex Spectra,” *Physical Review*, vol. 34, no. 10, pp. 1293–1322, Nov. 1929.
- [55] D. R. Hartree and W. Hartree, “Self-Consistent Field, with Exchange, for Beryllium,” *Proceedings of the Royal Society of London Series A*, vol. 150, no. 869, pp. 9–33, May 1935.
- [56] L. Piela, *Idee Chemii Kwantowej*. Warszawa: Wydawnictwo naukowe PWN, 2011, tł.: Kisiel, A., Melzacki, K.
- [57] F. Jensen, *Introduction to Computational Chemistry*. Wiley, 2017. [Online]. Available: <https://books.google.fr/books?id=UZOVDQAAQBAJ>
- [58] J. Dunning, Thom H., “Gaussian basis sets for use in correlated molecular calculations. I. The atoms boron through neon and hydrogen,” *The Journal of Chemical Physics*, vol. 90, no. 2, pp. 1007–1023, Jan. 1989.
- [59] J. Klos and F. Lique, “Chapter 2 cold molecular collisions: Quantum scattering calculations and their relevance in astrophysical applications,” in *Cold Chemistry: Molecular Scattering and Reactivity Near Absolute Zero*. The Royal Society of Chemistry, 2018, pp. 46–91. [Online]. Available: <http://dx.doi.org/10.1039/9781782626800-00046>
- [60] D. Flower, *Molecular Collisions in the Interstellar Medium*, 2nd ed., ser. Cambridge Astrophysics. Cambridge University Press, 2007.
- [61] A. M. Arthurs, A. Dalgarno, and D. R. Bates, “The theory of scattering by a rigid rotator,” *Proc. R. Soc. Lond. A*, vol. 256, no. 1287, pp. 540–551, 1960. [Online]. Available: <https://royalsocietypublishing.org/doi/abs/10.1098/rspa.1960.0125>
- [62] S. Green, “Rotational excitation of symmetric top molecules by collisions with atoms: Close coupling, coupled states, and effective potential calculations for NH₃–He,” *The Journal of Chemical Physics*, vol. 64, no. 8, pp. 3463–3473, 1976. [Online]. Available: <https://aip.scitation.org/doi/abs/10.1063/1.432640>
- [63] P. Pechukas, J. C. Light, and C. Rankin, “Statistical theory of chemical kinetics : Application to neutral-atom—molecule reactions,” *The Journal of Chemical Physics*, vol. 44, no. 2, pp. 794–805, 1966. [Online]. Available: <https://doi.org/10.1063/1.1726760>
- [64] T. González-Lezana, “Statistical quantum studies on insertion atom–diatom reactions,” *International Reviews in Physical Chemistry*, vol. 26, no. 1, pp. 29–91, 2007. [Online]. Available: <https://doi.org/10.1080/03081070600933476>

- [65] K. Park and J. C. Light, “Microcanonical statistical study of ortho-para conversion in the reaction $\text{H}_3^++\text{H}_2\rightarrow(\text{H}_5^+)^*\rightarrow\text{H}_3^++\text{H}_2$ at very low energies,” *The Journal of Chemical Physics*, vol. 126, no. 4, p. 044305, 2007. [Online]. Available: <https://doi.org/10.1063/1.2430711>
- [66] J. Loreau, A. Faure, and F. Lique, “Scattering of CO with H₂O: Statistical and classical alternatives to close-coupling calculations,” *The Journal of Chemical Physics*, vol. 148, no. 24, p. 244308, 2018. [Online]. Available: <https://doi.org/10.1063/1.5036819>
- [67] B. R. Johnson, “New numerical methods applied to solving the one-dimensional eigenvalue problem,” *The Journal of Chemical Physics*, vol. 67, no. 9, pp. 4086–4093, 1977. [Online]. Available: <https://aip.scitation.org/doi/abs/10.1063/1.435384>
- [68] T. Karman, L. M. C. Janssen, R. Sprenkels, and G. C. Groenenboom, “A renormalized potential-following propagation algorithm for solving the coupled-channels equations,” *The Journal of Chemical Physics*, vol. 141, no. 6, p. 064102, 2014. [Online]. Available: <https://doi.org/10.1063/1.4891809>
- [69] F. Olver, D. Lozier, R. Boisvert, and C. Clark, *The NIST Handbook of Mathematical Functions*. Cambridge University Press, New York, NY, 2010-05-12 00:05:00 2010.
- [70] M. H. Alexander and D. E. Manolopoulos, “A stable linear reference potential algorithm for solution of the quantum close-coupled equations in molecular scattering theory,” *The Journal of Chemical Physics*, vol. 86, no. 4, pp. 2044–2050, 1987. [Online]. Available: <https://doi.org/10.1063/1.452154>
- [71] J. Hutson and S. Green, “Computer code molscat, version 14,” *CCP6, Daresbury*, 1994.
- [72] *The HIBRIDON package was written by M. H. Alexander, D. E. Manolopoulos, H.-J. Werner and B. Follmeg, with contributions by P. F. Vohralik, D. Lemoine, G. Corey, R. Gordon, B. Johnson, T. Orlikowski, A. Berning, A. Degli-Esposti, C. Rist, P. Dagdigian, B. Pouilly, G. van der Sanden, M. Yang, F. de Weerd, S. Gregurick, J. Kłos and F. Lique.* [Online]. Available: <http://www2.chem.umd.edu/groups/alexander>
- [73] van der Tak, F. F. S., Black, J. H., Schöier, F. L., Jansen, D. J., and van Dishoeck, E. F., “A computer program for fast non-lte analysis of interstellar line spectra* - with diagnostic plots to interpret observed line intensity ratios,” *A&A*, vol. 468, no. 2, pp. 627–635, 2007. [Online]. Available: <https://doi.org/10.1051/0004-6361:20066820>
- [74] V. V. Sobolev, *Moving Envelopes of Stars*. Cambridge, MA and London, England: Harvard University Press, 1960. [Online]. Available: <https://doi.org/10.4159/harvard.9780674864658>
- [75] J. Surdej, “Contribution to spectral line formation in moving stellar envelopes. Radiation field and statistical equilibrium equations.” *Astronomy and Astrophysics*, vol. 60,

no. 3, pp. 303–311, Sep. 1977.

- [76] T. R. Phillips, S. Maluendes, and S. Green, “Collision dynamics for an asymmetric top rotor and a linear rotor: Coupled channel formalism and application to H₂O–H₂,” *The Journal of Chemical Physics*, vol. 102, no. 15, pp. 6024–6031, 1995. [Online]. Available: <https://doi.org/10.1063/1.469337>
- [77] Y. Scribano, A. Faure, and D. Lauvergnat, “Rotational excitation of H₂O by para-H₂ from an adiabatically reduced dimensional potential,” *The Journal of Chemical Physics*, vol. 136, no. 9, p. 094109, 2012. [Online]. Available: <https://doi.org/10.1063/1.3690881>
- [78] G. J. Herczeg, A. Karska, S. Bruderer, L. E. Kristensen, E. F. van Dishoeck, J. K. Jørgensen, R. Visser, S. F. Wampfler, E. A. Bergin, U. A. Yıldız, K. M. Pontoppidan, and J. Gracia-Carpio, “Water in star-forming regions with herchel/i: highly excited molecular emission from the NGC 1333 IRAS 4b outflow,” *Astronomy and Astrophysics*, vol. 540, p. A84, mar 2012. [Online]. Available: <https://doi.org/10.1051/0004-6361/201117914>
- [79] Goicoechea, J. R., Cernicharo, J., Karska, A., Herczeg, G. J., Polehampton, E. T., Wampfler, S. F., Kristensen, L. E., van Dishoeck, E. F., Etxaluze, M., Berné, O., and Visser, R., “The complete far-infrared and submillimeter spectrum of the class 0 protostar serpens smm1 obtained with herchel - characterizing uv-irradiated shocks heating and chemistry,” *A&A*, vol. 548, p. A77, 2012. [Online]. Available: <https://doi.org/10.1051/0004-6361/201219912>
- [80] Daniel, F., Dubernet, M.-L., and Grosjean, A., “Rotational excitation of 45 levels of ortho/para-H₂O by excited ortho/para-H₂ from 5 K to 1500 K: state-to-state, effective, and thermalized rate coefficients,” *A&A*, vol. 536, p. A76, 2011. [Online]. Available: <https://doi.org/10.1051/0004-6361/201118049>
- [81] M. P. Ziemkiewicz, C. Pluetzer, D. J. Nesbitt, Y. Scribano, A. Faure, and A. van der Avoird, “Overtone vibrational spectroscopy in H₂ - H₂O complexes: A combined high level theoretical ab initio, dynamical and experimental study,” *Journal of Chemical Physics*, vol. 137, no. 8, pp. 084301–084301, Aug. 2012.
- [82] A. Bergeat, A. Faure, S. B. Morales, A. Moudens, and C. Naulin, “Low-Energy Water-Hydrogen Inelastic Collisions,” *J. Phys. Chem. A*, vol. 124, no. 2, pp. 259–264, Jan. 2020.
- [83] B. Yang, M. Nagao, W. Satomi, M. Kimura, and P. C. Stancil, “Rotational quenching of rotationally excited H₂O in collision with He,” , vol. 765, no. 2, p. 77, feb 2013. [Online]. Available: <https://doi.org/10.1088/0004-637x/765/2/77>
- [84] T. Zeng, H. Li, R. J. Le Roy, and P.-N. Roy, “Adiabatic-hindered-rotor treatment of

- the parahydrogen-water complex,” *The Journal of Chemical Physics*, vol. 135, no. 9, p. 094304, 2011. [Online]. Available: <https://doi.org/10.1063/1.3626840>
- [85] H. M. Butner, S. B. Charnley, C. Ceccarelli, S. D. Rodgers, J. R. Pardo, B. Parise, J. Cernicharo, and G. R. Davis, “Discovery of Interstellar Heavy Water,” , vol. 659, no. 2, pp. L137–L140, Apr. 2007.
- [86] Y. Scribano, A. Faure, and L. Wiesenfeld, “Communication: Rotational excitation of interstellar heavy water by hydrogen molecules,” *The Journal of Chemical Physics*, vol. 133, no. 23, p. 231105, 2010. [Online]. Available: <https://doi.org/10.1063/1.3507877>
- [87] D. R. Flower and F. Lique, “Excitation of the hyperfine levels of ^{13}CN and ^{15}N in collisions with H_2 at low temperatures,” *Monthly Notices of the Royal Astronomical Society*, vol. 446, no. 2, pp. 1750–1755, 11 2014. [Online]. Available: <https://doi.org/10.1093/mnras/stu2231>
- [88] Daniel, F., Faure, A., Pagani, L., Lique, F., Gérin, M., Lis, D., Hily-Blant, P., Bacmann, A., and Roueff, E., “ N_2H^+ and N_2NH^+ toward the prestellar core 16293E in L1689N,” *Astronomy and Astrophysics*, vol. 592, p. A45, 2016. [Online]. Available: <https://doi.org/10.1051/0004-6361/201628192>
- [89] F. Dumouchel, F. Lique, A. Spielfiedel, and N. Feautrier, “Hyperfine excitation of C_2H and C_2D by para- H_2 ,” *Monthly Notices of the Royal Astronomical Society*, vol. 471, no. 2, pp. 1849–1855, 07 2017. [Online]. Available: <https://doi.org/10.1093/mnras/stx1707>
- [90] F. Dumouchel, J. Klos, R. Toboła, A. Bacmann, S. Maret, P. Hily-Blant, A. Faure, and F. Lique, “Fine and hyperfine excitation of NH and ND by He : On the importance of calculating rate coefficients of isotopologues,” *The Journal of Chemical Physics*, vol. 137, no. 11, p. 114306, 2012. [Online]. Available: <https://doi.org/10.1063/1.4753423>
- [91] A. J. Misquitta, R. Podeszwa, B. Jeziorski, and K. Szalewicz, “Intermolecular potentials based on symmetry-adapted perturbation theory with dispersion energies from time-dependent density-functional calculations,” *The Journal of Chemical Physics*, vol. 123, no. 21, p. 214103, 2005. [Online]. Available: <https://doi.org/10.1063/1.2135288>
- [92] M. P. Metz and K. Szalewicz, “A statistically guided grid generation method and its application to intermolecular potential energy surfaces,” *The Journal of Chemical Physics*, vol. 152, no. 13, p. 134111, 2020. [Online]. Available: <https://doi.org/10.1063/1.5141777>
- [93] E. Q. Sánchez and M.-L. Dubernet, “Theoretical study of HCN –water interaction: five dimensional potential energy surfaces,” *Phys. Chem. Chem. Phys.*, vol. 19, pp. 6849–6860, 2017. [Online]. Available: <http://dx.doi.org/10.1039/C6CP07894J>

- [94] K. A. Peterson, D. E. Woon, and T. H. Dunning, “Benchmark calculations with correlated molecular wave functions. IV. The classical barrier height of the $H + H_2 \rightarrow H_2 + H$ reaction,” *The Journal of Chemical Physics*, vol. 100, no. 10, pp. 7410–7415, 1994. [Online]. Available: <https://doi.org/10.1063/1.466884>
- [95] O. Denis-Alpizar, Y. Kalugina, T. Stoecklin, M. H. Vera, and F. Lique, “A new ab initio potential energy surface for the collisional excitation of HCN by para- and ortho- H_2 ,” *The Journal of Chemical Physics*, vol. 139, no. 22, p. 224301, 2013. [Online]. Available: <https://doi.org/10.1063/1.4833676>
- [96] F. Dumouchel, J. Klos, and F. Lique, “The rotational excitation of the interstellar HNC by para- and ortho- H_2 ,” *Phys. Chem. Chem. Phys.*, vol. 13, pp. 8204–8212, 2011. [Online]. Available: <http://dx.doi.org/10.1039/C0CP02436H>
- [97] E. Sarrasin, D. B. Abdallah, M. Wernli, A. Faure, J. Cernicharo, and F. Lique, “The rotational excitation of HCN and HNC by he: new insights on the HCN/HNC abundance ratio in molecular clouds,” *Monthly Notices of the Royal Astronomical Society*, feb 2010. [Online]. Available: <https://doi.org/10.1111%2Fj.1365-2966.2010.16312.x>
- [98] M. Hernández Vera, F. Lique, F. Dumouchel, P. Hily-Blant, and A. Faure, “The rotational excitation of the HCN and HNC molecules by H_2 revisited,” *Monthly Notices of the Royal Astronomical Society*, vol. 468, no. 1, pp. 1084–1091, 02 2017. [Online]. Available: <https://doi.org/10.1093/mnras/stx422>
- [99] B. M. Hays, D. Gupta, T. Guillaume, O. Abdelkader Khedaoui, I. R. Cooke, F. Thibault, F. Lique, and I. R. Sims, “Collisional excitation of HNC by He found to be stronger than for structural isomer HCN in experiments at the low temperatures of interstellar space,” *Nature Chemistry*, pp. 1–5, 2022.
- [100] S. Green, “Rotational excitation in H_2 – H_2 collisions: Close-coupling calculations,” *The Journal of Chemical Physics*, vol. 62, no. 6, pp. 2271–2277, 1975. [Online]. Available: <https://doi.org/10.1063/1.430752>
- [101] J. Chen, J. Li, J. M. Bowman, and H. Guo, “Energy transfer between vibrationally excited carbon monoxide based on a highly accurate six-dimensional potential energy surface,” *The Journal of Chemical Physics*, vol. 153, no. 5, p. 054310, 2020. [Online]. Available: <https://doi.org/10.1063/5.0015101>
- [102] R. Dawes, X.-G. Wang, and T. Carrington, “CO Dimer: New Potential Energy Surface and Rovibrational Calculations,” *The Journal of Physical Chemistry A*, vol. 117, no. 32, pp. 7612–7630, 2013, pMID: 23738948. [Online]. Available: <https://doi.org/10.1021/jp404888d>
- [103] Z.-F. Sun, M. C. van Hemert, J. Loreau, A. van der Avoird, A. G.

- Suits, and D. H. Parker, “Molecular square dancing in CO-CO collisions,” *Science*, vol. 369, no. 6501, pp. 307–309, 2020. [Online]. Available: <https://www.science.org/doi/abs/10.1126/science.aan2729>
- [104] L. A. Surin, D. N. Fourzikov, T. F. Giesen, S. Schlemmer, G. Winnewisser, V. A. Panfilov, B. S. Dumesh, G. W. M. Vissers, and A. van der Avoird, “Higher energy states in the co dimer: millimeter-wave spectra and rovibrational calculations,” *The Journal of Physical Chemistry A*, vol. 111, no. 49, pp. 12 238–12 247, 2007, pMID: 17824677. [Online]. Available: <https://doi.org/10.1021/jp0743471>
- [105] M. A. Cordiner, I. M. Coulson, E. Garcia-Berrios, C. Qi, F. Lique, M. Zoltowski, M. de Val-Borro, Y.-J. Kuan, W.-H. Ip, S. Mairs, N. X. Roth, S. B. Charnley, S. N. Milam, W.-L. Tseng, and Y.-L. Chuang, “A SUBLIME 3d model for cometary coma emission: The hypervolatile-rich comet c/2016 r2 (PanSTARRS),” *The Astrophysical Journal*, vol. 929, no. 1, p. 38, apr 2022. [Online]. Available: <https://doi.org/10.3847/1538-4357/ac5893>
- [106] J. M. Hutson and C. R. L. Sueur, “molscat: A program for non-reactive quantum scattering calculations on atomic and molecular collisions,” *Computer Physics Communications*, vol. 241, pp. 9–18, aug 2019. [Online]. Available: <https://doi.org/10.1016%2Fj.cpc.2019.02.014>